Biophysical Investigations into Microbial Physiology and Behavior

by

Matthew Douglas Stilwell

A dissertation submitted in partial fulfillment of

the requirements for the degree of

Doctor of Philosophy

(Biophysics)

at the

UNIVERSITY OF WISCONSIN-MADISON

2017

Date of Final Oral Examination: 12/12/2017

This dissertation is approved by the following members of the Final Oral Committee:

Douglas B. Weibel, Professor, Biochemistry, Chemistry, Biomedical Engineering
James C. Weisshaar, Professor, Chemistry
Qiang Cui, Professor, Chemistry
Jade Wang, Professor, Bacteriology
Randall H. Goldsmith, Assistant Professor, Chemistry

TABLE OF CONTENTS

ACKNOWLEDGEMENTS

I've heard it said in many ways, but always to the same effect: graduate school is challenging. I could not have accomplished the work that went into this dissertation without the tremendous amount of support, guidance, encouragement, friendship, and love that I received along the way. There are far too many people to thank than I can express here, so please know that even if your name is not included in this section, I am still immensely grateful for the help you've given me along the way.

I would first like to thank my advisor, Doug Weibel. Doug gave me the freedom to probe different areas of science. Some of these attempts ended in success, others, less so. I am so grateful that I had the opportunity to try to answer many questions, and I think I am more curious because of it. Doug also gave me the freedom to explore different career trajectories during my time in graduate school and supported me while I did so. Doug taught me to follow my passions, to attempt great things, and that achieving great things requires teamwork. I plan to bring these lessons with me for future challenges. I am thankful to Doug for all the help and support he has given me over the years, from letters of recommendation to writing help to insightful meetings.

Thank you to all the funding sources that helped me succeed in graduate school: NIH, NSF, the Bill & Melinda Gates Foundation, and WARF. I would like to thank my committee members for their guidance throughout the years. I would especially like to

thank Jim Weisshaar for his expertise and guidance, as well as the members of his lab. I am grateful to Heidi Goodrich-Blair for her expertise, guidance, and compassion. I am also grateful to Erin Goley for her cloning tips and for her scientific insights. Thank you to the UW-Madison MRSEC and the Discovery Outreach team for the opportunities they have given me over the years, with special thanks to Anne Lynn Gillian-Daniel and Ben Taylor from the MRSEC and to Val Blair and Elizabeth Clawson from the Discovery Outreach team, as well as to Travis Tangen from WARF.

I am very lucky to have had such wonderful labmates. There have been too many people in the lab over the years to name all of them, but I am thankful to each and every one of you for teaching me something and helping me grow as a co-worker, a scientist, and a person. In particular, I am thankful to Piercen Oliver for his mentorship and friendship, John Crooks for his experience, Na Yin for her kindness, and Thiago Santos, Ti-Yu Lin, Rishi Trivedi, and Julia Nepper for their help, support, and friendship. I am thankful to have had such great collaborators in Julia Nepper, Nikolai Radzinski, and Mengyi Cao, who are also great friends. Thank you to the whole Weibel Lab for many great memories.

I wouldn't be where I am today if it wasn't for my friends. I am incredibly thankful for all of my friends, from friends old and far (Robert Stafford, Charley Parker, Kyle Conrad, Levi Miller, Tristan Storz, Brenden Villars, Mike Dixon, Gordon Osterman, David Choi, Nick Kramer, and many others) to friends new and near (the

Gebelsteins, the Budde-Lorties, Marc Brousseau, Hilary Friedman, Sarah Sprangers, Ryan Clark, Dan Agnew, Mark Politz, and many others). I am so lucky to have friends like you in my life, and I always look forward to our next encounter. I would also like to thank my Sensei, Sam Bonilla, for helping me grow, learn, and better myself.

I am grateful for my wonderful family. I am so thankful for my parents. My mom and dad have always supported me, taught me many lessons, and been great role models. I am thankful for the best brother in the world. Dan, we are brothers! I've had so much fun with you in my life and I can't wait for more adventures in the future. Thank you also for finding such a great sister-in-law. Elise, I am so glad you're a part of our family and that you love Magic, and my brother. I am also blessed with a supportive and caring family-in-law. Thank you, Mark, Laura, and Ben, for being so warm, gracious, generous, and for loading us up with leftovers and furniture.

There is one person left I have to thank, and I would never have made it to the end of my dissertation without her. Renee Dana Kramer, thank you for everything. Thank you for listening to me talk about my work, helping when my experiments ran long, being patient when I'm slow, encouraging me when I need it, and talking through problems along the way. I am thankful for fate putting us into the same apartment building and for love uniting us. You are my rock, and I love you.

Biophysical Investigations into Microbial Physiology and Behavior

Matthew Douglas Stilwell

Under the supervision of Professor Douglas B. Weibel

Department of Biochemistry

University of Wisconsin-Madison, Madison, WI

In the 1670s, Antonie van Leeuwenhoek first observed microbes through his self-made microscope. Since then, the study of microbes has exploded into diverse fields. Today, we recognize that microbes exhibit a wide range of shapes, sizes, and behaviors, and that microbes form relationships with every kingdom of life and in every ecosystem.

In the first part of this dissertation, we investigate the biophysical basis for the differing sizes of *Caulobacter crescentus* daughter cells. *C. crescentus* grows into two morphologically distinct daughter cells, with one cell being longer and larger than the other. The essential protein MipZ positions the division apparatus in these cells with the help of the chromosomal partitioning protein ParB and polar organizing protein PopZ. We employ epifluorescence microscopy, single particle tracking photoactivatable localization microscopy, and deterministic simulations to understand the biophysics of MipZ, ParB, and PopZ.

In the second part of this dissertation, we use a novel microfluidic device to study the behavioral response of *Escherichia coli* bacteria to a panel of chemicals. The microfluidic device we developed enables the quantification of bacterial chemotaxis (response to chemicals) using passive mechanisms and enables the screening of multiple chemicals in parallel.

The third part of this dissertation focuses on using microfluidics to isolate individual, living *Steinernema carpocapsae* nematodes for long-term microscopy of their bacterial symbionts, *Xenorhabdus nematophila*. The microfluidic device we present facilitates the study of multiple nematodes within a single device and with minimal microfluidics expertise necessary to operate. We use the device to observe bacterial outgrowth within the living nematode intestine over days and weeks.

In the fourth part of this dissertation, we use a desktop craft cutter and inexpensive office supplies to fabricate microfluidic devices for the study of nematode chemotaxis and electrotaxis (response to electric fields). We used these microfluidic devices in informal outreach settings and evaluated the activities we developed with anonymous responses from K-12 participants.

CHAPTER 1

General Introduction

Introduction to Cell Shape and Size

"To be brutally honest, few people care that bacteria have different shapes. Which is a shame, because the bacteria seem to care very much." –Kevin Young

Bacteria exist in a remarkably diverse range of shapes and sizes (1, 2). In fact, students are taught to identify and classify bacteria using cell shape, with the three most well-known shapes being spheres, rods, and spirals (1, 2). An incredibly varied range of displayed shapes exists in nature, however. Bacteria can be flat-sided disks, lemon-shaped, square, branched, star-shaped, and grow in sheathed or unsheathed chains, just to name a few (1-3). In terms of surface tension, the lowest energy shape is a sphere (4), yet bacteria do not all exist as spheres, and instead maintain their specific shapes. The great variety of shapes and strict conforming to a particular shape by each species suggests that these shapes have evolved due to selective pressures (1-3).

Indeed, shape confers a number of selective advantages, such as increased swimming efficiency (4-6), evading predation (7-9), and nutrient uptake (10-12). Even small changes in a bacterium's behavior can have drastic effects on its survival (5). For instance, a 0.01% increase in growth rate can lead to a fitness advantage of approximately 10% compared to those without the increase (5). Bacteria seem to regulate their shape and must expend resources to do so, presumably to give them a selective advantage in their native environment (1-3, 5). For example, the shape regulating protein Crescentin in *Caulobacter crescentus* grants the bacterium its

distinctive curve (13, 14), which has been shown to aid in surface colonization and motility (6, 15). Deletion of this protein causes the cell lose its banana-like curve and instead to grow as a straight rod (13). *C. crescentus* also modifies its shape by growing a stalk during the progression of the cell cycle (16-18).

One aspect of cell shape is the cell size, which bacteria also seem to care about (19, 20). When grown on a surface experiencing shear flows, *Bacillus subtilis* changes its size (21). The introduction of shear flows causes *B. subtilis* to reduce their width and length each by half compared to growing without shear flows, decreasing their cross-sectional area by one quarter but their length by half, effectively doubling their attachment to shear stress ratio (21). *Escherichia coli,* when grown under shear forces, elongate in order to increase the amount of cell attached to a surface without increasing the area exposed to the flow (22). *E. coli* also changes size depending on nutrient availability, becoming wider and longer in more nutrient-rich media (19, 23, 24).

Cell size is a crucial determinant of swimming efficiency, especially in high-viscosity fluids and near surfaces (25, 26). The optimal ratio of cell length to cell width for efficient swimming is ~3.7 (27). The length to width ratio of *C. crescentus* swarmer cells is approximately the optimal 3.7 (19), which is no coincidence, as these are aquatic bacteria (18). Their length isn't the only aspect of swimming in which *C. crescentus* excels, as their flagellar motors have close to 100% energy conversion efficiency (28). The optimal swimming size ratio of *C. crescentus* cells, one of the most efficient flagellar

motors, and a curved shape to help generate thrust while swimming make *C. crescentus* a remarkable swimmer (6, 28), likely helping it thrive in nutrient-poor aquatic environments.

Unlike *E. coli, C. crescentus* uses a different mechanism to alter its size in response to nutrient limitation (23, 24, 29). Whereas *E. coli* cells become smaller as nutrients become limiting (23, 24), *C. crescentus* elongates its polar stalk (specifically in response to phosphorus limitation) (29), increasing nutrient uptake more efficiently than by cell filamentation (30). The small diameter of the stalk enables a drastic increase in the cell's surface area to volume ratio without a significant increase in biomass, a more efficient strategy for nutrient uptake than cell filamentation (30). Interestingly, the size of the *C. crescentus* cell body (excluding the stalk) does not change drastically in response to nutrient availability, temperature, or phase of exponential growth (Figure 1)(19). The fact that the length of the cell body does not drastically change in response to environmental cues (19), while the length of the stalk does change (29), suggests that the cell regulates the size of its cell body (1), perhaps in order to maintain an optimum swimming efficiency.

Recent work has shown that cells settle on a cell size distribution over several divisions and maintain their cell size distributions over many subsequent divisions and across the population (19, 20). These narrow cell size distributions are thought to aid the cells in partitioning chromosomes and biomaterials necessary for the survival of both

daughter cells (1, 19). For *C. crescentus*, not only do cells achieve a narrow distribution of cell sizes that do not appreciably alter in response to external conditions, the two daughter cells display different cell lengths at birth (19, 31). The cell sizes of the two daughter cells at birth also show a narrow distribution over generations, with a coefficient of variance of less than 20% (Figure 1), similar to other organisms that regulate their cell size (19). One explanation as to how these cells might achieve their cell size distributions is through an "adder" mechanism, in which the cells add a constant amount of cell length/area/volume before each division (19, 20). It has been suggested that the cell may use its chromosome as a molecular ruler to measure this addition and to determine the appropriate division time, which would couple cell cycle information with cell size and cell division machinery (19).

The observed cell size asymmetry between daughter cells of *C. crescentus* is curious. If other aspects of cell shape and size confer selective advantages, then perhaps this observed cell size asymmetry does as well. The swarmer cell is the smaller of the two daughter cells (19, 31), which, similar to the molecular ruler hypothesis, could give these swarmer cells a mechanism to sense the nutrient conditions of the environment through their growth rate and give swarmer cells time to explore in search of healthier habitats (32). Whatever the case, each cell division event must be well regulated and precise (33). For *E. coli* cells, the division machinery is reported to localize precisely, such that using a normalized cell length (one pole is 0, the other pole is 1), *E. coli* cells

divide at 0.500 ± 0.005 (34). *C. crescentus* cells also display precision in the localization of their division machinery, dividing (using a normalized cell length) at 0.537 ± 0.001 (31). Whatever advantage this cell size asymmetry imparts to the cell, it must be worth the costs, as *C. crescentus* seems to take care to ensure the placement of the division machinery yields differently sized daughter cells (35). The *why* of this oddity will require further investigation, but perhaps the *how* will be easier to answer.

Introduction to the Regulation of Cell Division Location

Cell division is a fundamental event that all cells must undergo in order to proliferate. Bacterial cells have evolved diverse mechanisms to localize their division machinery (1, 36, 37). The main target of many of these systems is the widely conserved prokaryotic protein FtsZ, one of the first proteins to localize to the division plane and thought to provide the force for cell constriction during division (38-40). The Min system is perhaps the most well studied regulator of cell division location (33). This system exists in both *E. coli* and *B. subtilis*, with the *E. coli* version containing the proteins MinC, MinD, and MinE, whereas in *B. subtilis* the system consists of MinC, MinD, and DivIVA (33). The most notable feature of the Min system is that, in *E. coli*, the system spatially oscillates along the long axis of the cell, generating a time-averaged gradient with the highest concentrations at the cell poles (the system is stationary in *B. subtilis*) (41, 42). In both *E. coli* and *B. subtilis*, MinC is the protein responsible for

interacting with and positioning the division machinery (43, 44). MinD binds to the membrane in an ATP-dependent fashion and, when bound to the membrane, recruits MinC (44, 45). MinE stimulates the removal of MinD from the membrane and in so doing removes MinC (46).

The Min system oscillates because of a few key elements. First, MinD binds to the cytoplasmic membrane cooperatively (46, 47). This cooperativity allows a great number of MinD dimers to bind to the membrane in more-or-less the same spot in the cell. Second, MinE displays a form of "persistent binding" or "processivity", in that it is able to interact with the membrane and release multiple MinD dimers from the membrane in a short amount of time (46, 48). Last, but certainly not least, is the role that the geometry of the cell plays (46, 48-51). It is important, especially in reaction-diffusion systems such as this, to bear in mind that while no direct measurement for membrane-bound MinD or MinE exists, the diffusion coefficients for membrane-bound proteins are typically two to three orders of magnitude smaller than those of their cytoplasmic counterparts (51). MinD cooperatively binds the membrane and interacts with other MinD dimers, drastically slowing its diffusion and effectively isolating the dimer to one half of the cell. MinE then dimerizes and binds the membrane, albeit closer to the cell center than the cell pole, most likely due to the lower MinD concentration at mid-cell coupled with the positive feedback displayed by the MinE/MinD ratio (46, 48, 52). The membrane binding of MinE stimulates the ATPase activity of MinD, and once MinD hydrolyzes its

ATP, its affinity for the membrane is greatly reduced, so it detaches from the membrane increasing its diffusion coefficient by several orders of magnitude. The average distance that MinD diffuses before rebinding the membrane can be thought of as the l_{diff}, or diffusion length, which is described by this equation (48):

$$l_{diff}^2 = \frac{D}{\omega}$$

where D is the diffusion coefficient of the free state and ω is the attachment rate. In *E. coli*, the l_{diff} is comparable to the length of the cell, such that when MinD is detached from the membrane, it will typically diffuse to the other side of the cell before reattaching (48). This process is repeated as long as there is ATP, generating an oscillatory behavior.

Another well-known regulator of division site selection includes the nucleoid occlusion system, mediated by SlmA in *E. coli* and by Noc in *B. subtilis* (53). These DNA-binding proteins, when bound to DNA, block the formation of the FtsZ-ring (53). As long as SlmA and Noc are bound to the chromosome, their negative regulation of FtsZ ensures the division site does not form over the chromosome, keeping all copies of the chromosome intact (54, 55). Positive regulators of FtsZ localization, such as the replication-terminus structuring factor MatP, also ensure proper localization of the division machinery (56). MatP is a DNA-binding protein that binds to *matS* sites of the chromosome in the terminus region and directs this portion of the chromosome to mid-

cell. MatP interacts with the divisome protein ZapB, facilitating divisome assembly at the mid-cell and proper segregation of the chromosomes to each daughter cells (56).

C. crescentus employs none of the above proteins to localize its division machinery (31, 57, 58). As of the writing of this dissertation, only one known division regulator exists in *C. crescentus*, MipZ. MipZ (Mid-cell positioning of FtsZ) is an essential ATPase in the same family of proteins as MinD (57). MipZ inhibits FtsZ polymerization in an ATP dependent manner (57). Within the cell, MipZ forms an intracellular bipolar gradient through interactions with the polarly localized ParB proteins (57, 58). Because of this, FtsZ is forced to the lowest concentration of MipZ, which is found slightly towards the new pole from mid-cell (31). It is currently unknown how the asymmetric MipZ gradient and subsequent asymmetric placement of the division ring is controlled (59).

Introduction to Microfluidics

Microfluidics is a young scientific field that emerged in the 1990's as a byproduct of the burgeoning computer industry (60). Shrinking the computer from a room-sized machine to the powerful handheld devices that we rely on today was driven by our ability to make ever smaller electronic circuitry (60). These same advances in miniaturization also provided a route to manipulate fluids at the microscale. The ability to control fluids in microscopic channels is quietly fueling a revolution across many

scientific disciplines, particularly in biology (60, 61). Microfluidics has been instrumental in driving down the cost of DNA sequencing and other high throughput molecular assays, and will be a key driver for the future of the '-omics' era in biology (60, 61). Microfluidics also offers researchers unparalleled spatial control over single cells and organisms, which has led to many new insights in cell biology (61). Microfluidics promises a future where we build entire human tissues from scratch, so called organs-on-a-chip, enabling doctors to test for side-effects and toxicity from drugs using organ-on-a-chips grown from the patient's cells (62, 63). There are many real-world engineering problems that microfluidics research is searching for answers to (64, 65). Microfluidic technology's ability to miniaturize and simplify chemical and biological detection strategies may revolutionize our lives, and perhaps one day our classrooms. (60, 65). Just as computers migrated from research laboratories into our homes and our pockets, complex microfluidic assays to monitor personal health may soon become as ubiquitous as the toothbrush (glucose monitors and home pregnancy tests are merely the beginning) (66).

Microfluidic devices function on the small scale. The size of microfluidic channels usually ranges from 1 to 300 um (the diameter of a human hair is ~50 um). One advantage of microfluidics is that these smaller devices use smaller volumes of reagents and consume far less chemicals than macro-scale experiments, making them useful for diagnostic assays and high-throughput screens (60, 67, 68). A less obvious advantage of

small scale is automation, as a carefully designed device can run many experiments in parallel, or can transport fluids from one reaction chamber to another without human intervention, another boon for potential technologies (60, 65). All of these attributes of small scale conspire to lower the cost and increase the speed of microfluidic experiments relative to their macro-scale complements (60).

Introduction to Bacterial Chemotaxis

Chemotaxis refers to the response of an organism to chemical cues from the environment (69-71). The molecular and biophysical details underlying chemotaxis are particularly well understood in model bacterial species (69, 72, 73). In particular, the gamma-proteobacterium *Escherichia coli* is the most extensively studied in the chemotaxis field. The extent to which chemotaxis guides bacterial behaviors in natural environments remains less well characterized, and yet chemotaxis is a determinant in important bacterial processes, including bacterial-host interactions, such as colonization of hosts by *Vibrio cholera* during infection, and bacterially induced geochemical fluxes, such as nitrogen cycling in soils (74-77). This knowledge gap reflects a technological limitation, as widely available bacterial chemotaxis assays are often qualitative, technically cumbersome, and low throughput.

Advances in microfluidics—specifically in the ability to control chemical gradients—have stimulated the development of bacterial chemotaxis assays in

microchannels that overcome some of the limitations of established macro-scale assays (78). These microfluidic chemotaxis assays are either flow-based or flow-free (78). In flow-based systems, bacteria are injected into a chemoeffector gradient that is established by diffusion of the chemoeffector between parallel fluid streams (as in a Y-shaped microfluidic device). Such devices are remarkably sensitive and their application has detected chemotactic responses at much lower chemoeffector concentrations than those observed in macro-scale assays (79). However, bacteria in these systems experience a continuous bulk flow that introduces shear effects, which can make it difficult to decouple chemotactic migration from mechanical perturbations resulting from fluid flow (80, 81). A second factor complicating the analysis of cells in these systems is the shape of the chemoeffector gradient, which varies with the distance along the channel and exposes bacteria transiting the channel to an uneven gradient with time (78).

Another class of devices enables the study of cell chemotaxis in the absence of flow. These devices typically consist of hydrogel placed between chemoeffector solutions and a bacterial suspension (78, 82-85). The hydrogel acts as a physical barrier to cell movement, yet small molecule chemoeffectors readily diffuse through the gel into the liquid that fills the compartment containing bacterial cells (82-85). Chemotaxis is quantified as bacteria migrate *en masse* toward or away from the chemoeffector that diffuses through the hydrogel (82-85). Flow-free devices remove the ambiguity of

whether cell behavior is due to chemotaxis or shear forces and can be designed to create a stable gradient in which a population of cells responds to an invariable gradient over extended timescales (often on the order of hours)(82-85). Both flow-based and flow-free devices may require external equipment to operate and technical finesse that restricts the number of assays that can be performed in parallel, placing limitations on data collection. These restrictions often necessitate a separate device to monitor the chemotactic response of cells to each chemical, making the approach impractical for studying a broad range of chemosensory agents.

In Chapter 3, we present a novel microfluidic device that produces a flow-free environment with stable spatial chemical gradients (at time scales ≥ 24 h), is simple to operate, and can be multiplexed to an arbitrarily large number of parallel experiments. We describe a theoretical framework for understanding the underlying principle of gradient formation, and use this model to demonstrate how the gradient can be tuned by varying several experimental parameters. We use this new device for parallel bacterial chemotaxis measurements as a proof-of-principle and discover new insights into how global chemotaxis strategies are regulated.

Introduction to Symbiosis and Phenotypic Variation

Symbiosis, or prolonged interactions between organisms, is a feature of all living systems studied to date (86). Animals, for instance, form relationships with bacteria that

are either beneficial to both partners (mutualism), harmful to the animal host (pathogenesis), or somewhere in between (commensalism) (86). Some microbes are obligate pathogens or obligate mutualists, while others can and do switch between these two extremes of symbiosis (87-89). Bacteria's ability to switch between mutualistic and pathogenic states is of great importance for human health and agricultural productivity (90, 91), but little is known regarding its molecular underpinnings in living hosts. Bacteria exhibiting phenotypic variation (individual cells within a population expressing distinct behaviors) cause many vector-borne diseases and facilitate transmission among hosts (92-94). The phenotypic switch is often coordinated with pathogen transmission, but not well characterized in living hosts, in large part due to technical challenges of studying these systems *in vivo* (95, 96).

Steinernema nematodes and *Xenorhabdus* bacteria have been established as a successful model system to investigate microbial pathogenesis and mutualism (88, 97). The bacterium *Xenorhabdus nematophila* forms a mutualistic relationship with entomopathogenic (insect-eating) *Steinernema carpocapsae* nematodes, colonizing a specialized intestinal pocket of the nematode host in a species-specific manner (98, 99). Together these organisms prey on a wide range of insects. The infective juvenile nematode will encounter insects and enter them through natural openings in the insect, such as the mouth, anus, or spiracles. Once inside the insect, the nematode will release its population of *Xenorhabdus* bacteria to evade the host immune system and kill the

insect host (88, 97, 99). These two organisms then use the insect cadaver for nutrients and reproduction, re-associating once the nutrients have been depleted (88, 97, 99). During the lifecycle of *X. nematophila*, certain networks of genes are regulated to confer either a pathogenic or mutualistic state depending on the environment and host (92-94). These networks of genes are driven by varying levels of the *X. nematophila* global transcription regulator, leucine-responsive regulatory protein (Lrp), responsible for regulating ~65% of the proteome and over 10% of the genome (100). Studies of *X. nematophila* and *S. carpocapsae* are restricted to population level studies, masking any dynamics within individual hosts (101, 102).

Studies tracking individual hosts and their bacterial counterparts have the potential to reveal key details in the switching of bacteria from mutualistic or commensal relationships to parasitic ones. Performing these experiments in living hosts raises technical challenges, e.g. seeing within the host in real-time, and ethical issues, e.g. host confinement and potentially harmful experimental conditions. As such, nematodes and their bacterial counterparts, like *S. carpocapsae* and *X. nematophila*, offer a unique avenue for studying phenotypic switching due to the optical transparency of the invertebrate nematodes, their ease of growth, and molecular cloning techniques that enable the generation of bacterial mutants, such as those that express fluorescent reporters for visualization (103, 104).

Microfluidics offers a potential solution to some of the technical challenges of studying symbiosis systems (105, 106). Through the precise manipulation of objects in microfluidic devices, nematodes can be arranged such that they can be studied individually and over time (105, 106). Microfluidic devices have been used to study nematodes for a variety of purposes and have used different mechanisms to confine the nematode. Some devices squeeze the nematode in tapered channels (107). Other devices encapsulate and isolate nematodes in droplets, while others use solidifying gels to eliminate nematode movements during image acquisition (108, 109). However, nematodes in these experiments are often studied on timescales that are too short to study the dynamics of bacterial-host interactions (107). These microfluidic devices also require considerable microfluidic expertise to operate, limiting the range of research labs that can use of them.

In Chapter 4, we describe a microfluidic device for the isolation and maintenance of individual nematodes over days and weeks. In our microfluidic device, a central channel is filled with a suspension of nematodes. The application of a vacuum to the side channels pulls nematodes into small channels that trap nematodes and prevent their escape. Once nematodes are isolated and secured in the side channels, we flow water through the main channel to maintain the nematodes for weeks-long experiments. We use this device to visualize the bacterial population within immobilized, individual nematodes.

Introduction to Nematode Behavior and Accessible Microfluidics

In a changing world, organisms need to adapt. Entomopathogenic nematodes are no exception and have developed mechanisms to respond to a range of external stimuli (110-112). Two stimuli these nematodes respond to are chemicals and electric fields through processes called chemotaxis and electrotaxis, respectively (110-112).

Entomopathogenic nematodes use chemotaxis to find and infect prey insects and evade harmful conditions (112). Organic molecules secreted by the insect prey, such as insect pheromones, provide the nematode with a trail to follow. Some plants take advantage of the nematode chemotaxis as well, releasing compounds that attract the nematodes to the plant when it is under attack from insects as a defense mechanism while providing the nematodes with a food source (113). Other molecules may signal to the nematodes that soil conditions are unsafe and the nematode should avoid the area (112).

Electrotaxis also provides the nematodes with certain benefits. Insects crawling along the surface of the ground accumulate a slight negative charge on their body, which the nematodes can sense (114, 115). Nematodes of the genus *Steinernema* are capable of jumping from the soil surface onto a passing insect (112). The nematode's electrotaxis and chemotaxis tell the nematode when it is time to jump onto an

unsuspecting prey. Species of entomopathogenic nematodes differ in their electrotaxis, with some moving up an electrical potential gradient, others moving down, and others displaying no preference (114, 115).

As mentioned above, microfluidic devices are poised to become more ubiquitous instruments in hospitals, pharmacies, and homes (60). Part of the barrier microfluidics must clear in order to achieve this vision is the ease of fabrication (116). Currently, most microfluidics are created using an elastomer cured around a device master (60). These device masters are usually created using soft lithography, a technique that enables high precision, but requires special environments, such as a cleanroom, and special equipment, such as spin coaters and fume hoods (116). These requirements are considerable barriers to entry, drastically limiting the number of people who can easily prototype designs and develop microfluidics for broad uses. This high barrier to entry also limits the ability to teach microfluidics in both university and K-12 classrooms.

In the hopes of providing accessible microfluidics, multiple alternative methods have been developed for fabricating microfluidic devices. Some of these methods involve moving away from the standard elastomer for microfluidic devices, poly(dimethylsiloxane) (PDMS), towards less expensive alternatives, such as gelatin (117). Other methods have focused on novel methods of fabrication of the device master, such as using “Shrinky-Dinks” (118). These novel methods of device fabrication have enabled hobbyist experimentation, citizen science projects, and classroom

activities. The accessibility and ease of prototyping these microfluidic devices enables educators to achieve many of the NGSS HS Science and Engineering Practices, making microfluidics a great research and classroom tool for scientific investigations (119).

In Chapter 5, we present an easily accessible activity for students to quantitatively observe dynamic group behavior in response to external stimuli. We fabricate microfluidics using a desktop craft cutter, plastic transparency sheets, and double-sided adhesive paper. Our method of device fabrication is quick, easy, and can be customized for many classroom and research investigations. We tested our devices and their ability to engage students as they quantitatively probed the chemotaxis and electrotaxis of entomopathogenic nematodes in outreach settings.

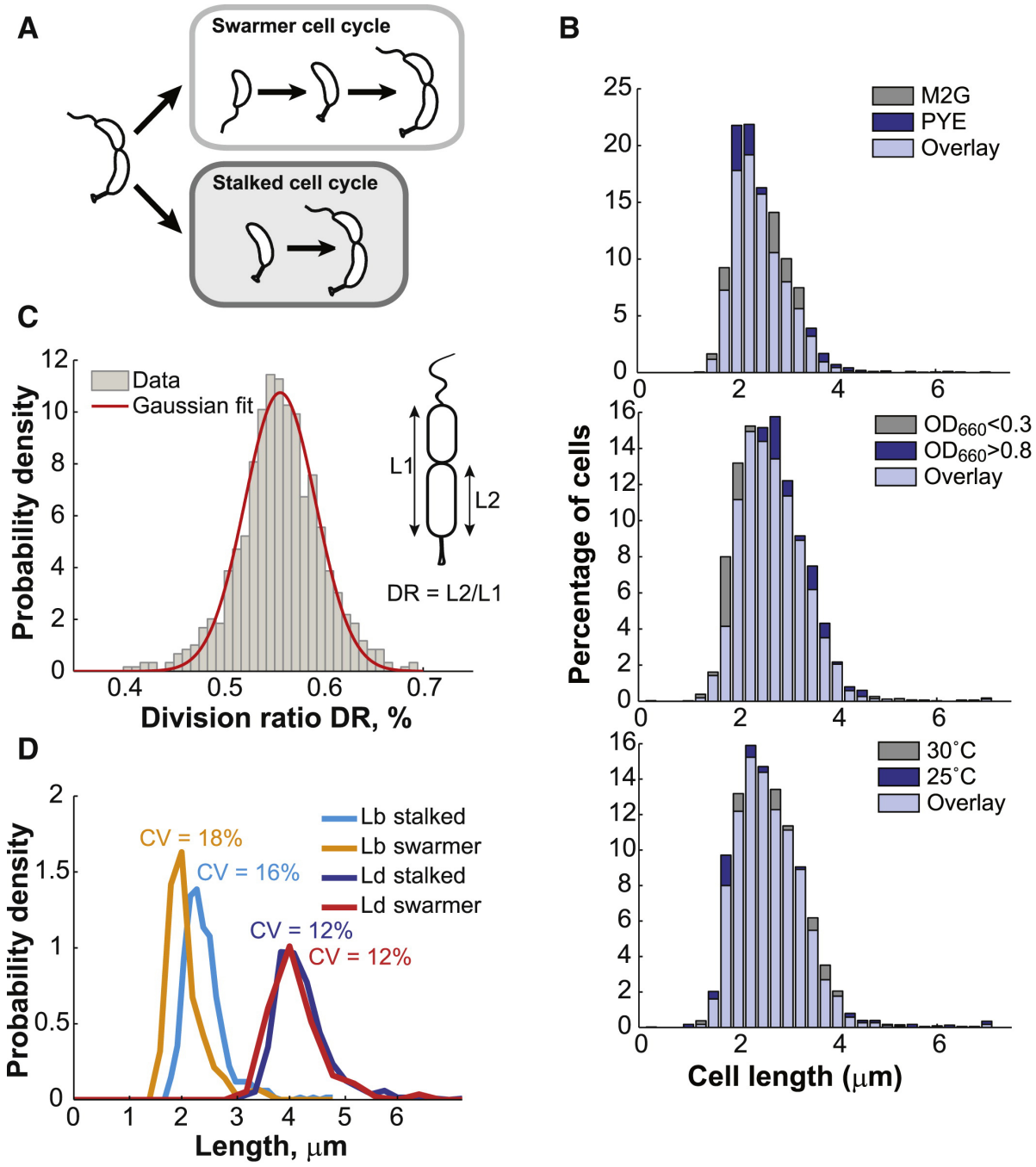
A
Swarmer cell cycle
Stalked cell cycle
B
M2G
PYE
Overlay
Percentage of cells
OD660<0.3
OD660>0.8
Overlay
30˚C
25˚C
Overlay
Cell length (μm)
C
Data
Gaussian fit
L1
L2
DR = L2/L1
Probability density
Division ratio DR, %
D
Lb stalked
Lb swarmer
Ld stalked
Ld swarmer
CV = 18%
CV = 16%
CV = 12%
CV = 12%
Probability density
Length, μm

Figure 1

Figure 1. Figure and caption from (19). (A) Schematic of the dimorphic cell cycle of *C. crescentus*. Each division generates two different progeny: the smaller swarmer cell and the longer stalked cell. The swarmer cell is motile thanks to a polar flagellum until the cell transitions to a stalked cell. (B) Distribution of *C. crescentus* CB15N lengths under different environmental conditions. Cells were grown in M2G at 30°C and imaged on 1% agarose pads at an $OD_{660nm} < 0.3$ except if stated otherwise. (C) Histogram representing the distribution of the division ratio *DR* for *C. crescentus* CB15N cells (n = 706) grown in M2G medium and imaged on 0.3% agarose pads. (D) Distribution of cell length at birth *Lb*, and at division *Ld* for stalked cells (n = 565) and swarmer cells (n = 141) grown in M2G medium at 30°C and imaged at $OD_{660nm} < 0.3$ on 0.3% agarose pads. The coefficient of variation (SD/mean) for each distribution is shown.

REFERENCES

1. Young KD. The selective value of bacterial shape. Microbiol Mol Biol Rev. 2006;70(3):660-703.

2. Young KD. Bacterial morphology: why have different shapes? Curr Opin Microbiol. 2007;10(6):596-600.

3. Yang DC, Blair KM, Salama NR. Staying in Shape: the Impact of Cell Shape on Bacterial Survival in Diverse Environments. Microbiol Mol Biol Rev. 2016;80(1):187-203.

4. Dusenbery DB. Fitness landscapes for effects of shape on chemotaxis and other behaviors of bacteria. J Bacteriol. 1998;180(22):5978-83.

5. Mitchell JG. The energetics and scaling of search strategies in bacteria. Am Nat. 2002;160(6):727-40.

6. Liu B, Gulino M, Morse M, Tang JX, Powers TR, Breuer KS. Helical motion of the cell body enhances Caulobacter crescentus motility. Proc Natl Acad Sci U S A. 2014;111(31):11252-6.

7. Hahn MW, Hofle MG. Grazing of protozoa and its effect on populations of aquatic bacteria. FEMS Microbiol Ecol. 2001;35(2):113-21.

8. Jurgens K, Matz C. Predation as a shaping force for the phenotypic and genotypic composition of planktonic bacteria. Antonie Van Leeuwenhoek. 2002;81(1-4):413-34.

9. Sherr EB, Sherr BF. Significance of predation by protists in aquatic microbial food webs. Antonie Van Leeuwenhoek. 2002;81(1-4):293-308.

10. Beveridge TJ. The bacterial surface: general considerations towards design and function. Can J Microbiol. 1988;34(4):363-72.

11. Koch AL. What size should a bacterium be? A question of scale. Annu Rev Microbiol. 1996;50:317-48.

12. Schulz HN, Jorgensen BB. Big bacteria. Annu Rev Microbiol. 2001;55:105-37.

13. Ausmees N, Kuhn JR, Jacobs-Wagner C. The bacterial cytoskeleton: an intermediate filament-like function in cell shape. Cell. 2003;115(6):705-13.

14. Kim JS, Sun SX. Morphology of Caulobacter crescentus and the Mechanical Role of Crescentin. Biophys J. 2009;96(8):L47-9.

15. Persat A, Stone HA, Gitai Z. The curved shape of Caulobacter crescentus enhances surface colonization in flow. Nat Commun. 2014;5:3824.

16. Curtis PD, Brun YV. Getting in the loop: regulation of development in Caulobacter crescentus. Microbiol Mol Biol Rev. 2010;74(1):13-41.

17. Goley ED, Iniesta AA, Shapiro L. Cell cycle regulation in Caulobacter: location, location, location. J Cell Sci. 2007;120(Pt 20):3501-7.

18. Skerker JM, Laub MT. Cell-cycle progression and the generation of asymmetry in Caulobacter crescentus. Nat Rev Microbiol. 2004;2(4):325-37.

19. Campos M, Surovtsev IV, Kato S, Paintdakhi A, Beltran B, Ebmeier SE, et al. A constant size extension drives bacterial cell size homeostasis. Cell. 2014;159(6):1433-46.

20. Taheri-Araghi S, Bradde S, Sauls JT, Hill NS, Levin PA, Paulsson J, et al. Cell-size control and homeostasis in bacteria. Current biology : CB. 2015;25(3):385-91.

21. Sahoo S, Verma RK, Suresh AK, Rao KK, Bellare J, Suraishkumar GK. Macro-level and genetic-level responses of Bacillus subtilis to shear stress. Biotechnol Prog. 2003;19(6):1689-96.

22. Edwards N, Beeton S, Bull AT, Merchuk JC. A novel device for the assessment of shear effects on suspended microbial cultures. Applied microbiology and biotechnology. 1989;30(2):190-5.

23. Akerlund T, Nordstrom K, Bernander R. Analysis of cell size and DNA content in exponentially growing and stationary-phase batch cultures of Escherichia coli. J Bacteriol. 1995;177(23):6791-7.

24. Schaechter M, Maaloe O, Kjeldgaard NO. Dependency on medium and temperature of cell size and chemical composition during balanced grown of Salmonella typhimurium. J Gen Microbiol. 1958;19(3):592-606.

25. Berg HC, Turner L. Movement of microorganisms in viscous environments. Nature. 1979;278(5702):349-51.

26. Frymier PD, Ford RM, Berg HC, Cummings PT. Three-dimensional tracking of motile bacteria near a solid planar surface. Proc Natl Acad Sci U S A. 1995;92(13):6195-9.

27. Cooper S, Denny MW. A conjecture on the relationship of bacterial shape to motility in rod-shaped bacteria. FEMS Microbiology Letters. 1997;148(2):227-31.

28. Li G, Tang JX. Low flagellar motor torque and high swimming efficiency of Caulobacter crescentus swarmer cells. Biophys J. 2006;91(7):2726-34.

29. Poindexter JS. The role of calcium in stalk development and in phosphate acquisition in Caulobacter crescentus. Arch Microbiol. 1984;138(2):140-52.

30. Wagner JK, Setayeshgar S, Sharon LA, Reilly JP, Brun YV. A nutrient uptake role for bacterial cell envelope extensions. Proc Natl Acad Sci U S A. 2006;103(31):11772-7.

31. Schofield WB, Lim HC, Jacobs-Wagner C. Cell cycle coordination and regulation of bacterial chromosome segregation dynamics by polarly localized proteins. EMBO J. 2010;29(18):3068-81.

32. Lawaree E, Gillet S, Louis G, Tilquin F, Le Blastier S, Cambier P, et al. Caulobacter crescentus intrinsic dimorphism provides a prompt bimodal response to copper stress. Nat Microbiol. 2016;1(9):16098.

33. Lutkenhaus J. Assembly dynamics of the bacterial MinCDE system and spatial regulation of the Z ring. Annu Rev Biochem. 2007;76:539-62.

34. Mannik J, Wu F, Hol FJ, Bisicchia P, Sherratt DJ, Keymer JE, et al. Robustness and accuracy of cell division in Escherichia coli in diverse cell shapes. Proc Natl Acad Sci U S A. 2012;109(18):6957-62.

35. Goley ED, Yeh YC, Hong SH, Fero MJ, Abeliuk E, McAdams HH, et al. Assembly of the Caulobacter cell division machine. Mol Microbiol. 2011;80(6):1680-98.

36. Rothfield L, Taghbalout A, Shih YL. Spatial control of bacterial division-site placement. Nat Rev Microbiol. 2005;3(12):959-68.

37. Monahan LG, Harry EJ. Identifying how bacterial cells find their middle: a new perspective. Mol Microbiol. 2013;87(2):231-4.

38. Erickson HP, Anderson DE, Osawa M. FtsZ in bacterial cytokinesis: cytoskeleton and force generator all in one. Microbiol Mol Biol Rev. 2010;74(4):504-28.

39. Mingorance J, Rivas G, Velez M, Gomez-Puertas P, Vicente M. Strong FtsZ is with the force: mechanisms to constrict bacteria. Trends Microbiol. 2010;18(8):348-56.

40. Harry EJ. Bacterial cell division: regulating Z-ring formation. Mol Microbiol. 2001;40(4):795-803.

41. Raskin DM, de Boer PA. Rapid pole-to-pole oscillation of a protein required for directing division to the middle of Escherichia coli. Proc Natl Acad Sci U S A. 1999;96(9):4971-6.

42. Kelly CB, Giuliani M, Dutcher JR. Precise Measurement of Min Protein Oscillations in Bacterial Cells Using TIRF Microscopy. Phys Can. 2011;67(185).

43. de Boer PA, Crossley RE, Rothfield LI. Central role for the Escherichia coli minC gene product in two different cell division-inhibition systems. Proc Natl Acad Sci U S A. 1990;87(3):1129-33.

44. de Boer PA, Crossley RE, Rothfield LI. Roles of MinC and MinD in the site-specific septation block mediated by the MinCDE system of Escherichia coli. J Bacteriol. 1992;174(1):63-70.

45. Zhou H, Lutkenhaus J. Membrane binding by MinD involves insertion of hydrophobic residues within the C-terminal amphipathic helix into the bilayer. J Bacteriol. 2003;185(15):4326-35.

46. Loose M, Kruse K, Schwille P. Protein self-organization: lessons from the min system. Annu Rev Biophys. 2011;40:315-36.

47. Lackner LL, Raskin DM, de Boer PA. ATP-dependent interactions between Escherichia coli Min proteins and the phospholipid membrane in vitro. J Bacteriol. 2003;185(3):735-49.

48. Bonny M, Fischer-Friedrich E, Loose M, Schwille P, Kruse K. Membrane binding of MinE allows for a comprehensive description of Min-protein pattern formation. PLoS Comput Biol. 2013;9(12):e1003347.

49. Zieske K, Schwille P. Reconstitution of self-organizing protein gradients as spatial cues in cell-free systems. Elife. 2014;3.

50. Varma A, Huang KC, Young KD. The Min system as a general cell geometry detection mechanism: branch lengths in Y-shaped Escherichia coli cells affect Min oscillation patterns and division dynamics. J Bacteriol. 2008;190(6):2106-17.

51. Lippincott-Schwartz J, Snapp E, Kenworthy A. Studying protein dynamics in living cells. Nat Rev Mol Cell Biol. 2001;2(6):444-56.

52. Loose M, Fischer-Friedrich E, Ries J, Kruse K, Schwille P. Spatial regulators for bacterial cell division self-organize into surface waves in vitro. Science. 2008;320(5877):789-92.

53. Ortiz C, Natale P, Cueto L, Vicente M. The keepers of the ring: regulators of FtsZ assembly. FEMS Microbiology Reviews. 2016;40(1):57-67.

54. Tonthat NK, Arold ST, Pickering BF, Van Dyke MW, Liang S, Lu Y, et al. Molecular mechanism by which the nucleoid occlusion factor, SlmA, keeps cytokinesis in check. EMBO J. 2011;30(1):154-64.

55. Wu LJ, Ishikawa S, Kawai Y, Oshima T, Ogasawara N, Errington J. Noc protein binds to specific DNA sequences to coordinate cell division with chromosome segregation. EMBO J. 2009;28(13):1940-52.

56. Espeli O, Borne R, Dupaigne P, Thiel A, Gigant E, Mercier R, et al. A MatP-divisome interaction coordinates chromosome segregation with cell division in E. coli. EMBO J. 2012;31(14):3198-211.

57. Thanbichler M, Shapiro L. MipZ, a spatial regulator coordinating chromosome segregation with cell division in Caulobacter. Cell. 2006;126(1):147-62.

58. Kiekebusch D, Michie KA, Essen LO, Lowe J, Thanbichler M. Localized dimerization and nucleoid binding drive gradient formation by the bacterial cell division inhibitor MipZ. Mol Cell. 2012;46(3):245-59.

59. Kiekebusch D, Thanbichler M. Spatiotemporal organization of microbial cells by protein concentration gradients. Trends Microbiol. 2014;22(2):65-73.

60. Whitesides GM. The origins and the future of microfluidics. Nature. 2006;442(7101):368-73.

61. Weibel DB, Whitesides GM. Applications of microfluidics in chemical biology. Curr Opin Chem Biol. 2006;10(6):584-91.

62. Huh D, Hamilton GA, Ingber DE. From 3D cell culture to organs-on-chips. Trends Cell Biol. 2011;21(12):745-54.

63. Sivagnanam V, Gijs MA. Exploring living multicellular organisms, organs, and tissues using microfluidic systems. Chem Rev. 2013;113(5):3214-47.

64. Dittrich PS, Manz A. Lab-on-a-chip: microfluidics in drug discovery. Nat Rev Drug Discov. 2006;5(3):210-8.

65. Nge PN, Rogers CI, Woolley AT. Advances in microfluidic materials, functions, integration, and applications. Chem Rev. 2013;113(4):2550-83.

66. Yetisen AK, Akram MS, Lowe CR. Paper-based microfluidic point-of-care diagnostic devices. Lab Chip. 2013;13(12):2210-51.

67. Kaminski TS, Jakiela S, Czekalska MA, Postek W, Garstecki P. Automated generation of libraries of nL droplets. Lab Chip. 2012;12(20):3995-4002.

68. Guo MT, Rotem A, Heyman JA, Weitz DA. Droplet microfluidics for high-throughput biological assays. Lab Chip. 2012;12(12):2146-55.

69. Wadhams GH, Armitage JP. Making sense of it all: bacterial chemotaxis. Nat Rev Mol Cell Biol. 2004;5(12):1024-37.

70. Berg HC. Chemotaxis in bacteria. Annu Rev Biophys Bioeng. 1975;4(00):119-36.

71. Adler J. Chemotaxis in bacteria. Annu Rev Biochem. 1975;44:341-56.

72. Sourjik V, Wingreen NS. Responding to chemical gradients: bacterial chemotaxis. Curr Opin Cell Biol. 2012;24(2):262-8.

73. Berg HC, Purcell EM. Physics of chemoreception. Biophys J. 1977;20(2):193-219.

74. Freter R, O'Brien PC. Role of chemotaxis in the association of motile bacteria with intestinal mucosa: chemotactic responses of Vibrio cholerae and description of motile nonchemotactic mutants. Infect Immun. 1981;34(1):215-21.

75. Raterman EL, Welch RA. Chemoreceptors of Escherichia coli CFT073 play redundant roles in chemotaxis toward urine. PLoS One. 2013;8(1):e54133.

76. Pandya S, Iyer P, Gaitonde V, Parekh T, Desai A. Chemotaxis of Rhizobium sp.S2 towards Cajanus cajan root exudate and its major components. Curr Microbiol. 1999;38(4):205-9.

77. Seymour JR, Simo R, Ahmed T, Stocker R. Chemoattraction to dimethylsulfoniopropionate throughout the marine microbial food web. Science. 2010;329(5989):342-5.

78. Ahmed T, Shimizu TS, Stocker R. Microfluidics for bacterial chemotaxis. Integr Biol (Camb). 2010;2(11-12):604-29.

79. Mao H, Cremer PS, Manson MD. A sensitive, versatile microfluidic assay for bacterial chemotaxis. Proc Natl Acad Sci U S A. 2003;100(9):5449-54.

80. Marcos, Stocker R. Microorganisms in vortices: a microfluidic setup. Limnology and Oceanography: Methods. 2006;4(10):392-8.

81. Walker GM, Sai J, Richmond A, Stremler M, Chung CY, Wikswo JP. Effects of flow and diffusion on chemotaxis studies in a microfabricated gradient generator. Lab Chip. 2005;5(6):611-8.

82. Diao J, Young L, Kim S, Fogarty EA, Heilman SM, Zhou P, et al. A three-channel microfluidic device for generating static linear gradients and its application to the quantitative analysis of bacterial chemotaxis. Lab Chip. 2006;6(3):381-8.

83. Cheng SY, Heilman S, Wasserman M, Archer S, Shuler ML, Wu M. A hydrogel-based microfluidic device for the studies of directed cell migration. Lab Chip. 2007;7(6):763-9.

84. Kim M, Kim T. Diffusion-Based and Long-Range Concentration Gradients of Multiple Chemicals for Bacterial Chemotaxis Assays. Analytical Chemistry. 2010;82(22):9401-9.

85. Si G, Yang W, Bi S, Luo C, Ouyang Q. A parallel diffusion-based microfluidic device for bacterial chemotaxis analysis. Lab Chip. 2012;12(7):1389-94.

86. McFall-Ngai M, Hadfield MG, Bosch TC, Carey HV, Domazet-Loso T, Douglas AE, et al. Animals in a bacterial world, a new imperative for the life sciences. Proc Natl Acad Sci U S A. 2013;110(9):3229-36.

87. Goodrich-Blair H, Clarke DJ. Mutualism and pathogenesis in Xenorhabdus and Photorhabdus: two roads to the same destination. Mol Microbiol. 2007;64(2):260-8.

88. Herbert EE, Goodrich-Blair H. Friend and foe: the two faces of Xenorhabdus nematophila. Nat Rev Microbiol. 2007;5(8):634-46.

89. Newton AC, Fitt BD, Atkins SD, Walters DR, Daniell TJ. Pathogenesis, parasitism and mutualism in the trophic space of microbe-plant interactions. Trends Microbiol. 2010;18(8):365-73.

90. Beck JJ, Vannette RL. Harnessing Insect-Microbe Chemical Communications To Control Insect Pests of Agricultural Systems. J Agric Food Chem. 2017;65(1):23-8.

91. Chaston J, Goodrich-Blair H. Common trends in mutualism revealed by model associations between invertebrates and bacteria. FEMS Microbiol Rev. 2010;34(1):41-58.

92. Park Y, Herbert EE, Cowles CE, Cowles KN, Menard ML, Orchard SS, et al. Clonal variation in Xenorhabdus nematophila virulence and suppression of Manduca sexta immunity. Cell Microbiol. 2007;9(3):645-56.

93. Hussa EA, Casanova-Torres AM, Goodrich-Blair H. The Global Transcription Factor Lrp Controls Virulence Modulation in Xenorhabdus nematophila. J Bacteriol. 2015;197(18):3015-25.

94. Cao M, Patel T, Rickman T, Goodrich-Blair H, Hussa EA. High Levels of the Xenorhabdus nematophila Transcription Factor Lrp Promote Mutualism with the Steinernema carpocapsae Nematode Host. Appl Environ Microbiol. 2017;83(12).

95. McFall-Ngai MJ. Giving microbes their due--animal life in a microbially dominant world. J Exp Biol. 2015;218(Pt 12):1968-73.

96. Murfin KE, Dillman AR, Foster JM, Bulgheresi S, Slatko BE, Sternberg PW, et al. Nematode-bacterium symbioses--cooperation and conflict revealed in the "omics" age. Biol Bull. 2012;223(1):85-102.

97. Richards GR, Goodrich-Blair H. Masters of conquest and pillage: Xenorhabdus nematophila global regulators control transitions from virulence to nutrient acquisition. Cell Microbiol. 2009;11(7):1025-33.

98. Murfin KE, Lee MM, Klassen JL, McDonald BR, Larget B, Forst S, et al. Xenorhabdus bovienii Strain Diversity Impacts Coevolution and Symbiotic Maintenance with Steinernema spp. Nematode Hosts. MBio. 2015;6(3):e00076.

99. Goodrich-Blair H. They've got a ticket to ride: Xenorhabdus nematophila-Steinernema carpocapsae symbiosis. Curr Opin Microbiol. 2007;10(3):225-30.

100. Cowles KN, Cowles CE, Richards GR, Martens EC, Goodrich-Blair H. The global regulator Lrp contributes to mutualism, pathogenesis and phenotypic variation in the bacterium Xenorhabdus nematophila. Cell Microbiol. 2007;9(5):1311-23.

101. Martens EC, Heungens K, Goodrich-Blair H. Early colonization events in the mutualistic association between Steinernema carpocapsae nematodes and Xenorhabdus nematophila bacteria. J Bacteriol. 2003;185(10):3147-54.

102. Singh S, Reese JM, Casanova-Torres AM, Goodrich-Blair H, Forst S. Microbial population dynamics in the hemolymph of Manduca sexta infected with Xenorhabdus nematophila and the entomopathogenic nematode Steinernema carpocapsae. Appl Environ Microbiol. 2014;80(14):4277-85.

103. H K Kaya a, Gaugler R. Entomopathogenic Nematodes. Annual Review of Entomology. 1993;38(1):181-206.

104. Murfin KE, Chaston J, Goodrich-Blair H. Visualizing bacteria in nematodes using fluorescent microscopy. J Vis Exp. 2012(68).

105. San-Miguel A, Lu H. Microfluidics as a tool for C. elegans research. WormBook : the online review of C elegans biology. 2013:1-19.

106. Hwang H, Lu H. Microfluidic tools for developmental studies of small model organisms--nematodes, fruit flies, and zebrafish. Biotechnol J. 2013;8(2):192-205.

107. Hulme SE, Shevkoplyas SS, Apfeld J, Fontana W, Whitesides GM. A microfabricated array of clamps for immobilizing and imaging C. elegans. Lab Chip. 2007;7(11):1515-23.

108. Shi W, Qin J, Ye N, Lin B. Droplet-based microfluidic system for individual Caenorhabditis elegans assay. Lab Chip. 2008;8(9):1432-5.

109. Krajniak J, Lu H. Long-term high-resolution imaging and culture of C. elegans in chip-gel hybrid microfluidic device for developmental studies. Lab Chip. 2010;10(14):1862-8.

110. Hui E, Webster JM. Influence of insect larvae and seedling roots on the host-finding ability of Steinernema feltiae (Nematoda: Steinernematidae). Journal of invertebrate pathology. 2000;75(2):152-62.

111. Dillman AR, Guillermin ML, Lee JH, Kim B, Sternberg PW, Hallem EA. Olfaction shapes host-parasite interactions in parasitic nematodes. Proc Natl Acad Sci U S A. 2012;109(35):E2324-33.

112. Hallem EA, Dillman AR, Hong AV, Zhang Y, Yano JM, DeMarco SF, et al. A sensory code for host seeking in parasitic nematodes. Current biology : CB. 2011;21(5):377-83.

113. Ali JG, Alborn HT, Stelinski LL. Subterranean herbivore-induced volatiles released by citrus roots upon feeding by Diaprepes abbreviatus recruit entomopathogenic nematodes. J Chem Ecol. 2010;36(4):361-8.

114. Ilan T, Kim-Shapiro DB, Bock CH, Shapiro-Ilan DI. Magnetic and electric fields induce directional responses in Steinernema carpocapsae. Int J Parasitol. 2013;43(10):781-4.

115. Shapiro-Ilan DI, Lewis EE, Campbell JF, Kim-Shapiro DB. Directional movement of entomopathogenic nematodes in response to electrical field: effects of species, magnitude of voltage, and infective juvenile age. Journal of invertebrate pathology. 2012;109(1):34-40.

116. Xia Y, Whitesides, G.M. Soft Lithography. Angewandte Chemie International Edition. 1998;37:550-75.

117. Paguirigan A, Beebe DJ. Gelatin based microfluidic devices for cell culture. Lab Chip. 2006;6(3):407-13.

118. Grimes A, Breslauer DN, Long M, Pegan J, Lee LP, Khine M. Shrinky-Dink microfluidics: rapid generation of deep and rounded patterns. Lab Chip. 2008;8(1):170-2.

119. Yang CW, Ouellet E, Lagally ET. Using inexpensive Jell-O chips for hands-on microfluidics education. Anal Chem. 2010;82(13):5408-14.

CHAPTER 2

Examining daughter cell size asymmetry in *Caulobacter crescentus*

ABSTRACT

Caulobacter crescentus is a freshwater α-proteobacterium that divides into two asymmetric daughter cells. These curved, rod-shaped cells differ in their chromosome replication fates and in their cell length at division. *C. crescentus* divides into a replication-competent 'stalked' cell and a smaller, replication-quiescent 'swarmer' cell. The site of cell division is dictated by the polymerization of the eukaryotic tubulin homologue, FtsZ. MipZ is an essential ATPase and inhibitor of FtsZ polymerization. MipZ forms an intracellular bipolar gradient that directs FtsZ to the lowest concentration of MipZ, which is found at mid-cell, slightly towards the new pole. This localization bias leads to two differently sized daughter cells. To better understand how MipZ directs FtsZ to this off-center location, we employed wide-field epifluorescence microscopy, single-particle tracking photoactivated localization microscopy (sptPALM), and deterministic simulations to understand the subcellular distribution of proteins involved in FtsZ localization and to recreate the asymmetric MipZ gradient *in silico*. These simulations produce a distribution of cell lengths after cell division similar to those observed *in vivo*. These studies provide more insight into the asymmetric division of *C. crescentus*, but further questions remain regarding the nature of the asymmetric division.

INTRODUCTION

Cell division is a fundamental process that cells undertake as a part of their growth (1-5). During cell division, cells accurately and faithfully orient the location of division in order to partition chromosomes to each daughter cell, ensure that each daughter cell has the components necessary for survival, and to temporally coordinate cell division events (1-5). Dividing cells employ diverse mechanisms to achieve the faithful positioning of the division site, and prokaryotes are no exception (1-6). For bacteria, much of our current understanding of division site regulation comes from a few model organisms: the gram-negative, rod-shaped *Escherichia coli*, the gram-positive, rod-shaped *Bacillus subtilis*, and the gram-negative, rod-shaped *Caulobacter crescentus*, with *E. coli* being the best studied (1-6).

Bacterial division sites are determined by the localization and regulation of the major cytoskeletal cell division protein, FtsZ (1-6). FtsZ is widely conserved in bacteria and is thought to be the ancestor to eukaryotic tubulin (2, 7, 8). FtsZ forms short, overlapping protofilaments that eventually create a ring on the innermost part of the membrane in the cytoplasm of the cell (2, 7, 8). As this protein is the major landmark for the localization of other division proteins, it is often directed to the center of the cell, i.e. the future site of cell division (2, 7, 8). Besides acting as a landmark for other cell division proteins, FtsZ is thought to be the main driving force for cell constriction through its GTPase activity (2, 7-9). Prokaryotes employ diverse systems to ensure the

accurate localization of FtsZ and to prevent FtsZ from initiating cell constriction before the cell has finished replicating and partitioning its chromosomes (1-6).

Organisms like *E. coli* and *B. subtilis* employ multiple systems to regulate FtsZ activity and localization (1-6). Perhaps the best studied FtsZ regulator is the Min system, consisting of three proteins, MinC, MinD, and MinE in *E. coli* and MinC, MinD, and DivIVA in *B. subtilis*, which negatively regulates the ability of FtsZ protofilaments to form larger bundles (5). In *E. coli*, the Min system spatially oscillates along the long axis of the cell, creating a time-averaged gradient with a minimum at mid-cell and directing FtsZ polymerization to this location in the cell (5, 10, 11). This spatial oscillation is first achieved by cooperative binding of ATP-bound MinD to the cell membrane (12-14). Membrane-bound MinD recruits MinC, which is responsible for the regulation of FtsZ (12, 15). MinE displaces MinC from MinD and is capable of stimulating the ATPase activity of MinD, which, along with the low affinity of ADP-bound MinD to the membrane, causes the release of MinD from the membrane (14, 16). MinE has been shown to have a sort of processivity for the stimulation of membrane-bound MinD and creates a ring-like structure in the cell as it removes MinD from the membrane (16, 17). The ratios of these proteins and the geometry of the cell dictate the period of oscillation for this system (16-20). In contrast to *E. coli*, the *B. subtilis* Min system does not oscillate and instead forms a static gradient (10, 11). DivIVA recruits

MinC and MinD to the cell poles, creating a spatial gradient with a minimum at mid-cell (5, 10, 11).

While the Min system has been shown to increase the accuracy of division localization in both *E. coli* and *B. subtilis*, it is not alone in regulating FtsZ activity and localization (1-5, 21). Both *E. coli* and *B. subtilis* depend on another negative regulator of FtsZ activity in the nucleoid occlusion system, mediated by SlmA in *E. coli* and Noc in *B. subtilis* (1-5, 21). These DNA-binding proteins ensure that the division ring does not form around the chromosome (1-5, 21). To further ensure accurate localization of FtsZ, these organisms also employ positive regulators of FtsZ activity, such as MatP, a DNA-binding protein that binds near the terminus of the chromosome and interacts with ZapA and ZapB to localize the divisome (22). With the Min system preventing the formation of the division ring at the cell poles, the nucleoid occlusion system preventing ring formation over the chromosome, and terminus-bound proteins stabilizing the ring near mid-cell, these organisms divide symmetrically and accurately over many generations (1-5, 21).

C. crescentus has been established as another model bacterial organism for cell cycle, cell shape, and protein localization studies (1-5, 21, 23). The *Caulobacter* cell cycle differs from that of *E. coli* and *B. subtilis* in that cells undergo DNA replication only once per cell cycle, whereas *E. coli* can undergo multiple rounds of DNA replication given enough nutrients (23-26). For *C. crescentus*, each round of cell division yields two

morphologically distinct daughter cells with different cell fates (23-25). One daughter cell is a sessile cell (called the stalked cell and discussed in more detail below) capable of initiating DNA replication as soon as division is finished (23-25). The other daughter cell is a motile cell (called the swarmer cell) that cannot initiate DNA replication until it differentiates into a stalked cell through the shedding of its flagellum and growth of a prosethecae called a stalk (23-25). After this differentiation, the cell can begin the next round of division by initiating DNA replication (23-25). DNA replication initiates at a single origin, which is maintained at the cell poles (23-25). As DNA replication progresses, the chromosomal origins are separated to opposite cell poles through interactions between ParA and ParB (27, 28). ParA forms a gradient in the cell with a higher protein concentration at the new pole (27, 28). ParB binds to *parS* sites near the chromosomal origins, interacts with ParA in a burnt-bridge Brownian ratchet mechanism that segregates the ParB clusters towards opposite poles and is tethered to the cell poles through an interaction with the polar organizing protein-Z, PopZ (27-29).

C. crescentus also differs from *E. coli* and *B. subtilis* in many respects, with its asymmetries being perhaps the most striking (26, 30). For instance, *C. crescentus* is an excellent model organism for the study of protein localization (6, 28, 31, 32). *C. crescentus* localizes many proteins to specific regions of the cell, with some proteins localizing to parts of the chromosome, others localizing to certain sides of the cell wall, and others localizing to one or both poles (6, 31, 32). The most easily visualized cases of

asymmetry in polarly localized proteins are the polar appendages of the organism (23-25, 30). On one cell pole, *C. crescentus* grows a prosthecae called a stalk, which it uses both to attach to and colonize surfaces and for nutrient uptake (23-25, 30). The opposite cell pole grows a flagellum, which the daughter cell uses to navigate aquatic environments in search of a suitable habitat (23-25).

These two daughter cells, termed the stalked and swarmer cells, respectively, maintain asymmetries in their DNA replication competence fates, with the stalked cell being DNA replication competent and the swarmer cell being DNA replication quiescent (23-25). This difference in DNA replication competence is caused by asymmetric distributions of DNA replication regulatory proteins (23-25). One such protein is CtrA, an essential dual-function master regulator that controls the transcription of cell division and other important genes and forms a phosphorylated protein gradient along the long axis of the cell (23-25). Another regulator or DNA replication is the protease ClpXP, which is selectively targeted to the stalked pole (23-25, 33).

Another interesting asymmetry in the two daughter cells of *C. crescentus* is their cell sizes (23, 34). Many well-studied bacteria, like *Eschirichia coli* or *Bacillus subtilis*, divide symmetrically, such that both daughter cells are the same size, which these cells achieve with great accuracy (35, 36). In *C. crescentus*, the stalked cell is longer than its swarmer cell counterpart, even excluding the length of the stalk (34, 35). One

explanation for this cell size asymmetry is a non-uniform growth rate, such that one half of the cell grows faster than the other, although this explanation has been disproven (34).

To better understand this cell size asymmetry, the mechanisms that *C. crescentus* utilizes to position FtsZ, and thus the division site, must be understood. Unlike *E. coli* and *B. subtilis* that employ multiple systems for FtsZ localization (1-5), *C. crescentus* has only one known protein responsible for positioning FtsZ (6, 37, 38). Instead of utilizing the Min system or nucleoid occlusion to localize FtsZ, *C. crescentus* uses MipZ (Mid-cell positioning of FtsZ) (37, 38). MipZ is an essential protein in *C. crescentus* and is part of the Mrp/MinD family of P-loop ATPases (37, 38). Within the cell, MipZ forms an intracellular bipolar gradient with a minimum at mid-cell through a crucial interaction with ParB (37, 38).

Immediately following cell constriction, FtsZ is located at the new pole and both ParB and MipZ are located at the old pole (37, 38). As the cell replicates its DNA, the chromosomal origins segregate through an interaction between ParA and ParB (27, 28, 37, 38). As one ParB cluster travels to and arrives at the new pole, a MipZ cluster follows and displaces FtsZ once it reaches the new pole (28, 37, 38). ATP-bound MipZ molecules form dimers in the cell that bind non-cooperatively and nonspecifically to DNA through a positively charged DNA binding cleft, and only the ATP-bound MipZ dimers are capable of negatively regulating FtsZ (Figure 1A) (38). These ATP-bound

MipZ dimers stimulate the GTPase activity of FtsZ, causing the disassembly of FtsZ bundles and subsequent repositioning to the location with the lowest concentration of MipZ, i.e. mid-cell (37, 38). In the first study of MipZ, Thanbichler & Shapiro noted that the concentration of MipZ in the cell was too low for efficient dimerization (37). To overcome this problem, ATP-bound MipZ monomers interact with ParB, effectively increasing the local concentration of MipZ and stimulating the dimerization of ATP-bound MipZ monomers (Figure 1A) (37, 38). These MipZ dimers bind to DNA, effectively isolating them to one spot in the cell until they undergo ATP hydrolysis, at which point they unbind from DNA, become freely diffusing monomers, and undergo nucleotide exchange to begin the cycle anew (Figure 1A) (38). The stimulation of dimerization of MipZ by ParB causes MipZ to colocalize with ParB (37, 38). Therefore, as one ParB cluster traverses the length of the cell and arrives at the new pole, one MipZ cluster follows, creating a bipolar MipZ concentration gradient highest at the poles and lowest at the mid-cell, directing FtsZ to the middle of the cell (Figure 1B)(37, 38).

Previous work, and work discussed in this chapter, has shown that the MipZ gradient is slightly asymmetric (6, 28, 37, 38). The minimum concentration of MipZ is not the exact mid-cell, but rather is skewed towards the new pole (6, 28, 37, 38). This concentration minimum colocalizes with the positioning of FtsZ (6, 28, 37, 38). Previous work has also shown that mutants lacking the polar landmark protein, TipN (Tip of

New pole) display a reversed cell size asymmetry such that the stalked cell is shorter on average than the swarmer cell (28, 39).

We set out to understand the biophysical basis of asymmetric bipolar gradient formation of cell division protein inhibitors (MipZ) and subsequent asymmetric placement of division site by FtsZ. We used wide-field epifluorescence imaging, single molecule imaging, and computer simulations to understand the asymmetric MipZ gradient and the proteins responsible for its localization.

MATERIALS AND METHODS

Bacterial Strains, Plasmids, Growth Conditions, and Cell Synchronization

E. coli NEB5α and DH5α were used for general cloning purposes. All *C. crescentus* strains used in this study are derived from the synchronizable wild-type CB15N (also known as NA1000). Generalized transduction was performed with phage ΦCR30 following a previously described protocol and briefly described below (40). Transformations in *E. coli* were performed using chemical transformations, as per the NEB5α cell instructions. Electrocompetent *C. crescentus* cells were prepared as described (41). Both *E. coli* and *C. crescentus* cells were grown aerobically, with the *E. coli* cells grown at 37 °C in Luria-Bertani broth and the *C. crescentus* cells grown at 30 °C in PYE or M2G (40). For *E. coli*, kanamycin was used at the following concentration (μg/mL; liquid/solid media): (25/50). For *C. crescentus*, antibiotics were used at the following concentration (μg/mL; liquid/solid media): kanamycin (5/25), gentamycin (0.5/5).

Generalized transduction using the phage ΦCR30 was performed in the following manner: To prepare the phage lysate, the donor strain was grown overnight in PYE media. At least 4 mL of PYE top agar (0.3% agar in PYE) per lysate was melted and placed in a 42 °C water bath. 1 μL of the phage ΦCR30 was added to 100 μL of donor cell culture, and this mixture was incubated for 15 min at 30 °C. The cells were then added to the PYE top agar and poured onto a pre-warmed PYE agar plate. After the top agar cooled and solidified, the plate was incubated at 30 °C overnight (right side

up). The following morning, the top agar was removed from the agar plate and transferred to a 50 mL conical tube. 100 μL of chloroform was added to the tube and the tube was vortexed to kill any remaining cells. This tube was then incubated at room temperature for 1 h. After another round of vortexing, the tube was centrifuged at 3400 x g for 10 mins. The supernatant was transferred to a clean petri dish and irradiated, without the lid, for 1 min with a UV light source (365 nm) held at a distance of approximately 10 cm. The liquid was then transferred to a clean 15 mL conical tube and an additional 100 μL of chloroform was added to the tube. The lysate was stored at 4 °C. To transduce the cells, the recipient strain was grown overnight in PYE. 500 μL of this culture was mixed with 475 mL PYE and 25 μL of the phage lysate. These cells were grown for 1 h at 30 °C, then collected by centrifugation and plated on selective media.

Chromosomal integration of constructs into *C. crescentus* was achieved using the allele exchange plasmid pNPTS138 (42). The exchange of alleles was performed as follows (adapted from (37)): *C. crescentus* cells were electroporated with the desired construct, grown for at least 3 h in PYE at 30 °C, and then plated on PYE agar plates containing kanamycin to select for cells that integrated the non-replicating plasmid into their chromosome via single homologous recombination. Single colonies were grown in liquid PYE with kanamycin overnight to ensure incorporation of the plasmid. These cultures were then diluted >1000 fold in PYE without antibiotic until stationary phase. 2-5 μL of these stationary phase cultures were then plated on PYE+3% sucrose agar

plates and incubated at 30 °C. Single colonies were then replica-patched in parallel onto plates containing PYE with kanamycin and PYE without kanamycin. Kanamycin-sensitive clones, which had lost the integrated plasmid due to a second recombination event, were tested for the presence of the mutated allele by PCR.

Plasmids were constructed for the gene of interest with the desired fluorescent protein marker in the following manner: For all plasmids used, the construct was designed such that the primers starting at 500-600 bp upstream and downstream of the stop codon of the gene of interest amplified up to, but not including, the stop codon. These primers also contained 21-28 bp of the pNPTS138 plasmid at the SalI or HindIII restriction digest sites. Another set of primers was designed to amplify the fluorescent protein of choice. These three fragments were then combined using either overlap PCR or Gibson assembly. The pNPTS138 plasmid was linearized by restriction digest with SalI and HindIII. These components were then combined using either Infusion cloning or Gibson cloning reagents and transformed into DH5α or NEB5α, grown in SOC media for at least 1 h at 37 °C and subsequently plated on LB agar plates containing the appropriate antibiotic.

C. crescentus cells were synchronized as described here. First, cells were grown overnight in PYE at 30 °C. This culture was diluted in 30 mL of PYE or M2G and grown at 30 °C until the culture was at OD_{600} of 0.5 or 0.1 for PYE or M2G, respectively. 25 mL of this culture was transferred to a clean 50 mL conical tube and cells were collected by

centrifugation at 6,000 x g and 4 °C for 10 min. The supernatant was discarded and cells were re-suspended in 750 μL of cold M2G. This suspension was mixed thoroughly with 750 μL of cold Percoll, a colloidal suspension used for centrifugation gradients. This mixture was then placed in a bench-top centrifuge for 20 min at 11,000 rpm and 4 °C. A visible band of cells towards the bottom of the tube contained the swarmer cells. These cells were collected and transferred to a new microcentrifuge tube containing 1000 μL of cold M2G. The cells were washed by centrifugation at 8,000 rpm for 1 min at 4 °C, (note: this wash step can be repeated). The supernatant was discarded and cells were suspended in 2-15 mL of pre-warmed media.

Light and Fluorescence Microscopy & Analysis

For oscillation time-lapse experiments, images were acquired using fast shutters (Uniblitz LS2; Vincent Associated, Rochester, NY) to synchronize illumination and image acquisition. Images were recorded by a back-illuminated electron-multiplying charge-coupled device (EMCCD) camera with 256 x 256 pixels of 16 x 16 μm each (iXon DV-887 from Andor Technology, South Windsor, CT). Cell meshes were obtained using the open source, MATLAB-based software MicrobeTracker (43). Further quantitative analysis from cell meshes was performed with MATLAB (MathWorks, Inc.). Cross-correlations were performed using MATLAB's xcorr function.

For division ratio, volume ratio, and axial profiles, all epifluorescence images were acquired using an Eclipse Ti inverted microscope (Nikon, Tokyo, Japan) equipped with a CoolSNAP HQ2 camera (Photometrics, Munich, Germany). Images were acquired using a 100x objective (Nikon Plan Apo 100/1.40 oil DM). Cell meshes were obtained using the open source, MATLAB-based software Oufti (44). Further quantitative analysis from cell meshes was performed with MATLAB (MathWorks, Inc.). To determine cell polarity, cell meshes were oriented using the unipolar fluorescence signal at the first time point of the time lapse (when cells are in the swarmer stage) or by visual identification of the stalk; the half of the cell that contained the polar fluorescence focus or the stalk was defined as the stalked pole, or 0 for figures with normalized cell length.

Single Molecule Microscopy Conditions & Analysis

Cells were prepared and synchronized as described above. To prepare the cells for microscopy, we placed 10 μL of the synchronized cell suspension on a small section of M2G agar (1%). The sections of M2G agar we used were cut from agar plates. Once the cell suspension had dried, the agar pad was inverted and placed on a clean coverslip. Single-molecule imaging experiments were performed at 30 °C.

Single molecule imaging experiments were performed using an Eclipse Ti inverted microscope (Nikon Instruments, Melville, NY) equipped with an oil immersion

objective (CFI Plan Apo Lambda DM 100x Oil, 1.45 NA from Nikon Instruments), a 1.5x tube lens, and the Perfect Focus System (Nikon Instruments, Melville, NY). Images were recorded using a fast electron-multiplying charge-coupled device (EMCCD) camera with 128 x 128 pixels of 24 x 24 μm each (iXon 860 from Andor Technology, South Windsor, CT). Data were collected at a frame rate in the range of 1-200 Hz, with exposure times within each frame of 2-50 ms.

MipZ-Dendra2 was photoswitched with a 405 nm diode laser (CrystaLaser, Reno, NV) and subsequently imaged with a 561 nm laser (Sapphire 561 CW lasers; Coherent, Bloomfield, CT). The power density of the 405 nm laser at the sample was 0.1-1.5 W/cm^2. The power density of the 561 nm laser at the sample was about 1 kW/cm^2. To minimize the phototoxic effect of the laser, cells were imaged for less than 2 min. Emission was collected through a 617/73 bandpass filter (bright line 617/73-25; Semrock, Rochester, NY).

To analyze the sptPALM data, single-molecule trajectories were obtained using a centroid algorithm to locate molecules, as described in (45, 46). The population-averaged mean-square displacement versus lag time was calculated by pooling trajectories from multiple movies and from different sets of cells.

Analytical and Deterministic Modeling Parameters

Simulations were performed in MATLAB ((MathWorks, Inc.) using custom script. In order to produce simulated gradient profiles with error for the three state system, we solved Equations 1-3 by randomly choosing the parameter values from a distribution that had a mean and standard deviation from either a measurement from the literature or similar to what could be expected from a measurement of the parameter (37, 38). This process was iterated 500 times to produce a distribution of solutions. The simulated symmetric axial gradient profile for the three state system, Figure 7A, was produced from solving Equations 1-3 using 0.01±0.001 s^{-1} as k_1, 0.1±0.001 $\mu M^{-1}s^{-1}$ as k1, 0.01±0.001 s^{-1} as k2, 0.5±0.001 s^{-1} as k3, 1.0±0.01 μm^2s^{-1} as D_MipZ-apo, 1.0±0.01 μm^2s^{-1} as D_MipZ-ADP, and 0.01±0.001 μm^2s^{-1} as D_MipZ-ATP. The simulated asymmetric axial gradient profile for a three state system, Figure 7C, was produced from solving Equations 1-3 using 0.01±0.002 s^{-1} as k_1, 0.01±0.001 $\mu M^{-1}s^{-1}$ as k1, 0.01±0.001 s^{-1} as k2, 0.5±0.003 s^{-1} as k3, 1.0±0.01 μm^2s^{-1} as D_MipZ-apo, 1.0±0.01 μm^2s^{-1} as D_MipZ-ADP, and 0.01±0.001 μm^2s^{-1} as D_MipZ-ATP at the stalked pole and 0.012±0.002 s^{-1} as k_1, 0.01±0.001 $\mu M^{-1}s^{-1}$ as k1, 0.015±0.001 s^{-1} as k2, 0.5±0.003 s^{-1} as k3, 1.0±0.01 μm^2s^{-1} as D_MipZ-apo, 1.0±0.01 μm^2s^{-1} as D_MipZ-ADP, and 0.01±0.001 μm^2s^{-1} as D_MipZ-ATP at the swarmer pole. The simulated division ratios for both the symmetric and asymmetric models were produced by determining the minimum point between the two polar maxima for each instance of a solution.

In order to produce simulated gradient profiles with error for the three state system, we solved Equations 4-5 by randomly choosing the parameter values from a distribution that had a mean and standard deviation from either a measurement from the literature or similar to what could be expected from a measurement of the parameter (37, 38). This process was iterated 500 times to produce a distribution of solutions. The simulated symmetric axial gradient profile for the two state system, Figure 7E, was produced from solving Equations 4-5 using 0.1±0.01 s^{-1} as kcat, 0.1±0.001 s^{-1} as kon, 9.424±0.98 $\mu m^2 s^{-1}$ as D_fast, and 0.07136±0.0167 $\mu m^2 s^{-1}$ as D_slow. The simulated asymmetric axial gradient profile for the two state system, Figure 7G, was produced from solving Equations 1-3 using 0.1±0.01 s^{-1} as kcat, 0.1±0.001 s^{-1} as kon, 1.424±0.78 $\mu m^2 s^{-1}$ as D_fast, and 0.07136±0.0167 $\mu m^2 s^{-1}$ as D_slow at the stalked pole and 0.2±0.01 s^{-1} as kcat, 0.15±0.001 s^{-1} as kon, 9.424±0.98 $\mu m^2 s^{-1}$ as D_fast, and 0.07136±0.0167 $\mu m^2 s^{-1}$ as D_slow at the swarmer pole. The simulated division ratios for both the symmetric and asymmetric models were produced by determining the minimum point between the two polar maxima for each instance of a solution.

RESULTS

To understand the asymmetric placement of the division machinery, we first compared the daughter cell sizes of newly divided *C. crescentus* cells derived from the wild-type CB15N. We synchronized a population of cells and waited for them to near cell division. As the cells approached their first division event, we imaged them using phase contrast microscopy. We oriented the cells through visual recognition of the stalk and used Oufti to determine the cell outlines (44). We then measured the division ratio and volume ratio of the cells we imaged. We defined the division ratio as the length of the stalked cell divided by the length of both daughter cells (Figure 2A). We defined the volume ratio similarly, but used cell volume instead of cell length, assuming that the cells were cylindrical. As seen in Figure 2B&C, both the division and volume ratios were skewed such that the stalked cell was larger, confirming previously published results.

We hypothesized that there were three potential explanations for the observed asymmetric placement of the division ring. First, MipZ could display oscillations similar to those in the Min system (5), but in such a way as to linger at one pole longer than the other. Second, the number of MipZ molecules bound at the stalked pole could be higher than at the swarmer pole, giving rise to an asymmetric gradient. Third, since MipZ is a reaction-diffusion system (a system in which the molecule of interest diffuses in the cell and changes diffusive states through a chemical reaction), the biophysical

parameters of the reaction-diffusion system could differ from one pole to the other. The biophysical parameters of interest would be the diffusion coefficients and the reaction rates between the different diffusive states (47-49).

Wide-field Epifluorescence Microscopy for Oscillation Measurements

In order to determine the cause of the asymmetric division of *C. crescentus*, we first took note of a potentially interesting observation. Preliminary data seemed to show that the fluorescence intensity of the MipZ focus at one cell pole would increase as the fluorescence intensity at the opposite pole decreased. We then sought to determine if MipZ was acting similar to the well-studied Min system and was oscillating in the cell (5), if to a lesser extent. We performed time-lapse wide-field epifluorescence microscopy on both synchronous and asynchronous populations of cells expressing MipZ-eYFP (strain MT97) at varying temperatures. Cell outlines were determined through the open source MicrobeTracker using phase contrast images taken during fluorescence imaging (43). After cell meshes were created, the fluorescence signal (normalized by cell area and corrected for photobleaching) was analyzed using custom MATLAB script. Briefly, the fluorescence intensity at each polar focus was recorded for each timepoint, and the two time traces from each cell pole were compared via cross-correlation.

We found that the fluorescence intensity at each pole fluctuated aperiodically, although not nearly as dramatically as the oscillations reported for the Min system (16,

50). The fluorescence appeared to oscillate aperiodically (Figure 3, green lines), as seen by changes in fluorescence as compared to a time-averaged profile (Figure 3, black line). By performing a cross-correlation analysis of the fluorescence intensity at each cell pole, we determined that the dynamics at each pole was related to the dynamics at the opposite pole (Figure 4A). By comparing the cross-correlation analysis to a null hypothesis of a non-oscillating gradient, i.e. a system where each pole acts as both a source and a sink of MipZ and the fluorescence intensity fluctuates randomly, we found a significant difference between our observations of MipZ dynamics at the poles and the null hypothesis (Student's two-tailed T-test; $p<0.0001$). However, upon Fourier analysis of the time varying fluorescence signals, no periodicity to the oscillations was observed (Figure 4B).

Upon further discussion, we decided to look more closely at our methods of data acquisition and analysis to ensure any oscillations were not confounded by another source. We performed wide-field epifluorescence time-lapse experiments with varying exposure times and time between data acquisition. After reviewing a range of times between acquisitions, from 100 ms to 10 s, we found that the cross-correlations could give statistically significant differences from the null hypothesis, even when the intensities at the two poles clearly did not oscillate as seen by the polar intensity over time (Figure 5A-C). As an analysis control, we compared the fluorescence intensity at one pole to the fluorescence intensity at the mid-cell and found that this, too, could

create a statistically significant difference from the null hypothesis (Figure 5D). Closer inspection of our polar intensity time traces and analysis led us to believe that MipZ does not oscillate in a manner similar to the Min system, as explained in the Discussion section.

Deterministic Modeling of the MipZ Gradient

In silico experiments are capable of reconstructing patterns observed in nature as well as highlighting important details of a system that are not yet understood (16, 17, 51). Modeling thus provides useful insight into a system for determining what factors are essential for a phenomenon to occur while also guiding future experiments (17). For the division machinery regulating system of MinCDE proteins, much work has been done to model the observed spatial oscillations (17, 51). These modeling experiments shed light on which factors are important to the observed protein oscillations and predicted phenomena that were later experimentally confirmed as well as other phenomena that still require further investigation to confirm or repudiate (17, 51).

For a deterministic model of the MipZ system, we only considered changes in protein concentration in one direction (the long axis of the cell). Since MipZ is an ATPase, there are three states for nucleotide binding: apo (unbound), ADP-bound, and ATP-bound (Figure 6A). In order to simplify the equations, we ignored the dimerization step. This was partially compensated for by the fact that the rate of ATP binding (and

subsequent dimerization) is increased in the presence of ParB (see Figure 6A). The following three partial differential equations were solved in order to deterministically simulate the experimentally observed MipZ gradient.

$$\frac{\partial[MipZ]}{\partial t} = D_{MipZ}\frac{\partial^2[MipZ]}{\partial x^2} + k_{-1}[MipZ{:}\,ATP] + k_3[MipZ{:}\,ADP] - k_1[MipZ] \qquad (1)$$

$$\frac{\partial[MipZ{:}ATP]}{\partial t} = D_{MipZ:ATP}\frac{\partial^2[MipZ{:}ATP]}{\partial x^2} + k_1[MipZ] - (k_{-1} + k_2)[MipZ{:}\,ATP] \qquad (2)$$

$$\frac{\partial[MipZ{:}ADP]}{\partial t} = D_{MipZ:ADP}\frac{\partial^2[MipZ{:}ADP]}{\partial x^2} + k_2[MipZ{:}\,ATP] - k_3[MipZ{:}\,ADP] \qquad (3)$$

The known and unknown constants in these partial differential equations are highlighted in Table 1. Of the three diffusion coefficients, the ADP-bound and apo states should be indistinguishable from one another, as both should be monomers with nearly the same molecular weight and size. The ability of ParB to stimulate MipZ dimerization at the cell poles was accounted for in the model by a change in the rate of dimerization at the ParB foci (see Figure 6A). This deterministic model enabled us to simulate both a symmetric and an asymmetric MipZ gradient by having certain parameters increased or decreased at the swarmer pole in relation to the stalked pole.

Our first application of the deterministic model was to demonstrate that the three nucleotide states of MipZ (apo, ADP-bound, ATP-bound) could be simplified to two states. Two of the three nucleotide states of MipZ (apo and ADP-bound) are freely diffusing monomers in the cell, whereas the third nucleotide state of MipZ (ATP-

bound), is bound to a large macromolecule, i.e. the chromosome, which should decrease its diffusion coefficient drastically (20). As such, the three states should theoretically be able to be modeled instead as two states: fast, freely diffusing MipZ monomers and slow, DNA-bound MipZ dimers (Figure 6B). The equations for a deterministic model of this kind would be:

$$\frac{\partial[MipZ\_fast]}{\partial t} = D_{MipZ\_fast}\frac{\partial^2[MipZ\_fast]}{\partial x^2} + k_{cat}[MipZ\_slow] - k_{on}[MipZ\_fast] \quad (4)$$

$$\frac{\partial[MipZ\_slow]}{\partial t} = D_{MipZ\_slow}\frac{\partial^2[MipZ\_slow]}{\partial x^2} - k_{cat}[MipZ_{slow}] + k_{on}[MipZ\_fast] \quad (5)$$

In Figure 7, we demonstrate that modeling the MipZ gradient as a two state system is a valid simplification as determined by axial gradient profiles and simulated division ratios. We produced Figure 7E-H with the same iterative process as used for the three state model. Our modeling suggests that an asymmetric MipZ gradient can arise from differences in the kinetics and diffusion from one pole to the other. Our model also suggests that the MipZ system can be simplified from three states of the molecule to two. These results are in agreement with a recent modeling paper on MipZ (52).

Measuring the Biophysical Parameters of the Model with Single Molecule Imaging

To better probe the kinetic landscape in the cell, we attempted to measure the diffusion coefficients of the fast and slow states of MipZ, as well as the transition rates

between these two states in both the stalked and swarmer cell halves (20, 46, 53). We attempted this task using single particle tracking photoactivatable localization microscopy (sptPALM) (54).

The advent of super-resolution microscopy techniques, like PALM, has enabled the highest resolution images of living cells to date and has been incredibly valuable in the study of bacteria (54-57). Traditional microscopy techniques cannot achieve a resolution greater than ~250 nm in what is called the diffraction limit (54). Techniques like PALM take advantage of the fact that the point-spread function (PSF) of a single emitter can be localized to greater precision than the width of the PSF (54-56). In PALM, fluorescent proteins are photobleached, such that the sample is dark except for the occasional fluorescent protein re-entering a fluorescent state, or photoswitched, such that one or a few molecules are switched into a state that emits at a different wavelength than the bulk of the proteins (54). With sufficient photons detected, the PSF of this lone emitter can be localized with greater accuracy than the diffraction limit allows (54-56). The photons from PALM can be collected quickly (200 Hz and faster) and many image frames in a row can be collected (54, 56). By resolving the location of each single molecule to less than the diffraction limit and following its motion in the cell, as in sptPALM, quantitative information on the dynamics of the molecule can be obtained (46, 53, 54, 56).

We sought to measure the dynamics of MipZ in living cells using sptPALM. By measuring the changes in MipZ-Dendra2 location over time, sptPALM experiments can determine the diffusion coefficient of a molecule (46, 58). Since a DNA-bound state of MipZ should diffuse more slowly than a freely diffusing monomer, the diffusion coefficients of these two states should be able to be resolved using sptPALM, as demonstrated in previous work (46, 54). Other work has shown that sptPALM enables the measurement of the transition rates between the two states (58), which would be invaluable to our deterministic model.

Our results from sptPALM revealed relatively few surprises and agreed with some of our model predictions. We found the diffusion coefficient of the slow, DNA-bound state of MipZ to be 0.639±0.011 $\mu m^2 s^{-1}$ (mean ± 95% CI) and the diffusion coefficient of the fast, freely diffusing state to be 2.424±0.102 $\mu m^2 s^{-1}$ (mean ± 95% CI). The slow state value is a little larger than we anticipated (46), yet still revealed that MipZ can indeed be modeled as a two state system, supporting our modeling work.

To determine if two diffusive states of MipZ were sufficient to represent the sptPALM data we collected, we solved the cumulative distribution function (CDF) of molecular trajectories in our dataset by integrating the probability distribution function (PDF) of the displacement length between each image frame (r) for molecules with diffusion coefficient D at time t. For a more complete discussion on the derivation of

these equations, see (48). For a system with Brownian motion, the PDF of the molecules would be:

$$\mathrm{PDF}(r,t) = \frac{r}{2Dt}\exp\left(-\frac{r^2}{4Dt}\right) \quad (6)$$

The integration of Equation 6 would give the CDF

$$\mathrm{CDF}(r,t) = \int_0^r \mathrm{PDF}(r,t)\mathrm{d}r = 1 - \exp\left(-\frac{r^2}{4Dt}\right) \quad (7)$$

We determined a fit to our data by solving Equation 7 using only two diffusive states with the following fitting function

$$C_2(r) = A_1\left(1 - \exp\left(-\frac{r^2}{4D_1T_{tl}}\right)\right) + A_2\left(1 - \exp\left(-\frac{r^2}{4D_2T_{tl}}\right)\right) \quad (8)$$

The results of this fitting function to our data can be seen in Figure 8. We found this fit to be sufficient to support a modeling scheme with two diffusive states, as expected from previous work (46, 48). Our fit found that about one third of the MipZ-Dendra2 molecules were in the fast state and the rest were in the slow state.

Our attempts to uncover the transition rates between these two diffusive states of MipZ proved unsuccessful. We found it challenging to acquire sptPALM data accurately enough to measure the differences in diffusion coefficients and binding rates at the cell poles. We believe there are several reasons for this difficulty. Issues with dirt and non-optimal imaging conditions played a part, but these were most likely not the

main factors. In order to measure the transition rates between diffusive states, molecules must be observed switching between the states, which means that the fluorescent probes need to be stable enough for this observation to be achieved. We tried using both eYFP and Dendra2 to localize MipZ molecules, but were unable to observe molecule trajectories long enough to measure transitions. Low signal-to-noise ratios from dim fluorophores and photobleaching of molecules before transitions could be observed are likely the main culprits for why we were unable to measure transition rates.

Kinetic Landscape Measurements as a Function of DNA Density

To better understand the asymmetric placement of the division site, we investigated effects of DNA density. By using sptPALM on polar eGFP-ParB foci, we found that the eGFP-ParB foci diffused more slowly in the swarmer cell than in the stalked cell (Figure 9G). This difference in diffusion is explained by the change in function of PopZ during the cell cycle (59). PopZ has been shown to alter its role at the stalked pole from a centromere tether through its interaction with ParB to acting as a landmark for proteins involved in stalk development (59).

We also found that the diffusion coefficient of eGFP-ParB foci decreased as the SYTOX orange intensity per pixel increased at the same location in the cell (Figure 9H). This observation is potentially intriguing, as the DNA density, in which SYTOX orange

intensity serves as a proxy, could affect the diffusion of ParB clusters (60). This observation is in line with previous work demonstrating that DNA compaction can affect molecule distributions in a cell (60). We found that the distribution of SYTOX orange as measured by fluorescence intensity was fairly uniform, with perhaps a slightly lower intensity level in the swarmer cell, although more cells should be investigated in order to determine this discrepancy more accurately (Figure 9E&F).

Measuring Polar Differences with Wide-Field Epifluorescence Microscopy

The first paper to report on MipZ stated that the authors did not observe a significant difference between the fluorescence intensity at the stalked pole versus the swarmer pole (37). As such, we did not immediately pursue the aspect of our hypothesis that polar differences in the number of bound MipZ molecules would explain the asymmetric MipZ gradient. However, over the course of our experimentation, we found that the MipZ focus at the stalked pole was slightly brighter than at the swarmer pole. In order to investigate our hypothesis further, we measured the fluorescence intensity of MipZ-Dendra2 along the long axis of the cell via wide-field epifluorescence microscopy and did the same for eGFP-ParB and PopZ-mCherry, as seen in Figure 10B-D. We also decided to measure the cell width along its length to get a better understanding of the cell geometry in which these protein distributions occur, which can be seen in Figure 10A. The decrease in cell width from the stalked pole to the

swarmer pole explains the discrepancy between the division ratio and volume ratio of *C. crescentus* cells.

Through this method, we found that the fluorescence intensity of MipZ-Dendra2 was higher in the stalked pole compared to the swarmer pole and found this was the case for eGFP-ParB as well. PopZ-mCherry also displayed a higher intensity at the stalked pole compared to the swarmer pole, but this is to be expected, as PopZ accumulates at the new pole gradually over the cell cycle (61). The ratios of stalked pole intensity to swarmer pole intensity for MipZ-Dendra2, eGFP-ParB, and PopZ-mCherry in otherwise wild-type cells were 1.268 ± 0.664, 1.219 ± 0.508, and 1.391 ± 0.786 (mean ± standard deviation), respectively. We also found that the location in the cell in which the MipZ gradient was minimized colocalized with the division site, as previous research has shown (28, 37, 38). Intriguingly, we observed that the minimum of the ParB gradient was also asymmetric, although skewed further towards the new pole than the MipZ minimum (Figure 10D). To the best of our knowledge, this is the first report of an asymmetric ParB profile in the cell. To follow suit, we also found the PopZ-mCherry gradient to be asymmetric in the cell, with its minimum skewed further towards the new pole than the ParB minimum (Figure 10B&C).

We were curious how these gradients would be affected in cells lacking the polar landmark protein TipN (39). We measured the fluorescence intensity of MipZ-Dendra2, eCFP-ParB, and PopZ-mCherry along the long axis of the cell via wide-field

epifluorescence microscopy, as seen in Figure 12B-D. We also measured the cell width along its length to understand how the cell geometry changes without TipN, which can be seen in Figure 12A.

We found that the fluorescence intensity of MipZ-Dendra2 was higher in the stalked pole compared to the swarmer pole and found this was the case for eGFP-ParB and for PopZ-mCherry. The ratios of stalked pole intensity to swarmer pole intensity for MipZ-Dendra2, eCFP-ParB, and PopZ-mCherry in cells lacking TipN were 1.097 ± 0.400, 1.166 ± 0.397, and 2.250 ± 1.401 (mean ± standard deviation), respectively. To determine if the location in the cell in which the MipZ gradient was minimized colocalized with the division site, we first measured the division ratio and volume ratio for cells lacking TipN. These cells displayed a reversed asymmetry with shorter stalked cells than swarmer cells, confirming previous studies (28, 39). We found that the location in the cell in which the MipZ gradient was minimized colocalized with the division site. Intriguingly, we observed that the minimum of the ParB gradient was also asymmetric and colocalized with the minimum of the MipZ gradient (Figure 12C&E). The PopZ-mCherry gradient was asymmetric in the cell, with its minimum skewed further towards the old pole than either the MipZ-Dendra2 or eCFP-ParB minimum (Figure 12B).

DISCUSSION

In this chapter, we examined the asymmetric cell division of *C. crescentus* through the asymmetric gradient of the FtsZ regulating protein MipZ and its interacting partners. We investigated this asymmetry through optical microscopy techniques and computational methods. Through these experiments, we observed protein transport between the two cell poles, recreated the MipZ gradient *in silico*, and garnered insight into the asymmetric nature of proteins involved in positioning MipZ, which then directs FtsZ to the appropriate location in the cell. We examined aspects of this system in mutants lacking the polar landmark protein TipN and discovered more about the reversed cell size asymmetry in those mutants.

Our first attempts at understanding the asymmetric MipZ gradient were through investigating a potential oscillation along the long axis of the cell, similar to the Min system of proteins found in *E. coli*. While we did observe protein flux from one pole to the other, as measured by wide-field epifluorescence time-lapse axial profiles (Figure 3), we found that the MipZ system does not oscillate, as shown by fast Fourier transforms of the cross correlations of the polar fluorescence intensity time traces (Figures 4 and 5).

Closer analysis of the key aspects of the Min system oscillation reveals that this conclusion is consistent with our understanding of oscillatory systems (16, 17, 62, 63). The MinCDE system in *E. coli* and the MipZ system in *C. crescentus* display several similarities, such as MinD and MipZ both being ATPase of similar types and both

molecules existing in two major diffusive states, one freely diffusing and one bound to a large substrate (the cell membrane in the case of MinD and the chromosome in the case of MipZ) (16, 38). These two systems also display several key differences. The first key difference is that MinD binds cooperatively to its large substrate, while MipZ has been shown to bind non-cooperatively (14, 16, 38). Modeling work on MinD shows that the membrane-binding cooperativity is an essential component of oscillations, as it allows a significant amount of protein to transition to a slower diffusive state in one portion of the cell in a relatively short amount of time (17). The second key difference is that MinE can processively remove MinD dimers from the membrane, causing a significant amount of protein to transition to the faster diffusive state in a relatively short amount of time (16, 17), while, as of the writing of this thesis, we are not aware of any actors in *C. crescentus* that stimulate the ATPase activity of MipZ to cause rapid unbinding of large amounts of protein from the DNA. These two key differences are sufficient to explain why no oscillations were observed in the MipZ system.

It is interesting to note that previous experimental and modeling work has shown that oscillations can be induced in the MipZ system (28, 52). The overproduction of ParA within the cell can cause ParA to forego its usual gradient (increasing towards the new pole) and accumulate at the old pole for a time, then back to the new, in an oscillatory manner with a period on the order of tens of minutes (28). ParB interacts with ParA, so as ParA oscillates, so does ParB, and since ParB stimulates dimer

formation of MipZ, MipZ colocalizes with ParB in the cell (28, 37, 38). This observed oscillation is reminiscent of the oscillating regimes of Par proteins involved in plasmid segregation in *E. coli* (64).

Through our deterministic modeling work and our sptPALM analysis of MipZ-Dendra2, we show that the MipZ gradient can be explained as a system with two diffusive states and polar differences in the kinetics and/or diffusion of MipZ. We first demonstrated that the three nucleotide state model of MipZ can be simplified into two states, as shown by modeling the asymmetric gradient and simulated division ratios (Figure 7G&H). We found this simplification to be supported by our sptPALM data, since a two state CDF fit our molecular trajectories well (Figure 8C). This modeling simplification is also supported by recent modeling work (52). We found that in order for our deterministic model to accurately recreate the experimentally observed MipZ gradient, our model parameters needed to be different by amounts that likely would not be measured *in vivo*. For instance, our sptPALM data showed that the diffusion coefficients between the two states were only about an order of magnitude different, whereas our model necessitated they differ by two orders of magnitude. This discrepancy could arise from sub-optimal conditions for our sptPALM data. In our experimentation, our acquisition conditions differed depending on whether we were trying to capture molecules in the slow state or the fast state. The data presented in Figure 8 was a middle ground of sorts, potentially missing some of the faster molecules

and some of the slower molecules. Future work will be necessary in order to more accurately model the MipZ gradient and to measure the biophysical parameters of gradient formation.

In an attempt to examine the effects of DNA density on cell division, we performed sptPALM on eGFP-ParB foci diffusion and measured DNA density by SYTOX orange staining. We observed eGFP-ParB foci diffusing more slowly in the swarmer cell than in the stalked cell (Figure 9G). This result is supported by previous research on ParB-PopZ interactions and the role of PopZ throughout the cell cycle and adds more evidence to the hypothesis that PopZ changes from centromere tether to polar landmark for stalk development (59).

ParB diffusion was also observed to be slower as the DNA density at the same location increased, as measured by SYTOX orange fluorescence intensity, as seen in Figure 9H. Previous research has shown that DNA density can affect protein distributions (60). Our results add to this body of work. We did not observe any immediately obvious differences in SYTOX orange intensity along the cell length (Figure 9E&F), so further study will be needed in order to determine if DNA density differences affect the distributions of these division proteins.

Through the use of wide-field epifluorescence microscopy, we examined the axial profiles of the three major proteins involved in FtsZ localization, namely MipZ, ParB, and PopZ. In agreement with previous research, we found that the location in the

cell in which the MipZ gradient was minimized matched the location of cell division (Figure 10D). However, unlike previous research, we found that there was a difference in fluorescence intensity between the two poles, with the stalked pole exhibiting higher fluorescence intensities of MipZ-Dendra2 than the swarmer pole (Figure 10D&F). The difference between what we report and that published by Thanbichler & Shapiro could be subtle. Thanbichler & Shapiro state that they "have not detected a significant difference in the fluorescence intensity of MipZ-YFP at the two poles" (37). It is unclear what threshold they used in order to determine if the difference was significant. It is also worth noting that Thanbichler & Shapiro did not display a fluorescence profile of MipZ along the full length of the cell with associated error (37). Thanbichler & Shapiro do acknowledge that some asymmetry must exist, stating that "a bias in the subcellular distribution of MipZ could lead to a higher concentration of the protein at the stalked pole, skewing the placement of the Z-ring such that it localizes closer to the incipient swarmer cell pole" (37).

Using the same wide-field epifluorescence technique, we observed that the fluorescence intensity of eGFP-ParB was higher at the stalked pole than at the swarmer pole (Figure 10C&F). To the best of our knowledge, this is the first instance of ParB asymmetry being reported. This asymmetry could potentially be valuable to modelers, as the report by Shtylla assumes that ParB concentrations are the same at each pole. The fluorescence intensity difference we observed may not lead to a drastic difference in the

model outcome, but would be interesting to investigate nonetheless. Upon discovering this asymmetry, we wondered how this ParB asymmetry could arise. Differences in DNA-binding and polar anchoring proteins at the cell poles may help explain this observation (31, 32).

We also observed that the PopZ-mCherry fluorescence intensity was higher at the stalked pole than at the swarmer pole (Figure 10B&F). This observation is in agreement with previous research, as PopZ has been shown to slowly accumulate at the new pole over the course of the cell cycle (61).

Our investigation into the fluorescence profiles of MipZ, ParB, and PopZ in cells lacking TipN revealed several interesting results. First, we observed that the division ratio of these cells was reversed, with the stalked cell being shorter than the swarmer cell after division (Figure 11). This observation is in agreement with previous research (28, 39). The fluorescence intensity profile of MipZ-Dendra2 was asymmetric, such that the minima colocalized with the site of cell division (Figure 12D). As shown in previous research, we found that the ratio of fluorescence intensities of MipZ-Dendra2 at the two cell poles was similar to that of cells with TipN (28). The bipolar gradient minima being reversed were also observed for the fluorescence intensity profile of eCFP-ParB and of PopZ-mCherry. We also found that the ratio of fluorescence intensities of eCFP-ParB and of PopZ-mCherry at the two cell poles was similar to cell with TipN.

Recent modeling work suggests the asymmetric MipZ gradient arises from competition between ParA and MipZ for interactions with ParB (52). Since ParA is unevenly distributed in the cell with a concentration increasing towards the new pole, the biggest effect of this competition should be observed at the swarmer pole (27, 52). Our modeling work supports this in at least some respect, as we found that the asymmetric gradient can be reproduced by polar differences in binding/unbinding. However, we present data here that invalidates some of the assumptions made in the modeling paper (52). First, the model assumes that the ParB concentration is the same at both poles, but this is not what we observed (Figure 10C&F). Second, the model assumes a uniform cell width along its length, which again we did not find to be the case (Figure 10A). The amount that these observations change the model is unclear. We found that kinetic differences alone are enough to recreate the experimentally observed, asymmetric MipZ gradient.

We verify and build upon previous research on MipZ, ParB, and PopZ within *C. crescentus* cells. Bacteria have evolved incredible mechanisms to ensure their faithful reproduction, and in the case of *C. crescentus*, cellular asymmetry. Our findings in this chapter add to the intricate system that *Caulobacter* uses to couple its chromosomal replication and segregation to its positioning of the cell division machinery. The work we describe in this chapter expands on one small aspect of a complicated network of

interacting proteins that make *C. crescentus* such an interesting organism to study now and in the future.

FUTURE DIRECTIONS

The most complete model of the MipZ gradient is most likely that of Shtylla (52). As such, we envision the majority of future experiments focused on testing this model. In particular, the model proposes a "saturation hypothesis", or that competition between MipZ and ParA for ParB interactions is sufficient to create the observed, asymmetric MipZ gradient (52). The reasoning for this hypothesis is that both MipZ and ParA interact with ParB and ParB likely has a limited number of binding sites. Due to a gradient of ParA with the highest concentration at the swarmer pole, the most significant competition for ParB would occur at this new pole, skewing the MipZ gradient such that its minimum is closer to the swarmer pole (27, 52). Here we outline several experiments that may be useful in refining the model by Shtylla and testing its robustness.

One potential avenue for testing the saturation hypothesis proposed by Shtylla is to measure the kinetics of MipZ at each pole. Like we attempted, sptPALM could be useful in this regard (46, 53, 54, 56). With sufficient single molecule trajectories, the transition rates between the fast and slow states of MipZ could be measured at each cell pole (53, 58). Since this data can be difficult to acquire, methods like those employed by Liao et al. could help simplify the analysis of this data (47). Another technique that might give insight into the kinetics at each cell pole is fluorescence recovery after photobleaching, or FRAP (20). FRAP experiments on MipZ could potentially show a

general difference in binding and unbinding kinetics between the stalked and swarmer poles, as the rates at which the photobleaching recovers may differ between the poles. If a difference in the kinetics were observed between the two poles, these experiments would help support the saturation hypothesis.

Another interesting set of experiments that would test this saturation hypothesis involves varying the levels of ParA in the cell. Mutants with inducible ParA would enable studies over a range of ParA concentrations in the cell (42). At each concentration of ParA, one could measure the division and volume ratios of the cell, as well as the fluorescence intensity axial profiles of MipZ, ParB, and PopZ. If the saturation hypothesis is correct, then lower levels of ParA should result in division and volume ratios closer to 0.5. The MipZ gradient should then also display a minimum closer to 0.5, as there is less ParA to compete for ParB interactions. As the concentration of ParA increases, so should the division ratio, up until the point at which the ParA concentration is high enough to induce oscillatory behavior (28). Another interesting experiment would be to measure the kinetics through sptPALM or FRAP at both poles while varying the induction of ParA. Ideally, as the concentration of ParA is increased, the larger the difference in MipZ kinetics between the two cell poles. This experiment may be challenging with sptPALM, so if FRAP is able to measure polar kinetic differences, then it would be preferred for these experiments.

It is unknown where on the proteins MipZ and ParB interact. Studies investigating the residues responsible for their interaction might provide a more detailed view of their interactions. Point mutations along both proteins may shed light on where their interactions arise, potentially enabling a new target for antibiotic treatment. Novel small molecules could be developed to disrupt the interaction between MipZ and ParB, disabling the cell from faithfully positioning the division plane and disrupting microbial proliferation.

In order to test the robustness of the saturation hypothesis and the Shtylla model, it would be interesting to examine the effects of the removal of TipN. All of the experiments outlined above could be performed in cells lacking TipN. Some of the modeling done by Shtylla incorporates cells without TipN (52), so further study of these cells could provide new insights into the maintenance of the asymmetric MipZ gradient.

The model proposed by Shtylla also makes several assumptions that we found to be inconsistent with our data (52). The model assumes that ParB concentrations are the same at each cell pole, which differs from our results. The model also assumes the cell width is uniform along its length, which is also inconsistent with our results. These differences would be interesting to incorporate into the model.

We were intrigued by the asymmetric nature of the ParB gradient as well. Why is the gradient of this protein asymmetric? What other proteins does ParB interact with

that might affect its cellular distribution? Are there differences in DNA-binding affinity between the two chromosomal origins? What other proteins might affect the affinity of ParB for the chromosome? Many questions arise from our observation of an asymmetric ParB gradient.

We are curious as to how many PopZ molecules are required to tether ParB to the cell poles. We are also curious as to why the minimum of the PopZ distribution shifted in similar amounts as the minima of the ParB and MipZ gradients. The observation that PopZ changes function during the course of the cell cycle from centromere tether to polar landmark for stalk development proteins further complicates our understanding of the system (59). The ParB cluster at the stalked pole diffuses faster than that at the swarmer pole, but it is unclear how the ParB cluster at the stalked pole remains relatively stationary over the course of the cell cycle without the PopZ tether. Overall, we think many fascinating directions exist for future research in this area.

ACKNOWLEDGEMENTS

We are grateful to Somenath Bakshi for help designing and conducting experiments for oscillation measurements. We are grateful to Yejin Eun for modeling help and guides. We are grateful to James C. Weisshaar for designing experiments and for excellent advice. We are thankful to Nikolai Radzinski for help designing and conducting experiments, analyzing data, and productive discussions. We would like to thank the labs and PIs of the following labs: the Lucy Shapiro lab, the Erin Goley lab, the Christine Jacobs-Wagner lab, the Grant Bowman lab, and the Martin Thanbichler lab for strains and cloning advice.

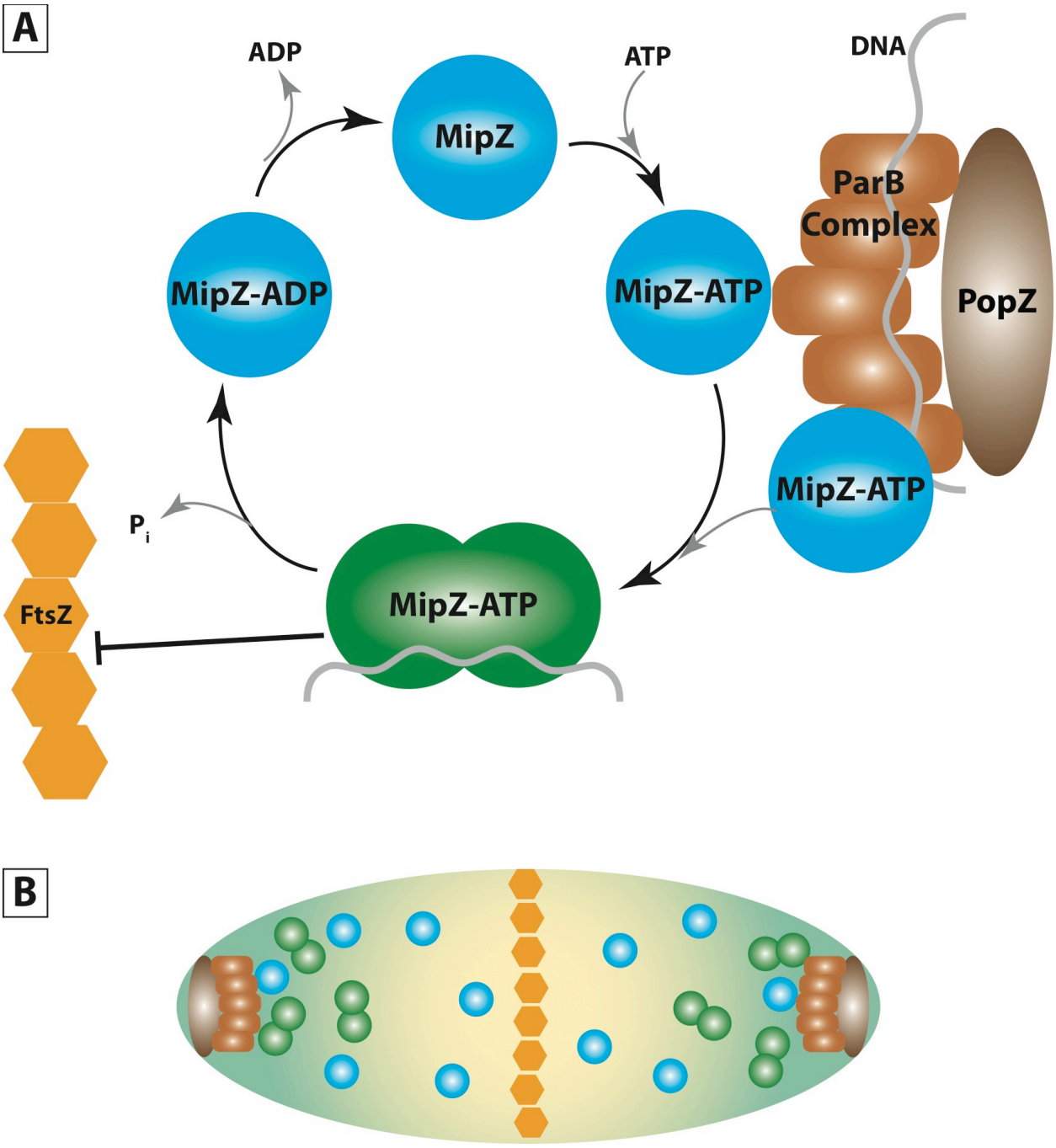
A
ADP
MipZ
ATP
DNA
ParB
Complex
PopZ
MipZ-ADP
MipZ-ATP
MipZ-ATP
P
i
FtsZ
MipZ-ATP
B

Figure 1

Figure 1: Cartoon model of the MipZ lifecycle and its cellular distribution. A) MipZ Lifecycle. MipZ monomers (blue circles) can bind ATP and interact with ParB (light brown curved rectangles), stimulating their dimerization and binding to DNA. MipZ dimers (green double circles) negatively regulate FtsZ assembly by stimulating the GTPase activity of FtsZ (yellow hexagons) before undergoing ATP hydrolysis and beginning the cycle anew. PopZ (dark brown oval) tethers ParB to the cell poles. B) PopZ is found at the cell poles and anchors ParB to the same location. MipZ interacts with ParB and positions FtsZ to the mid-cell.

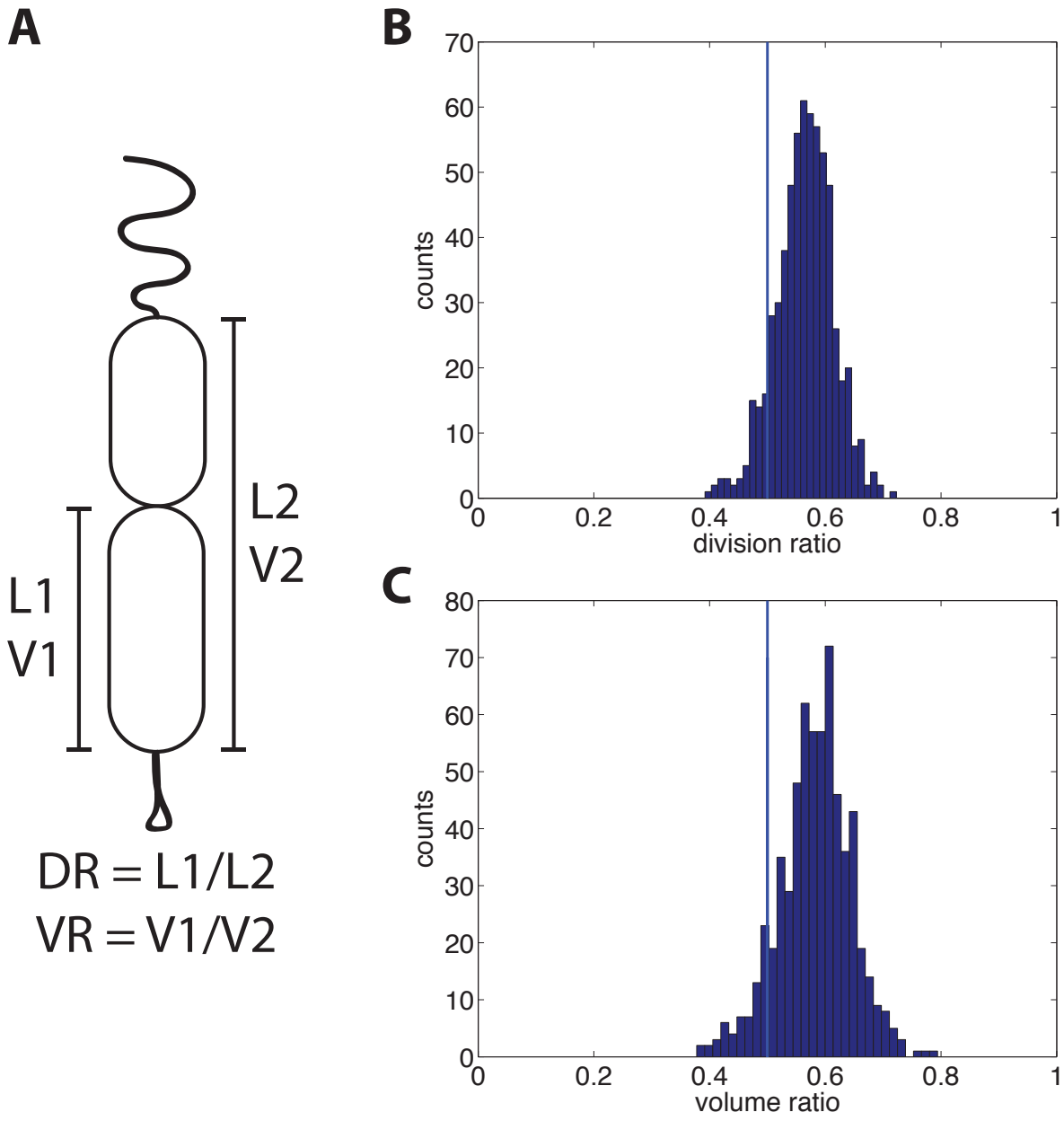
A
L2
V2
L1
V1
DR = L1/L2
VR = V1/V2
B
counts
division ratio
C
counts
volume ratio

Figure 2

Figure 2: Quantification of cell division and volume ratios for wild-type CB15N cells. A) Cartoon representation of how the division and volume ratios are calculated. The cell on the bottom is the stalked cell and the cell on the top is the swarmer cell. B) Distribution of division ratios for CB15N (N = 632). Vertical dark blue line represents 0.5 or perfectly even cell lengths. C) Distribution of volume ratios for CB15N (N = 632). Vertical dark blue line represents 0.5 or perfectly even cell volumes.

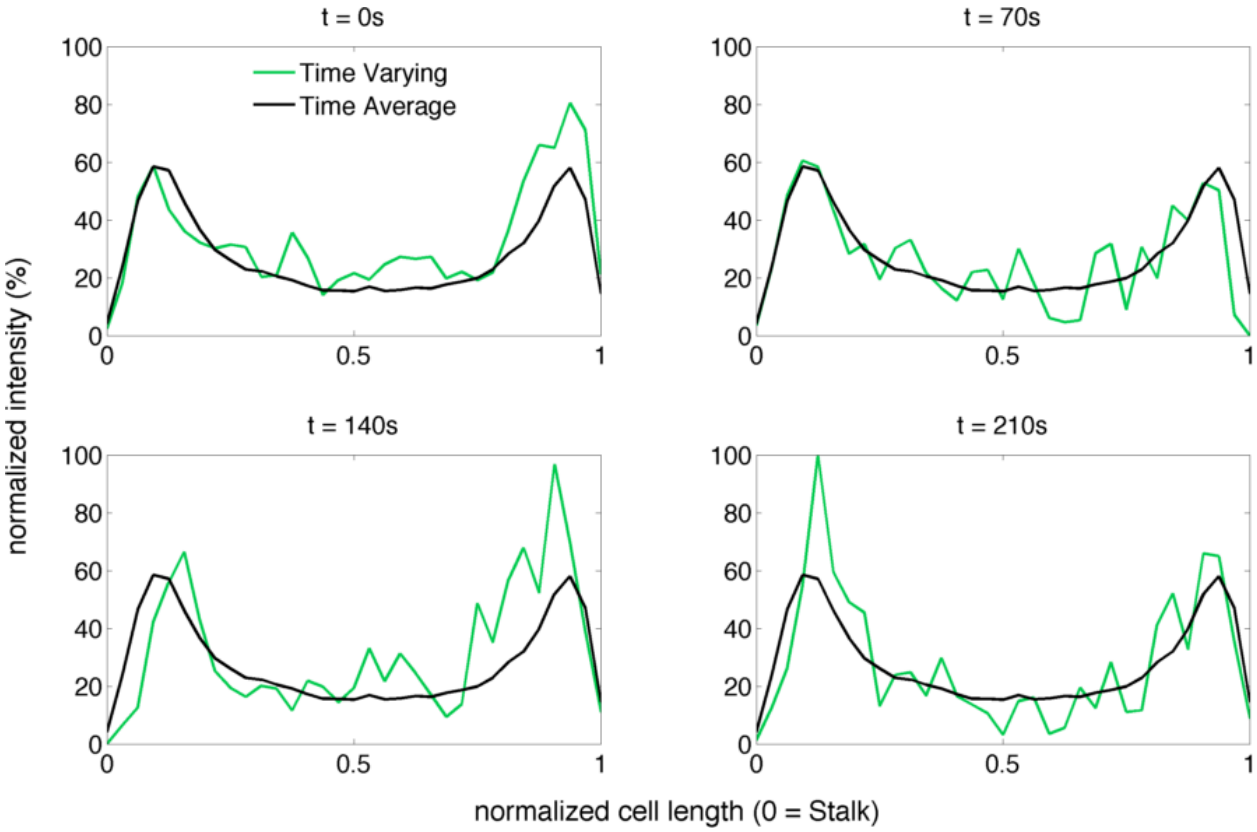
t = 0s
t = 70s
t = 140s
t = 210s
Time Varying
Time Average
normalized intensity (%)
normalized cell length (0 = Stalk)
0
20
40
60
80
100
0
0.5
1

Figure 3

Figure 3: MipZ dynamics look like oscillations when compared to time-averaged gradient. All x-axes are normalized cell length, with 0 representing the stalked pole. All y-axes are normalized fluorescence intensity of MipZ-eYFP.

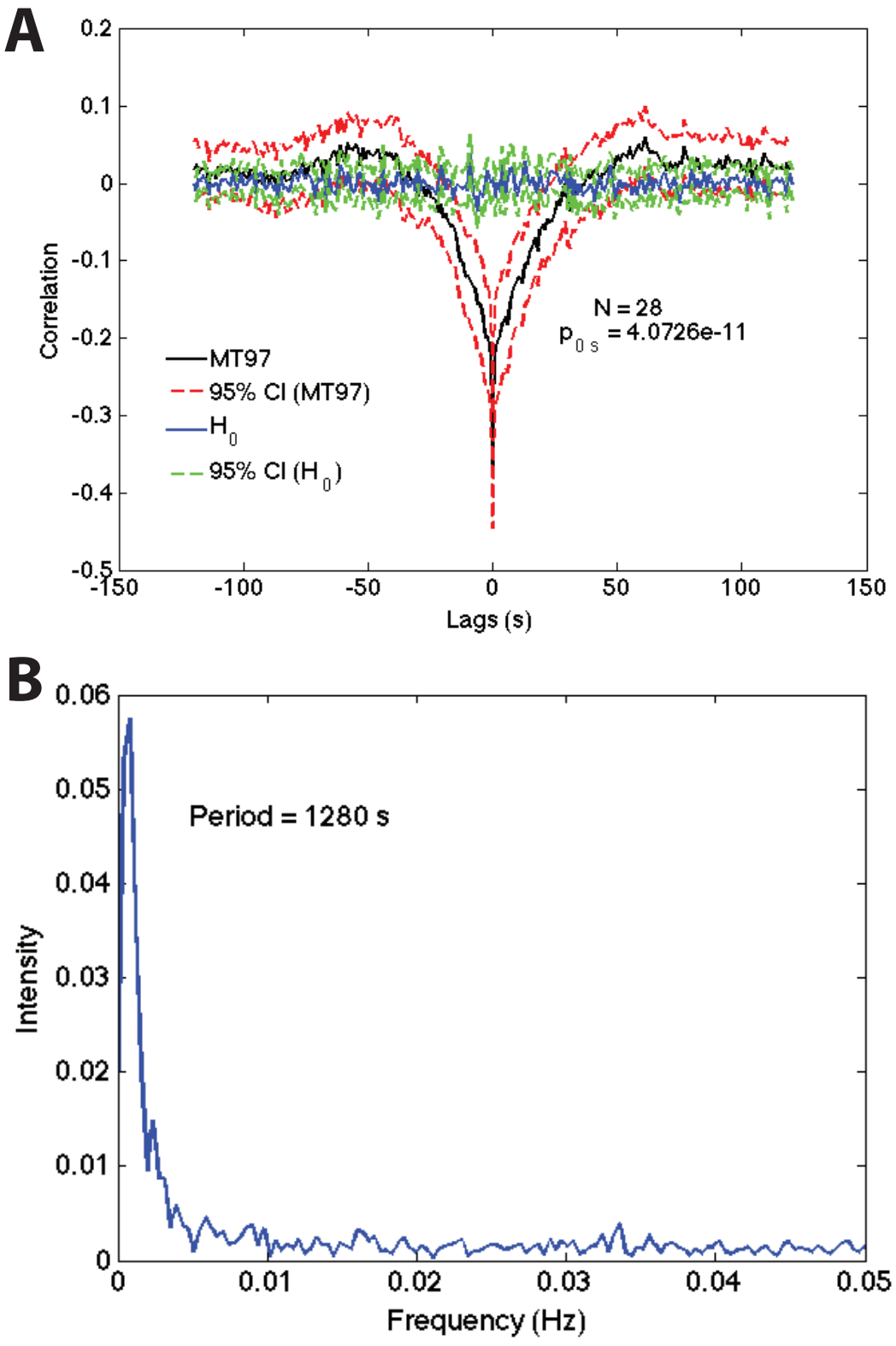
A
0.2
0.1
0
-0.1
-0.2
-0.3
-0.4
-0.5
Correlation
-150
-100
-50
0
50
100
150
Lags (s)
N = 28
p0 s = 4.0726e-11
MT97
95% CI (MT97)
H0
95% CI (H0)
B
0.06
0.05
0.04
0.03
0.02
0.01
0
Intensity
Period = 1280 s
0
0.01
0.02
0.03
0.04
0.05
Frequency (Hz)

Figure 4

Figure 4: Cross-correlation of MipZ-eYFP polar intensity profiles and fast Fourier transform of the cross-correlation. A) Cross-correlation of fluorescence intensity over time at each pole of MipZ-eYFP (black and red lines) compared to a null hypothesis of randomly fluctuating intensities (blue and green lines). B) Fast Fourier transform of the cross-correlation in A).

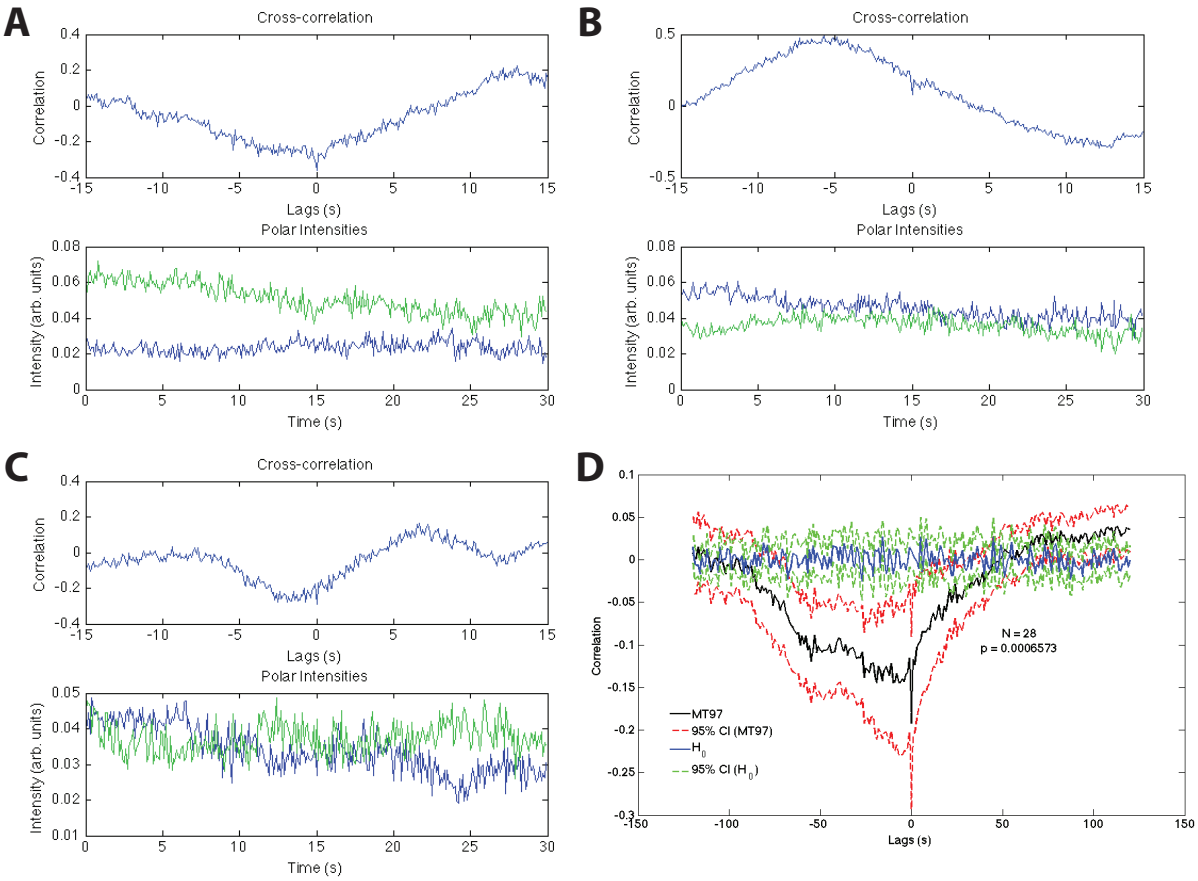
A
Cross-correlation
Correlation
Lags (s)
Polar Intensities
Intensity (arb. units)
Time (s)
B
Cross-correlation
Correlation
Lags (s)
Polar Intensities
Intensity (arb. units)
Time (s)
C
Cross-correlation
Correlation
Lags (s)
Polar Intensities
Intensity (arb. units)
Time (s)
D
Correlation
Lags (s)
N = 28
p = 0.0006573
MT97
95% CI (MT97)
H0
95% CI (H0)

Figure 5

Figure 5: Analysis demonstrating lack of oscillation of MipZ. A-C) Top of each panel: Cross-correlations of polar intensity profiles of MipZ-eYFP. Bottom of each panel: Fluorescence intensity profiles at the cell poles over time that were used in the respective top panel. D) Analysis control of polar intensity vs mid-cell (black and red lines) compared to a null hypothesis of randomly fluctuating intensities (blue and green lines).

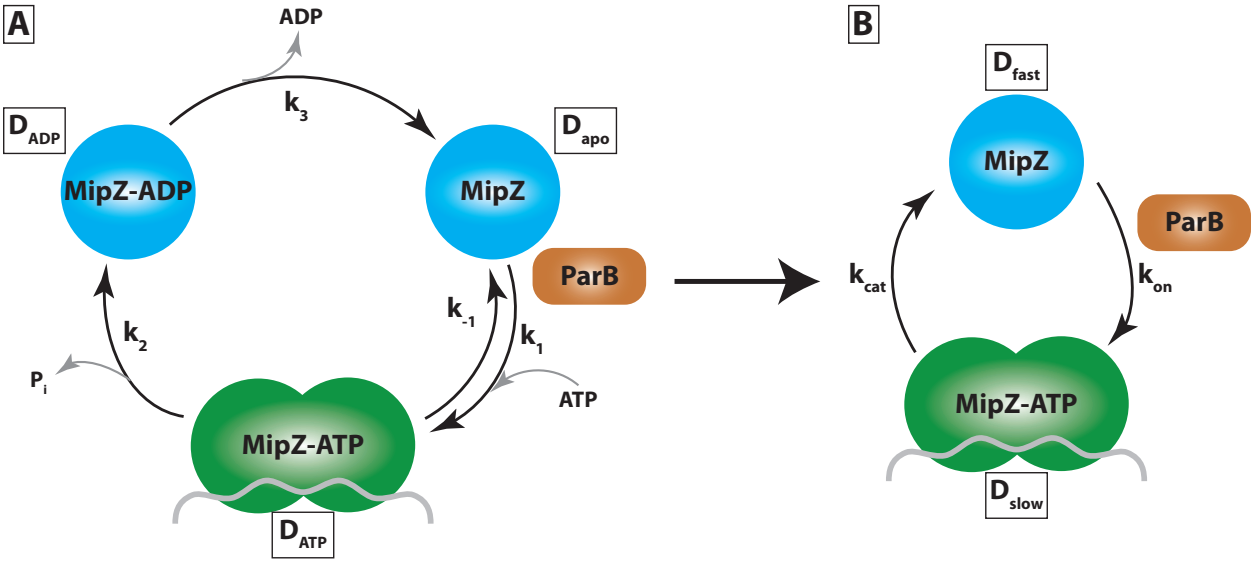
A
ADP
k3
DADP
Dapo
MipZ-ADP
MipZ
ParB
k2
k-1
k1
Pi
ATP
MipZ-ATP
DATP
B
Dfast
MipZ
ParB
kcat
kon
MipZ-ATP
Dslow

Figure 6

Figure 6: Cartoon model of three and two state MipZ systems for modeling. A) MipZ exists in three nucleotide states, ATP-bound, ADP-bound, and apo, each with their own diffusion coefficients and kinetic rates between the different states. B) MipZ exists in two states, monomer and dimer, each with their own diffusion coefficients and kinetic rates between the two states.

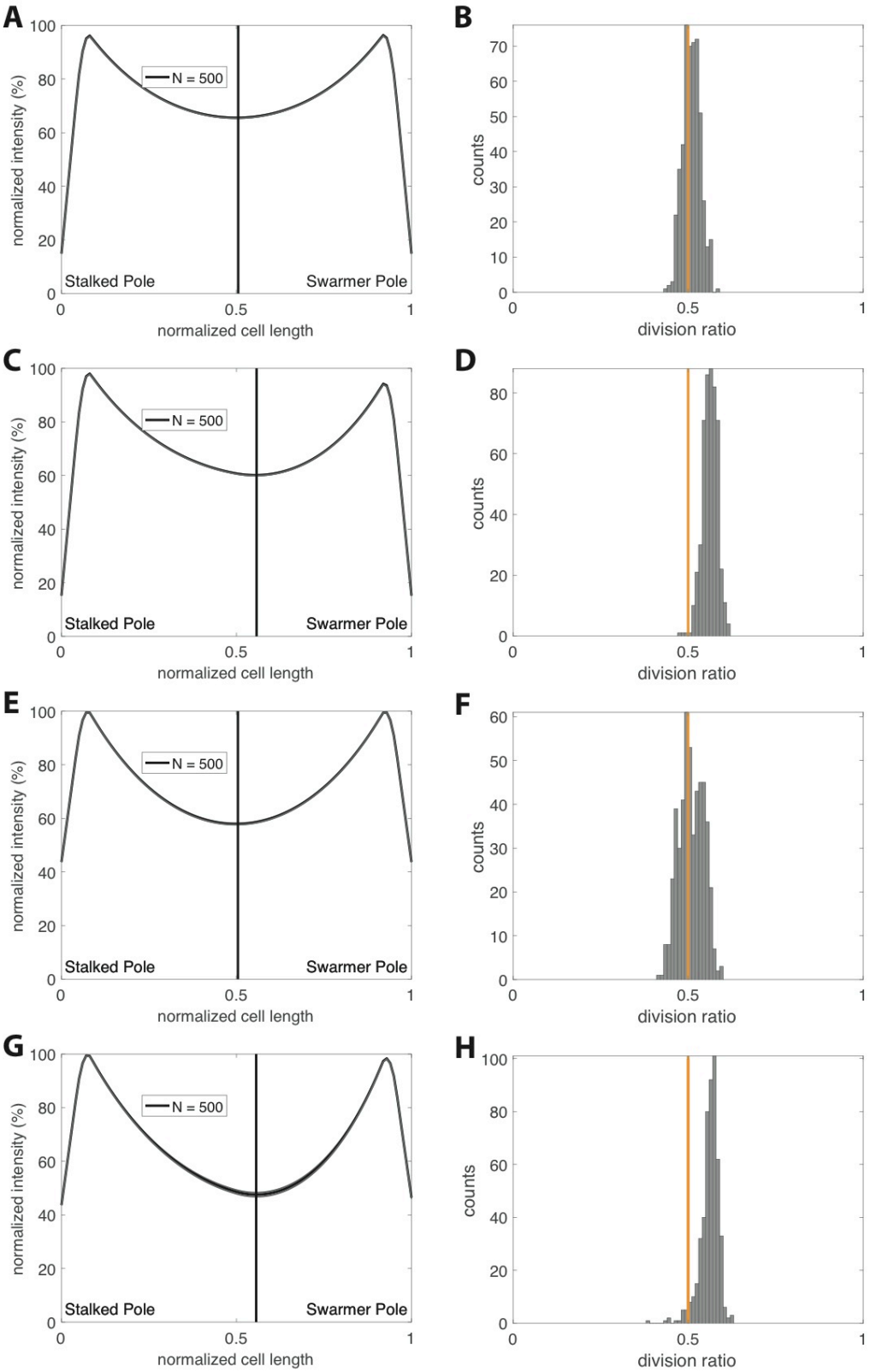
A
B
C
D
E
F
G
H
N = 500
normalized intensity (%)
normalized cell length
Stalked Pole
Swarmer Pole
counts
division ratio

Figure 7

Figure 7: Simulated MipZ gradients and division ratios. A) Simulated, symmetric, one dimension MipZ gradient using the three state model. Vertical black line represents the minimum of the gradient between the two polar maxima. B) Simulated, symmetric division ratios of cell with MipZ gradients in A), where the division location is determined by the MipZ minimum between the two polar maxima. Vertical orange line represents 0.5. C) Simulated, asymmetric, one dimension MipZ gradient using the three state model. Vertical black line represents the minimum of the gradient between the two polar maxima. D) Simulated, asymmetric division ratios of cell with MipZ gradients in C), where the division location is determined by the MipZ minimum between the two polar maxima. Vertical orange line represents 0.5. E) Simulated, symmetric, one dimension MipZ gradient using the two state model. Vertical black line represents the minimum of the gradient between the two polar maxima. F) Simulated, symmetric division ratios of cell with MipZ gradients in E), where the division location is determined by the MipZ minimum between the two polar maxima. Vertical orange line represents 0.5. G) Simulated, asymmetric, one dimension MipZ gradient using the two state model. Vertical black line represents the minimum of the gradient between the two polar maxima. H) Simulated, asymmetric division ratios of cell with MipZ gradients in G), where the division location is determined by the MipZ minimum between the two polar maxima. Vertical orange line represents 0.5.

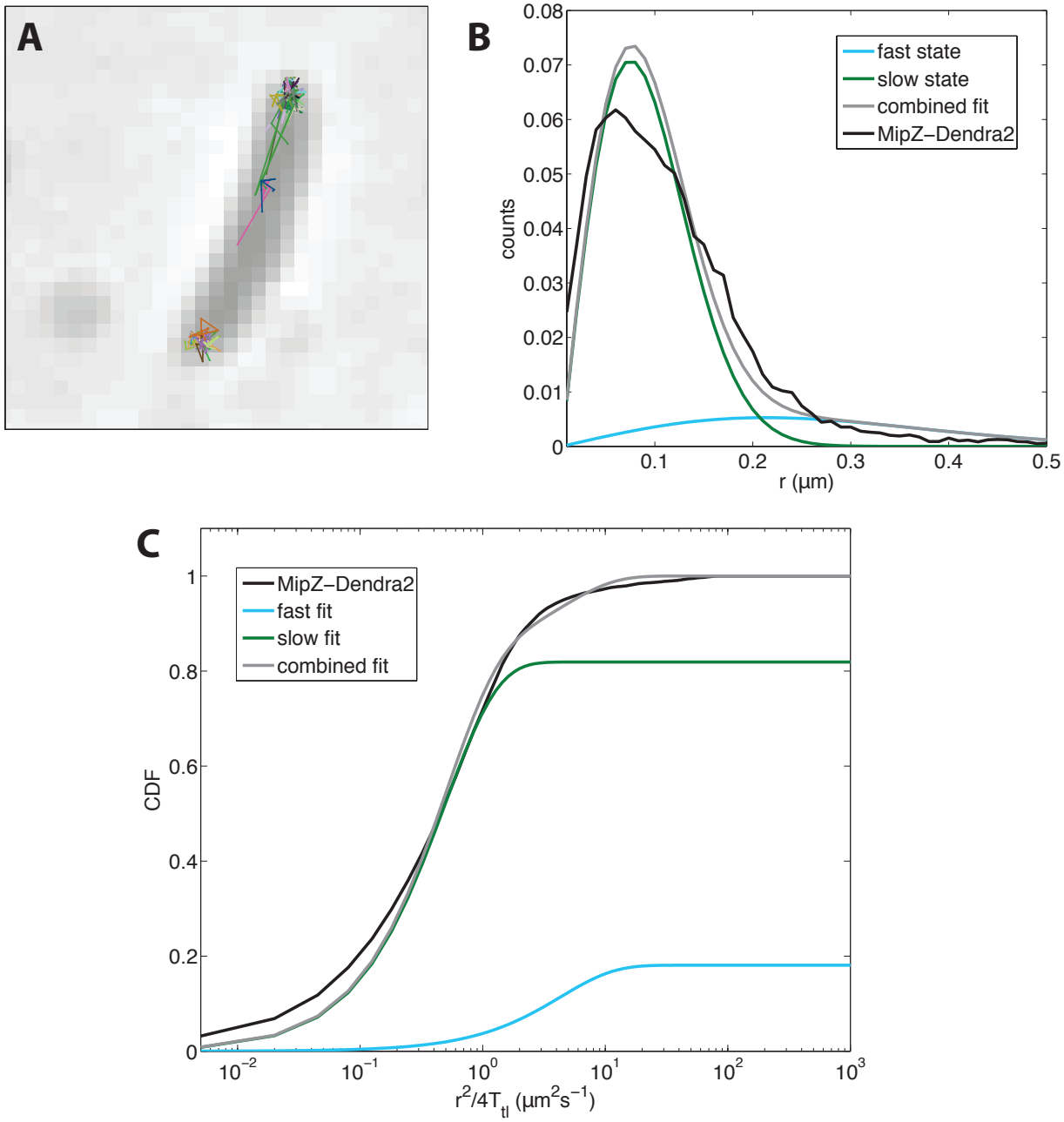
A
B
fast state
slow state
combined fit
MipZ–Dendra2
counts
r (μm)
C
MipZ–Dendra2
fast fit
slow fit
combined fit
CDF
r²/4T_tl (μm²s⁻¹)

Figure 8

Figure 8: sptPALM data and analysis. A) Single-molecule trajectories of MipZ-Dendra2 superimposed on a phase contrast image of a cell. B) Distribution of single step lengths of MipZ-Dendra2 molecules and associated two state fitting. C) Cumulative distrubition function fitting of data in A) and B), assuming a two state system.

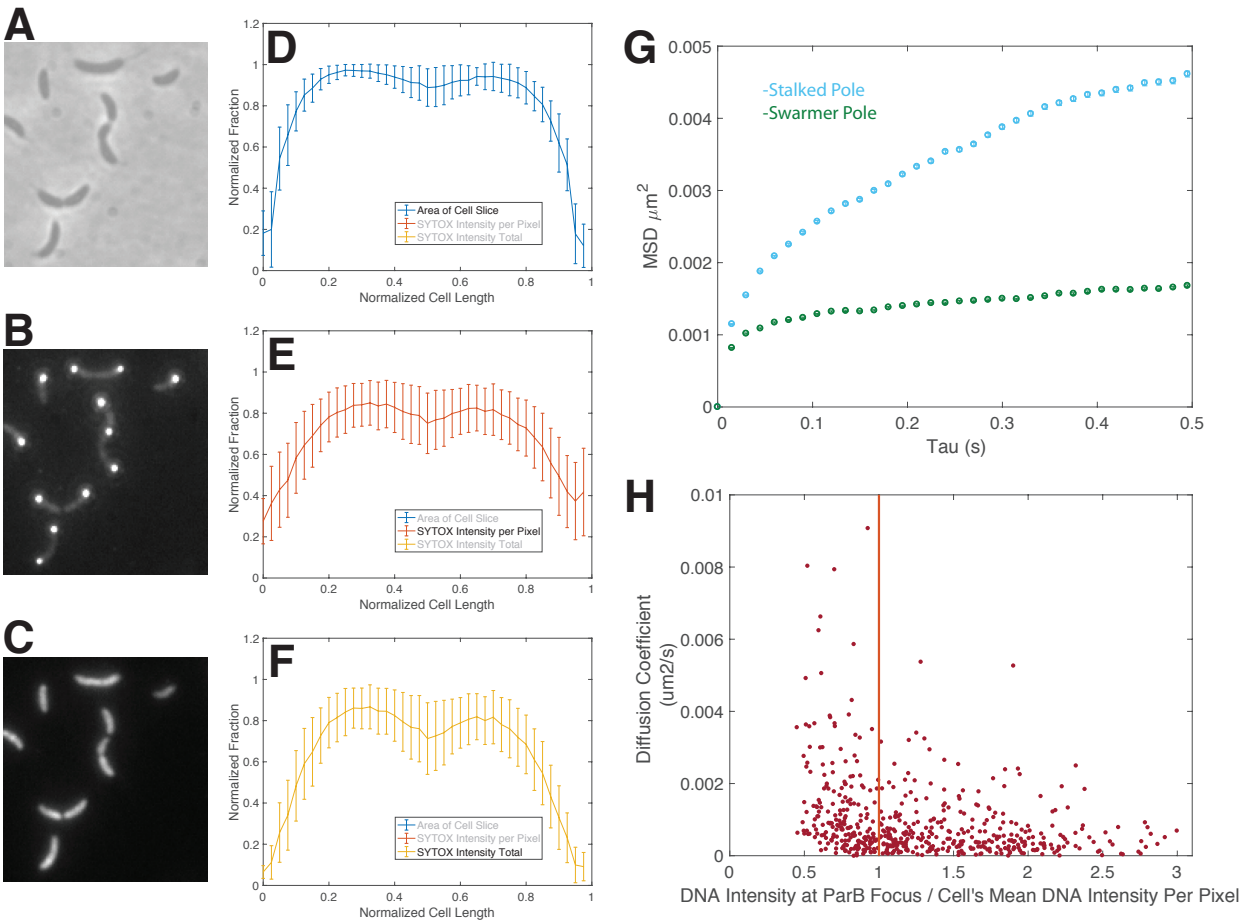
A
B
C
D
E
F
G
H
Normalized Fraction
Normalized Cell Length
Area of Cell Slice
SYTOX Intensity per Pixel
SYTOX Intensity Total
-Stalked Pole
-Swarmer Pole
MSD μm^2
Tau (s)
Diffusion Coefficient (um2/s)
DNA Intensity at ParB Focus / Cell's Mean DNA Intensity Per Pixel

Figure 9

Figure 9: DNA density via SYTOX orange and ParB diffusion. A-C) Images of phase contrast (A), eGFP-ParB (B), and SYTOX orange in MT174 cells. D-F) Analysis of SYTOX orange distribution. D) Area of cell slice as determined by Oufti along the length of the cell. E) SYTOX orange intensity per pixel along the length of the cell. F) SYTOX orange total intensity along the length of the cell. G) Mean square displacement of eGFP-ParB. Blue circles represent eGFP-ParB foci at the stalked pole. Green circles represent eGFP-ParB foci at the swarmer pole. H) Diffusion coefficients of eGFP-ParB as a function of the SYTOX orange intensity at the eGFP-ParB focus normalized by the mean SYTOX orange intensity in the same cell.

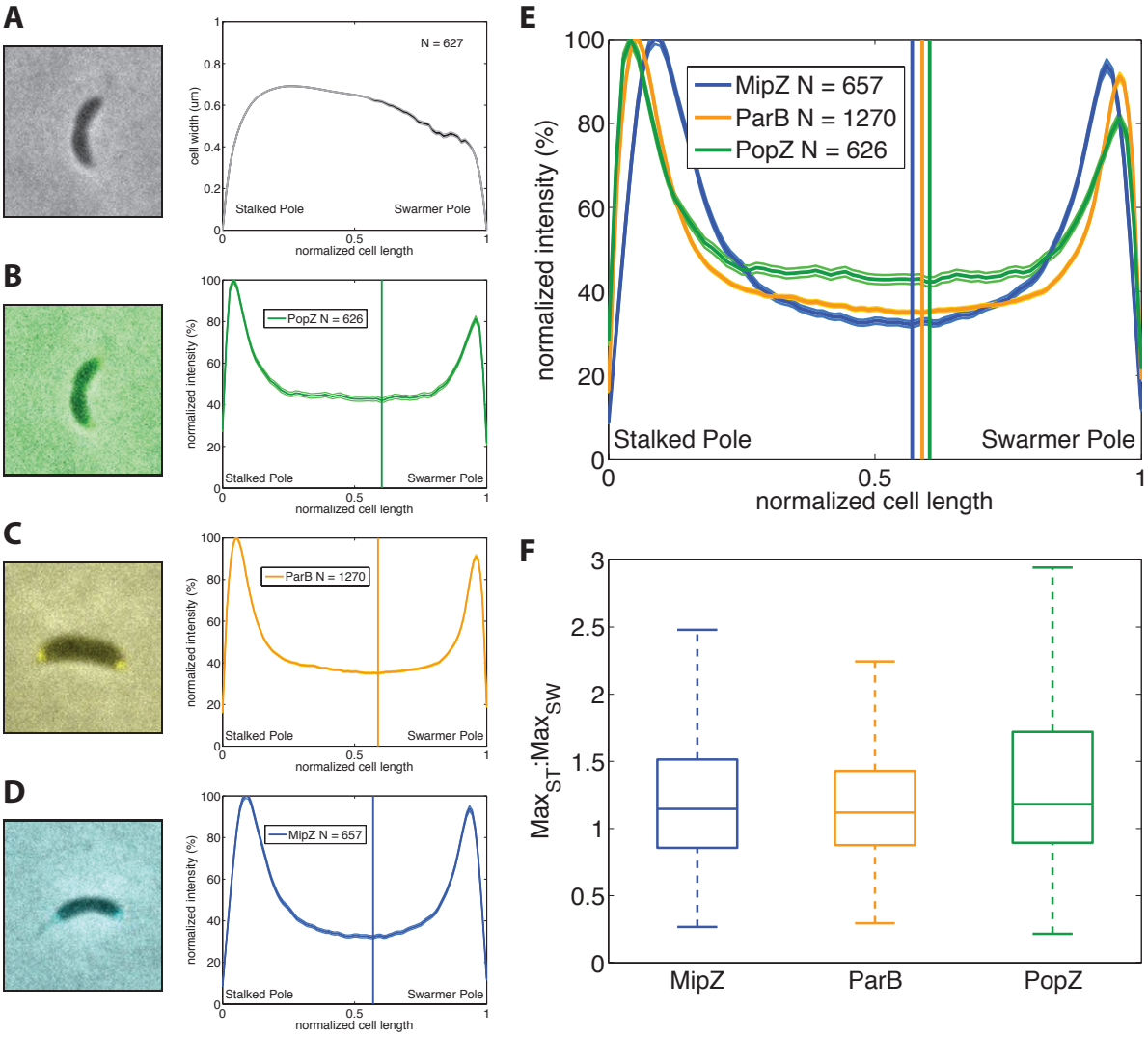
A
B
C
D
E
F
N = 627
cell width (um)
Stalked Pole
Swarmer Pole
normalized cell length
PopZ N = 626
normalized intensity (%)
ParB N = 1270
MipZ N = 657
MipZ N = 657
ParB N = 1270
PopZ N = 626
Max_ST:Max_SW
MipZ
ParB
PopZ

Figure 10

Figure 10: Analysis of epiflourescence microscopy of MipZ-Dendra2, eGFP-ParB, and PopZ-mCherry in otherwise wild-type cells. A) Phase contrast image of wild-type CB15N and the width of the cell along the length of the cell. The stalked pole is represented by 0 and the swarmer pole by 1 on the x-axis. (N = 627) B) Epifluorescence image of PopZ-mCherry and normalized PopZ-mCherry intensity along the length of the cell. (N = 626). Vertical line represents the minimum of the distribution between the two maxima. C) Epifluorescence image of eGFP-ParB and normalized eGFP-ParB intensity along the length of the cell. (N = 1270). Vertical line represents the minimum of the distribution between the two maxima. D) Epifluorescence image of MipZ-Dendra2 and normalized MipZ-Dendra2 intensity along the length of the cell. (N = 657). Vertical line represents the minimum of the distribution between the two maxima. E) Overlay of normalized fluorescence intensities along the length of the cell from B-D). F) Ratio of fluorescence intensity at the stalked pole to the fluorescence intensity at the swarmer pole for MipZ-Dendra2, eGFP-ParB, and PopZ-mCherry.

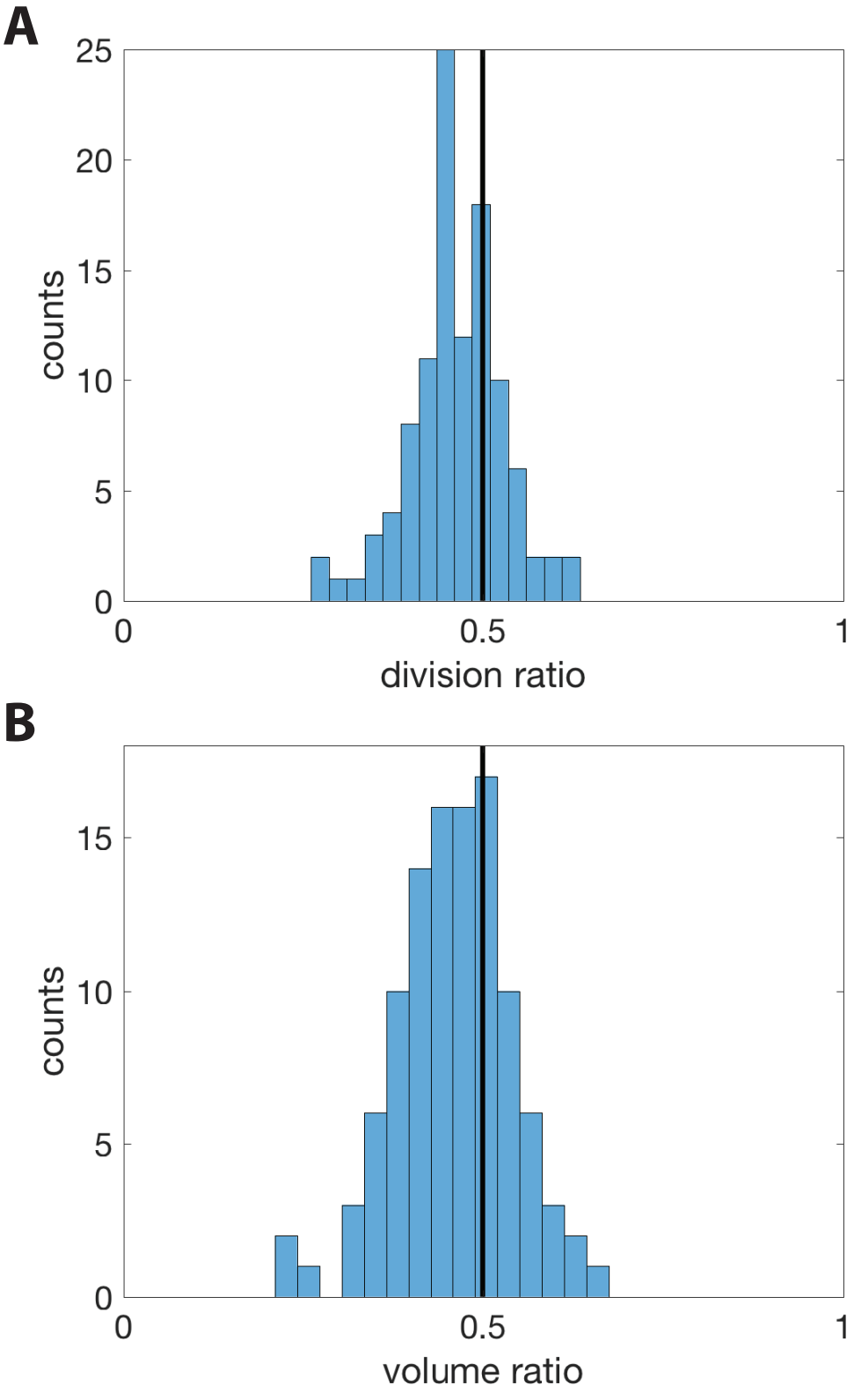
A
25
20
15
10
5
0
counts
0
0.5
1
division ratio
B
15
10
5
0
counts
0
0.5
1
volume ratio

Figure 11

Figure 11: Quantification of cell division and volume ratios for ΔtipN cells. A) Distribution of division ratios for ΔtipN cells (N = 107). Vertical black line represents 0.5 or perfectly even cell lengths. B) Distribution of volume ratios for ΔtipN cells (N = 107). Vertical black line represents 0.5 or perfectly even cell volumes.

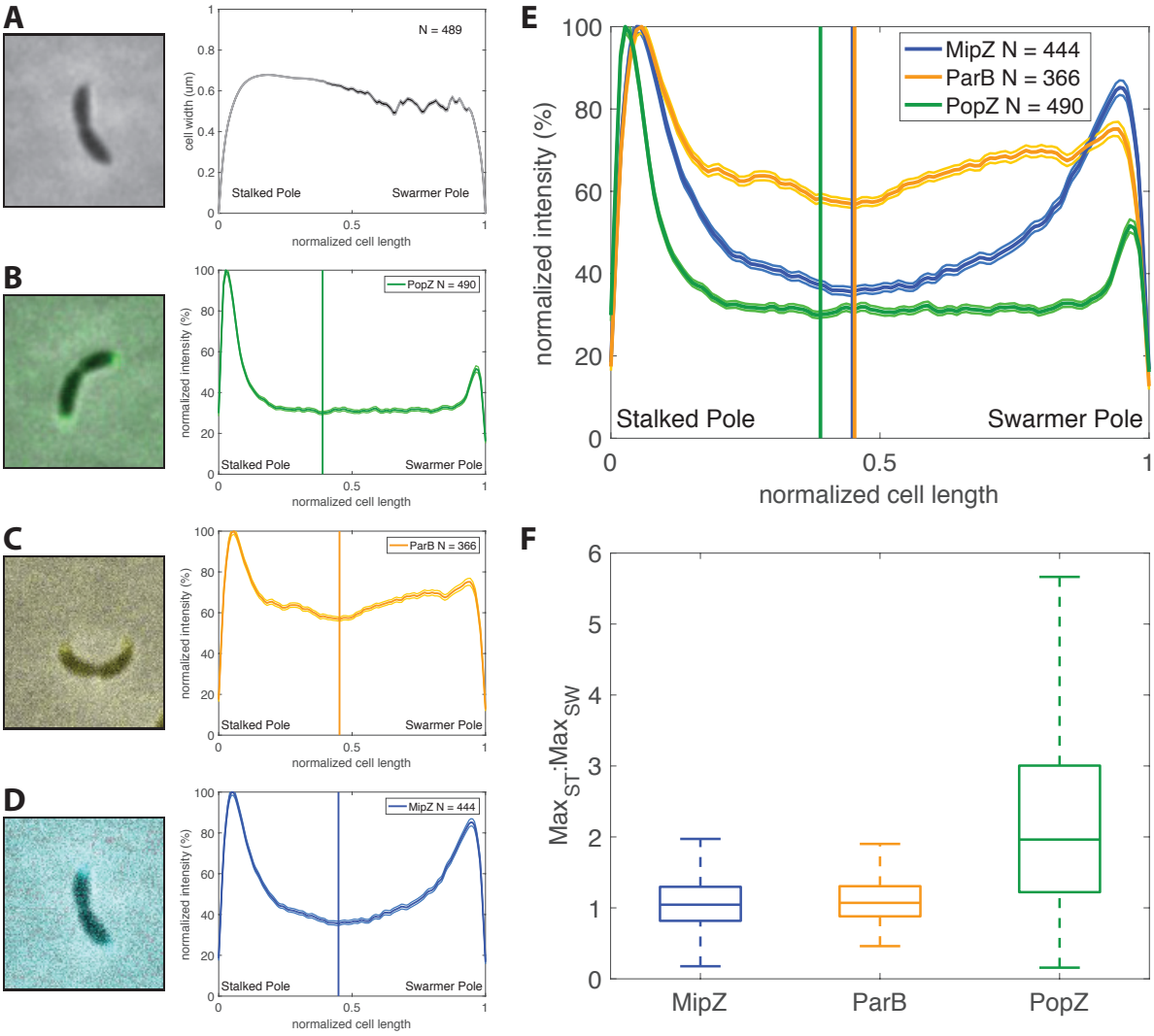
A
N = 489
cell width (um)
Stalked Pole
Swarmer Pole
normalized cell length
B
PopZ N = 490
normalized intensity (%)
Stalked Pole
Swarmer Pole
normalized cell length
C
ParB N = 366
normalized intensity (%)
Stalked Pole
Swarmer Pole
normalized cell length
D
MipZ N = 444
normalized intensity (%)
Stalked Pole
Swarmer Pole
normalized cell length
E
MipZ N = 444
ParB N = 366
PopZ N = 490
normalized intensity (%)
Stalked Pole
Swarmer Pole
normalized cell length
F
Max_ST:Max_SW
MipZ
ParB
PopZ

Figure 12

Figure 12: Analysis of epiflourescence microscopy of MipZ-Dendra2, eCFP-ParB, and PopZ-mCherry in ΔtipN cells. A) Phase contrast image of ΔtipN cells and the width of the cell along the length of the cell. The stalked pole is represented by 0 and the swarmer pole by 1 on the x-axis. (N = 489) B) Epifluorescence image of PopZ-mCherry and normalized PopZ-mCherry intensity along the length of the cell. (N = 490). Vertical line represents the minimum of the distribution between the two maxima. C) Epifluorescence image of eCFP-ParB and normalized eCFP-ParB intensity along the length of the cell. (N = 366). Vertical line represents the minimum of the distribution between the two maxima. D) Epifluorescence image of MipZ-Dendra2 and normalized MipZ-Dendra2 intensity along the length of the cell. (N = 444). Vertical line represents the minimum of the distribution between the two maxima. E) Overlay of normalized fluorescence intensities along the length of the cell from B-D). F) Ratio of fluorescence intensity at the stalked pole to the fluorescence intensity at the swarmer pole for MipZ-Dendra2, eCFP-ParB, and PopZ-mCherry.

Table 1: Parameter values for deterministic modeling

Parameter	Value	Reference
k_1	0.07 μM^{-1} s^{-1}	(38)
k_{1B}	-	This study
k_{-1}	2.1 s^{-1}	(38)
k_2	-	This study
k_3	-	This study
D_{MipZ}	-	This study
$D_{MipZ\text{-}ATP}$	-	This study
$D_{MipZ\text{-}ADP}$	-	This study

REFERENCES

1. Margolin W. Themes and variations in prokaryotic cell division. FEMS Microbiol Rev. 2000;24(4):531-48.

2. Harry EJ. Bacterial cell division: regulating Z-ring formation. Mol Microbiol. 2001;40(4):795-803.

3. Margolin W. Spatial regulation of cytokinesis in bacteria. Curr Opin Microbiol. 2001;4(6):647-52.

4. Rothfield L, Taghbalout A, Shih YL. Spatial control of bacterial division-site placement. Nat Rev Microbiol. 2005;3(12):959-68.

5. Lutkenhaus J. Assembly dynamics of the bacterial MinCDE system and spatial regulation of the Z ring. Annu Rev Biochem. 2007;76:539-62.

6. Kiekebusch D, Thanbichler M. Spatiotemporal organization of microbial cells by protein concentration gradients. Trends Microbiol. 2014;22(2):65-73.

7. Erickson HP, Anderson DE, Osawa M. FtsZ in bacterial cytokinesis: cytoskeleton and force generator all in one. Microbiol Mol Biol Rev. 2010;74(4):504-28.

8. Mingorance J, Rivas G, Velez M, Gomez-Puertas P, Vicente M. Strong FtsZ is with the force: mechanisms to constrict bacteria. Trends Microbiol. 2010;18(8):348-56.

9. Li Z, Trimble MJ, Brun YV, Jensen GJ. The structure of FtsZ filaments in vivo suggests a force-generating role in cell division. EMBO J. 2007;26(22):4694-708.

10. Raskin DM, de Boer PA. Rapid pole-to-pole oscillation of a protein required for directing division to the middle of Escherichia coli. Proc Natl Acad Sci U S A. 1999;96(9):4971-6.

11. Kelly CB, Giuliani M, Dutcher JR. Precise Measurement of Min Protein Oscillations in Bacterial Cells Using TIRF Microscopy. Phys Can. 2011;67(185).

12. de Boer PA, Crossley RE, Rothfield LI. Roles of MinC and MinD in the site-specific septation block mediated by the MinCDE system of Escherichia coli. J Bacteriol. 1992;174(1):63-70.

13. Zhou H, Lutkenhaus J. Membrane binding by MinD involves insertion of hydrophobic residues within the C-terminal amphipathic helix into the bilayer. J Bacteriol. 2003;185(15):4326-35.

14. Lackner LL, Raskin DM, de Boer PA. ATP-dependent interactions between Escherichia coli Min proteins and the phospholipid membrane in vitro. J Bacteriol. 2003;185(3):735-49.

15. de Boer PA, Crossley RE, Rothfield LI. Central role for the Escherichia coli minC gene product in two different cell division-inhibition systems. Proc Natl Acad Sci U S A. 1990;87(3):1129-33.

16. Loose M, Kruse K, Schwille P. Protein self-organization: lessons from the min system. Annu Rev Biophys. 2011;40:315-36.

17. Bonny M, Fischer-Friedrich E, Loose M, Schwille P, Kruse K. Membrane binding of MinE allows for a comprehensive description of Min-protein pattern formation. PLoS Comput Biol. 2013;9(12):e1003347.

18. Zieske K, Schwille P. Reconstitution of self-organizing protein gradients as spatial cues in cell-free systems. Elife. 2014;3.

19. Varma A, Huang KC, Young KD. The Min system as a general cell geometry detection mechanism: branch lengths in Y-shaped Escherichia coli cells affect Min oscillation patterns and division dynamics. J Bacteriol. 2008;190(6):2106-17.

20. Lippincott-Schwartz J, Snapp E, Kenworthy A. Studying protein dynamics in living cells. Nat Rev Mol Cell Biol. 2001;2(6):444-56.

21. Ortiz C, Natale P, Cueto L, Vicente M. The keepers of the ring: regulators of FtsZ assembly. FEMS Microbiology Reviews. 2016;40(1):57-67.

22. Espeli O, Borne R, Dupaigne P, Thiel A, Gigant E, Mercier R, et al. A MatP-divisome interaction coordinates chromosome segregation with cell division in E. coli. EMBO J. 2012;31(14):3198-211.

23. Goley ED, Iniesta AA, Shapiro L. Cell cycle regulation in Caulobacter: location, location, location. J Cell Sci. 2007;120(Pt 20):3501-7.

24. Skerker JM, Laub MT. Cell-cycle progression and the generation of asymmetry in Caulobacter crescentus. Nat Rev Microbiol. 2004;2(4):325-37.

25. Curtis PD, Brun YV. Getting in the loop: regulation of development in Caulobacter crescentus. Microbiol Mol Biol Rev. 2010;74(1):13-41.

26. Akerlund T, Nordstrom K, Bernander R. Analysis of cell size and DNA content in exponentially growing and stationary-phase batch cultures of Escherichia coli. J Bacteriol. 1995;177(23):6791-7.

27. Ptacin JL, Lee SF, Garner EC, Toro E, Eckart M, Comolli LR, et al. A spindle-like apparatus guides bacterial chromosome segregation. Nat Cell Biol. 2010;12(8):791-8.

28. Schofield WB, Lim HC, Jacobs-Wagner C. Cell cycle coordination and regulation of bacterial chromosome segregation dynamics by polarly localized proteins. EMBO J. 2010;29(18):3068-81.

29. Bowman GR, Comolli LR, Zhu J, Eckart M, Koenig M, Downing KH, et al. A polymeric protein anchors the chromosomal origin/ParB complex at a bacterial cell pole. Cell. 2008;134(6):945-55.

30. Poindexter JS. The role of calcium in stalk development and in phosphate acquisition in Caulobacter crescentus. Arch Microbiol. 1984;138(2):140-52.

31. Treuner-Lange A, Sogaard-Andersen L. Regulation of cell polarity in bacteria. J Cell Biol. 2014;206(1):7-17.

32. Laloux G, Jacobs-Wagner C. How do bacteria localize proteins to the cell pole? J Cell Sci. 2014;127(Pt 1):11-9.

33. Williams B, Bhat N, Chien P, Shapiro L. ClpXP and ClpAP proteolytic activity on divisome substrates is differentially regulated following the Caulobacter asymmetric cell division. Mol Microbiol. 2014;93(5):853-66.

34. Campos M, Surovtsev IV, Kato S, Paintdakhi A, Beltran B, Ebmeier SE, et al. A constant size extension drives bacterial cell size homeostasis. Cell. 2014;159(6):1433-46.

35. Young KD. The selective value of bacterial shape. Microbiol Mol Biol Rev. 2006;70(3):660-703.

36. Mannik J, Wu F, Hol FJ, Bisicchia P, Sherratt DJ, Keymer JE, et al. Robustness and accuracy of cell division in Escherichia coli in diverse cell shapes. Proc Natl Acad Sci U S A. 2012;109(18):6957-62.

37. Thanbichler M, Shapiro L. MipZ, a spatial regulator coordinating chromosome segregation with cell division in Caulobacter. Cell. 2006;126(1):147-62.

38. Kiekebusch D, Michie KA, Essen LO, Lowe J, Thanbichler M. Localized dimerization and nucleoid binding drive gradient formation by the bacterial cell division inhibitor MipZ. Mol Cell. 2012;46(3):245-59.

39. Lam H, Schofield WB, Jacobs-Wagner C. A landmark protein essential for establishing and perpetuating the polarity of a bacterial cell. Cell. 2006;124(5):1011-23.

40. Ely B. Genetics of Caulobacter crescentus. Methods Enzymol. 1991;204:372-84.

41. Viollier PH, Thanbichler M, McGrath PT, West L, Meewan M, McAdams HH, et al. Rapid and sequential movement of individual chromosomal loci to specific

subcellular locations during bacterial DNA replication. Proc Natl Acad Sci U S A. 2004;101(25):9257-62.

42. Thanbichler M, Iniesta AA, Shapiro L. A comprehensive set of plasmids for vanillate- and xylose-inducible gene expression in Caulobacter crescentus. Nucleic Acids Res. 2007;35(20):e137.

43. Sliusarenko O, Heinritz J, Emonet T, Jacobs-Wagner C. High-throughput, subpixel precision analysis of bacterial morphogenesis and intracellular spatio-temporal dynamics. Mol Microbiol. 2011;80(3):612-27.

44. Paintdakhi A, Parry B, Campos M, Irnov I, Elf J, Surovtsev I, et al. Oufti: an integrated software package for high-accuracy, high-throughput quantitative microscopy analysis. Mol Microbiol. 2016;99(4):767-77.

45. Wang T, Ingram C, Weisshaar JC. Model lipid bilayer with facile diffusion of lipids and integral membrane proteins. Langmuir. 2010;26(13):11157-64.

46. Bakshi S, Dalrymple RM, Li W, Choi H, Weisshaar JC. Partitioning of RNA polymerase activity in live Escherichia coli from analysis of single-molecule diffusive trajectories. Biophys J. 2013;105(12):2676-86.

47. Liao Y, Schroeder JW, Gao B, Simmons LA, Biteen JS. Single-molecule motions and interactions in live cells reveal target search dynamics in mismatch repair. Proc Natl Acad Sci U S A. 2015;112(50):E6898-906.

48. Yang F, Chen TY, Krzeminski L, Santiago AG, Jung W, Chen P. Single-molecule dynamics of the molecular chaperone trigger factor in living cells. Mol Microbiol. 2016;102(6):992-1003.

49. Yu J. Single-Molecule Studies in Live Cells. Annu Rev Phys Chem. 2016;67:565-85.

50. Touhami A, Jericho M, Rutenberg AD. Temperature dependence of MinD oscillation in Escherichia coli: running hot and fast. J Bacteriol. 2006;188(21):7661-7.

51. Huang KC, Meir Y, Wingreen NS. Dynamic structures in Escherichia coli: spontaneous formation of MinE rings and MinD polar zones. Proc Natl Acad Sci U S A. 2003;100(22):12724-8.

52. Shtylla B. Mathematical modeling of spatiotemporal protein localization patterns in C. crescentus bacteria: A mechanism for asymmetric FtsZ ring positioning. J Theor Biol. 2017;433:8-20.

53. Flomenbom O, Klafter J, Szabo A. What can one learn from two-state single-molecule trajectories? Biophys J. 2005;88(6):3780-3.

54. Manley S, Gillette JM, Lippincott-Schwartz J. Single-particle tracking photoactivated localization microscopy for mapping single-molecule dynamics. Methods Enzymol. 2010;475:109-20.

55. Betzig E, Patterson GH, Sougrat R, Lindwasser OW, Olenych S, Bonifacino JS, et al. Imaging intracellular fluorescent proteins at nanometer resolution. Science. 2006;313(5793):1642-5.

56. Manley S, Gillette JM, Patterson GH, Shroff H, Hess HF, Betzig E, et al. High-density mapping of single-molecule trajectories with photoactivated localization microscopy. Nat Methods. 2008;5(2):155-7.

57. Biteen JS, Moerner WE. Single-molecule and superresolution imaging in live bacteria cells. Cold Spring Harb Perspect Biol. 2010;2(3):a000448.

58. Persson F, Linden M, Unoson C, Elf J. Extracting intracellular diffusive states and transition rates from single-molecule tracking data. Nat Methods. 2013;10(3):265-9.

59. Bowman GR, Comolli LR, Gaietta GM, Fero M, Hong SH, Jones Y, et al. Caulobacter PopZ forms a polar subdomain dictating sequential changes in pole composition and function. Mol Microbiol. 2010;76(1):173-89.

60. Kuhlman TE, Cox EC. Gene location and DNA density determine transcription factor distributions in Escherichia coli. Mol Syst Biol. 2012;8:610.

61. Laloux G, Jacobs-Wagner C. Spatiotemporal control of PopZ localization through cell cycle-coupled multimerization. J Cell Biol. 2013;201(6):827-41.

62. Lenz P, Sogaard-Andersen L. Temporal and spatial oscillations in bacteria. Nat Rev Microbiol. 2011;9(8):565-77.

63. Hoffmann M, Schwarz US. Oscillations of Min-proteins in micropatterned environments: a three-dimensional particle-based stochastic simulation approach. Soft Matter. 2014;10(14):2388-96.

64. Bignell C, Thomas CM. The bacterial ParA-ParB partitioning proteins. J Biotechnol. 2001;91(1):1-34.

CHAPTER 3

Decoding the chemical language of motile bacteria using high throughput microfluidic assays

Adapted from

J.A. Crooks, M.D. Stilwell, P.M. Oliver, Z. Zhong, D.B. Weibel. Decoding the chemical language of motile bacteria by using high-throughput microfluidic assays. *ChemBioChem* 2015, **16**, 2151-2155.

JAC designed and conducted experiments, analyzed data, and wrote the paper. MDS designed and conducted experiments and analyzed data. PMO & ZZ designed experiments. DBW wrote the paper.

ABSTRACT

Motile bacteria navigate chemical environments using chemoreceptors. The output of these protein sensors is linked to motility machinery and enables bacteria to follow chemical gradients. Understanding the chemical specificity of different families of chemoreceptors is essential for predicting and controlling bacterial behavior in ecological niches, including mutualistic and pathogenic interactions with plants and mammals. The identification of chemical(s) recognized by specific families of receptors is limited by the low throughput and complexity of chemotaxis assays. To address this challenge, we developed a microfluidic-based chemotaxis assay that is quantitative, simple, and enables high throughput measurements of bacterial behavior to different chemicals. Using the model bacterium *Escherichia coli*, we demonstrate a strategy for identifying molecules that activate chemoreceptors from a diverse compound library and how global behavioral strategies are tuned to chemical environments.

INTRODUCTION

Motile bacteria have evolved a sophisticated strategy—referred to as chemotaxis—for navigating gradients of small molecules and ions. Chemotaxis enables motile bacteria to find nutrients, evade harmful compounds, and identify locations for growth and community formation. Pathogenic and symbiotic bacteria adapt to host microenvironments using chemotaxis, and recent studies have demonstrated that deficiencies in chemotaxis can impair pathogenesis (1-3). The collective migration of chemotactic bacteria facilitates large-scale ecological processes, including carbon cycling in oceans (4). Chemotaxis affects a wide range of bacterial processes and provides a unique pharmacological target for modifying bacterial behavior and altering pathogenic phenotypes (5).

Bacteria use sensitive chemical sensors referred to as chemoreceptors to monitor extracellular gradients of ions and chemicals. Different families of chemoreceptor proteins define the chemical vocabulary of bacteria. Genome sequencing and bioinformatics suggests that each motile bacterial species contains 10 – 20 different chemoreceptor types that each recognizes a set of structurally related molecules (6). Molecular biology, biochemistry, and biophysics revealed the molecular mechanisms underlying the chemotaxis systems, however the chemoreceptors in most bacterial species are not chemically characterized. The absence of a general census of cognate

chemical/chemoreceptor pairs makes it extremely difficult to predict bacterial behavior in chemical environments.

A fundamental barrier to assigning chemical/receptor pairs is the low throughput of current bacterial chemotaxis assays. The capillary assay is the gold standard for measuring chemotaxis (7), however these assays require considerable finesse to achieve reproducibility, and are generally serial and not designed for multiplexing. Other techniques have emerged more recently (8), including several based on microfluidics that are designed to increase the sensitivity of chemotaxis measurements and enable users to control experimental parameters, such as the shape of chemical gradients (9). A recent paper described chemotaxis assays to screen a library of 80 compounds for antagonists of a known *Escherichia coli* chemoreceptor (5).

We report a simple system for performing an arbitrarily large number of parallel chemotaxis assays. Our approach incorporates a passive architecture to fill microfluidic channels, generate stable chemical gradients rapidly, and quantify assay output quickly and easily. These assays can be performed without specialized external equipment, are scalable, and are accessible to non-expert end users. Using the model chemotactic bacterium *Escherichia coli*, we characterize the sensitivity of the device and perform a small-scale chemical-genetic screen that demonstrates how high throughput can facilitate the identification of chemical/receptor pairs. Furthermore, we demonstrate

that global chemotaxis strategies are tuned to the presence of specific environmental chemicals.

MATERIALS AND METHODS

In-frame deletion of bacterial chemoreceptor genes

All strains described in this paper were derived from the same wild-type *E. coli* MG1655 strain. Splicing by overlap extension (SOE)(10) followed by allelic exchange was used to generate in-frame, marker-less deletions of each chemoreceptor gene (Δ*tar,* Δ*tsr*, Δ*trg,* Δ*tap,* and Δ*aer*), and Δ*cheY*. Briefly, an approximately 500-bp fragment upstream of, and including, the start codon of each of the chemoreceptor genes was amplified using primers P1 and P2 designated for each gene (see Table 1 for a complete list of primers used in this study). An approximately 500-bp fragment downstream of, and including, the stop codon was amplified using primers P3 and P4 for each gene. Primers P2 and P3 contained ~20 bp of complementary sequence to facilitate SOE (10). Each deletion fragment was cloned into a suicide vector, pDS132, containing an R6K conditional replication origin using an In-Fusion HD cloning kit (Clontech Laboratories Inc., Mountain View, CA) (11). The resulting deletion constructs were transformed into the cloning host *E. coli* DH5α λpir and then sub-transformed into the conjugation host *E. coli* MFD λpir. Deletion constructs were conjugated into wild-type *E. coli* MG1655. Tranconjugants were plated on LB plates supplemented with chloramphenicol (Cm) to select for Cm^R plasmid integrants. Integrants were subsequently grown in LB supplemented with 100 μg/ml Cm and serial dilutions of grown cultures were plated on LB plates (without NaCl) with 5% sucrose (Suc) (w/v) to select for Suc^R allelic

replacement candidates. Candidates were verified to be Cm^S by growing them in liquid LB with Cm. All gene deletions in Cm^S clones were confirmed by DNA sequencing using a separate primer set that flanked the deleted region (Table 1). Finally, all *E. coli* strains used in this study were transformed with plasmid p67T1 to constitutively produce the fluorescent protein dTomato (12).

Bacterial cell culture and preparation

Bacterial cells were prepared as follows before being loaded into a microfluidic assay. Cultures were grown to saturation overnight in LB (1% w/v tryptone, 0.5% w/v yeast extract, 1% w/v NaCl). These cultures were diluted 100-fold in 10 mL of fresh tryptone broth (TB) (1% w/v tryptone, 0.5% w/v NaCl) in a 125 mL Erlenmeyer flask. Diluted subcultures were grown for ~3.5 h in a 30°C shaking incubator (200 RPM) to mid-exponential phase (optical density of 0.45 – 0.55, λ = 600 nm). Cells from 1 mL of mid-exponential cultures were collected by centrifugation (3000 x g for 5 min). The resulting pellet was washed with 1 mL of motility buffer (10 mM KH_2PO_4, 67 mM NaCl, 0.1 mM EDTA, 0.01% (w/v) Brij-35, pH 7.0) and cells were collected by centrifugation. This wash step was repeated two more times to ensure that the concentration of chemical contaminants from the subculture medium was negligible in our assay. Finally, cells were resuspended in motility buffer to an absorbance of 0.04 (λ = 600 nm) before they were used in microfluidic assays.

The cells used to create the data in Figure 7 (global chemotaxis experiment) were grown as above, with several amendments. 100 μL of a saturated overnight culture was collected by centrifugation, as above, and resuspended in 1 mL of M9 minimal media (prepared according to ref. 4). This wash step was repeated two more times, and the final pellet was resuspended in 100 μL of M9 before being diluted 100-fold in 10 mL of M9 containing a designated nutrient supplement. For the experiments described in Figure 7, we prepared four supplemented M9 medias: 15 mM galactose + 15 mM glycerol, 15 mM serine + 15 mM glycerol, 15 mM aspartate + 15 mM glycerol, and 15 mM glycerol only (the addition of glycerol to each condition was necessary to support growth). Stock solutions of all added supplements were filter sterilized, and were diluted to their final concentration in autoclaved M9. Diluted subcultures were grown as above, in 10 mL of supplemented M9 for ~12 h to an absorbance of 0.35 – 0.45, λ = 600 nm. Cells were washed in motility buffer as described above before they were loaded in microfluidic assays.

Assay device fabrication and operation

All devices were fabricated using soft lithography (13). Briefly, masters were patterned in two layers using photolithography with SU-8 3050 and SU-8 2100 photoresist (Microchem, Newton, MA, USA) on silicon wafers. A layer of SU-8 3050 was first spun onto a clean wafer at 3000 RPM for 40 s using a benchtop spin coater (Laurell

Technologies Corp., New Wales, PA, USA). All bake steps, and UV exposure, were performed according to the photoresist manufacturer's recommendations. A negative photomask (CAD/Art Services Inc., Bandon, OR, USA) containing the pattern for the entire microfluidic network was aligned and patterned into the photoresist using a custom aligner and UV light source. Following the post-exposure bake, the wafer was cooled to room temperature, and a second layer of SU-8 2100 was spun on the wafer at 3000 RPM for 40 s. A second negative photomask containing a pattern that only included the pool chambers of the device was then aligned with the wafer and UV exposed. Excess resist was removed using SU-8 Developer (Microchem, Newton, MA, USA). All microfluidic channels had a height of 50 μm. The diameter of source chambers was 2 mm, while the pool chambers had a height of 300 μm and a diameter of 3 mm. The height of each layer was confirmed using a Tencor AlphaStep 200 surface profilometer (KLA-Tencor, Milpitas, CA, USA). (Tridecafluoro-1,1,2,2-tetrahydrooctyl)trichlorosilane (Gelest Inc., Morristown, NJ, USA) was deposited on the photoresist masters under vacuum for > 4 h to facilitate the removal of the embossed poly(dimethylsiloxane) (PDMS) layers from the masters. We cast PDMS (10 : 1 ratio of base to crosslinking agent; Sylgard 184, Dow Corning, Midland, MI, USA) on the masters to a depth of ~ 4 mm, then cured the polymer at 120°C for > 4 h. The cured PDMS layer containing the microfluidic design was separated from the master and trimmed with a razor to a suitable size for bonding to a glass slide. A 0.5 mm diameter

tissue bore was used to punch an inlet in each device. 1 μL droplets of the chemicals of interest (chemoattractants) were spotted on the source chambers of clean layers of PDMS embossed with channels and source chambers. All fluorescein and chemoattractant stock solutions were prepared in sterile deionized water (18.2 MΩ), and all chemoattractants were purchased at analytical grade. Cysteine, histidine, isoleucine, glucose, glutamic acid, glycine, lysine, phenylalanine, serine, tyrosine, valine, 2-aminoisobutyric acid (AiBu), succinic acid, and Pro-Leu were from Sigma-Aldrich (St. Louis, MO, USA). Ribose and galactose were from Acros Organics (Geel, Belgium), and all other chemicals were from Alfa Aesar (Ward Hill, MA, USA). We dried the 1 μL droplets completely at room temperature. For tracking gradient formation, fluorescein was treated the same as all other attractants: fluorescein stock solutions were deposited and dried on the PDMS prior to the measurements. The PDMS layer containing the dried reagents was then pressed into conformal contact with a clean glass slide to create the final microfluidic device. Prior to assembly, the glass was exposed to oxygen plasma for 1 min (Harrick Plasma, Ithaca, NY) to improve adhesion between glass and PDMS. Fully assembled devices were placed in a vacuum chamber for >90 min at ~ 25 Pa. Immediately after removal from vacuum, we covered the inlet with a 120 μL drop of the bacterial suspension in motility buffer described above. The entire microfluidic network filled in ~15-20 min via degas-driven flow (14, 15). While the devices filled, a 100 μL drop of mineral oil (Sigma-Aldrich) was layered on top of

the excess motility buffer that remains exposed at the inlet to limit evaporation. The assays were incubated at room temperature for 3 h before data was acquired.

Data acquisition and analysis

All epifluorescence images were acquired using an Eclipse Ti inverted microscope (Nikon, Tokyo, Japan) equipped with a CoolSNAP HQ^2 camera (Photometrics, Munich, Germany). To image source chambers, we used a Nikon Plan Apo 4X objective. In a single field of view, >90% of a source chamber's area could be visualized. Thus single images were used for data analysis. However, the full source chambers displayed in Figure 3a were stitched together from four images. For microparticle tracking experiments, we used 3-μm diameter latex microparticles (Polybead® Carboxylate Blue Dyed Microspheres, Polysciences, Warrington, PA, USA) that were diluted 100-fold in a 0.1% Tween-20 aqueous solution. A Nikon S Plan Fluor ELWD 40X objective was used to image the movement of microparticles.

Quantitative analysis of fluorescently labeled bacterial cells was performed using a custom script in R (16). Briefly, background fluorescence signal was subtracted using a low-pass filter generated by applying a Gaussian blur (from the EBImage package)(17) with a large kernel size ($\sigma = 50$). The fluorescence intensity within a circular mask (corresponding to the source chamber) was then integrated and gave a highly reproducible measure of bacterial accumulation.

The half-maximal effective concentration (EC_{50}) and peak response measurements reported in Table 2 were determined using a custom script in R (16). Briefly, functions were fit to each concentration-response curve via cubic spline interpolation. The derivatives of these functions were determined, and the maximum values were taken as the EC_{50}. The maximum values of the spline interpolation functions were reported as peak responses.

Quantitative analyses of fluorescein gradients and fluorescent microparticles were performed using custom scripts in IGOR Pro 6 (Wavemetrics, Portland, OR, USA).

Swim agar assays

The migration of swimming bacterial colonies was quantified in low percentage agar as previously described (18), with minor modifications. Migrating colonies were inoculated in 0.25% (w/v) agar gel infused with a supplemented M9 media (prepared as described above). The diameter of migrating circular colonies was measured after incubation in a static 30°C incubator at ~90% relative humidity for 80 h. All reported values represent the mean of three independent swim colonies.

To photograph the swim colonies, plates were illuminated using two fluorescent light sources positioned to illuminate through the edge of the plates. Scattered light from the swim colonies was captured from above the plates using a conventional digital camera.

RESULTS

Our parallel chemotaxis assay is illustrated in Figure 1. For simplicity, we used a single microfluidic design for all of the chemotaxis experiments outlined here. This radial design enables 45 separate compounds to be assayed in a single experiment. In our design, 45 identical microchannels (50-μm tall and 100-μm wide) emanate from a central inlet (Figure 1a), all of which are embossed into a layer of poly(dimethylsiloxane) (PDMS). Each channel terminates with two circular chambers. We refer to the larger chamber (300-μm tall and 3-mm diameter) as the *pool*, and the smaller, terminal chamber (50-μm tall and 2-mm diameter) as the *source* (Figure 1e). As detailed below, our assay generates a stable chemical gradient that extends from the source to the pool. Chemotactic responses to the chemical gradients are quantified by measuring the accumulation of bacteria in the source chamber.

To assemble the assay, we added 1 μL droplets of compound solutions to each source chamber (Figure 1a). After drying, we inverted the PDMS layer and brought it into conformal contact with a glass or plastic slide to seal the microfluidic channels (Figure 1b).

The microfluidic channels were filled with a dilute bacterial suspension using a passive pumping method referred to as degas-driven flow (14, 15, 19). Briefly, degas-driven flow leverages the gas-permeability of the polymer used to construct the microfluidic network (here, PDMS), and is particularly useful for filling dead-end

channels, such as those in our design. We placed the fully assembled assays in a vacuum for ≥90 min to reduce the amount of gas dissolved in the PDMS. After removing the assay from the vacuum, we placed a 120-μL drop of a dilute bacterial suspension over the central inlet (Figure 1c). As the PDMS returned to atmospheric pressure, the PDMS walls of the microfluidic channels absorbed the trapped air in the microfluidic network and drew the bacterial suspension into the microchannels (Figure 1c and d). Degas-driven flow filled the entire channel network uniformly in ~20 min. To limit evaporation of the bacterial solution at the inlet, we placed a drop of mineral oil on top of the water (Figure 1c). Once filled, the chemicals in the source chambers dissolved and diffused toward the pool.

To generate stable chemical gradients, we took advantage of permeation-driven flow. PDMS is slightly water permeable and the absorption of water into the walls of microchannels generates predictable fluid flows (20). This subtle permeation-driven flow opposes the diffusion of chemicals from the source chambers, and equilibration of these two opposing flows produces a stable chemical gradient (Figure 1e). The formation of a stable gradient can be understood by considering how the contributions of permeation-driven flow versus diffusion change with the distance from the source chamber. At small distances from the source, the flux of chemicals due to diffusion is large while permeation-driven flow approaches zero, thus chemicals are driven out of the source by diffusion at short distances. However, permeation-driven flow increases

with the distance from the source while the flux due to diffusion decays. Thus, at larger distances permeation-driven flow dominates and prevents the chemical gradient from diffusing ad infinitum. The equilibration of these two effects generates stable gradients with characteristic lengths on the order of a millimeter for small molecules (20). To confirm this mechanism of gradient formation we monitored the formation of fluorescein gradients and their stability over time (Figure 2). Gradients were stable after ~120 min and remained stable for >12 h (Figure 2). By tracking the velocity of fluorescent particles (3-μm diameter) in our design, we confirmed that permeation-driven flow travels from the inlet toward the dead-end at a velocity that is >100 times slower than the swimming velocity of motile bacteria. A simple 1D diffusion-advection model was in close agreement with our empirical observations of chemical gradient formation (Figure 2), demonstrating that permeation-driven flow and molecular diffusion are the dominant forces contributing to stable gradient formation.

Theoretical model for stable chemical gradient formation

Microfluidic devices are often fabricated in the inexpensive soft elastomer PDMS as it offers several unique characteristics that make it suitable for microfluidic-based experiments of cell behavior, including optical transparency that enables cell tracking and gas permeability that facilitates gas exchange (21, 22). The permeability of PDMS to water vapor creates a permeation-driven flow mechanism in which water is transported

out of microfluidic channels and through the elastomer as vapor (20). This flow is largely ignored in microfluidic devices, except in cases where the channels are small, on the order of single micrometers. We observed a very slow flow of fluid along microfluidic channels from the inlet to the source chamber containing the chemoeffector. To confirm that the device had a finite and measurable permeation-driven flow, we tracked and measured the mean velocity of fluorescent polymer beads (d = 3 μm) in the microchannels to be 290 nm s^{-1}. We take advantage of this permeation-driven flow to establish a stable gradient, and while we acknowledge our microfluidic assay is not flow-free in the strictest sense, the flow derived from permeation is negligible when monitoring chemotaxis, since the flow is ~ 100 times slower than the velocity of most bacteria ($v_{E.\ coli}$ ~ 30 μm s^{-1})(9) and is more than 10^3 times slower than most flow-based chemotaxis assays (23, 24).

The low Reynolds number associated with microchannels eliminates turbulence and molecules mix only by diffusion. We use molecular diffusion to establish a gradient in an observation channel connected to a source chamber. Fick's second law of diffusion states that in the absence of advection (or flow) a gradient evolves according to

$$\frac{\partial c}{\partial t} = D\nabla^2 c \qquad (1)$$

where c is the concentration of the compound, D is the diffusion coefficient of the compound in solvent, and t is time. Including an advective flux term to account for permeation-driven flow changes Eq. 1 to

$$\frac{\partial c}{\partial t} = -u\nabla c + D\nabla^2 c \tag{2}$$

in which u represents the flow velocity vector. In one-dimension, and including the assumption of a constant source of compound, the solution to Eq. 2 is

$$c(x, t > 0) = \frac{c_0}{2}\left(erfc\left(\frac{x - ut}{2\sqrt{Dt}}\right) + e^{(xu/D)}erfc\left(\frac{x + ut}{2\sqrt{Dt}}\right)\right) \tag{3}$$

where x represents the position along the channel (11, 25, 26). We approximate that the concentration of chemoeffector in the source chamber is constant compared to the concentration in the channel. We approximate the three-dimensional channel as one-dimensional for modeling purposes, which is a valid assumption as the difference in chemoeffector concentration across the width and height of the channel is negligible. We found that Eq. 3 matches our experimentally observed gradients (Figure 2).

Experimental characterization of stable gradient formation

We characterized chemical gradient profiles generated by our assay by imaging fluorescein gradient formation using an epifluorescence microscope (Figure 2a). To simplify our boundary conditions for the theoretical model described below, these

experiments were performed in straight-channel designs that lacked pool chambers. Fluorescein is a useful marker for characterizing gradients in these experiments, as it does not influence bacterial chemotaxis and has a diffusion coefficient ($D_{fluorescein}$ = 4.3 x 10^{-10} m^2 s^{-1}) that is similar to many chemoeffectors (27, 28). For these experiments, we used a 100 μM concentration of fluorescein in the source chamber and filled devices with motility buffer. Under these conditions, the spatial gradient profile at x = 1 mm was stable after ~2 h (Figure 2c) and remained stable for >12 h (data not shown). Our observations of the fluorescein gradient agreed with the predictions of the physical model for at least the first 7 h, as seen in Figure 2c.

Our chemotaxis experiments focused on the model bacterium *E. coli*, as its chemotaxis system has been well characterized and the chemical specificity of each chemoreceptor is known. *E. coli* contains four canonical chemoreceptors—Tar (aspartate sensing), Tsr (serine), Trg (ribose, galactose), and Tap (dipeptides)—and an additional chemoreceptor (Aer) that acts together with Tsr to perform 'energy taxis', which is a general response for sensing oxygen, redox levels, and other small molecule metabolites (29). These chemoreceptors are sensitive (capable of detecting nM concentrations) and operate over a concentration range that can extend over 5 orders of magnitude (30). Our assay accurately measures chemotaxis over this entire dynamic range (Figure 3).

When the device was initially filled, bacteria were uniformly distributed at a low concentration (λ=600 nm, absorbance=0.04) throughout the microfluidic channels. As

the chemical gradients formed, bacteria responded to attractants by swimming up gradients and accumulated in the source chambers. We counted the number of bacteria that accumulated in the source chambers using microscopy to quantitatively measure bacterial chemotaxis. To acquire these measurements, we used *E. coli* strains that constitutively expressed the fluorescent protein, dTomato. 3 h after the channels were filled we imaged the fluorescent signal from the source chambers using an epifluorescence microscope. Using fluorescently labeled bacteria increased our signal-to-noise ratio, however unlabeled bacteria can also be measured using a brightfield microscope with phase optics, or by the opacity of the source chamber. Figure 3a shows the fluorescence intensity from a source chamber containing an attractant (100 μM aspartate) compared to an empty control chamber. To quantify the chemotactic response, we divide the integrated intensity of an attractant source (I_x) by the integrated intensity of an empty source (I_0) to provide relative response values (I_x/I_0) that are consistent between assays.

Calibration curve of cell concentration versus fluorescence signal

Wild-type *E. coli* constitutively expressing the fluorescent protein dTomato were cultured and prepared as described above. The devices used to acquire the calibration curve were facsimiles of the main design used throughout the paper, except they contained only two chemotaxis assays connected to a central inlet, rather than 45 (all

other relevant design parameters were identical). Cell suspensions were adjusted to concentrations of 0, 0.04, 0.1, 0.5, and 1 (absorbance, λ = 600 nm) prior to being loaded into the assays. The chemotaxis assays were then run as described above, except no chemoattractant was added to any of the source chambers. After 3 h of incubation at room temperature the fluorescent signal from the source chambers was acquired.

We found that there is a linear relationship between cell concentration and the fluorescence signal in our assay (Figure 4). The range of cell concentrations tested extends above (by more than two-fold) the highest cell concentrations measured in all of our reported experiments.

Utilizing the device for relative response and global chemotaxis measurements

Using relative response measurements, we acquired concentration-response curves for 27 different chemicals. Figure 3b shows concentration-response curves of wild-type *E. coli* to several canonical attractants recognized by different chemoreceptors (curves for all additional chemicals that gave measureable responses are shown in Figure 5). For each chemical tested, our measurements of half maximal effective concentration (EC_{50}) and peak response were consistent with previously reported values acquired using capillary assays (Table 2) (31). In contrast to the capillary assay, we acquired quantitative data on dozens of chemoattractants rapidly and in parallel and

found the assay to be remarkably reproducible (see standard error of the mean in Figures 3, 6, 7).

To demonstrate how high throughput chemotaxis assays enable the assignment of the chemical specificity of uncharacterized chemoreceptors, we performed a small-scale screen to 'identify' the chemical specificities of the chemoreceptors in *E. coli*. We established a panel of 8 chemicals that included attractants recognized by each chemoreceptor in *E. coli*, integrated it into one device, and simultaneously assayed each chemical at its peak response concentration (Figure 6a). We constructed single gene deletions for all five chemoreceptors in *E. coli* (Δ*tar*, Δ*tsr*, Δ*trg*, Δ*tap*, and Δ*aer*) from the parental strain MG1655. Figure 6b shows the response of each deletion strain to the small molecule panel; the specificity of each chemoreceptor is represented by the lack of a response to the chemicals that are specifically recognized by the deleted chemoreceptor. Although the specificities of the chemoreceptors in *E. coli* are established, our experiments provide a proof-of-principle for how high-throughput assays can be used to increase the pace at which new chemical/receptor pairs are discovered for the majority of motile bacteria, which have uncharacterized chemotaxis systems.

In addition to assigning chemical/receptor pairs, high throughput chemotaxis studies can reveal how bacteria optimize their global chemotaxis strategies based on changing environmental inputs. Several reports have shown that culturing conditions

can have profound effects on chemotactic responses (32, 33). We found that changing chemical environments alters the *E. coli* response to the carbon source provided during growth and toward other compounds (Figure 7). Interestingly, when grown in the presence of galactose, *E. coli* had an increased response to every canonical chemoeffector added. Conversely, when grown in the presence of serine, all of the responses were repressed. This reduced chemotactic response extended to bacterial colonies grown on low percentage agar that was supplemented with serine (Figure 8). Based on these results, we believe our assay can be a valuable tool for understanding how complex environmental signals are integrated into a global chemotactic response. Importantly, these experiments highlight capabilities of this high-throughput chemotaxis assay that would be challenging to achieve using standard chemotaxis assays.

DISCUSSION

We describe a simple, quantitative microfluidic assay for performing high throughput measurements of bacterial chemotaxis and characterizing cognate chemical/receptor pairs. In our experiments we describe a radial device that performs 45 parallel chemotaxis assays, but the system can be redesigned to perform an arbitrary number of assays with different layouts. As a proof of principle, we demonstrated a chemical-genetics screening strategy to identify chemical/receptor pairs in *E. coli*. Our future efforts are aimed at expanding this chemical screening approach to investigate uncharacterized chemoreceptors in diverse bacterial species. This assay can be used to investigate how bacteria regulate their global chemotaxis strategy in response to changing chemical conditions. Most chemotaxis measurements are performed using cells grown under standardized conditions. Our results demonstrate that *E. coli* adjusts its global chemotactic responses in response to the nutrient source used for its growth. This result is interesting in light of bacterial mechanisms of adaptation and survival in fluctuating chemical environments. Monitoring global chemotactic responses was enabled by the high throughput of our chemotaxis assay, and is an exciting area for future investigations.

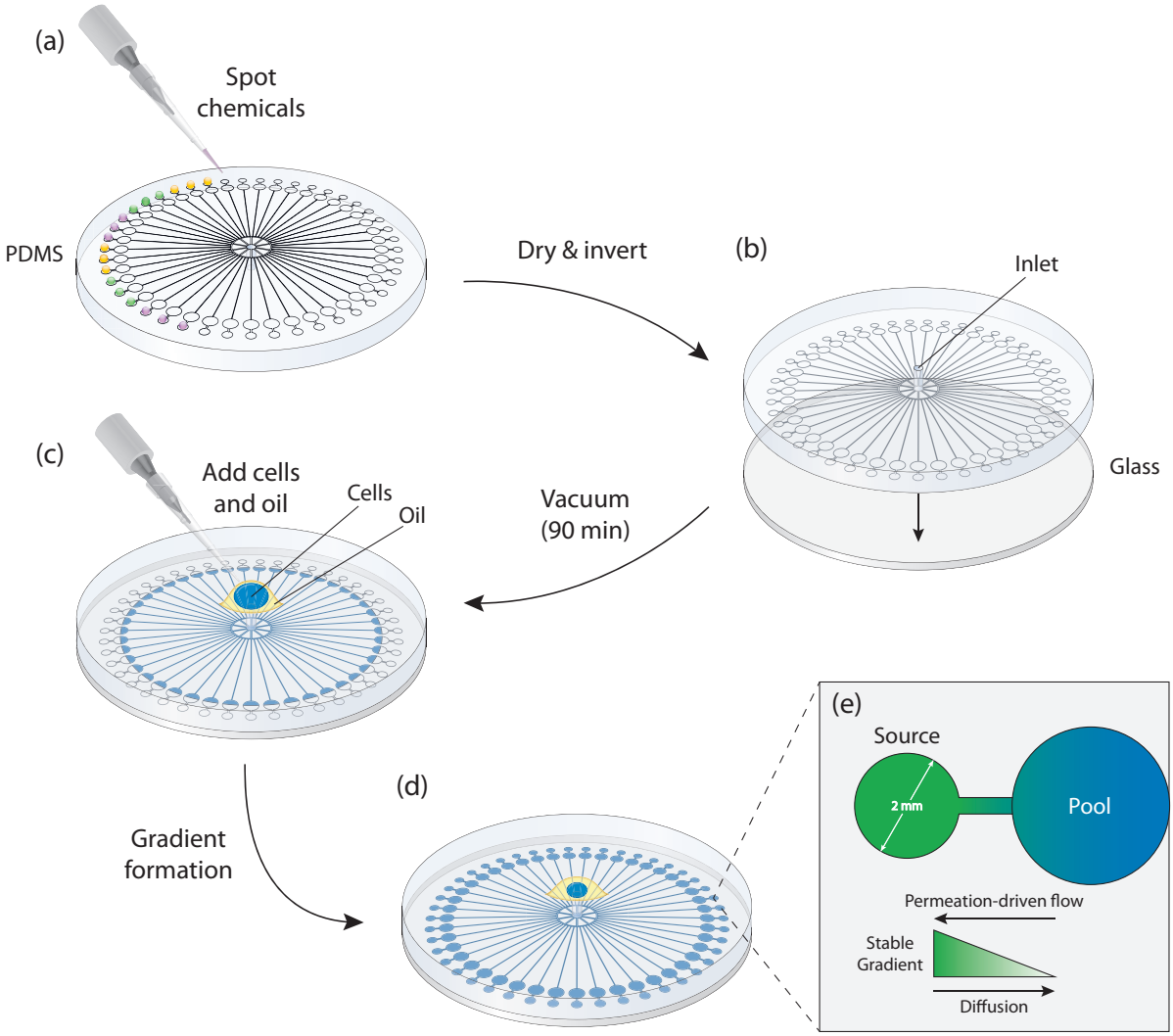
(a)
Spot
chemicals
PDMS
Dry & invert
(b)
Inlet
Glass
(c)
Add cells
and oil
Cells
Oil
Vacuum
(90 min)
Gradient
formation
(d)
(e)
Source
2 mm
Pool
Permeation-driven flow
Stable
Gradient
Diffusion

Figure 1

Figure 1. To assemble the assay, each chemical of interest is spotted in a source chamber located at the periphery of the design (a). Once the spots have dried, the PDMS layer is inverted and brought into conformal contact with bare glass to seal the microfluidic channels (b). After the PDMS is degassed under vacuum, a dilute bacterial solution is placed over the inlet and passively fills the assay via degas-driven flow. Mineral oil is layered over the inlet to minimize evaporation (c). The channels fill completely in ~20 min (d). Once filled, a stable chemical gradient forms between the source and the pool over 90 min due to a balance of diffusion and permeation-driven flow (e).

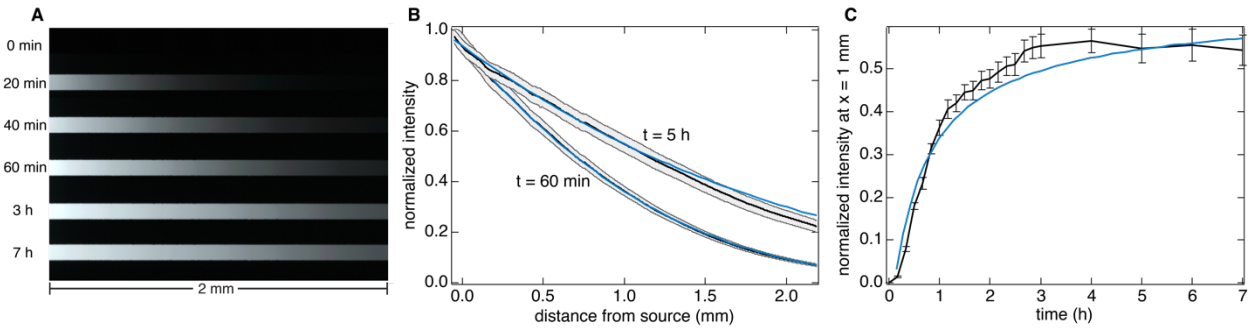
A
0 min
20 min
40 min
60 min
3 h
7 h
2 mm
B
normalized intensity
distance from source (mm)
t = 5 h
t = 60 min
C
normalized intensity at x = 1 mm
time (h)

Figure 2

Figure 2. Observations of stable gradient formation agree with the theoretical model. (A) Epifluorescence images of fluorescein in the first 2 mm along the channel at 0 min, 20 min, 40 min, 60 min, 3 h, and 7 h demonstrate that the gradient reaches a steady-state in less than 3 h. In these images, the source chamber is just out of frame and positioned to the left. (B) The normalized intensity of fluorescein emission along the channel is plotted as solid black lines, and the standard deviation is shown in gray (n = 15). The corresponding gradient profiles predicted by the theoretical model (Eq. 3) are shown in blue. (C) Intensity versus time at x = 1 mm from the source shows that the fluorescence intensity increases rapidly until the system achieves equilibrium between 2 and 3 h.

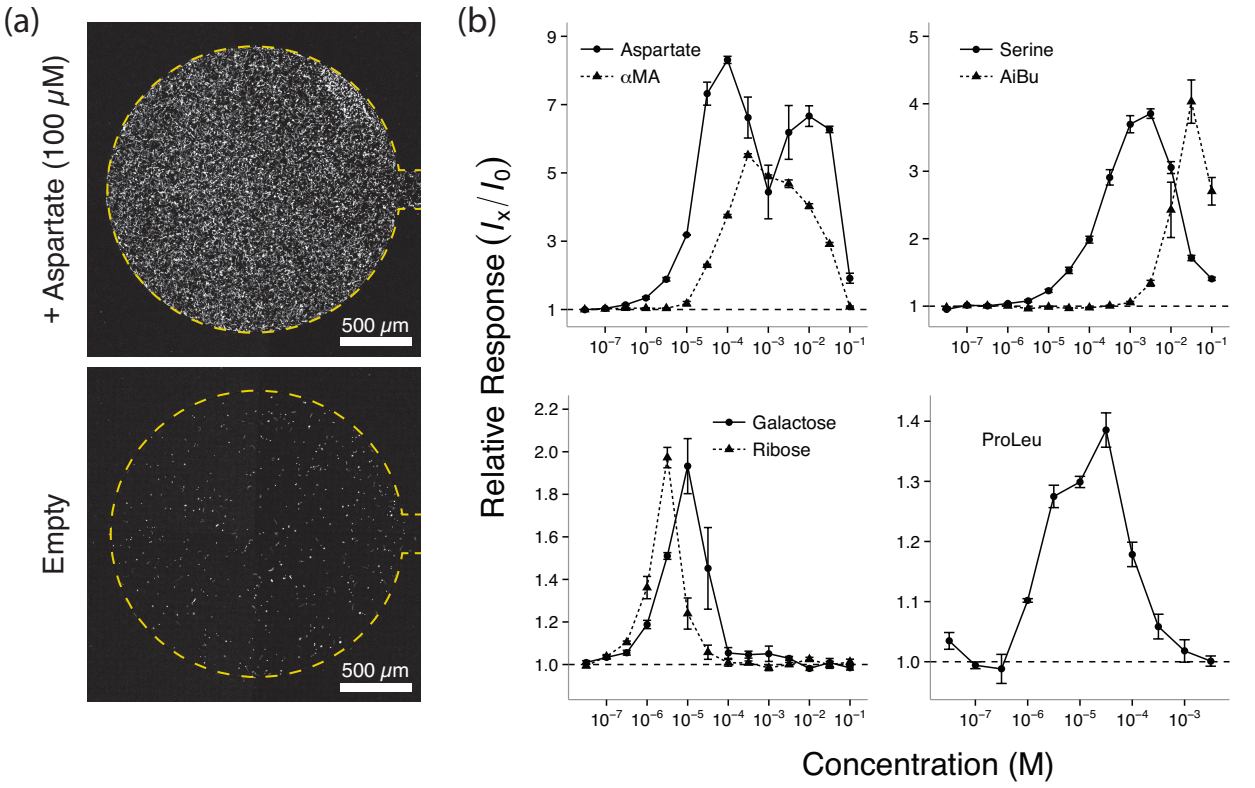
(a)
+ Aspartate (100 μM)
500 μm
Empty
500 μm
(b)
Relative Response (I_x/I_0)
Aspartate
αMA
Serine
AiBu
Galactose
Ribose
ProLeu
Concentration (M)

Figure 3

Figure 3. (a) Fluoresence micrographs of *E. coli* MG1655 cells constitutively expressing the fluorescent protein dTomato in a source containing an attractant (100 μM aspartate) compared to an empty source. The yellow dashed lines mark the edges of the source chambers. (b) Chemotactic response curves toward several canonical chemoattractants are plotted as a function of chemoattractant concentration. Here, relative response represents the sum intensity of a source containing a chemical of interest (I_x), over the sum intensity of an empty source (I_0). α-Methyl-DL-aspartate (αMA) and 2-Aminoisobutyrate (AiBu) are non-metabolizable analogs of Asp and Ser that are specifically recognized by Tar and Tsr, respectively. Each value represents the mean of 3 measurements (n = 3) acquired on separate devices, and error bars indicate the standard error of the mean (SEM).

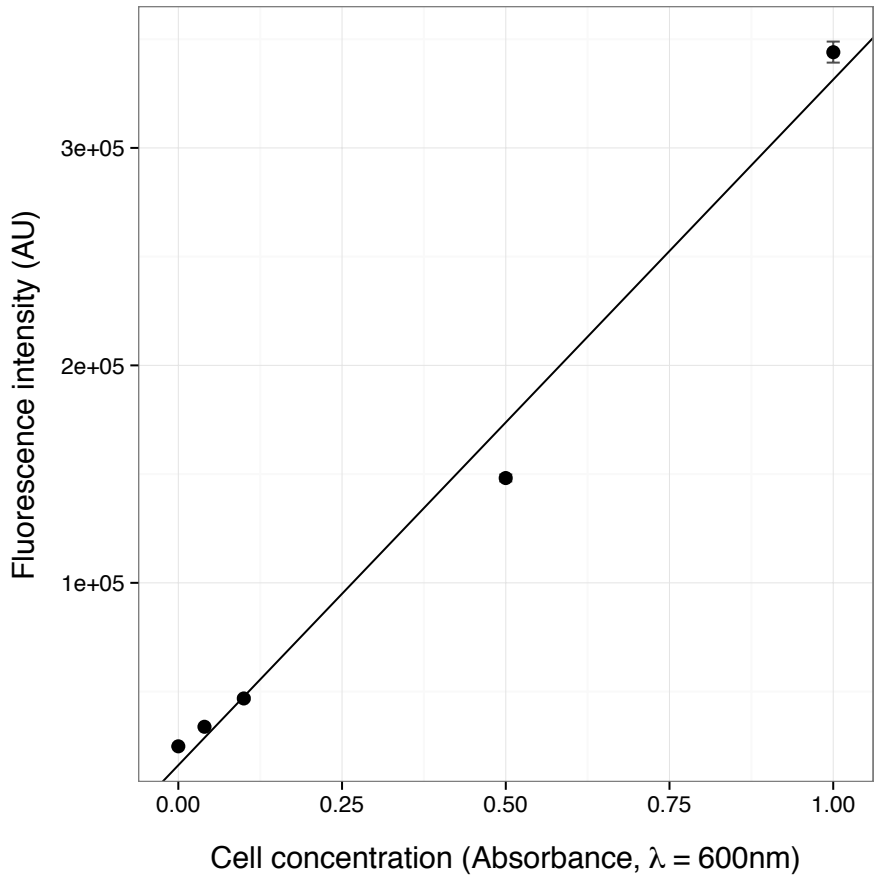
Fluorescence intensity (AU)
3e+05
2e+05
1e+05
0.00
0.25
0.50
0.75
1.00
Cell concentration (Absorbance, λ = 600nm)

Figure 4

Figure 4. The cell concentration versus the fluorescence signal from the chemotaxis assay shows a linear relationship. Wild-type *E. coli* constitutively expressing the fluorescent protein dTomato were added to chemotaxis assays at concentrations of 0, 0.04, 0.1, 0.5, and 1 (absorbance, λ=600 nm). Each point represents the mean of 4 measurements acquired on two separate devices. Further experimental details are provided above. Error bars represent the SEM. The solid black line was determined using simple linear regression (adjusted $R^2 = 0.986$).

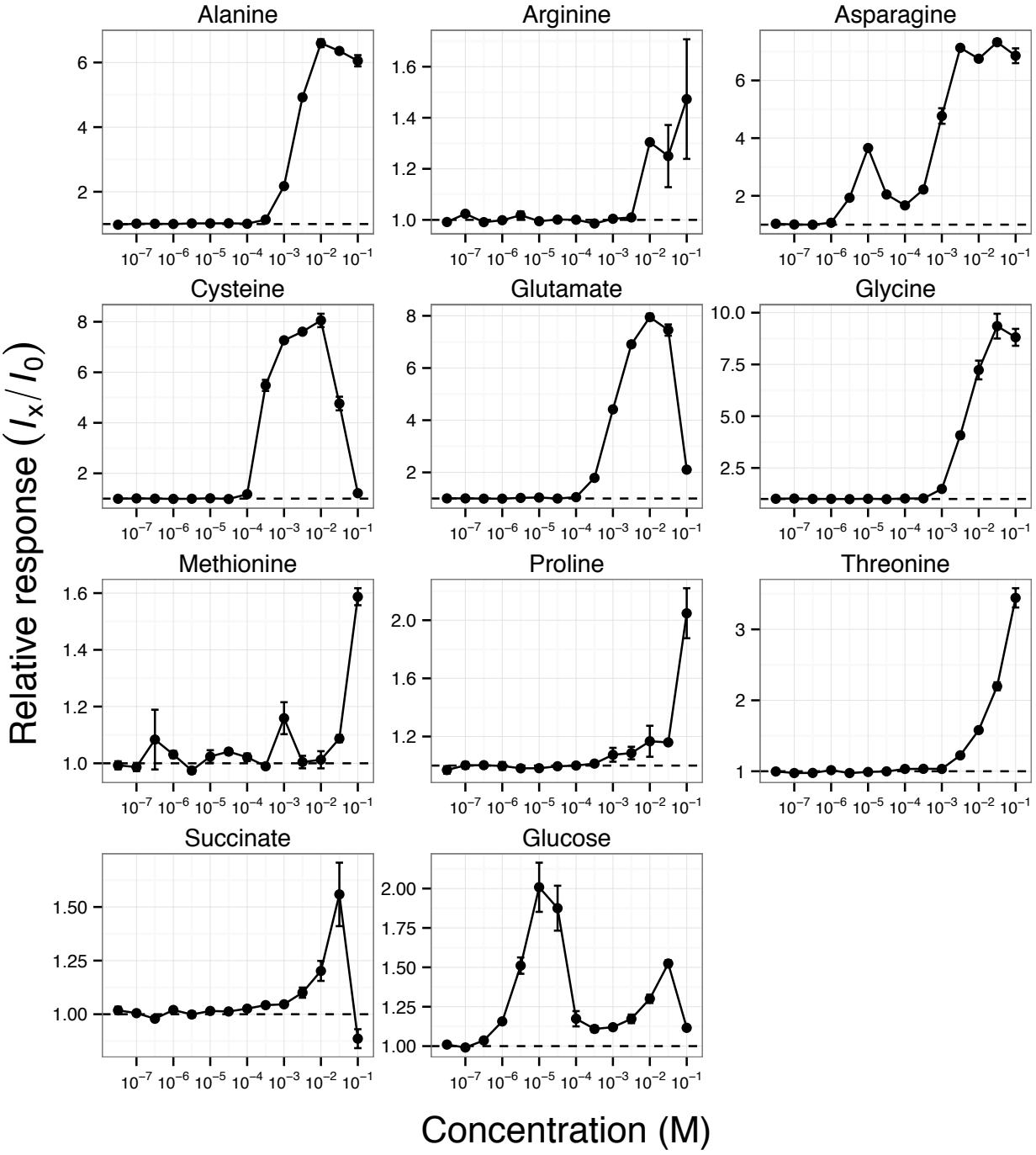
Alanine
Arginine
Asparagine
Cysteine
Glutamate
Glycine
Methionine
Proline
Threonine
Succinate
Glucose
Relative response (I_x/I_0)
Concentration (M)

Figure 5

Figure 5. Concentration-response curves for all chemicals that gave a measureable response and were not displayed in the main text. Relative response is reported as the sum intensity of a source containing a chemical of interest (I_x), over the sum intensity of an empty source (I_0). Each value represents the mean of 3 measurements (n = 3) from separate devices, and error bars indicate the standard error of the mean (SEM).

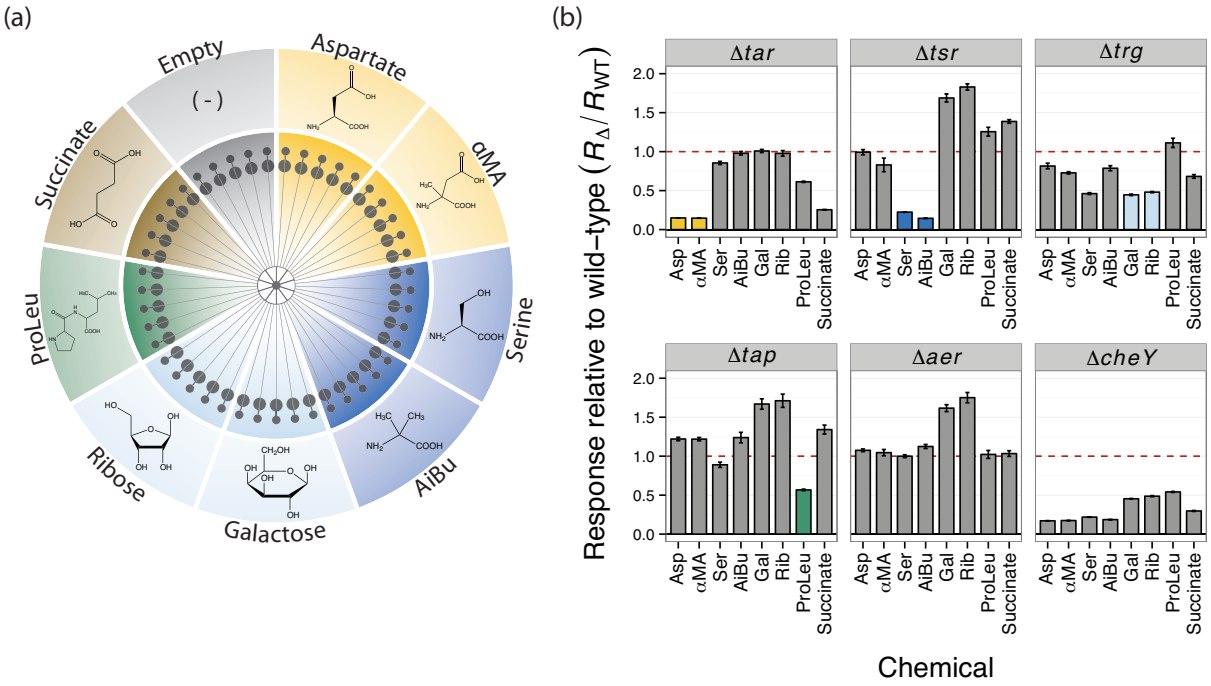
(a)
Empty
(-)
Aspartate
αMA
Serine
AiBu
Galactose
Ribose
ProLeu
Succinate
(b)
Δtar
Δtsr
Δtrg
Δtap
Δaer
ΔcheY
Response relative to wild–type (R_Δ / R_{WT})
2.0
1.5
1.0
0.5
0.0
Asp
αMA
Ser
AiBu
Gal
Rib
ProLeu
Succinate
Chemical

Figure 6

Figure 6. (a) A layout of the chemicals that were tested against each chemoreceptor deletion *E. coli* MG1655 mutant. Chemicals with matching colors are recognized specifically by the same chemoreceptor. The concentrations used were derived from the peak response values in Table 2. (b) Responses of each chemoreceptor deletion strain to the panel of chemicals shown in 3a. Here, the relative response values of the chemoreceptor deletion strains (R_{Δ}) are normalized to the relative responses of wild-type *E. coli* MG1655 (R_{WT}), where a response of 1 (red dashed line) indicates no change from wild-type *E. coli* cells. The colored bars in each panel indicate the molecules that are specifically recognized by the deleted chemoreceptor. The Δ*cheY* mutant was included as a negative control (lower-right panel), as this strain is motile but does not chemotax. Each value represents the mean of 10 measurements (n = 10) performed on two separate assay devices. Error bars indicate the SEM.

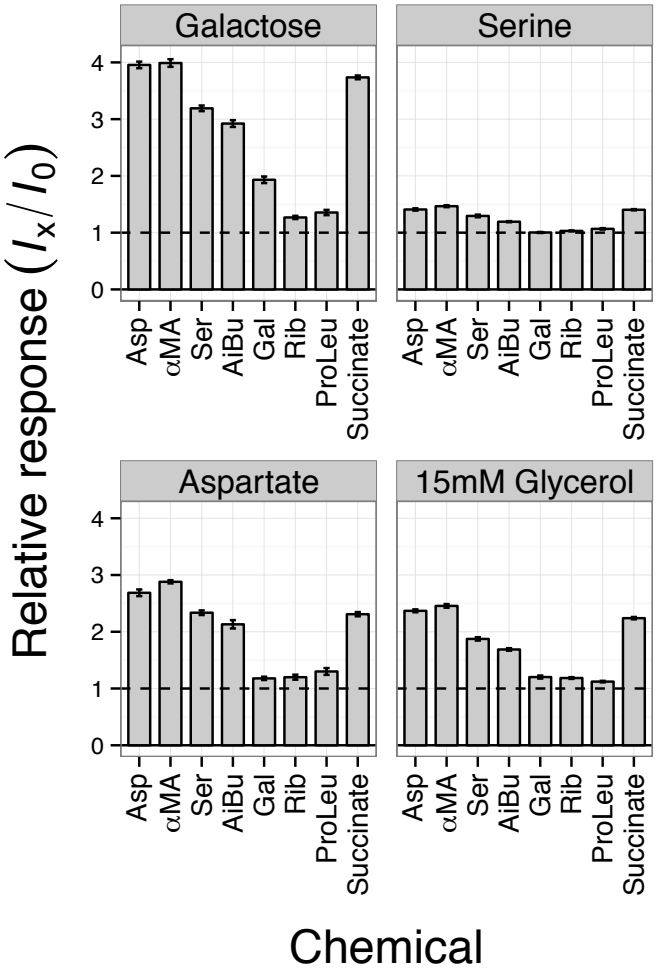
Galactose
Serine
Aspartate
15mM Glycerol
Relative response (I_x / I_0)
0
1
2
3
4
Asp
αMA
Ser
AiBu
Gal
Rib
ProLeu
Succinate
Chemical

Figure 7

Figure 7. Global chemotaxis response of wild-type *E. coli* MG1655 cells grown on different carbon sources. Cells were raised in M9 minimal media supplemented with 15 mM of the chemical indicated above each plot (every condition was also supplemented with 15 mM glycerol to support growth). Chemotactic responses were measured against the same panel of molecules depicted in Figure 6a. Each value represents the mean of 10 measurements (n = 10) performed on two separate assay devices. Error bars indicate the SEM.

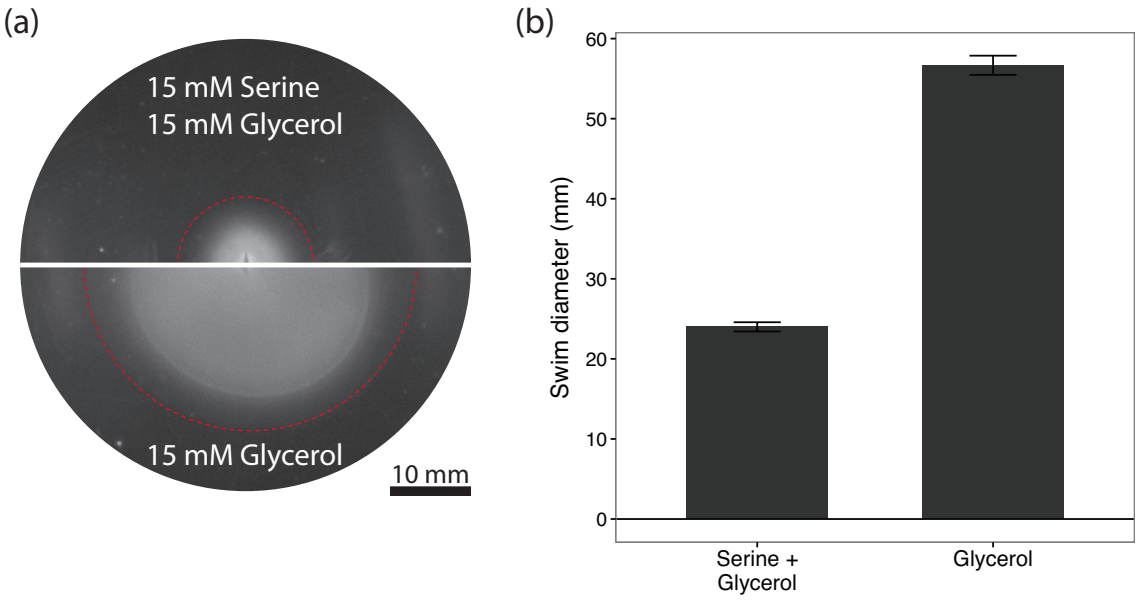
(a)
15 mM Serine
15 mM Glycerol
15 mM Glycerol
10 mm
(b)
Swim diameter (mm)
60
50
40
30
20
10
0
Serine +
Glycerol
Glycerol

Figure 8

Figure 8. Bacterial swimming is reduced in low percentage agar in the presence of serine. (a) Top views of two representative swim agar plates. The plate shown in the upper half of the collage contained serine + glycerol. The lower half contained glycerol alone. The red dashed lines indicate the perimeter of the swim colonies. (b) Mean diameters of swim colonies obtained under both conditions shown in panel (a). Diameters were measured in triplicate (n=3). Error bars represent the SEM.

Table 1.

Primer name	Primer sequence (5′ to 3′)
Δ*tar*, P1	CTTCTAGAGGTACCGCGCCGCCTGAATGAGTAAAA
Δ*tar*, P2	TCCCAGTTTGGATCTTGTTCAGCCCATTACCAACAGCGTGACTAC
Δ*tar*, P3	GTAGTCACGCTGTTGGTAATGGGCTGAACAAGATCCAAACTGGGA
Δ*tar*, P4	GAGAGCTCGATATCGTTTTGCAATCCCCTGACGTG
Δ*tsr*, P1	CTTCTAGAGGTACCGCAGATACACCGATACAGAGGC
Δ*tsr*, P2	AAATGTTTCCCAGTTCTCCTCGCCATGGTTTCTCTTTCCTGTGGAC
Δ*tsr*, P3	GTCCACAGGAAAGAGAAACCATGGCGAGGAGAACTGGGAAACATTT
Δ*tsr*, P4	GAGAGCTCGATATCGGCTGGTCAACGGTTACGTTAC
Δ*trg*, P1	CTTCTAGAGGTACCGCAACCTCCTTATCACCGTCC
Δ*trg*, P2	TCACACCGTAGCGAAACTAACTCGCTGTGAGGGAGTTGTATTC
Δ*trg*, P3	AGTTTCGCTACGGTGTGAAAA
Δ*trg*, P4	GAGAGCTCGATATCGCACCCGCTACTTCAGGAGAAC
Δ*tap*, P1	CTTCTAGAGGTACCGGTAATCTTGCCAGTCGCAGC
Δ*tap*, P2	CACTTCAGGATACCACTGGCGAAACATCAACGCTCCCCATCAG
Δ*tap*, P3	CTGATGGGGAGCGTTGATGTTTCGCCAGTGGTATCCTGAAGTG
Δ*tap*, P4	GAGAGCTCGATATCGATCACTGGCAAACACTTTCC
Δ*aer*, P1	CTTCTAGAGGTACCGCATGATCCAGCGTTCGCTTC
Δ*aer*, P2	TGCAGTACCGTCACCGCGTTGCTGGGTGACATACGGATGAG
Δ*aer*, P3	CTCATCCGTATGTCACCCAGCAACGCGGTGACGGTACTGCA
Δ*aer*, P4	GAGAGCTCGATATCGGATTACCATCCGCGAAGAGG
Δ*cheY*, P1	CTTCTAGAGGTACCGGTGGAACTGAGGCAATTCGT
Δ*cheY*, P2	AGTTTTTCCTCCAGCGTCGCATCCGCCATTTCACACTCCTGATT
Δ*cheY*, P3	AATCAGGAGTGTGAAATGGCGGATGCGACGCTGGAGGAAAAACT
Δ*cheY*, P4	GAGAGCTCGATATCGTGACATCCATCATCCGCTTA
Δ*tar*, sequencing, fwd	ATTTCTGCTGCGACCATTCT
Δ*tar*, sequencing, rev	GCAGTGAGGAAATCCGAAAG
Δ*tsr*, sequencing, fwd	GCGCGCGTAAAGTAAGGTAA
Δ*tsr*, sequencing, rev	CACTAATCATCTGCGGTTGC
Δ*trg*, sequencing, fwd	TGAGGTTTCCTTAGGGACGA
Δ*trg*, sequencing, rev	GGAATACTGACCCGCGTAGA
Δ*tap*, sequencing, fwd	GAAGAACAGGCGAGTCGTTT
Δ*tap*, sequencing, rev	CATGTCGCGTTTATGGTCAG
Δ*aer*, sequencing, fwd	GCACGTTTTCAGGGCAATAA
Δ*aer*, sequencing, rev	TTTACGCGTCAACCAGAGC
Δ*cheY*, sequencing, fwd	GAAGCAAGTTGCGTGGTGT
Δ*cheY*, sequencing, rev	GCGGTCATCTGCACAACATA

Table 2. A list of half-maximal effective concentration (EC_{50}) and peak response values for each chemical that gave a measurable chemotaxis response. Values were derived from chemotactic response curves like those shown in Figure 3b.

Chemical	EC_{50} (M)	Peak (M)
Amino acids		
Alanine	2.1×10^{-3}	1.4×10^{-2}
Arginine	-----	$>1 \times 10^{-1}$
Asparagine	7.0×10^{-4}	4.7×10^{-2}
Aspartate	1.8×10^{-5}	7.4×10^{-2}
Cysteine	2.0×10^{-4}	7.5×10^{-3}
Glutamate	8.5×10^{-4}	1.5×10^{-2}
Glycine	4.1×10^{-3}	4.8×10^{-2}
Methionine	-----	$>1 \times 10^{-1}$
Proline	-----	$>1 \times 10^{-1}$
Threonine	-----	$>1 \times 10^{-1}$
Serine	2.4×10^{-4}	2.2×10^{-3}
Non-metabolizable amino acids		
αMA	1.4×10^{-4}	3.3×10^{-3}
AiBu	1.4×10^{-2}	4.1×10^{-2}
Dipeptide		
ProLeu	1.4×10^{-6}	2.8×10^{-5}
Sugars		
Galactose	1.6×10^{-6}	3.5×10^{-6}
Ribose	1.4×10^{-6}	3.0×10^{-6}
Glucose	4.5×10^{-6}	1.5×10^{-5}
Non-specific metabolite		
Succinate	1.6×10^{-2}	3.5×10^{-2}

REFERENCES

1. Aihara E, Closson C, Matthis AL, Schumacher MA, Engevik AC, Zavros Y, et al. Motility and chemotaxis mediate the preferential colonization of gastric injury sites by Helicobacter pylori. PLoS Pathog. 2014;10(7):e1004275.

2. Burall LS, Harro JM, Li X, Lockatell CV, Himpsl SD, Hebel JR, et al. Proteus mirabilis genes that contribute to pathogenesis of urinary tract infection: identification of 25 signature-tagged mutants attenuated at least 100-fold. Infect Immun. 2004;72(5):2922-38.

3. Josenhans C, Suerbaum S. The role of motility as a virulence factor in bacteria. Int J Med Microbiol. 2002;291(8):605-14.

4. Stocker R, Seymour JR. Ecology and physics of bacterial chemotaxis in the ocean. Microbiol Mol Biol Rev. 2012;76(4):792-812.

5. Bi S, Yu D, Si G, Luo C, Li T, Ouyang Q, et al. Discovery of novel chemoeffectors and rational design of Escherichia coli chemoreceptor specificity. Proc Natl Acad Sci U S A. 2013;110(42):16814-9.

6. Lacal J, Garcia-Fontana C, Munoz-Martinez F, Ramos JL, Krell T. Sensing of environmental signals: classification of chemoreceptors according to the size of their ligand binding regions. Environ Microbiol. 2010;12(11):2873-84.

7. Adler J. A method for measuring chemotaxis and use of the method to determine optimum conditions for chemotaxis by Escherichia coli. J Gen Microbiol. 1973;74(1):77-91.

8. Hegde M, Englert DL, Schrock S, Cohn WB, Vogt C, Wood TK, et al. Chemotaxis to the quorum-sensing signal AI-2 requires the Tsr chemoreceptor and the periplasmic LsrB AI-2-binding protein. J Bacteriol. 2011;193(3):768-73.

9. Ahmed T, Shimizu TS, Stocker R. Microfluidics for bacterial chemotaxis. Integr Biol (Camb). 2010;2(11-12):604-29.

10. Warrens AN, Jones MD, Lechler RI. Splicing by overlap extension by PCR using asymmetric amplification: an improved technique for the generation of hybrid proteins of immunological interest. Gene. 1997;186(1):29-35.

11. Philippe N, Alcaraz JP, Coursange E, Geiselmann J, Schneider D. Improvement of pCVD442, a suicide plasmid for gene allele exchange in bacteria. Plasmid. 2004;51(3):246-55.

12. Singer JT, Phennicie RT, Sullivan MJ, Porter LA, Shaffer VJ, Kim CH. Broad-host-range plasmids for red fluorescent protein labeling of gram-negative bacteria for use in the zebrafish model system. Appl Environ Microbiol. 2010;76(11):3467-74.

13. Xia Y, Whitesides, G.M. Soft Lithography. Angewandte Chemie International Edition. 1998;37:550-75.

14. Cira NJ, Ho JY, Dueck ME, Weibel DB. A self-loading microfluidic device for determining the minimum inhibitory concentration of antibiotics. Lab Chip. 2012;12(6):1052-9.

15. Ho JY, Cira NJ, Crooks JA, Baeza J, Weibel DB. Rapid identification of ESKAPE bacterial strains using an autonomous microfluidic device. PLoS One. 2012;7(7):e41245.

16. Team RC. R: A language and environment for statistical computing Vienna, Austria: R Foundation for Statistical Computing; 2015 [Available from: http://www.r-project.org/.

17. Pau G, Fuchs F, Sklyar O, Boutros M, Huber W. EBImage--an R package for image processing with applications to cellular phenotypes. Bioinformatics. 2010;26(7):979-81.

18. Santos TM, Lin TY, Rajendran M, Anderson SM, Weibel DB. Polar localization of Escherichia coli chemoreceptors requires an intact Tol-Pal complex. Mol Microbiol. 2014;92(5):985-1004.

19. Monahan J, Gewirth AA, Nuzzo RG. A method for filling complex polymeric microfluidic devices and arrays. Anal Chem. 2001;73(13):3193-7.

20. Randall GC, Doyle PS. Permeation-driven flow in poly(dimethylsiloxane) microfluidic devices. Proc Natl Acad Sci U S A. 2005;102(31):10813-8.

21. Weibel DB, Whitesides GM. Applications of microfluidics in chemical biology. Curr Opin Chem Biol. 2006;10(6):584-91.

22. Whitesides GM. The origins and the future of microfluidics. Nature. 2006;442(7101):368-73.

23. Lanning LM, Ford RM, Long T. Bacterial chemotaxis transverse to axial flow in a microfluidic channel. Biotechnol Bioeng. 2008;100(4):653-63.

24. Mao H, Cremer PS, Manson MD. A sensitive, versatile microfluidic assay for bacterial chemotaxis. Proc Natl Acad Sci U S A. 2003;100(9):5449-54.

25. Bhushan D, Jaiswal DK, Ray D, Basu D, Datta A, Chakraborty S, et al. Dehydration-responsive reversible and irreversible changes in the extracellular matrix: comparative proteomics of chickpea genotypes with contrasting tolerance. J Proteome Res. 2011;10(4):2027-46.

26. Ogata A, Banks, R.B. U.S. Geological Survey Professional Paper 411-A. 1961.

27. Culbertson CT, Jacobson SC, Michael Ramsey J. Diffusion coefficient measurements in microfluidic devices. Talanta. 2002;56(2):365-73.

28. Stocker R, Seymour JR, Samadani A, Hunt DE, Polz MF. Rapid chemotactic response enables marine bacteria to exploit ephemeral microscale nutrient patches. Proc Natl Acad Sci U S A. 2008;105(11):4209-14.

29. Alexandre G, Zhulin IB. More than one way to sense chemicals. J Bacteriol. 2001;183(16):4681-6.

30. Neumann S, Hansen CH, Wingreen NS, Sourjik V. Differences in signalling by directly and indirectly binding ligands in bacterial chemotaxis. EMBO J. 2010;29(20):3484-95.

31. Adler J. Chemotaxis in bacteria. Annu Rev Biochem. 1975;44:341-56.

32. Adler J, Hazelbauer GL, Dahl MM. Chemotaxis toward sugars in Escherichia coli. J Bacteriol. 1973;115(3):824-47.

33. Clancy M, Madill KA, Wood JM. Genetic and biochemical requirements for chemotaxis to L-proline in Escherichia coli. J Bacteriol. 1981;146(3):902-6.

CHAPTER 4

Investigating the symbiotic bacterium *Xenorhabdus nematophila* in individual, living *Steinernema carpocapsae* nematodes using microfluidics

Adapted from

M.D. Stilwell*, M. Cao*, H. Goodrich-Blair, D.B. Weibel, Studying the symbiotic bacterium *Xenorhabdus nematophila* in individual, living *Steinernema carpocapsae* nematodes using microfluidic systems (submitted).

* Denotes equal contribution

MDS & MC designed and conducted experiments, analyzed data, and wrote the paper.

HGB & DBW wrote the paper.

ABSTRACT

Animal-microbe symbioses are ubiquitous in nature and scientifically important in diverse areas including ecology, medicine, and agriculture. *Steinernema* nematodes and *Xenorhabdus* bacteria compose an established, successful model system for investigating microbial pathogenesis and mutualism. The bacterium *Xenorhabdus nematophila* is a species-specific mutualist of insect-infecting *Steinernema carpocapsae* nematodes. The bacterium colonizes a specialized intestinal pocket within the infective stage of the nematode, which transports the bacteria between insects that are killed and consumed by the pair for reproduction. Current understanding of the interaction between the infective stage nematode and its bacterial colonizers is based largely on population level, snapshot time point studies on these organisms. This limitation arises because investigating temporal dynamics of the bacterium within the nematode is impeded by the difficulty of isolating and maintaining individual living nematodes and tracking colonizing bacterial cells over time. To overcome this challenge, we developed a microfluidic system that enables us to spatially isolate and microscopically observe individual, living *Steinernema* nematodes and monitor the growth and development of the associated *X. nematophila* bacterial communities—starting from a single cell or a few cells—over weeks. Our data demonstrate the first direct, temporal, *in vivo* analysis of a bacteria-nematode symbiosis system and the application of this system to reveal continuous dynamics of the symbiont population in the living host animal.

INTRODUCTION

Microbes form symbiotic relationships with organisms in every kingdom of life and in every ecosystem, ranging from mutualism (all partners benefit) to parasitism (some partners benefit, others are harmed or killed) (1). Many bacterial species are obligate mutualists or obligate pathogens, while others can switch between these two extremes depending on aspects of their external environment, such as host identity (2, 3), abiotic parameters (e.g. temperature) (4–6) , or microbial community partners (7). Microbial symbioses are important in a wide and growing range of areas—including medicine and agriculture (8)—as these relationships play a crucial role in host health, development, and nutrition (1, 9). An understanding of the processes underlying the initiation and maintenance of microbial symbioses is important in predicting conditions in which they emerge, as well as strategies to control, prevent, or engineer them. Insights into these processes requires surpassing the limitations of traditional microbiology approaches that rely heavily on the *in vitro* growth of microbes in synthetic conditions; techniques that make it possible to study microbes *in situ* within complex and dynamic host environments could have an important impact on the symbiosis field (10, 11). To bypass the logistic, technical, and ethical constraints associated with studying symbiosis in vertebrate mammals, numerous labs have developed model systems centered on invertebrate animals to investigate principles of symbiosis (9, 12).

Invertebrate animals (e.g., nematodes, ants, squid, and coral) and their microbial symbionts provide tractable model systems for studying basic mechanisms and dynamics in host-microbe interactions (9, 13). These model organisms have yielded insights into signaling, recognition, persistence (long-term survival in the host), host development, and nutrient exchange between hosts and symbionts (13). Nematodes are particularly useful model organisms for studying bacterial symbiosis, as they are small, transparent, relatively simple in terms of multicellular organisms, and occupy diverse environmental niches (14). Several bacteria-nematode model systems have been developed to explore basic mechanisms of host-microbe symbiotic interactions, including: terrestrial entomopathogenic nematodes associated with gamma-proteobacteria; *Laxus oneistus* marine nematodes with surface-colonizing thiotrophic bacteria; and filarial nematodes interacting with their intracellular symbiotic bacteria, *Wolbachia* (11). Recent studies have also explored microbial symbiosis in the model nematode *Caenorhabditis elegans* in the context of recognizing its association with diverse microbes in its natural environment (11, 15).

A well-characterized model of nematode-bacterium symbiosis is the soil dwelling and entomopathogenic *Steinernema* nematode species and their *Xenorhabdus* bacterial partners. An emerging hypothesis indicates that these mutually beneficial symbionts may have co-adapted and co-evolved, and studies have revealed molecular determinants that promote transmission and maintenance of their species-specific

pairings (16, 17). Among this family of organisms, the *Steinernema carpocapsae* nematode and *Xenorhabdus nematophila* bacterium symbiotic pair and their insect prey together have been established as a tractable system to investigate pathogenesis and mutualism in microbial symbiosis and a relatively simple model to investigate animal-microbe interactions *in vivo* (3, 18, 19).

X. nematophila cells occupy an intestinal pocket called the receptacle in the non-feeding, developmentally arrested stage of nematodes referred to as infective juveniles (IJs) (see Fig. 1). As they prey on insects, *S. carpocapsae* IJ nematodes transport bacteria housed in the receptacle, where the bacteria can attach to the intravesicular structure (IVS) (the IVS is seen as the 'void' around which the bacteria grow in the top part of Fig. 1D)(20). Upon entering the insect hemocoel (literally 'bag of blood'), *S. carpocapsae* nematodes release the population of *X. nematophila* and together the nematode and bacteria kill the insect and use its nutrients for reproduction. IJ nematodes grow into adults, mate sexually, and produce eggs, which hatch into juvenile nematodes. With sufficient nutrients, juvenile nematodes develop into adults and start the next round of the reproductive cycle (3, 18). A high density of nematodes and depletion of nutrients triggers the formation of pre-IJ nematodes, a transient developmental stage that leads to the formation of colonized IJs (21). Immature IJs leave the cadaver, become mature IJs, and seek a new insect host (22, 23) (see Fig. 1).

Entomopathogenic nematodes can be raised and propagated in the laboratory using inexpensive and straightforward techniques (24). The transparency and hardiness of *S. carpocapsae* nematodes makes them amenable to optical microscopy to study the anatomical structures of bacterial localization. This is further facilitated by the genetic tractability of *X. nematophila* and by strains that stably express fluorescent proteins, making them visible within nematodes (Fig. 1) (25). Studies using such tools have revealed discrete stages of bacterial colonization of nematodes in juvenile, adult, pre-IJ, and IJ forms (21) and have demonstrated that these colonization events are species-specific, such that only *X. nematophila* and not other *Xenorhabdus* species associate with *S. carpocapsae* nematodes (26). Previous research also revealed that the final population of bacterial cells in the IJ nematode is clonal and that a period of outgrowth occurs in which the bacterial population expands to fill the receptacle (22). In contrast to the smooth exponential growth of *X. nematophila* in laboratory medium, outgrowth in the IJ receptacle appears to result from periodic increases and decreases in population size (22). Based on these observations, a colonization bottleneck has been proposed in which entry into the receptacle is limited to one or a few cells, or in which cells within the receptacle compete during outgrowth resulting in a single dominant clonal type (21, 22).

The studies described above relied on destructive sampling from nematode populations: bacteria are extracted by grinding hundreds of IJs and bacterial colony forming units (CFU) are quantified to calculate an average CFU per IJ across the

population of nematodes. Alternatively, bacteria are observed within individual nematodes, but only at discrete stages, since the process of sample preparation (e.g. paralysis) and dehydration ultimately leads to nematode death. As such, no studies have achieved the direct visualization and quantification of bacterial population dynamics in individual, living host nematodes over the course of days or weeks, which is necessary to examine the continuing progression of bacterial colonization events and persistence.

To bridge this methodological gap in the study of host-microbe interactions we developed a microfluidic system. Microfluidic channels have characteristic dimensions of ~1-100s of microns that enable the precise manipulation of small volumes of fluids to create controlled chemical environments (27) . Microfluidic systems have been designed for the isolation of individual nematodes and encompass a range of architectures and mechanisms for isolating individual nematodes, including: 1) trapping in droplets of liquid; 2) isolating in tapered channels; and 3) concentrating in straight channels sealed with valves (28, 29). However, these designs are typically used to study the adult stage of *C. elegans*, which is ~10-100X larger in body size than the dauer larval stage, a developmentally arrested phase similar to IJs of entomopathogenic nematodes (28, 30). These microfluidic devices usually keep whole-organisms alive for a relatively short time period—from minutes to hours (31). Much longer time frames—from days to weeks—are required to study the processes underlying the establishment and

persistence of long-term microbial symbioses. Thus, tools to study individual dauer or IJ stages of nematodes are not currently available.

This manuscript describes an experimental system for exploring symbiosis between bacteria and nematodes and its application in studying the relationship between *X. nematophila* and *S. carpocapsae*. Individual nematodes are confined within single microfluidic chambers in which a flow of cold water is periodically applied to temporarily immobilize worms during imaging by optical microscopy; many parallel chambers enable multiple nematodes to be studied simultaneously. The system is simple to operate, does not require chemically induced paralysis (e.g., using levamisole or CO_2), and eliminates the impact of these reagents and conditions on the population of symbiotic bacteria. We describe using our microfluidic design to isolate, maintain, and track individual, living nematodes for the study of host-microbe interactions over days and weeks.

MATERIALS AND METHODS

Bacterial strain construction and growth

We created the GFP-expressing *X. nematophila* strain HGB 2110 inserting the *gfp* in plasmid pURR25 (mini-Tn7-KS-GFP) (25, 52) from *E. coli* donor strain (HGB 1262) into the attTn7 site in the genome of recipient *Xenorhabdus nematophila* wild type bacterial strain (HGB 1969) using tri-parental conjugation with pUX-BF13 (HGB 283) as a helper plasmid. The site-specific insertion at attTn7 was confirmed by antibiotic resistance, sensitivity, and PCR amplification using primers mTn7-befKanR (GTCGACTGCAGGCCAACCAGATAAGT) and AttTn7-ext (TGTTGGTTTCACATCC) yielding positive a band of ~500 base pairs.

We streaked bacteria on LB agar supplemented with 1 g/L sodium pyruvate (53). Overnight cultures were grown in LB liquid media incubated at 30 °C with rotation on a cell roller. Agar or liquid media were supplemented with the appropriate concentration of antibiotics: kanamycin: 50 μg/mL; chloramphenicol: 30 μg/mL for *E. coli*, or 15 μg/mL for *X. nematophila*. We incubated bacteria growing in liquid media or on agar infused with liquid media at 30 °C in the dark.

Nematode propagation and aposymbiotic IJ preparation

S. carpocapsae nematodes were propagated through *Galleria mellonella* insect larvae (Grubco) and stored in water at room temperature. Conventional nematodes produced

from three independent rounds of propagations were used to prepare independent batches of axenic eggs and aposymbiotic nematodes (nematodes do not carry bacterial symbionts in the receptacle) (25), each used in one independent experiment.

Nematode colonization assay and immature IJ isolation

We grew bacterial lawns by plating 600 µl of an overnight culture of *X. nematophila* onto lipid agar (54) and incubated the at 25 °C for 48 h in dark. For each replicate, 5000 aposymbiotic IJs (500 µL of 10 IJs/µL in LB media) were surface-sterilized, added to the bacterial lawn, and incubated at 25 °C in the dark. 6 days later, we sampled nematodes from the bacterial lawn and examined them by microscopy to confirm the formation of immature IJs. Immature IJs were isolated by adding sterile, deionized water to the lipid agar plates to suspend the nematodes. The nematodes were allowed to settle, after which the supernatant was removed and the nematodes were re-suspended in a 1% SDS solution (in water), followed by 20 min of shaking (22). The SDS solution kills nematodes in other developmental stages except for IJ, which we centrifuged for 10 min at 3000rpm. We then discarded the supernatant and resuspended the nematodes in sterile water. After immature IJs isolation and washing, we performed a modified surface-sterilization protocol (54) by treating samples with 0.5% bleach for 2 min. The suspension was then filtered through a filter, followed by 3 washes with sterile water

using vacuum aspiration. This bleach treatment removed cadavers of dead nematodes (mostly non-IJs) in the sample, leaving us with isolated IJ nematodes.

Microfluidic device fabrication and operation

We fabricated microfluidic device masters using standard soft lithography techniques (32). Briefly, we created masters by transferring a pattern from a CAD computer file into SU-8 3025 photoresist (Microchem, Newton, MA, USA) on silicon wafers using photolithography. We used a benchtop spincoater (Laurell Technologies Corp., New Wales, PA, USA) to deposit a thin layer of SU-8 3025 onto a clean wafer at 3000 RPM for 30 s, followed by a post-exposure bake step, and UV exposure to transfer the pattern into photoresist. To transfer the pattern into SU-8 3025, we used negative photomasks (CAD/Art Services Inc., Bandon, OR, USA) and a custom aligner and UV light source. Excess photoresist was removed using SU-8 developer (Microchem, Newton, MA, USA). Microfluidic channels had a height of 25 μm and microfluidic elements had the dimensions described in the paper and outlined in Table S1. The width of the primary channel was 500 μm, the distance between the inlet and outlet was 8 mm. The device contained 38 traps. The traps had variable entrance widths, ranging from 10 to 25 μm. The traps then widened to 10-25 μm with a length of 600 μm. The traps then narrowed to 10 μm and connected to the vacuum port via a set of filtering channels. We silanized masters with a vapor of (tridecafluoro-1,1,2,2-tetrahydrooctyl) trichlorosilane (Gelest

Inc., Morristown, NJ, USA) to facilitate removal of cured layers of poly(dimethylsiloxane) (PDMS) from the master. We cast PDMS (10:1 ratio of base to crosslinking agent; Sylgard 184, Dow Corning, Midland, MI, USA) on the masters to a depth of ~ 3 mm, then cured the polymer at 100°C for >2 h. We peeled cured PDMS layers embossed with microfluidic designs from the master and trimmed them with a razor to a suitable size for bonding to a glass slide. A 1-mm diameter tissue bore was used to punch inlets and outlets in the PDMS device. We cleaned the surface of PDMS devices with frosted scotch tape, immersed the PDMS layers in a container with acetone placed in a sonicating water bath for 20-30 min, then dried them using compressed air. Glass coverslips and clean, dry PDMS devices were exposed to oxygen plasma for 1 min and pressed into conformal contact to bond the glass and PDMS. Devices were put into a 100°C oven for >30 min to ensure efficient bonding. To create the connections to the microfluidic device, we trimmed 19 gauge needles to ~1 cm pieces and blunted the ends. These connectors were inserted into Tygon Micro Bore PVC tubing (0.030″ ID, 0.090″ OD, 0.030″ Wall), which had been cut to a length amenable to our workspace, and inserted into the PDMS device via the inlet, outlet, and vacuum port. The other end of the tubing was connected to a blunted 19 gauge needle attached to a syringe (for the introduction of nematodes, hydration, and vacuum) or inserted into a waste beaker (for the outlet) (See Fig. S4 for representation of experimental set up).

We diluted nematodes to a concentration of <10 nematodes per μL and introduced them into the device with a 1 mL Luer lock syringe. Simultaneously, we applied a vacuum to pull nematodes into the chamber with a 5 mL Luer lock syringe. Once nematodes were loaded, we used a syringe pump to flow water into the device at a rate of 1000 μL/h to maintain the hydration of the nematodes.

Symbiotic bacteria imaging in vivo

All epifluorescence images were acquired using an Eclipse Ti inverted microscope (Nikon, Tokyo, Japan) equipped with a CoolSNAP HQ^2 camera (Photometrics, Munich, Germany). Images were taken using a Nikon S Plan Fluor ELWD 40X objective. Each nematode was imaged with 9 x 1 μm steps to construct a z-stack to capture the depth of the receptacle. All confocal images were taken using a Nikon A1R-Si+ confocal microscope (Nikon, Tokyo, Japan) equipped with high sensitivity GaAsP detectors. Nematodes were sampled in 300 nm z-steps.

Data acquisition and analysis

Quantitative analysis of fluorescently labeled bacterial cells was performed using a custom script in IgorPro. Briefly, cells were detected using the ImageThreshold function, and then a mask was created in the area of detected cells. The pixel intensities were combined to produce an integrated fluorescence intensity. The number of pixels

was counted and converted to an area measurement based on a pixel-to-micron conversion. The integrated fluorescence intensity was converted to an approximate bacterial cell number by dividing the integrated intensity by the integrated intensity of a single cell. Single cell images were collected at the beginning of experiments and analyzed in ImageJ.

RESULTS

We focused our investigation on a key stage of mutualism between *X. nematophila* and *S. carpocapsae*—the nematode IJ stage that acts as a vector from the infection of one insect to another. To investigate *X. nematophila* colonization of and outgrowth in individual IJ receptacles, we fabricated a microfluidic device to isolate and maintain multiple IJ nematodes in individual chambers (referred to as traps) that enabled us to image by microscopy bacteria and nematodes (Fig. 2). We used several criteria in the design of the traps. First, each trap should contain an individual IJ. Second, the devices need to maintain IJ viability for weeks to enable long-term observations of the colonization process. Third, the IJs have to be immobilized without the use of chemical paralyzing agents that could impact the colonization process and obscure biological data. Fourth, the system should be simple to operate. The design we developed to meet these criteria isolates individual nematodes in traps and hydrates the nematodes with room temperature water flowing through the device, except during imaging when cold water temporarily immobilizes the IJs.

Device design and operation

We designed and fabricated a microfluidic system in the transparent silicone elastomer, poly(dimethylsiloxane) (PDMS) using soft lithography (32). We used a previous design for cell bending experiments (33) as a starting point and revamped it for this study. The

system consists of one inlet (through which nematodes and fluids are introduced) connected to an outlet through a straight, primary channel, with traps connected to each side of the primary channel that are attached to a set of filtering channels and terminate in a second outlet that serves as a vacuum port used to apply negative pressure to the channels and traps (Fig. 2). The entire system was 15 x 20 mm long, 3 mm tall, and fit on the stage of a standard inverted microscope. The height of all channels (including the traps) was 25 μm, while the primary channel was 500 μm wide and 8 mm long from inlet to outlet. The entrances into the nematode traps contained an arc to facilitate nematode loading, with entrance widths ranging from 10 to 25 μm (the body width of IJ nematodes varies with age; this range is for experiments with immature IJs or mature IJs, respectively) (see Table S1). The traps then widened at the region where the nematodes were positioned, such that water could flow around them during the course of the experiment. Each of the 38 microfluidic traps were 600-μm long (~1.5x longer than the average body length of mature IJ nematodes) and 25-μm wide (~1.5-2x wider than the nematode body (30)). The width of the traps can be chosen such that the device does not restrict the nematodes natural sigmoidal movement or energy expenditure, which may impact the nutritional conditions of the symbionts. The traps then narrowed to 10 μm and connected to the vacuum port via filtering channels. Note that different numbers of traps can be designed into this system for other applications.

We loaded IJ nematodes—isolated and prepared as described in the next section—in the inlet of the device using a hand-held syringe connected to tubing and attached to the inlet. As we pushed a suspension of the nematodes in water into the primary channel with a hand-held syringe, we applied negative pressure using another syringe connected by tubing to the vacuum port that pulled nematodes into the traps. After trapping the nematodes, we relieved the negative pressure and connected the inlet to a syringe through a section of tubing; the syringe was loaded on a syringe pump that perfused the traps with room temperature water to keep the IJ nematodes hydrated (see Fig. 2). The flow of water mimics the experimental conditions in previous research using populations of nematodes in which nematodes are stored in water between experiments measuring bacterial colonization (22, 25). Since *Steinernema* nematodes are soil dwelling, we also reduced light exposure by covering the system with aluminum foil except while imaging.

Preparation of colonized IJs and survival in microfluidic traps

To facilitate direct observation of bacteria within the IJ receptacle using microscopy, we cultivated nematodes colonized with *X. nematophila* cells engineered to express GFP from a constitutive *lac* promoter. Similar to the processes that occur in an insect cadaver, *S. carpocapsae* nematodes go through reproductive cycles and develop into IJs on an *X. nematophila* lawn (see Fig. 1). Previous research has shown that the *X. nematophila*

population exhibits the most drastic measurable changes during the outgrowth process in which few bacterial cells in newly formed, pre-migratory immature IJs grow into a population of tens to hundreds of bacterial cells during an IJ maturation process that lasts ~5 days (22). To capture the bacterial population profile during the stages of initiation of colonization (one or few cells in the IJ receptacle), bacterial outgrowth (one or a few colonized bacteria grow into a population of tens to hundreds of cells), and bacterial persistence in the IJ receptacle (maintenance of a steady bacterial population size as IJs age), we isolated immature IJs from a mixed population of nematodes from all developmental stages (see Fig. 1) (21, 22). We isolated immature *S. carpocapsae* IJs from the *X. nematophila* agar lawn by treating the mixed population of nematodes with 1% SDS, which kills nematodes at all developmental stages except for IJs, which are protected by a double cuticle (22). We purified immature IJs directly following the SDS treatment by breaking down the tissues of nematode cadavers using bleach. A previous study reported that 1 h after SDS treatment of nematodes, the survival rate of *S. feltiae* IJs was 11%-82% (34).

As the conditions for isolating nematodes in our experiments and physical confinement (e.g., restricted space for growth and movement in microfluidic traps) may alter the physiology of IJs, we initially monitored the survival of immature IJs in the device over a 5-day period (Fig. 3). Nematode death is accompanied by a characteristic rigid, straight body posture that lacks movement (Fig. 3A) followed by tissue

degradation (35). We searched for this phenotype by optical microscopy and counted the number of viable immature IJs in microfluidic traps during a 5-day period. Out of the total number of *S. carpocapsae* IJs loaded in the traps at the beginning of the experiment (n=60, 3 replicates with 18, 22, and 20 nematodes in each), we found that by the end of the experiment (time=112 h), 60% of the trapped nematodes were viable (n=39), 20% were dead (n=11), and 20% had escaped from the traps (n=10) (Fig. 3B). Nematodes have a distribution of body sizes, with a subset of IJ nematodes with body widths <10 μm. As such, these slender nematodes were smaller than the smallest physical dimensions of the channels and traps and were able to escape. Reducing the trap entrance width reduces the number of nematodes that escape, however we found that it makes trapping nematodes more difficult, as many nematodes are wider than the entrance dimensions. Consequently, we decided to leave the design and dimensions as-is and accept the loss of 20% of the nematodes during our experiments (still leaving us with the ability to track the majority of nematodes per experiment). Our maintenance data demonstrates that this approach to nematode isolation enables *in vivo* studies of bacteria-nematode interactions.

Bacterial population dynamics within individual IJs

In a typical experiment, we simultaneously monitored the population dynamics of *X. nematophila* cells in 10-18 live nematodes isolated in parallel microfluidic traps over a 5-

day period (Fig. 4). We imaged *X. nematophila* cells in the IJ receptacle using epifluorescence microscopy at 8 h intervals by vertically sectioning the entire structure in 9 x 1 μm steps (Fig. 4A displays micrographs of a representative IJ nematode using this approach). We chose to section the receptacle in this manner to image the majority of the receptacle for the majority of nematodes, although due to nematode-to-nematode differences, the actual receptacle size for each nematode varies. Using a custom IgorPro script, we converted the total integrated fluorescence intensity signal of each section of the receptacle to the approximate number of *X. nematophila* cells by quantifying the integrated GFP intensity across each z-stack and dividing by the fluorescence intensity for a single cell (Fig. 4B). Single cell fluorescence intensities were determined by analysis of early time point images containing few or single bacterial cells using ImageJ (see Fig. S1 for micrographs with isolated bacterial cells). We did not use phase contrast images for counting single cells, as it is very difficult to distinguish between bacterial cells and nematode cells in phase contrast images.

At the level of individual nematodes, we found that the number of *X. nematophila* cells per unit time fluctuated, such that the number of cells repeatedly increased and decreased in all of the nematodes we studied (n=50; selected nematodes are shown in Fig. 4B). The number of *X. nematophila* cells per unit time varied between individual nematodes. While some nematodes were initially colonized with tens of bacterial cells, others were colonized with a single bacterial cell. To the best of our knowledge, this is

the first time a single bacterium within an IJ has been observed. The number of colonized bacteria in a single nematode reached a maximum of 743 cells, although no other nematode had more than 500 bacterial cells colonizing it at any point. These data are consistent with temporally fluctuating bacterial population sizes observed in past studies based on destructive nematode sampling and ensemble averaging [(22), also see Fig. 5AB]. In these previously published experiments (presented here as Fig. 5AB), each data point was assessed by traditional microbiological CFU counting from grinding and plating a subpopulation of nematodes. We compared previous data on bacterial outgrowth (Fig. 5AB, republished with permission from (22)) and our data using fluorescence quantification (Fig. 5C). As expected, our direct, fluorescence microscopy measurements quantifying *X. nematophila* cells in *S. carpocapsae* nematodes indicated larger numbers of cells than revealed by CFU counting, as CFU counts can underestimate actual cell numbers (36). The comparison between the two techniques also reveals more variance in bacterial cell numbers when using bacterial CFU counts (Fig. 5). Note that the error bars in Fig. 5AB represent measurement error of the population mean, whereas the error bars in Fig. 5C represent the distribution of the population. We found striking variation in the number of bacterial cells colonizing different IJ nematodes and observed that the number of bacterial cells within a single nematode displayed repeated increases and decreases over time, further supporting the

idea that the *X. nematophila* population has periods of growth and death inside the nematode receptacle (see Fig. S2 for bacterial outgrowth dynamics in each IJ) (22).

The direct observation of bacterial populations within IJ nematodes enables both measurements of cell number and of bacterial colony morphology. As such, we quantified the cross-sectional area of colonization by measuring the area of fluorescence in each IJ receptacle (Fig. 4C). In agreement with previous experiments, we observed the cross-sectional area of colonization displaying an overall increase across the population of nematodes. We also observed that within individual nematodes, the cross-sectional area of colonization fluctuated, similar to what we observed with the number of bacterial cells, such that the cross-sectional area increased and decreased over time, while displaying an overall increase in area (Fig. 4C). Our direct, fluorescence based measurements enabled us to extrapolate the bacterial cell density within the IJ receptacle, which occasionally revealed intriguing, unexpected changes: the colonization cross-sectional area increased while the bacterial density decreased (Fig 4C and Fig. S3, green trace). These data suggest that symbionts within maturing IJ nematodes might experience repeated dissociation and re-association with each other or with the IVS.

Growth rates of the bacterial population in the nematode receptacle provide an approximate indication of environmental conditions and bacterial metabolism and physiology. To our knowledge, there has been only one study that measured the

growth rate of *X. nematophila* in *Steinernema* nematodes, although other studies have measured the growth rate in synthetic media (3, 22, 38). Using an average of individual *X. nematophila* growth curves from each experiment using the microfluidic device, and averaging those three independent experiments, we calculated a growth rate of 0.085 ± 0.060 doublings/h (mean ± standard deviation) (see Supplemental Information for growth rate calculations). This value is in good agreement with previous *in vivo* measurements (0.1 doublings/h in the IJ receptacle) and slower than the values measured in synthetic media (0.62 doublings/h in Lysogeny Broth) or insect hemolymph (0.41 doublings/h) (3, 22, 38). One advantage of our system compared to the traditional nematode grinding experiments is that a growth rate can be calculated for the bacteria within each individual nematode and is not limited to a population-based measurement (see Table S2). These data showed nematode-to-nematode differences in symbiont growth rates, with some nematodes showing overall positive symbiont growth (growth rate typically > 0 between any three consecutive timepoints) while other nematodes displayed overall negative growth or death of symbionts (growth rate typically < 0 between any three consecutive timepoints).

We next applied our microfluidic device to study the bacterial colonization of nematode hosts at single-cell resolution. For these experiments, we reduced the widths and heights of the microfluidic traps to ~10 μm to further restrict the movement of nematodes, enabling us to perform confocal microscopy on *X. nematophila* cells and

recreate the topology of the community in 3D. As in the epifluorescence measurements, we cooled the nematodes from room temperature to 4 °C for 30 min before imaging to further reduce nematode movements while shielding them from ambient light. Using this method, we imaged bacterial populations at single-cell resolution in the nematode receptacle over 21 days. We optically 'sectioned' the bacterial population in the receptacle in 300 nm steps once per day for the first five days, and once a week thereafter. Fig. 6 shows a 3D reconstruction of a representative bacterial population within a nematode receptacle over time. 3D reconstructions of the confocal micrographs revealed bacterial population topology changes in the IJ receptacle over weeks. For instance, between days 2 and 3, we observed a portion of the bacterial colony grow an offshoot (see Fig. 6, day 3, top part of colony) only to have the offshoot disappear the following day. Intriguingly, after the initial outgrowth period, the bacterial population was fairly steady until day 14, after which the population underwent another period of growth. Future experiments for longer durations and with increased temporal resolution will reveal more information on the dynamics of persistence in the IJ nematode.

DISCUSSION

In this report, we describe a microfluidic system that enables fundamental questions of host-microbe interactions to be addressed at the level of individual nematode hosts and individual bacterial cells. The data we acquired using this method are generally consistent with those published using traditional, culture-based microbiological methods, yet expand on earlier observations (22). First, by tracking individual nematodes we confirmed the previously established model that one or very few 'founder cells' initiate IJ colonization (22). Our microfluidic data made possible the novel observation of IJs with only one bacterial cell within the receptacle, which adds strong support to the founder cell model. Second, our data demonstrate increases and decreases of a population of *X. nematophila* cells in a single nematode over time. Due to technical caveats, previously observed fluctuations in apparent bacterial population size could be explained by sample-to-sample variation in nematode or bacterial physiology. Here we were able to directly observe bacterial growth and death within a single nematode, supporting the robust conclusion that bacterial populations within IJs are dynamic. Third, by combining microfluidic traps with confocal microscopy, we imaged individual living nematodes and their symbionts for >3 weeks and reconstructed the structure of the bacterial population over time. These experiments confirmed our previous data demonstrating dynamics in the bacterial population topology in the first few days of bacterial outgrowth while also revealing bacterial population dynamics

weeks after colonization. These experiments demonstrate a unique new capability for pushing the boundary of host-microbe interaction studies to a new level of resolution.

The sharp and repeated increases and decreases in the symbiont population of every nematode in our study is an intriguing phenomenon. We propose several hypothetical, non-mutually exclusive models to explain periodic changes in the symbiont population. In model 1, physiological changes—e.g., internal patterns created by a circadian rhythm or the nematode's physical movement—trigger nutrient influx to the receptacle that affects bacterial metabolism. Rhythmic physiological changes in other organisms have been shown to affect bacterial symbionts (39), however this phenomenon has not yet been studied in *S. carpocapsae* nematodes. Nematode movement may stimulate peristalsis in the gut, facilitate mixing, mass transport, and diffusion within this organ, and alter bacterial growth and structures in the receptacle. It is unknown whether the nematode host continuously provides nutrients for the bacteria during long-term colonization. This microfluidic device facilitates future investigations into the nutritional state of the receptacle in individual nematodes.

It is also possible that fluctuating populations sizes during outgrowth result from bacterial cell death and subsequent competition for the utilization of the nutrients released from dead cells. In this model, subpopulations of bacteria that are adapted to utilizing released nutrients would have a growth advantage within the nematode receptacle and become the dominant clone, in a process similar to the growth advantage

in stationary phase (GASP) phenomenon that has been reported for *Escherichia coli* (40). This type of competition could give rise to the observed mono- or bi-clonal symbiont population within IJs, which sector within the receptacle (22). Using the microfluidic device, we observed that in the initiation stage of immature IJ colonization, individual nematodes associated with 2-5 spatially separated individual cells or clusters (Fig. S1), which might indicate discrete clonal populations competing for nutrients. Future implementation of the microfluidic system using wild type, metabolic mutants and/or strains of *X. nematophila* expressing different colors of fluorescent proteins will enable direct visualization of the nutritional environment and competition over long timescales and would contribute significantly to our knowledge of the critical transmission stage of *Steinernema-Xenorhabdus* complex.

Our third model is that population growth and death arises due to phenotypic switching. *X. nematophila* exhibits a phenotypic variation phenomenon termed virulence modulation (VMO), in which cells switch between mutualistic and pathogenic states (41–43). The IJ transmits *X. nematophila* from a niche in which it expresses mutualistic behaviors (the insect cadaver in which it supports nematode reproduction) to one in which it expresses pathogenic behaviors (the blood cavity of a newly infected living insect host) (Fig. 1). It is hypothesized that the IJ environment selects for or induces symbiont switching from the mutualistic to the pathogenic state to pre-adapt bacterial cells for the upcoming infection stage (44). It is possible that repeated growth and death

of the bacteria in IJs reflects the process by which the mutualistic-to-pathogenic phenotypic switch is occurring. For example, population decline may be caused by selective death of cells in the 'mutualistic state', followed by division of cells in the 'pathogenic state'. The development of tools for monitoring bacteria within individual nematode hosts opens the door to observing such dynamics in real time, for example by examining nematodes colonized by *X. nematophila* expressing state-specific fluorescence reporters.

Measurement error likely also contributes to the repeated increases and decreases in bacterial population size. For instance, while imaging, some nematodes respond to the light and begin to squirm, which can interfere with fluorescence measurements. Using traps with smaller dimensions can help eliminate movements from the nematode. Epifluorescence microscopy images will collect light from above and below the sample as well, which can introduce uncertainty into fluorescence quantification. This effect can be overcome with techniques like confocal microscopy, but we found the analysis of confocal data to be more time-consuming and more difficult than with epifluorescence data, which adds another barrier when studying many nematodes. Confocal microscopes are also not as accessible as epifluorescence microscopes, so we chose to use epifluorescence to demonstrate what many labs can expect using our device. Another potential source of error may come from normalizing integrated intensity to single cell intensity, as fluorescence will vary from cell to cell.

Nematode to nematode differences coupled with the inability to synchronize the nematodes will also create uncertainty for population-based measurements.

Many microfluidic devices have been published that isolate individual nematodes, however the majority of these require microfluidics expertise to use (28, 45). Our goal was to provide the field with a tool that was simple enough that microbiology or nematology laboratories could perform long timescale, single nematode studies. Consequently, the number of accouterments required to operate the systems are minimal and consist of: disposable syringes, needles, and tubing. We provide a link to download the Adobe® Illustrator file in the SI; using this file, laboratories can purchase a device 'master' and fabricate their own microfluidic devices (see Supplemental Materials for device design downloads). The device operation is easy to operate and we anticipate that non-experts may find the device approachable and useful for their studies. We believe these devices will be of great use to microbiology and nematology labs and we hope they will be adapted for single organism studies with other model systems.

The device outlined in this manuscript overcomes several limitations of previous techniques. First, the device overcomes three key limitations of the CFU counting approach, which are 1) Combining different subsets of a nematode population for each time point is likely to increase variability in the number of CFUs measured per IJ, since both the number of nematodes in the sample and the colony growth conditions can

vary. 2) Culture based methods underestimate cell counts, as they do not accurately represent non-culturable or slow-growing cells (36). 3) The CFU counting approach is a population-based measurement, so measuring many nematodes at once will dilute any dynamics within a single nematode. As such, variations in CFU counts can only be attributed to experimental error and may miss bacterial population dynamics within a single nematode as the bacteria persist within the IJ, which is an important aspect of the symbiosis (13). Second, using microscopy, researchers have examined nematodes containing bacteria expressing a fluorescent protein and categorized the colonization by the fraction of receptacle filled. While valuable, this technique is highly subjective, as the fraction of receptacle occupied by bacteria is not measured, but rather is estimated relative to other nematodes in the sample. Our device enables a quantitative analysis of the cross-sectional area of colonization while approximating the number of bacterial cells in the receptacle, which is unachievable with traditional techniques. This feature facilitated the observation of the occasional symbiont population increasing in colonization area while decreasing in approximate cell numbers (Fig. 4, green trace). Third, since our device enables growth rate measurements of bacterial populations within individual nematodes, more accurate measurements of bacterial growth can be taken and new investigations of growth rates can be undertaken. For instance, future research could investigate if overall positive or negative symbiont growth in individual

nematodes is correlated to temperature, nematode gene expression, pheromone or small molecule production, or particular behaviors such as IJ dispersal.

We envision several ways this device can be improved upon or altered for future experiments and different studies. Temperature gradients could be introduced into the device such that different traps within the device experience different temperatures, potentially influencing the development of the symbiont relationship. Pressure-driven valves can be added to the device to aid in nematode trapping, potentially increasing the percentage of nematodes that remain trapped in the device during experiments (46). Alterations of the trap dimensions will enable the isolation of other organisms with a range of sizes for long-term studies (29).

Microfluidics provides one approach to immobilize and maintain individual nematodes and has been successfully applied to neuroscience and behavioral studies of *C. elegans* (47, 48). In *C. elegans,* population-based studies show that the nematode entry and development of dauer stage involves significant changes in the expression of genes of hormonal and metabolic regulations that controls the longevity and behaviors of the animals(49, 50). Recent research has begun to reveal that bacteria, a food source for *C. elegans,* influence the nematode dauer formation and longevity (51), stimulating questions about bacteria-nematode interactions and host responses using dauer stage *C. elegans* as an emerging model of symbiosis. The microfluidic platform we developed in this study provides a possible solution to track individual *C. elegans* dauer over long

periods of time to investigate the nematode physiological changes. In *Steinernema* nematodes, the IJ stage provides a valuable opportunity to study intriguing questions regarding symbiont and host physiology that are not currently known to occur in *C. elegans.* The small body size of nematodes and the technical demands for long-term time course experiments were not compatible with previous microfluidic systems for nematode studies. Redesign, testing, and optimization led us to a new microfluidic platform that is compatible with the constraints of loading, maintaining, and immobilizing IJ *Steinernema* nematodes and imaging their symbiotic bacteria. The design also serves as a template for more complicated experiments or experiments with other organisms, which may facilitate the study of microbes that cannot be grown with traditional microbiology methods and for studying microbiomes. The colonization, survival, growth and persistence of microbial symbionts in host animals is central to the health and function of these organisms and the details of which will be unraveled with the aid of new tools, such as the microfluidic system we describe in this paper.

ACKNOWLEDGEMENTS

We acknowledge support from NSF (DMR-1121288 to DBW and IOS-1353674 to HGB) and the Wisconsin Alumni Research Foundation (MSN135448 and 135-AAA6938). MDS acknowledges the National Institute of General Medical Sciences of the National Institutes of Health (NIH T32GM08293)

MC was supported by a UW-Madison U.S. Department of Agriculture (USDA) Hatch Multi-State Research Formula Fund (WIS01582 awarded to HGB), a UW-Madison Louis and Elsa Thomsen Wisconsin Distinguished Graduate Fellowship and a Department of Bacteriology Michael Foster Predoctoral Fellowship.

We thank Piercen M. Oliver for discussions on microfluidic device designs.

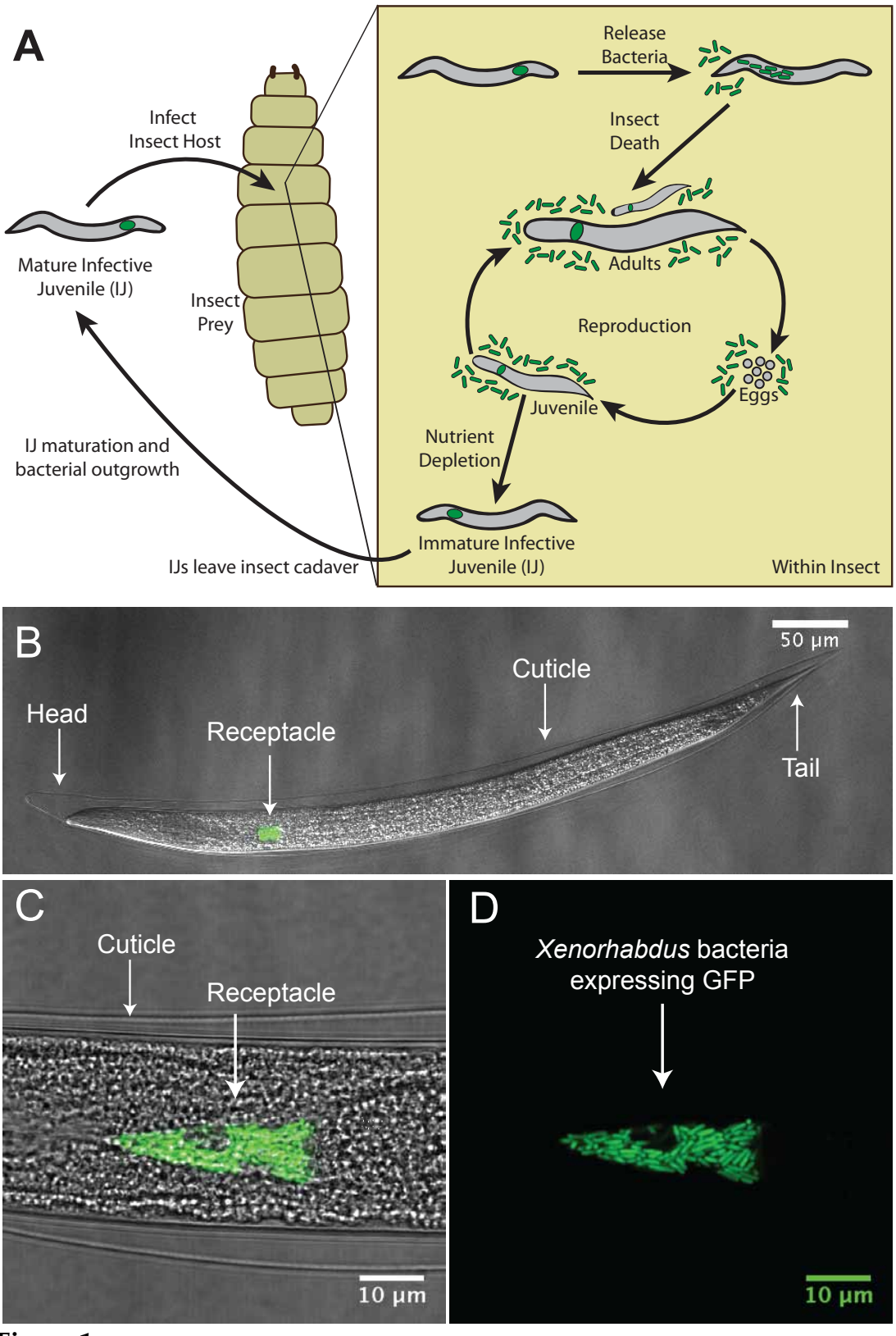
A
Infect
Insect Host
Mature Infective
Juvenile (IJ)
Insect
Prey
IJ maturation and
bacterial outgrowth
IJs leave insect cadaver
Release
Bacteria
Insect
Death
Adults
Reproduction
Eggs
Juvenile
Nutrient
Depletion
Immature Infective
Juvenile (IJ)
Within Insect
B
50 µm
Head
Receptacle
Cuticle
Tail
C
Cuticle
Receptacle
10 µm
D
Xenorhabdus bacteria
expressing GFP
10 µm

Figure 1

Figure 1. The mutualistic relationship between *Xenorhabdus nematophila* bacteria and *Steinernema carpocapsae* nematodes. A) A cartoon depicting the tripartite life cycle of *S. carpocapsae* nematodes. Infective juveniles (IJs) infect an insect prey and release *X. nematophila* cells to evade the host immune system and kill the host. Both species use the cadaver's nutrients for reproduction; upon nutrient depletion, both organisms re-associate and enter the soil to begin the cycle again. B-D) Confocal micrographs of the IJ stage of an *S. carpocapsae* nematode carrying GFP-expressing *X. nematophila* cells in the intestinal receptacle. The intravesicular structure (IVS) can be seen in D as the dark space below the white arrowhead and surrounded by bacterial cells.

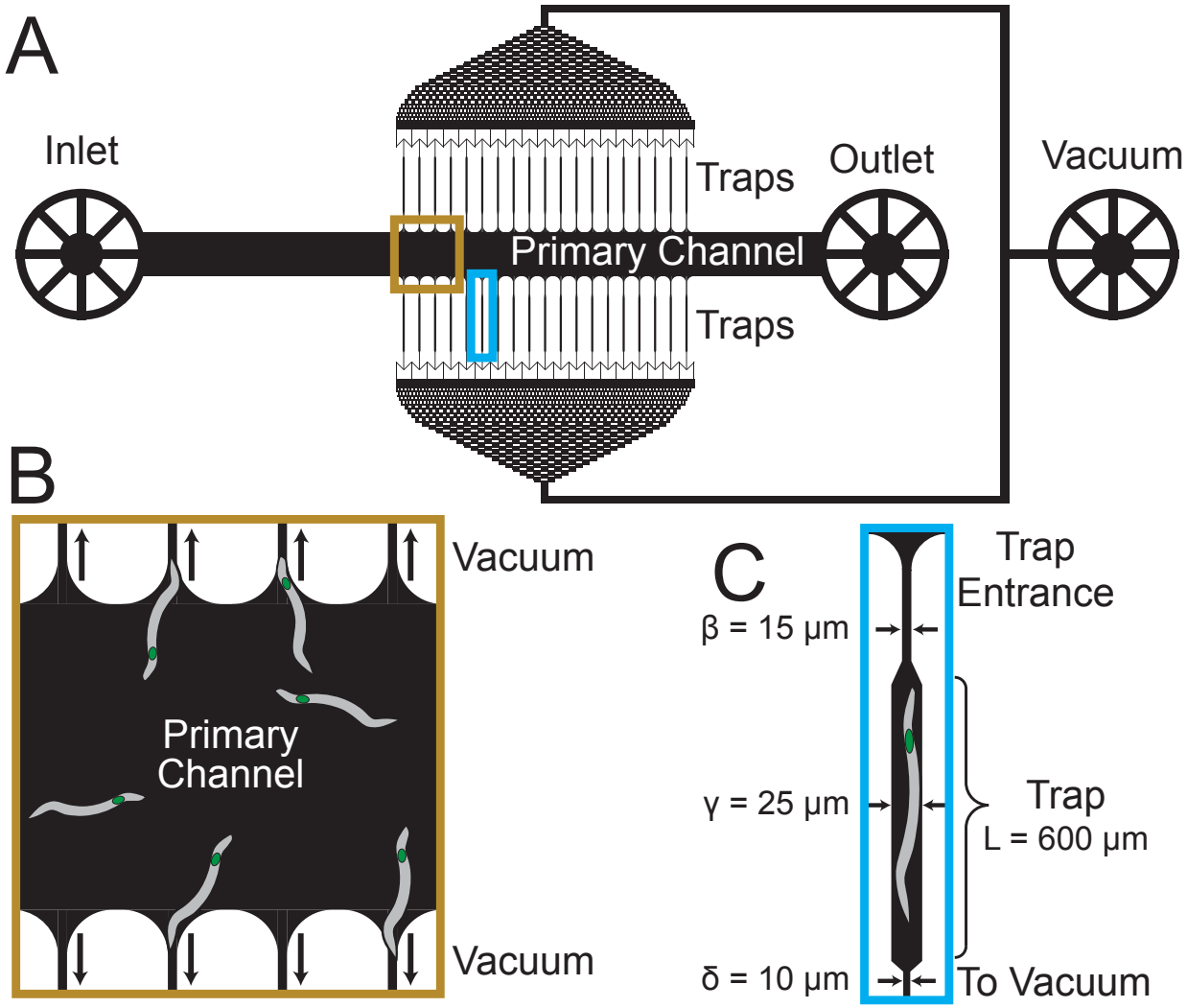
A
Inlet
Traps
Outlet
Vacuum
Primary Channel
Traps
B
Vacuum
Primary
Channel
Vacuum
C
Trap
Entrance
β = 15 μm
γ = 25 μm
Trap
L = 600 μm
δ = 10 μm
To Vacuum

Figure 2

Figure 2. Schematic of microfluidic device for *S. carpocapsae* nematode isolation and maintenance. (A) Device schematic. Nematodes are introduced through the inlet and pushed through the primary channel. Negative pressure applied from the vacuum port pulls nematodes into the traps. (B) Nematodes in the primary channel are pulled into traps with the aid of negative pressure from the vacuum. (C) Physical dimensions of the nematode traps. Note that while the dimensions in the cartoon have been exaggerated for ease of viewing, the labeled dimensions are accurate. For more detail on the trap dimensions, see Table S1.

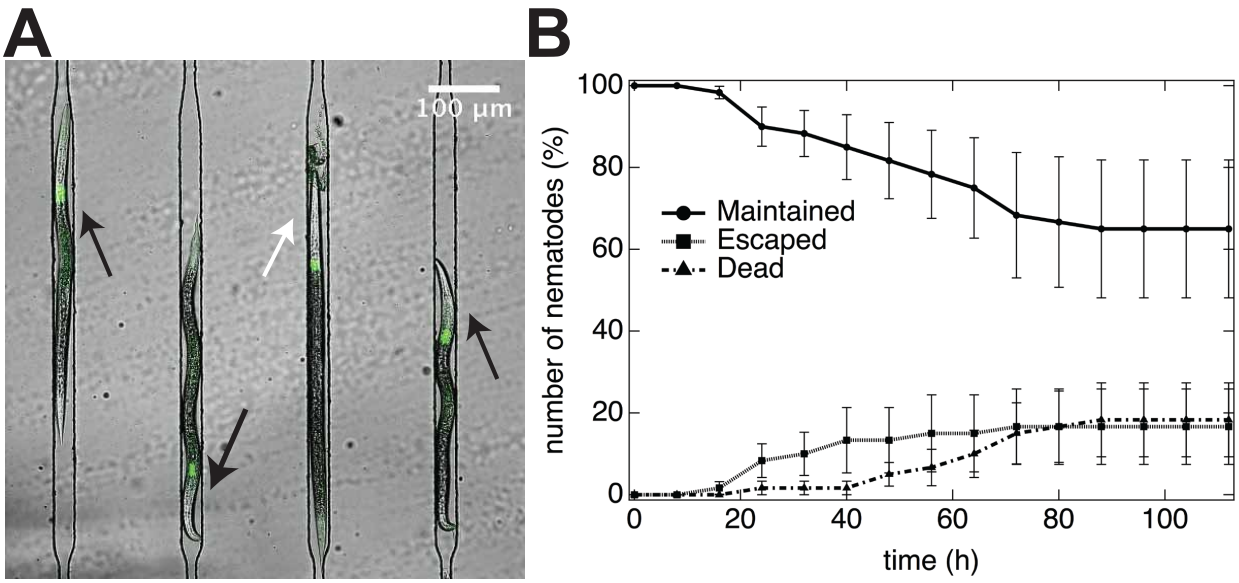
A
100 µm
B
number of nematodes (%)
time (h)
Maintained
Escaped
Dead
0
20
40
60
80
100

Figure 3

Figure 3. Nematode survival and maintenance. A) A confocal micrograph of 4 *S. carpocapsae* nematodes isolated in adjacent microfluidic traps. Living nematodes (highlighted with black arrows) display characteristic body curvature and movements associated with healthy nematodes; dead nematodes (highlighted with white arrow) display a straight body posture and disintegration of tissues. *X. nematophila* bacteria constitutively expressing GFP are colonized in the nematode receptacles. B) Percentage of nematodes in the microfluidic device isolated and alive (circle), escaped (square), or dead (triangle) over the course of 112 h at room temperature. The average of three independent experiments is indicated; total numbers of nematodes trapped in the device were 18, 22, and 20 respectively. Error bars indicate standard error (SEM).

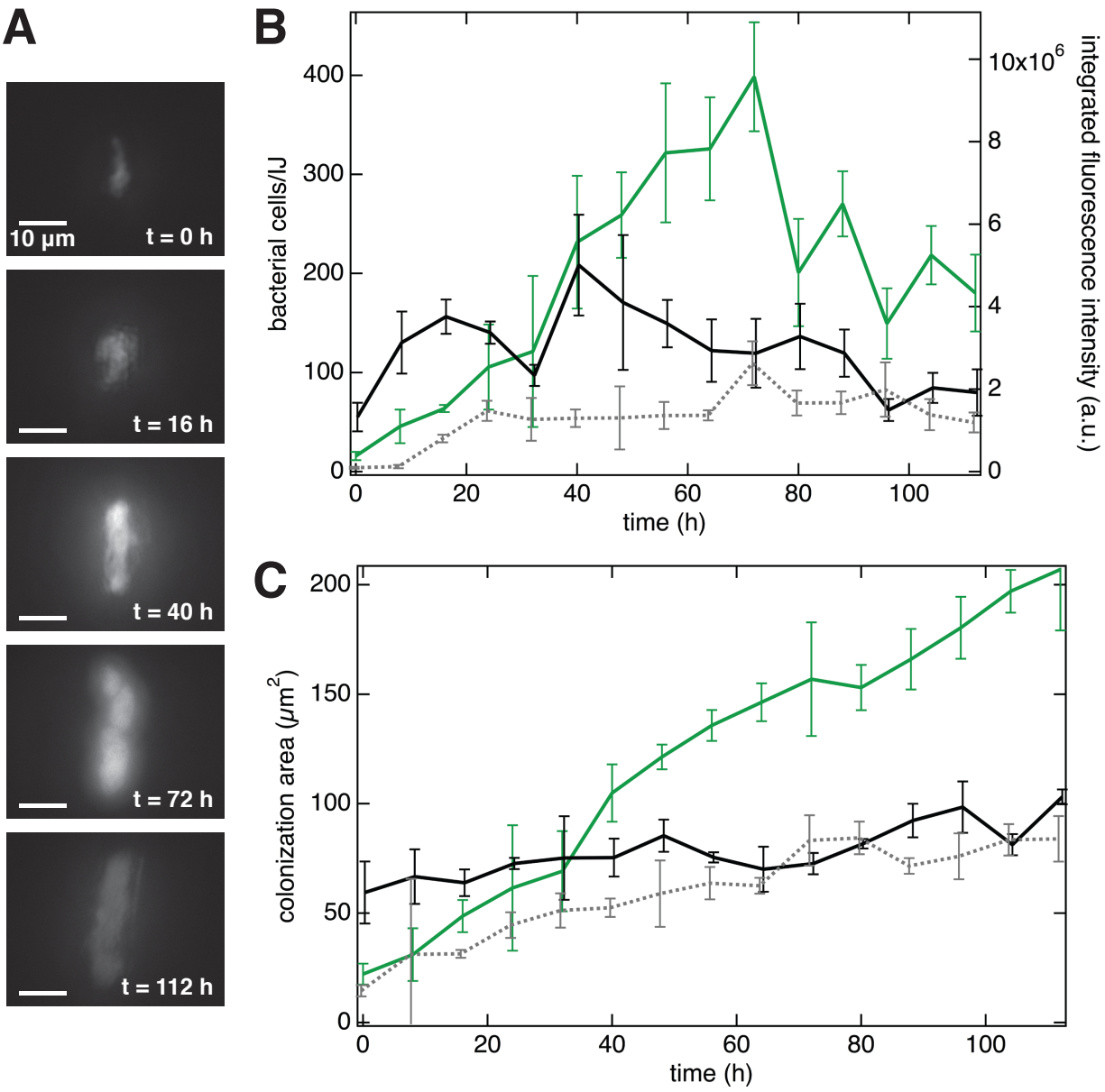
A
10 µm
t = 0 h
t = 16 h
t = 40 h
t = 72 h
t = 112 h
B
bacterial cells/IJ
integrated fluorescence intensity (a.u.)
10x10^6
time (h)
C
colonization area (µm^2)
time (h)

Figure 4

Figure 4. Qualitative and quantitative analysis of bacterial populations in individual, living IJ nematodes. (A) Epifluorescence micrographs of a living, immature IJ nematode receptacle at 0 -112 h post-trapping in microfluidic device. (B) Bacterial cell numbers and fluorescence intensity as measured in five individual nematode receptacles. Green trace represents data for bacterial cells in A. Error bars represent standard deviation. (C) Colonization cross-sectional area in the same five nematodes. Green trace represents data for bacterial cells in A. Error bars represent standard deviation.

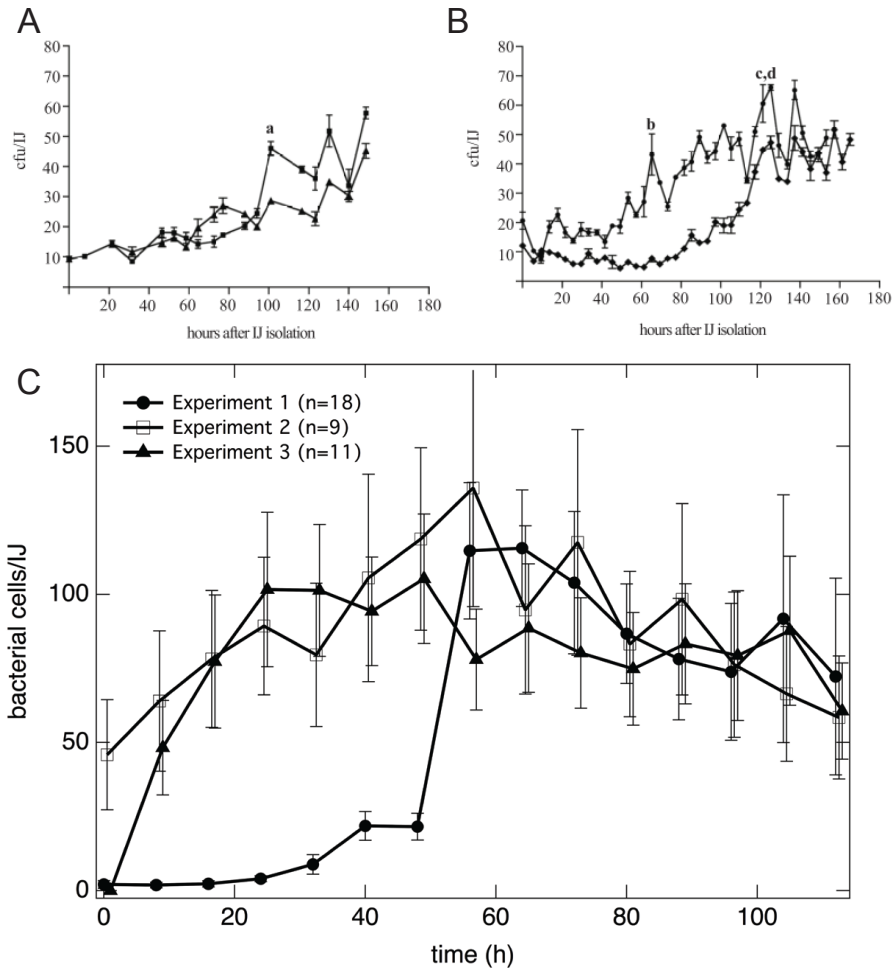
A
cfu/IJ
a
hours after IJ isolation
B
cfu/IJ
b
c,d
hours after IJ isolation
C
Experiment 1 (n=18)
Experiment 2 (n=9)
Experiment 3 (n=11)
bacterial cells/IJ
time (h)

Figure 5.

Figure 5. Comparison of traditional grinding experiments to microfluidic device experiments for quantification of *X. nematophila* bacterial population dynamics in *S. carpocapsae* nematodes. (A, B) Traditional grinding experiments include surface-sterilization, grinding a subpopulation of nematodes, plating on synthetic media and performing bacterial CFU counts. Subpopulations of immature IJs were isolated and assayed every 4-8h. A and B show two replicates each from two separate experiments, each point is the average result for three individual assays. Error bars indicate standard error (SEM) of three measurements of the population at each time. (C) Analysis of epifluorescence micrographs of GFP-expressing *X. nematophila* in individual *S. carpocapsae* trapped in a microfluidic device. Each plot represents the average of all living nematodes in experiment. Error bars indicate standard error (SEM) of the population distribution. (A and B are re-published from Martens et al., 2003 Figure 3 A and B, with permission).

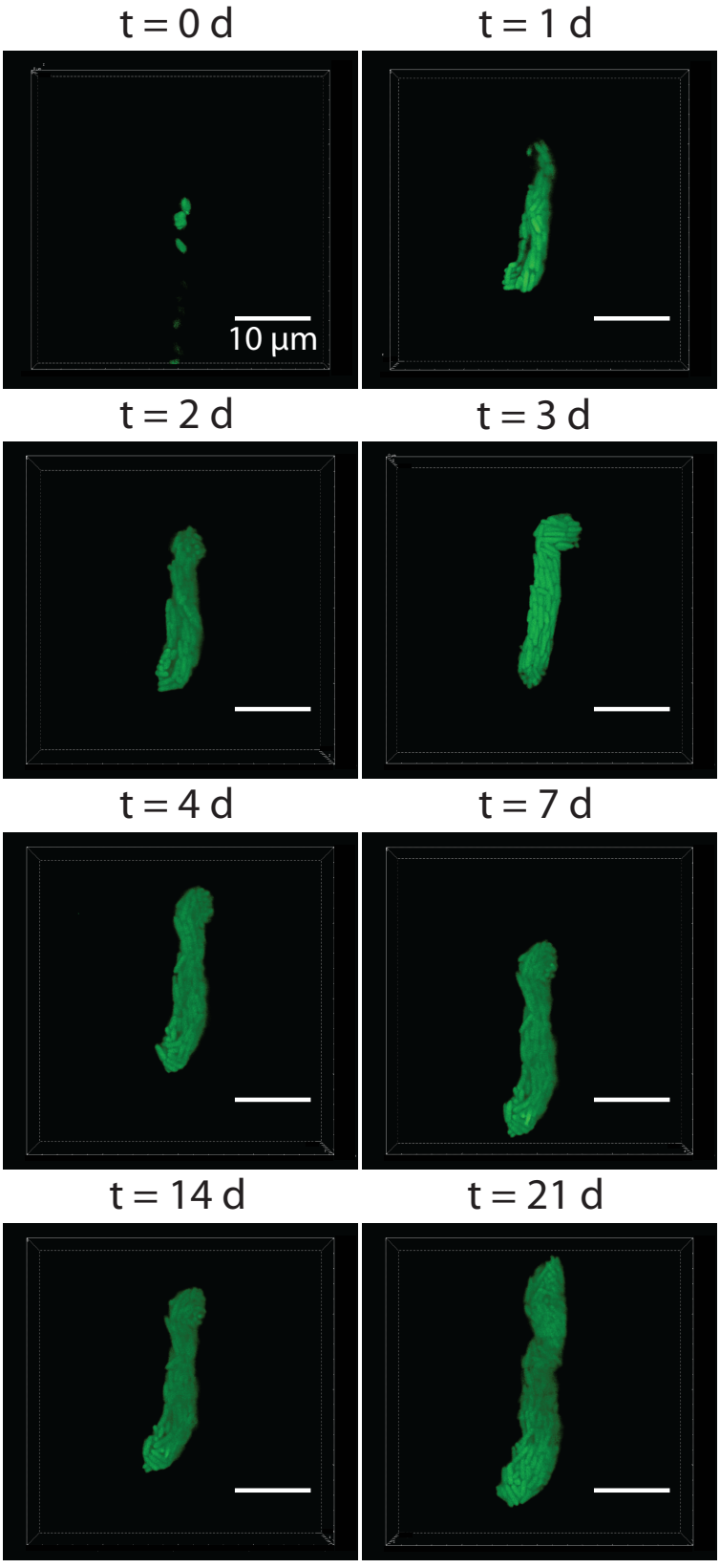

Figure 6

Figure 6. Confocal micrographs of a bacterial population in a receptacle over the course of 3 weeks. An individual living immature IJ nematode (head towards the top) was maintained in the microfluidic device and the GFP expressing bacterial population in the receptacle was imaged on day 0, 1, 2, 3, 4, 7, 14, and 21 post-trapping. Bacterial populations were sectioned in 300 nm z-steps.

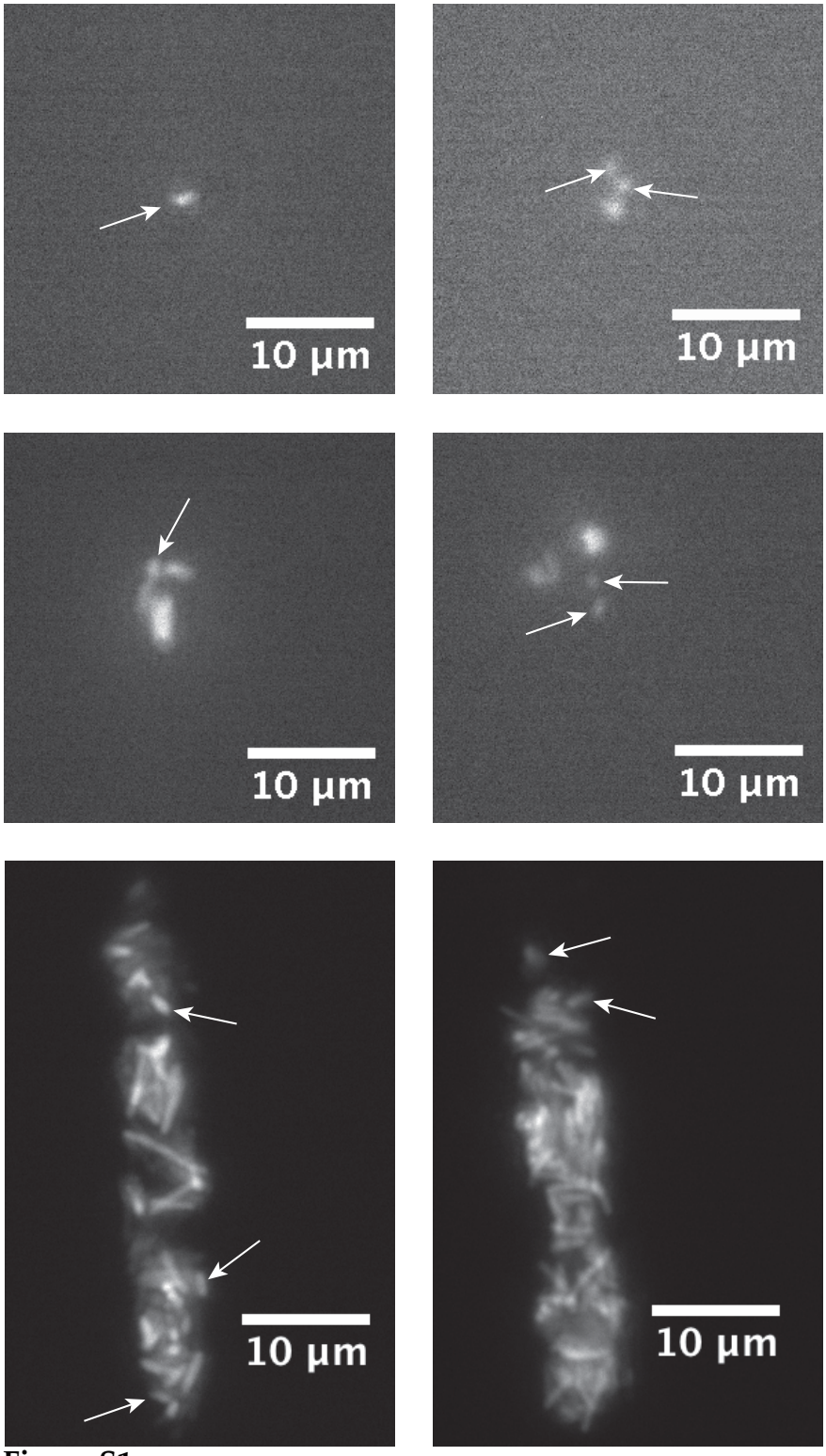

Figure S1.

Figure S1. Representative images of nematodes colonized with visible single cells. The top four images are from immature IJ nematodes and the bottom two are from mature IJ nematodes. Single cell intensity values were determined using ImageJ. Each experimental round was normalized to an average of >10 single cell intensity values from that experimental round.

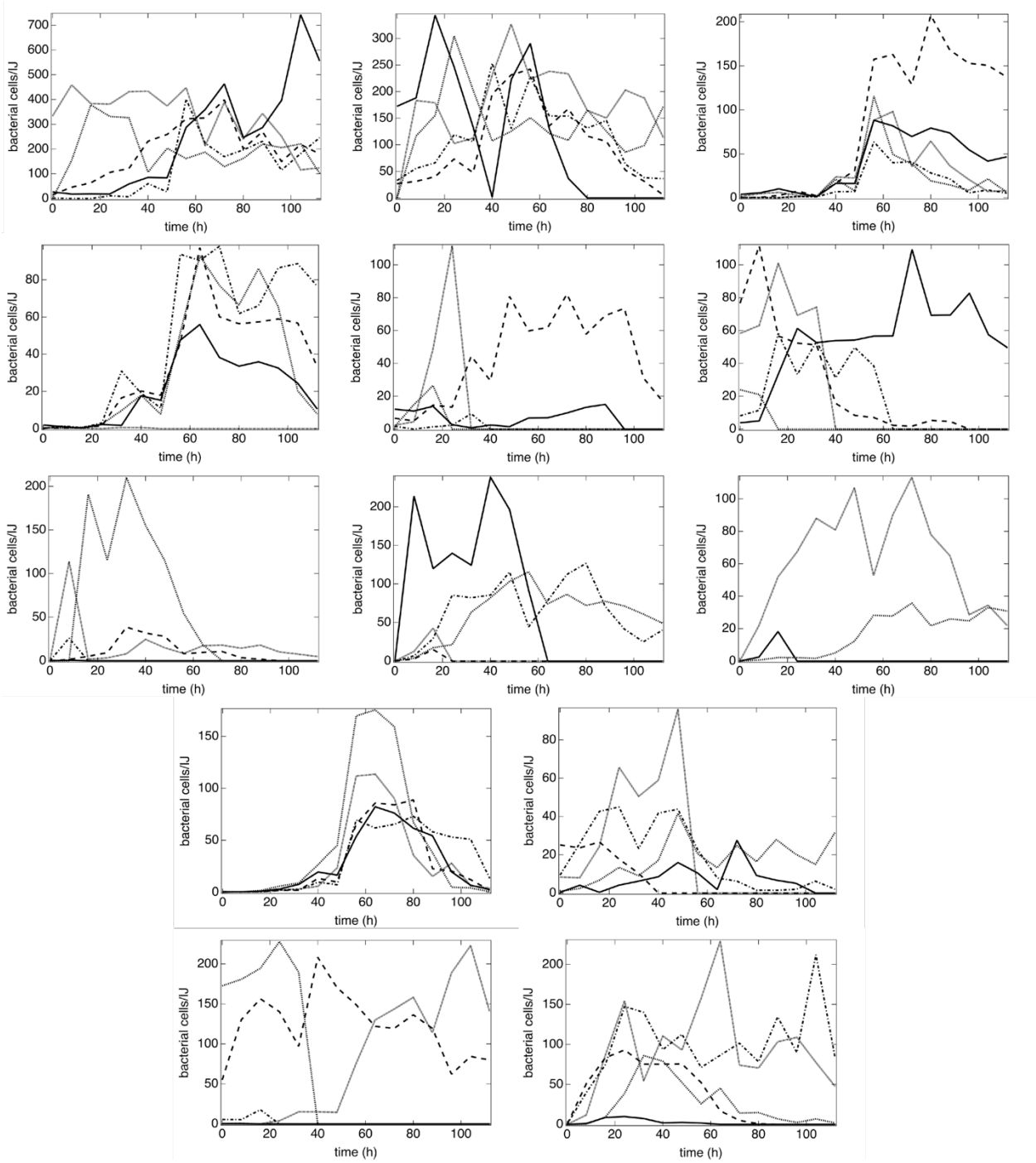

Figure S2.

Figure S2. Bacterial cell numbers within an individual IJ nematode over time. For ease of viewing, each plot contains data from no more than five nematodes.

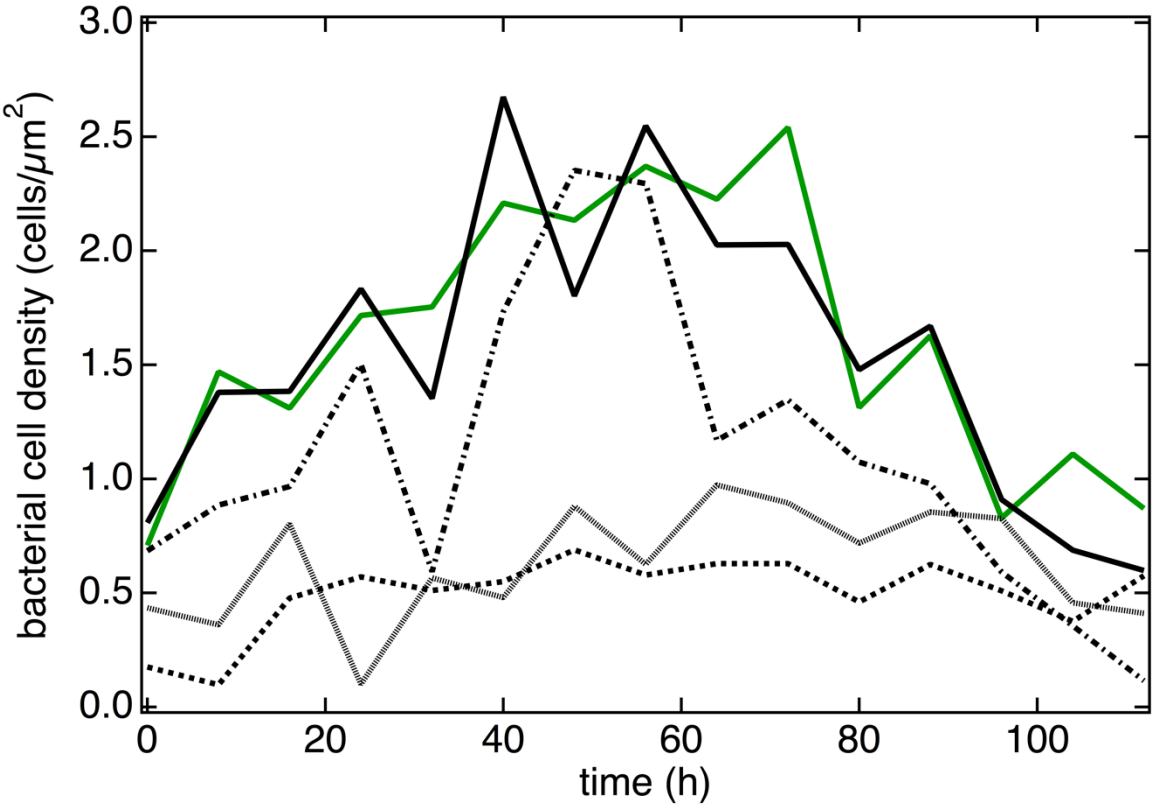
3.0
2.5
2.0
1.5
1.0
0.5
0.0
bacterial cell density (cells/μm²)
0
20
40
60
80
100
time (h)

Figure S3.

Figure S3. Quantitative analysis of epifluorescence micrographs of GFP-expressing *X. nematophila* in individual *S. carpocapsae* trapped in a microfluidic device. This plot shows bacterial cell density over time in the same five nematodes as shown in Figure 4. Green trace represents cells from Figure 4A. Bacterial cell density is calculated by dividing the number of bacterial cells by the cross-sectional area of colonization.

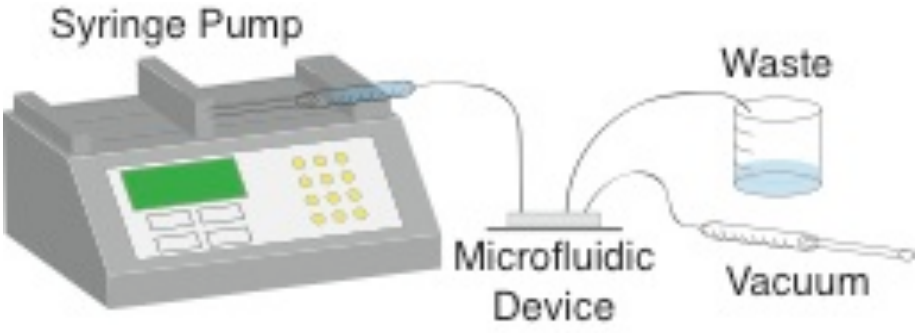

Figure S4.

Figure S4. Cartoon representation of device assembly. A syringe pump pushes water out of a syringe, through a piece of tubing, and into the microfluidic device for nematode hydration. Water exits the device through another piece of tubing and is collected in a waste beaker. Negative pressure is applied via a hand-held syringe connected to the device through tubing to pull nematodes into the microfluidic traps.

REFERENCES

1. **McFall-Ngai M**, **Hadfield M**, **Bosch TCG**, **Carey H V.**, **Domazet-Loso T**, **Douglas AE**, **Dubilier N**, **Eberl B**, **Fukami T**, **Gilbert SF**, **Hentschel U**, **King N**, **Kfelleberg S**, **Knoll AH**, **Natacha K**, **Mazmanian SK**, **Metcalf JL**, **Nealson K**, **Pierce NE**, **Rawls JF**, **Reid A**, **Ruby EG**, **Rumpho M**, **Sanders JG**, **Tautz D**, **Wernegreen J**. 2013. Animals in a bacterial world, a new imperative for the life sciences. Proc Natl Acad Sci **110**:3229–3236.
2. **Goodrich-Blair H**, **Clarke DJ**. 2007. Mutualism and pathogenesis in Xenorhabdus and Photorhabdus: Two roads to the same destination. Mol Microbiol **64**:260–268.
3. **Herbert EE**, **Goodrich-Blair H**. 2007. Friend and foe: the two faces of *Xenorhabdus nematophila*. Nat Rev Microbiol **5**:634–646.
4. **Schnitzler CE**, **Hollingsworth LL**, **Krupp DA**, **Weis VM**. 2012. Elevated temperature impairs onset of symbiosis and reduces survivorship in larvae of the Hawaiian coral, Fungia scutaria. Mar Biol **159**:633–642.
5. **Hadley G**. 1969. Celluose as a carbon source for orchid mycorrhiza. New Phytol **68**:933–939.
6. **Newton AC**, **Fitt BDL**, **Atkins SD**, **Walters DR**, **Daniell TJ**. 2010. Pathogenesis, parasitism and mutualism in the trophic space of microbeâ€"plant interactions. Cell Trends Microbiol **18**:365–373.
7. **Mazmanian SK**, **Round JL**, **Kasper DL**. 2008. A microbial symbiosis factor

prevents intestinal inflammatory disease. Nature **453**:620–625.

8. **Beck JJ**, **Vannette RL**. 2017. Harnessing Insect−Microbe Chemical Communications To Control Insect Pests of Agricultural Systems. J Agric Food Chem **65**:23–28.

9. **Chaston J**, **Goodrich-Blair H**. 2010. Common trends in mutualism revealed by model associations between invertebrates and bacteria. FEMS Microbiol Rev **34**:41–58.

10. **Mcfall-Ngai MJ**. 2015. Giving microbes their due – animal life in a microbially dominant world. J Exp Biol **218**:1968–1973.

11. **Murfin KE**, **Dillman AR**, **Foster JM**, **Bulgheresi S**, **Slatko BE**, **Sternberg PW**, **Goodrich-Blair H**. 2012. Nematode-bacterium symbioses-cooperation and conflict revealed in the "Omics" age. Biol Bull **223**:85–102.

12. **Hussa EA**, **Goodrich-Blair H**. 2013. It Takes a Village: Ecological and Fitness Impacts of Multipartite Mutualism. Annu Rev Microbiol **67**:161–78.

13. **Edward G. Ruby**. 2008. Symbiotic conversations are revealed under genetic interrogation. Nat Rev Microbiol **6**:752–762.

14. **Dillman AR**, **Chaston JM**, **Adams BJ**, **Ciche TA**, **Goodrich-Blair H**, **Stock SP**, **Sternberg PW**. 2012. An entomopathogenic nematode by any other name. PLoS Pathog **8**:e1002527.

15. **Tan M-W**, **Shapira M**. 2011. Genetic and molecular analysis of nematode-microbe

interactions. Cell Microbiol **13**:497–507.

16. **Murfin KE**, **Lee MM**, **Klassen JL**, **McDonald BR**, **Larget B**, **Forst S**, **Stock SP**, **Currie CR**, **Goodrich-Blair H**. 2015. *Xenorhabdus bovienii* strain diversity impacts coevolution and symbiotic maintenance with *Steinernema* spp. nematode hosts. MBio **6**:1–10.

17. **Goodrich-Blair H**. 2007. They've got a ticket to ride: *Xenorhabdus nematophila*–*Steinernema carpocapsae* symbiosis. Curr Opin Microbiol **10**:225–230.

18. **Richards GR**, **Goodrich-Blair H**. 2009. Masters of conquest and pillage: *Xenorhabdus nematophila* global regulators control transitions from virulence to nutrient acquisition. Cell Microbiol **11**:1025–1033.

19. **Bird AF**, **Akhurst RJ**. 1983. The nature of the intestinal vesicle in nematodes of the family steinernematidae. Int J Parasitol **13**:599–606.

20. **Martens EC**, **Goodrich-Blair H**. 2005. The *Steinernema carpocapsae* intestinal vesicle contains a subcellular structure with which *Xenorhabdus nematophila* associates during colonization initiation. Cell Microbiol **7**:1723–1735.

21. **Chaston JM**, **Murfin KE**, **Heath-Heckman EA**, **Goodrich-Blair H**. 2013. Previously unrecognized stages of species-specific colonization in the mutualism between *Xenorhabdus* bacteria and *Steinernema* nematodes. Cell Microbiol **15**:1545–1559.

22. **Martens EC**, **Heungens K**, **Goodrich-Blair H**. 2003. Early Colonization Events in

the Mutualistic Association between *Steinernema carpocapsae* Nematodes and *Xenorhabdus nematophila* Bacteria. J Bacteriol **185**:3147–3154.

23. **Kaplan F**, **Alborn HT**, **von Reuss SH**, **Ajredini R**, **Ali JG**, **Akyazi F**, **Stelinski LL**, **Edison AS**, **Schroeder FC**, **Teal PE**. 2012. Interspecific nematode signals regulate dispersal behavior. PLoS One **7**:e38735.

24. **Kaya HK**, **Gaugler R**. 1993. Entomopathogenic Nematodes. Annu Rev Entomol **38**:181–206.

25. **Murfin KE**, **Chaston J**, **Goodrich-Blair H**. 2012. Visualizing bacteria in nematodes using fluorescent microscopy. J Vis Exp.

26. **Cowles CE**, **Goodrich-Blair H**. 2008. The *Xenorhabdus nematophila nilABC* genes confer the ability of *Xenorhabdus* spp. to colonize *Steinernema carpocapsae* nematodes. J Bacteriol **190**:4121–4128.

27. **Whitesides GM**. 2006. The origins and the future of microfluidics. Nature **442**:368–373.

28. **San-Miguel A**, **Lu H**. 2013. Microfluidics as a tool for C. elegans research *. WormBook.

29. **Hwang H**, **Lu H**. 2013. Microfluidic tools for developmental studies of small model organisms -nematodes, fruit flies, and zebrafish. Biotechnol J **8**:192–205.

30. 2002. ENTOMOPATHOGENIC NEMATOLOGY. CABI, New York.

31. **Hulme SE**, **Shevkoplyas SS**, **Apfeld J**, **Fontana W**, **Whitesides GM**. 2007. A

microfabricated array of clamps for immobilizing and imaging C. elegans.

32. **McDonald JC**, **Duffy DC**, **Anderson JR**, **Chiu DT**, **Wu H**, **Schueller OJA**, **Whitesides GM**. 2000. Fabrication of microfluidic systems in poly(dimethylsiloxane). Electrophoresis **21**:27–40.

33. **Amir A**, **Babaeipour F**, **McIntosh DB**, **Nelson DR**, **Jun S**. 2014. Bending forces plastically deform growing bacterial cell walls. Proc Natl Acad Sci U S A **111**:5778–83.

34. **Rolston AN**, **Griffin CT**, **Downes MJ**. 2006. Emergence and Dispersal Patterns of Two Isolates of the Entomopathogenic Nematode Steinernema feltiae. J Nematol **38**:221–228.

35. **Johnson TE**, **Wood WB**. 1982. Genetic analysis of life-span in Caenorhabditis elegans. Genetics **79**:6603–6607.

36. **Keren I**, **Shah D**, **Spoering A**, **Kaldalu N**, **Lewis K**. 2004. Specialized Persister Cells and the Mechanism of Multidrug Tolerance in Escherichia coli **186**:8172–8180.

37. **Martens EC**, **Russell FM**, **Goodrich-Blair H**. 2005. Analysis of *Xenorhabdus nematophila* metabolic mutants yields insight into stages of *Steinernema carpocapsae* nematode intestinal colonization. Mol Microbiol **58**:28–45.

38. **Orchard SS**, **Goodrich-Blair H**. 2004. Identification and functional characterization of a *Xenorhabdus nematophila* oligopeptide permease. Appl

Environ Microbiol **70**:5621–7.

39. **Heath-Heckman EAC**. 2016. The Metronome of Symbiosis: Interactions Between Microbes and the Host Circadian Clock. Integr Comp Biol **56**:776–783.

40. **Zinser ER**, **Kolter R**. 1999. Mutations Enhancing Amino Acid Catabolism Confer a Growth Advantage in Stationary Phase. J Bacteriol **181**:5800–5807.

41. **Park Y**, **Herbert EE**, **Cowles CE**, **Cowles KN**, **Menard ML**, **Orchard SS**, **Goodrich-Blair H**. 2007. Clonal variation in *Xenorhabdus nematophila* virulence and suppression of *Manduca sexta* immunity. Cell Microbiol **9**:645–656.

42. **Hussa EA**, **Casanova-Torres ÁM**, **Goodrich-Blair H**. 2015. The global transcription factor Lrp controls virulence modulation in *Xenorhabdus nematophila*. J Bacteriol **197**:3015–3025.

43. **Cao M**, **Patel T**, **Goodrich-Blair H**, **Hussa EA**. 2017. High levels of Xenorhabdus nematophila transcription factor Lrp promote mutualism with *Steinernema carpocapsae* nematode hosts. Appl Environ Microbiol **83**:17.

44. **Cao M**, **Goodrich-Blair H**. 2017. Ready or Not: Microbial Adaptive Responses in Dynamic Symbiosis Environments. J Bacteriol JB.00883-16.

45. **Hwang H**, **Lu H**. 2013. Microfluidic tools for developmental studies of small model organisms--nematodes, fruit flies, and zebrafish. Biotechnol J **8**:192–205.

46. **Unger MA**, **Chou H-P**, **Thorsen T**, **Scherer A**, **Quake SR**. 2000. Monolithic Microfabricated Valves and Pumps by Multilayer Soft Lithography. Science **288**.

47. **Chung K**, **Zhan M**, **Srinivasan J**, **Sternberg PW**, **Gong E**, **Schroeder FC**, **Lu H**. 2011. Microfluidic chamber arrays for whole-organism behavior-based chemical screening. Lab Chip **11**:3689–97.

48. **Chung K**, **Crane MM**, **Lu H**. 2008. Automated on-chip rapid microscopy, phenotyping and sorting of C. elegans. Nat Methods **5**:637–643.

49. **Wang J**, **Kim SK**. 2003. Global analysis of dauer gene expression in Caenorhabditis elegans. Development **130**:1621–1634.

50. **Husson SJ**, **Schoofs L**. 2007. Altered neuropeptide profile of Caenorhabditis elegans lacking the chaperone protein 7B2 as analyzed by mass spectrometry.

51. **Khanna A**, **Kumar J**, **Vargas MA**, **Barrett L**, **Katewa S**, **Li P**, **McCloskey T**, **Sharma A**, **Naudé N**, **Nelson C**, **Brem R**, **Killilea DW**, **Mooney SD**, **Gill M**, **Kapahi P**. 2016. A genome-wide screen of bacterial mutants that enhance dauer formation in *C. elegans*. Sci Rep **6**:38764.

52. **Lambertsen L**, **Sternberg C**, **Molin S**. 2004. Mini-Tn7 transposons for site-specific tagging of bacteria with fluorescent proteins. Environ Microbiol **6**:726–732.

53. **Xu J**, **Hurlbert RE**. 1990. Toxicity of Irradiated Media for *Xenorhabdus* spp. Appl Environ Microbiol **56**:815–8.

54. **Vivas EI**, **Goodrich-Blair H**. 2001. *Xenorhabdus nematophilus* as a model for host-bacterium interactions: *rpoS* is necessary for mutualism with nematodes. J Bacteriol **183**:4687–93.

CHAPTER 5

Developing low-cost and easy-to-use microfluidic systems for K-12 classroom use

Adapted from:

M.D. Stilwell*, J.F. Nepper*, E.D. Clawson, V. Blair, T. Tangen, D.B. Weibel. Exploring predatory nematode chemotaxis using low-cost and easy-to-use microfluidics**.** *Am Biol Teach*. 2017; 79

and

E.D. Clawson, V. Blair, J.F. Nepper, M.D. Stilwell, T. Tangen, D.B. Weibel. Laboratory activity using accessible microfluidics to study nematode behavior in an electric field. *Submitted.*

* denotes equal contribution

MDS and JFN designed and conducted experiments, analyzed data, and wrote the first paper and analyzed data and wrote the second paper. EDC and VB, designed and conducted experiments, analyzed data, and wrote the second paper and analyzed data and wrote the first paper. TT and DBW wrote the first and second papers.

ABSTRACT

Microfluidic devices are used in a broad range of technology applications from creating ingredients for cosmetics to discovering new medicines. The small size of microfluidic channels makes it possible to isolate individual cells and multicellular organisms and study their biology, ecology, and behavior. Ecological studies are challenging to implement in K-12 classrooms because they often require multiple organisms (often very different in size) and complex environments that are difficult to replicate accurately (e.g., soil composition, temperature, pH, and humidity). These factors can make it difficult to quantitatively study changes in ecosystems. Microfluidics offers a solution to some of these challenges by enabling ecological systems to be simplified and controlled. However, a challenge with conventional microfluidic devices is that they are difficult and expensive to make, which has been a barrier for their entry into curricula and classrooms. We describe a simple and low-cost method for creating microfluidic devices that is designed for K-12 teachers and students and uses common materials. We use these devices to quantitatively study the behavior of nematodes in response to electrical and chemical cues. Nematodes are ecologically and agriculturally important organisms that respond to various environmental cues. In this activity, we demonstrate that nematodes swim through liquid in microfluidic channels in response to an applied electric field and chemical cues and describe the outcome of these activities on students.

INTRODUCTION

Symbiosis—the interaction between different species—is found in every ecosystem studied to date (1). To fully understand an ecosystem, one must look at all of the interacting partners to see how the actions of one species affect another. Most well-known examples of these interactions—e.g., sea anemones and clown fish (2, 3), or oxpecker and rhinoceros—are difficult to bring into a classroom (4). Microbes, on the other hand, are usually inexpensive and easy to acquire and grow. However, the small size of microbes (typically 1-50 microns) can make them difficult to study, especially when microscopes are not available. Nematodes (roundworms) are a terrific organism for studying biology in the classroom, as they are large enough to see with the naked eye (~1 mm), are not dangerous, are inexpensive, easy to acquire, and display a number of responses to environmental stimuli. They are also involved in several interesting interactions with other organisms, making them ideal for studying symbiosis.

Nematodes have adapted to almost every ecological niche on the planet, and are so abundant that four out of five animals on the planet are nematodes (5). Nematodes form mutualistic (mutually beneficial) relationships with bacteria to acquire nutrients. While numerous species are animal or plant parasites, many nematodes and their bacterial symbionts are useful for insect pest control in agriculture, making them excellent model organisms for academic studies of symbiosis (6, 7). For example, the soil-dwelling, entomopathogenic (insect-eating) nematode *Steinernema feltiae* forms a

symbiotic relationship with the bacterium *Xenorhabdus bovienii*, which helps it kill and digest its insect prey (8). *S. feltiae* navigates through soil towards its prey by responding to concentration gradients of chemical signals, or chemoeffectors, released by their insect prey in a process called chemotaxis (*chemo*, as in chemical; *taxis*, as in movement) (9). *Steinernema* nematodes respond to other environmental cues, such as carbon dioxide and electric fields (6, 10). Movement in response to electrical fields, or electrotaxis, differs from one species of entomopathogenic nematode to the next, with some moving towards the cathode, some moving towards the anode, and others displaying no net response (11).

Nematodes can infect a wide range of hosts, including insects, plants, and mammals (12). Entomopathogenic nematodes, such as *S. feltiae,* can infect and consume a wide range of insects (13). *S. feltiae* has a mutualistic relationship with the bacterium *Xenorhabdus bovienii*, which they carry in specialized pockets in their intestines (8, 14). *S. feltiae* senses chemical compounds produced and released by the insect prey and uses this information to track prey (Figure 1) (9). After catching its prey, the nematode burrows into natural openings in the insect such as its mouth, anus, or spiracles (breathing openings) (15). Once inside, nematodes release their symbiotic bacteria, which multiply and produce toxins and other compounds that kill and help digest the insect, which is then eaten by the nematode and the bacteria to provide energy for survival and reproduction. After the insect nutrients are depleted, the nematodes re-

associate with the bacteria, exit the insect cadaver, and traverse the soil in search of their next insect prey (Figure 2) (15).

It is easiest to study nematodes when their movement is confined. We use small microfluidic channels to accomplish this. These channels are shallow enough that their motion is essentially limited to two dimensions, making them easier to observe (16). Microfluidics experiments use very small volumes of fluids (down to 10^{-18} liters) in channels that have a width or height that is on the scale of micrometers (1 micrometer is one millionth of a meter) (17). Scientists and engineers use microfluidic technologies to reduce the size, cost, and materials needed for experiments ranging from chemical synthesis to DNA sequencing (18-20). The constraint imposed by microfluidic channels creates a phenomenon referred to as laminar flow (see goo.gl/BxIHNf for a demonstration of this property). Fluids exhibiting laminar flow move in 'sheets', which differs from the turbulent flow that is often observed in mixing fluids (Figure 3)(21). Laminar flow can be used to manipulate fluids very precisely(17).

Microfluidics is a powerful method to study chemotaxis, but traditional methods for creating microfluidic channels are often very expensive and require resources that are not commonly available (22). We use a technique that requires only inexpensive office supplies (double-sided adhesive and transparency sheets) and a craft cutter. Using open source vector graphic design software, we created layouts of microfluidic channels for different experiments and cut them into the adhesive craft paper using a

desktop craft cutter. Cutting and assembling a single device takes ~5 min. Using these microfluidic channels, we demonstrate an easy way to measure the response of nematodes to various chemicals and electrical fields. Using this approach, students can ask whether nematodes swim toward or away from different chemicals—including those released by insects. This gives them the tools to answer fundamental ecological questions about nematode behavior; in this case, how the nematode *S. feltiae* identifies and hunts insect prey.

The techniques presented in this chapter demonstrate how students can use simple and reusable microfluidic devices to study nematode behavior in response to electrical fields and chemical gradients. As the reason for the movement of nematodes in electric fields is not currently known, this activity provides an opportunity for students to propose hypotheses and potentially test them in subsequent experiments. These devices also enable students to experiment with different chemicals and measure the response of the nematodes to these chemical cues.

We field-tested the microfluidic devices in outreach activities that included observing the laminar flow of fluids and the behavior of microorganisms in response to an electric field and in response to chemical gradients. We successfully cleaned and reused these microfluidic devices multiple times. This approach creates opportunities for K-12 teachers to use microfluidic devices in a wide range of classroom investigations, including: physics (e.g., studies of fluid flows at low Reynold's

numbers), chemistry (e.g., chemical gradients), and biology (e.g., biological behavior of microorganisms) (23). We demonstrate how microfluidic devices can be used to study the behavior of nematodes. Using the devices to study nematode behavior is an excellent way to explore key biological concepts, such as: biological systems and models and making predictions about organism behavior (NGSS 4).

MATERIALS AND METHODS

Materials

Item	**Examples**
Craft cutter	Cricut Explore, Silhouette Portrait
Double-sided adhesive paper	Elizabeth Craft Designs Clear Double-Sided Adhesive
Laser printer transparency sheets	Apollo Laser Jet Printer and Copier Transparency film
1 or 3 mL Luer slip tip syringes	Flinn Scientific #AP5389
Plastic transfer pipettes (OR variable volume micropipettes)	Flinn Scientific #AP1516
Beneficial nematodes (one or more of the listed species)	Fungus Gnat Control Nematodes (*S. feltiae*) Grub & Soil Pest Exterminator (*H. bacteriophora)* Flea & Fly Exterminator (*S. carpocapscae*) Nema Globe Grub Busters (*S. glaseri*)
Fresh waxworms	Any brand
Agar powder	Any brand
Alligator clips	Any brand

32-gauge titanium wire	Kanthal A1 Resistance Wire
Plastic tubing 3/16” inside diameter	Tygon B-44-3 PVC Beverage Tubing
3-mm hole punch	Cmxsevenday No.97C3 Metal Handheld 1-Hole Metal Punch, 1/8" Hole Size
Vector design software	Inkscape, Adobe Illustrator
Misc.: Masking tape, timers, food coloring, sodium chloride, 70% isopropanol, 5% acetic acid, 9V alkaline batteries, cheesecloth, water bath, mortar & pestle, hot glue gun	

Methods

Basic microfluidic device design and assembly

1) Download Basic Microfluidic Device or design microfluidic devices in vector graphic design software.
   a) If using the provided Basic Microfluidic Device file, skip to Step 2.
   b) Create two layers in the file: one for the double-sided adhesive paper piece and one for the transparency pieces; note that the main channels will be in the adhesive layer and access holes will be necessary in the top piece of the transparency. Make each layer a different color.
   c) Make the bottom transparency piece at least twice as long as the top transparency piece to create an extended handle, making it easier to carry and manipulate

under a microscope.

d) Ensure each piece of the device is a single object. An easy way to do this is to use the software feature that subtracts one shape from another and results in a single object. In the open-source Inkscape, this feature is called "Difference". If two objects are sitting on top of each other (even if they are grouped), they will be cut as two separate pieces; each file should contain a single design that is ideally created by using the subtraction feature. (Example: the circles for holes should be subtracted from the top rectangle, not just circles sitting on top of the rectangle.) Save your file in Scalable Vector Graphics (.SVG) format.

2) Upload the file (e.g., SVG format) into your cutting machine's cutting software (Cricut® Design Space, Silhouette Studio® Designer Edition, etc.)

a) It is possible to design microfluidic channels directly in the cutting software, although they are usually less detailed than vector design software and may lack the same level of precision.

b) If available, use a slower "intricate cuts" setting on the double-stick layer to improve the cutting resolution.

3) Prepare designs for cutting per the instructions on your particular cutter and cut the pieces.

a) Check and clean the cutting blade regularly, as the double-stick paper adhesive can accumulate on the blade and decrease the cutting efficiency.

b) The inlet and outlet holes can either be included in the cutting design, or can be punched out using a small-diameter (1/8" or smaller) hole punch on the top transparency after the adhesive piece is attached and before the bottom transparency is attached. The linked designs instruct the craft cutter to cut the access holes in the top transparency (Figure 4).

4) Assemble device.

a) Remove one side of the adhesive backing.

b) To ensure that the pieces line up exactly, align the two pieces next to each other along the short end (Figure 5A) and carefully roll the double-stick piece down onto the transparency (Figure 5B). There is just enough stickiness on the edge of the piece to keep it aligned properly while rolling the pieces down on each other.

c) Smooth out any bubbles and rub firmly on the edges of the channels.

d) Remove the other backing paper and repeat the steps above to align the remaining pieces and complete the assembly of the microfluidic device (Figure 5C, Figure 4B).

5) If pre-printed grids are desired, print out the bottom pieces with grids onto laser printer transparency sheets, and cut to size using scissors, a paper trimmer, or craft knife with a ruler. Some digital cutters have print-and-cut capability, where the cutter will cut along the pre-printed outlines of the bottom piece. Follow the

directions for your cutter. Alternately, grids can be printed separately on transparency and taped to the bottom of the device.

6) Using the microfluidic device to create a laminar flow profile (to check for leaks):
   a) Place drops of desired solutions on the inlet hole; ensure that the liquid covers the entire hole (Figure 6A). Adding different food coloring to each solution aids in visualizing the laminar flow profile in the channels.
   b) Place the syringe over the outlet hole, ensuring that the syringe completely covers the hole (Figure 6B). A piece of tubing cut with a flat end and added over the syringe tip (Figure 6C) helps create a tight seal with the device and makes it easier to ensure that the hole is entirely covered. This step is particularly helpful when working with younger students.
   c) Gently pull up on the syringe plunger until the two liquids have entered the larger chamber in the device (Figure 6D).

Preparing Microfluidic Devices to Study Nematode Electrotaxis

As demonstrated previously (24), nematodes move in a predictable manner in an electrical field. This movement is dependent on nematode species and age, as well as the voltage of the electrical field. We demonstrate how to create an electrical field in the microfluidic device and observe how nematodes respond to this field.

1. Download Nematode Electrotaxis Device, or design your own. Make and assemble device as described above (Figures 4, 5, 7A, 7B).
2. Nematodes are shipped either in a small bag of sand, or with sand in a sponge. Depending on your situation, prepare a nematode suspension as below:
    a. Sand Extraction:
        i. Place a piece of cheesecloth (2-4 layers) over a shallow dish.
        ii. Place a square of delicate task wipe over the cheesecloth (most paper towels are too thick for this, though a strong facial tissue could be used if delicate task wipes are not available). Center the wipe over the dish. (Figure 8A)
        iii. Scoop out ~1 cm^3 of the nematode-containing sand and place into the center of the wipe. (Figure 8B)
        iv. Add water to the sand until all of the sand is dissolved. (Figure 8C). Let sit for 10-15 min, making sure sand does not dry out.
        v. Carefully gather the corners and edges of the wipe and cheesecloth and gently squeeze all the water out of the sand. (Figure 8D)
        vi. Tilt the dish up so the water sits at one end of the dish (Figure 8E). Let sit for 10-15 min. The nematodes will swim down to the bottom of the dish.

vii. Concentrate the nematodes by centrifuging 900 µl taken from the bottom of the dish above for about 10 sec. in a microcentrifuge. If a microcentrifuge is not available, the nematodes will migrate down to the bottom of the tube if left sitting for 20-30 min.

viii. Remove 600 µl of the supernatant and resuspend the nematodes in the remaining 300 µl. Proceed to Step 3.

b. Sponge Extraction:

i. Place the nematode-soaked sponge in room temperature tap water in a shallow container (Figure 8F).

ii. Allow nematodes to swim out of the sponge without squeezing the sponge. Squeezing the sponge may release the sand they are packaged with, which can clog the microfluidic channels.

3. Prepare a 2% agar solution with 0.01% sodium chloride. The salt increases the electrical conductivity of the agar. Aliquot into smaller volumes for ease of use (Figure 7C). Keep the agar in a liquid state at 50°C in a heat block or water bath. We were able to keep the agar sufficiently melted in hot tap water (Fig. S4D). This temperature is low enough to not cause nematode distress, but high enough to keep the agar melted.

4. Make electrode leads out of the titanium wire by bending a 5 cm piece of wire in half, and twisting to create a very small loop at one end that will fit into the

inlet/outlet holes of the device. Twist all the way to the end of the wire, then bend the free end over to create another, larger loop to use as an attachment for the alligator clips. Secure the ends by twisting them down tightly (Figure 9A).

5. Immediately prior to loading the devices, mix 3 parts nematode preparation to 1 part agar. We used 300 L nematodes to 100 L agar. Mix quickly and thoroughly by pipetting.
6. Promptly load the microfluidic device by placing a drop of the nematode/agar mixture on the inlet hole of the device (Figure 9B). Before the agar cools and solidifies, use the syringe to pull the nematodes into the device. Take care not to pull all the nematodes out the other end (Figure 9C).
7. After loading the devices, carefully insert the small, single-wire width loop of the titanium electrode leads into each of the inlet/outlet holes in the device, such that part of the small loop is partially out of the hole (Figure 9D). Use a small piece of masking tape to tape the leads to the device (Figure 9E).
8. Refer to the main text for the next steps of performing the experiment.

Preparing Microfluidic Devices to Study Nematode Chemotaxis

1. Assemble the microfluidic channels as described above and shown at https://youtu.be/BDFWlELvzJo. Cut the channels out of the double-sided adhesive, as well as the top and bottom out of the transparency sheet. Remove

the paper backing from the double-sided adhesive and attach to the smaller transparency. Ensure holes are cut out of the transparency either by the craft cutter or manually using the 3 mm hole punch. Remove the paper backing from the other side of the adhesive and adhere to the larger transparency (Figure 10). Push all layers together from end-to-end to avoid creases.

2. To create the chemoeffector reservoir and syringe adapter, cut two 0.5-0.75 cm pieces of tubing (we use Tygon PVC tubing, SAE, 3/16″; inside diameter, ¼″ outside diameter, 1/32″ wall). Hot glue one piece of tubing to one inlet to create a reservoir to hold the chemoeffector (Figure 10). Attach the other piece of tubing to the tip of the syringe to make pulling the solutions into the channel easier. Use caution with the hot glue to avoid burns. Avoid sealing the access holes to the microfluidic channel.
3. Prepare the chemoeffectors as outlined below

   Attractant: Waxworm extract. Use the mortar and pestle to grind five (5) frozen waxworms (freeze waxworms while they are fresh). Suspend the waxworm mash in 3 mL of 70% isopropanol. Prepare a twenty-fold dilution (e.g., 1 mL mash + 19 mL water) from this solution using water. Add food coloring to visualize the liquid. (Note: if sacrificing insects is not acceptable for the experiment, chemically pure chemoeffectors can be purchased from scientific supply companies.)

Repellant: Acetic acid (vinegar). Make a solution of 5% acetic acid in water (or use white vinegar, which is ~5% acetic acid in water) and add a second color of food coloring to visualize the liquid.

Control: Water. Add a third color of food coloring to visualize the liquid. Adding different colors to the solutions will make it easier to see the laminar flow profile and clarify that the channel is working as expected.

4. Suspend the nematode sponge in ~100 mL water, or half of a sponge in ~50 mL water.
5. Melt a 2% agar solution and keep warm in a water bath (approximately 55 °C). For ease of viewing, add a fourth color of food coloring.
6. For each experiment, prepare three microfluidic channels, one for attractant, repellant, and control, as outlined above, along with the 1 mL syringe connected to the extra piece of tubing and some sort of pipet.
7. Load a chemoeffector solution into the inlet tubing (as in Figure 11b). Meanwhile, mix the nematode suspension with the 2% agar solution in a 3:1 ratio, so that the final agar concentration is 0.5% (e.g. 0.5 mL of the nematode suspension with 1.5 mL of the 2% agar solution). Immediately after mixing, pipet the nematode-agar mixture onto the other inlet hole (as in Figure 11c). As soon as the nematode solution covers the inlet hole, quickly and gently draw the two solutions into the channel using the tubing-tipped syringe placed at the outlet

hole (as in Figure 11d). Note that the agar solution cools quickly, so this step needs to be performed quickly.

8. Repeat step 7 for the other two microfluidic channels and conditions.
9. Image the channels using a microscope. Record the number of nematodes in each side of the channel over time (e.g., 5, 10, 15 minutes). To quantify the nematode response to the chemoeffector, use the following equation to calculate the "chemotaxis index" (CI):

$$\mathrm{CI} = \frac{\#\ nematodes\ on\ chemoeffector\ side}{total\ \#\ of\ nematodes\ in\ device}$$

A chemotaxis index of 1 indicates that the chemical was a strong chemoattractant and a value of 0 indicates a strong chemorepellant.

Cleanup and disposal

Microfluidic devices and syringes can be easily cleaned and reused. To do so, flush the channel with hot water by pressing a water stream up to one of the inlet/outlet holes or soak the device in hot water, loosen and extract the agar with the syringe, and then flush with plain water. Syringes should also be flushed with hot water to remove any agar. Note that the agar/nematode mixture cannot be re-melted once it has solidified without killing the nematodes. The 2% agar solution with 0.01% sodium chloride can be saved and reheated. We recommend only mixing small amounts of agar and nematodes

as needed. The nematodes used here are naturally occurring, soil-dwelling nematodes and are not harmful to humans. They can be disposed of down the drain or in regular trash.

RESULTS

Method Development

Microscopic organisms move differently from larger ones (25). *Steinernema* nematodes move by pushing their body against solid objects, which makes it difficult to observe nematodes swimming in water (26). We filled channels with an agar solution, which produces a transparent gel in which the worms can swim (27). To form the gel, the agar solution must be boiled before allowing it to cool. We found the nematodes could survive brief exposure to the high temperature of the solution of melted agar, and after the gel set the nematodes could easily swim through the gel. The agar solution cools and solidifies rapidly, so filling the channels may require a level of coordination that is too challenging for elementary school students.

We designed two microfluidic systems, one for measuring chemotaxis and one for measuring electrotaxis. The chemotaxis device consisted of two straight inlet channels (with inlet holes) intersecting with a single central channel and ending in an outlet hole (the channel system looked like the letter 'Y'). The electrotaxis device consisted of a rectangular channel with thinner channels extending out opposite sides and leading to inlet holes. We used three layers of material to form the channels (Figure 10): 1) a layer of double-sided adhesive tape with the channels cut into it; 2) a top layer of transparency film forming the channel 'ceiling' with the shape and dimensions of the adhesive tape (this layer contained the inlet and outlet holes); and 3) a bottom layer of

transparency film forming the channel 'floor' with the shape of the adhesive tape but slightly longer to provide a handle. Note that if using laser printer transparency sheets, the bottom channel can be designed with 'ruler' lines to make counting nematodes in different areas of the device easier. We used a craft cutter to cut the channels out of the double-sided adhesive and to cut the top and bottom layers out of transparency sheets. We assembled the system by pressing a transparency film layer on each side of the adhesive, then hot gluing a small piece of Tygon tubing to one inlet (Figure 10). A microscope slide can be used instead of transparency film for the bottom layer of the channel if it makes visualization easier. A step-by-step video for device construction can be found at https://youtu.be/BDFWlELvzJo.

When using the chemotaxis device, we treated a section of tubing glued to the inlet as a reservoir for the chemoeffector, to ensure the channels would not become filled with air. We filled the tubing reservoir with our chemoeffector of interest while preparing for subsequent steps (note: if the tubing prevents the channel from fitting onto a microscope, the tubing can be removed after filling the channels by pulling it off or using scissors). After soaking the nematode-containing sponge in water, we mixed the nematode solution with the warm agar solution, pipetted it on the other inlet hole (without tubing), and drew the two solutions through the channel using a syringe positioned at the outlet (Figure 11). To create a better seal, we put a small piece of

tubing on the tip of the syringe. After a few minutes, the channel was moved to the microscope to visualize nematodes.

Our microfluidic chemotaxis system differs from those reported previously in a seemingly small but important way: we do not load channels entirely with a solution of agar. Instead, we dissolve chemoeffectors in water (rather than in an agar solution) and use laminar flow to fill one half of the main channel with chemoeffector and one half with agar and nematodes. After the agar sets, half of the channel contains the agar gel and the other half of the channel contains the chemoeffector solution. There are two primary advantages to this approach. First, the channels are much easier for students to load when agar is added to only one of the two inlets because it cools and solidifies rapidly. We found this task to be difficult, so younger students would certainly have trouble correctly loading two inlets worth of channels, which isn't an issue for the electrotaxis device as students only need to worry about one inlet for that device. Our second reason for loading chemoeffectors in water is that the nematodes swim well in the agar gel but not in the liquid, so chemotaxing nematodes are essentially trapped if they move to the chemoeffector side. This makes counting the worms easier. We have not observed any nematodes swimming into the chemoeffector area (liquid side) when a repellant is present, so we believe false positives are unlikely. We filled the electrotaxis device fully with agar so that nematodes could swim more easily throughout the entire device.

To test our chemotaxis system, we compared the nematodes' responses to an attractant (waxworm extract), a repellant (acetic acid: i.e., vinegar), and water (a control). In each experiment, we observed 4-12 nematodes in the main channel (note that the amount of water used to soak the nematode sponge can be adjusted to increase or decrease the number of worms suspended in liquid in each channel). To quantify the nematode response to each chemical, we calculated the "chemotaxis index" (CI) using the following equation:

$$\mathrm{CI} = \frac{\#\ nematodes\ on\ chemoeffector\ side}{total\ \#\ of\ nematodes\ in\ channel}$$

According to this equation, a perfect repellant will create a CI of 0 and a perfect attractant will yield a CI of 1. After performing the experiment in triplicate, we found that the waxworm extract yielded a CI of ~0.71, the vinegar yielded a CI of ~0.03, and the water yielded a CI of ~0.14 (see Table 1 for individual experimental values, or Figure 12 for a photo of the channels and quantification of the nematode response). (Note that ideally, as a control, water would yield a CI of 0.5). We found that adding food coloring to the chemoeffector solution greatly helped us visualize the boundary between the agar and the chemoeffector, and made it easier for us to see that both solutions were loaded into the channel. We also observed that the laminar flow profile in channels containing both the warm agar solution and the waxworm extract was not always evenly distributed, most likely due to the evaporation of the isopropanol in the

waxworm extract. An occasional 'wavy' boundary formed between the two solutions will not affect the outcome of the experiment.

To test the electrotaxis system, devices were loaded with nematodes suspended in a solution of agar. Once the agar filled the channels, the titanium electrodes were carefully inserted into both inlet holes. The device was placed under a microscope and taped to the microscope stage to keep it in place. The number of nematodes in each zone in the channels at time=0 was then counted (Figure 13). We performed this experiment with several groups of students. The students were allowed to choose how to count nematodes that may be positioned on the lines between zones, deciding to define them as either belonging to the zone to the right or to the left of the line, and using this counting approach consistently throughout experiments. Next, the titanium electrodes were attached to a 9V battery using alligator clips (Figure 14), such that the right lead was attached to the negative terminal, and the left lead was attached to the positive terminal. We measured the voltage across the channels to be 1.7-4.0 V with electrodes connected to a 9 V battery and channels filled with agar. Bubbles that may accumulate at the end of the channel connected to the negative terminal of the battery may disrupt the electric field and alter the directional movement of nematodes. After the battery was connected, students immediately started a timer and counted and recorded the number of nematodes in each zone every min for a total of 5-10 minutes.

In the Field

The chemotaxis experiment was completed by 76 middle school students lacking formal biology training. The students experienced this investigation in a field trip setting through Discovery Outreach Programs held at the Discovery Building at the University of Wisconsin-Madison. The teachers selected this workshop for their students from a number of other field trip options. To gain insight into the activity's impact on the students' enjoyment and engagement, we asked them to complete a short survey after the workshop. The survey was based on the learning activation surveys developed by Activation Lab (activationlab.org). The frame of reference for this survey was on looking at evaluative measures that would indicate how the activity impacted participants. The surveys were anonymous and optional. No identifying information was collected from the students and all responses were aggregated. Based on these attributes, Institutional Review Board staff deemed these evaluative measures to be exempt from IRB process.

We tested the electrotaxis activity successfully in several informal science lab activities for middle and high school students through Discovery Outreach Programs held at the Discovery Building at the University of Wisconsin-Madison. We used a customized version of the Science, Technology, Engineering, & Math (STEM) Learning Activation Survey (http://www.activationlab.org/), which assesses STEM learning activation in youth. Our customized survey focuses on self-reported engagement and a

brief analysis of the survey responses collected at the completion of the activity is summarized below (Figure 15). When asked to describe what they learned after the activity, select student responses mentioned nematode behavior, e.g. “I learned what nematodes are and how they react to certain variables,” and “I learned about the biology of a specific parasite”. Our activity is well suited for teachers to make connections to ecology-focused objectives in science curricula.

We found these activities to be a rich platform for collaboration and a reflection of the practices we do as scientists. For brevity, we aggregated responses from several questions addressing a similar concept (collaboration with others) into a single measure. (Figure 16a). When asked in anonymous surveys what they enjoyed most about the chemotaxis activity, more than half the students said “everything” or “we learned by doing things instead of listening the whole time”, while the rest “enjoyed being able to see the ways the nematodes reacted.” We observed students talking about what they were doing among themselves and working together to do the activity successfully, in much the same way that academic scientists collaborate in the research lab. Additionally, over 90% of the students reported that they asked questions, tried out new ideas, and discussed the experiment with their mentors and peers to aid their comprehension (Figure 16a). These are all hallmarks of a collaborative process that the activities framework provided.

The activities provided opportunities for high levels of engagement. 80-95% of the students' responses indicated that they were actively engaged and self-reported that they had learned something about science (Figure 16b). These activities can span engagement across age bands. We found these activities to be appropriate for students as young as 6th grade and can be adapted for students in high school and college by exploring the key concepts more deeply.

Entomopathogenic nematodes form relationships with bacteria that enable nematodes to infect and digest their insect prey. *S. feltiae* nematodes work with *X. bovienii* bacteria to obtain nutrients from prey insects. To learn more about the mutualistic relationship between *X. bovienii* and *S. feltiae*, students can create and study the behavior of "aposymbiotic nematodes" (ASN)—worms that lack bacterial symbionts. For a detailed protocol on making ASNs, see (28) (28). To confirm that the ASNs do not contain *Xenorhabdus*, students can grind up nematodes and inoculate them onto Luria-Bertani (LB) media plates and observe bacterial growth (29, 30). After obtaining ASNs, students can compare the ability of aposymbiotic worms to infect and kill prey insects versus bacteria-colonized nematodes (28).

DISCUSSION

Using simple, inexpensive, easy-to-make microfluidic channels, we demonstrated how students can identify and study environmental stimuli that alter the behavior of predatory nematodes, such as the chemicals that nematodes use in nature to track their prey and avoid danger. An important aspect of this activity is the engagement of students in the design of authentic scientific investigations. We often think of ecology on the scale of large animals and ecosystems, however this activity reinforces the importance of ecosystems of small animals and bacteria and enables teachers to investigate a complex and important ecological web using tools that are widely accessible and quantitative.

These activities can be expanded to fit within existing biology and environmental science curricula, as different aspects of symbiosis are reflected in this experiment: e.g., the mutualistic relationship between the worms and their symbiotic bacteria, as well as the pathogenic relationship between the worms and their insect prey. These concepts could fit in a curriculum studying bacteria, pathogens, chemical ecology, soil science, and insects. The activities can be modified to use different chemicals, voltages, temperatures, microfluidic channel shapes/designs, or species of nematode, and enables students to make predictions about the response of nematodes to those conditions.

Microfluidics makes possible the investigations described here because it imposes dimensions on liquids that bring out the unique laminar behavior of fluids.

Traditional methods for making microfluidic channels are tricky to incorporate into school activities because they require materials and facilities that are expensive and difficult to access. Our method uses inexpensive office materials, a craft cutter to pattern the double-sided adhesive and transparency sheets, and simple methods for assembly and introducing fluids. The ease of this method enables students to create and test new channel designs, and makes it possible to incorporate perspectives on engineering into lessons.

Educators will be able to incorporate the Educators Evaluating the Quality of Instructional Products (EQuIP) Rubric to measure the alignment to the Next Generation Science Standards (NGSS) to help determine which elements from these investigations connect to the science and engineering practices (SEP), disciplinary core ideas (DCI), and/or crosscutting concepts (CCC) of NGSS. The embedded tasks expected of students in these activities may demonstrate their proficiency of one or more performance expectations. For example, students develop and use SEPS, DCIs, and CCCs that fit within the EQuIP three dimensions framework. Teachers will need to identify the key CCCs relevant to their instructional framework so that students can translate specific information to general principles.

Looking deeper into the EQuIP (v3.0) rubric, there are intentional opportunities for students to explain phenomena and design solutions that are integrated into life science DCIs (MS-LS2-1,2,4 & HS-LS2-8) & and SEPs (MS/HS-ETS1). In particular, the

evidence statements reflected in NGSS HS-LS2-8 connect very well to the potential for students to develop a causal explanation on the group behavior dynamics of chemotaxing nematodes in microfluidic channels. Students will use science and engineering design practices in this activity and other potential investigations of ecosystems and inter-organism interactions.

ACKNOWLEDGEMENTS

We acknowledge funding that supported this project from the Dreyfus Foundation (SG-10-032), NSF (DMR-1121288, and predoctoral fellowship DGE-1256259 to J.F.N.), WARF (MSN193090), NSF (AISL-1241429), Madison Community Foundation (5947), and support provided by the Morgridge Institute for Research and the Wisconsin Alumni Research Foundation. We are grateful to Heidi Goodrich-Blair and Mengyi Cao for introducing us to this fascinating area of biology.

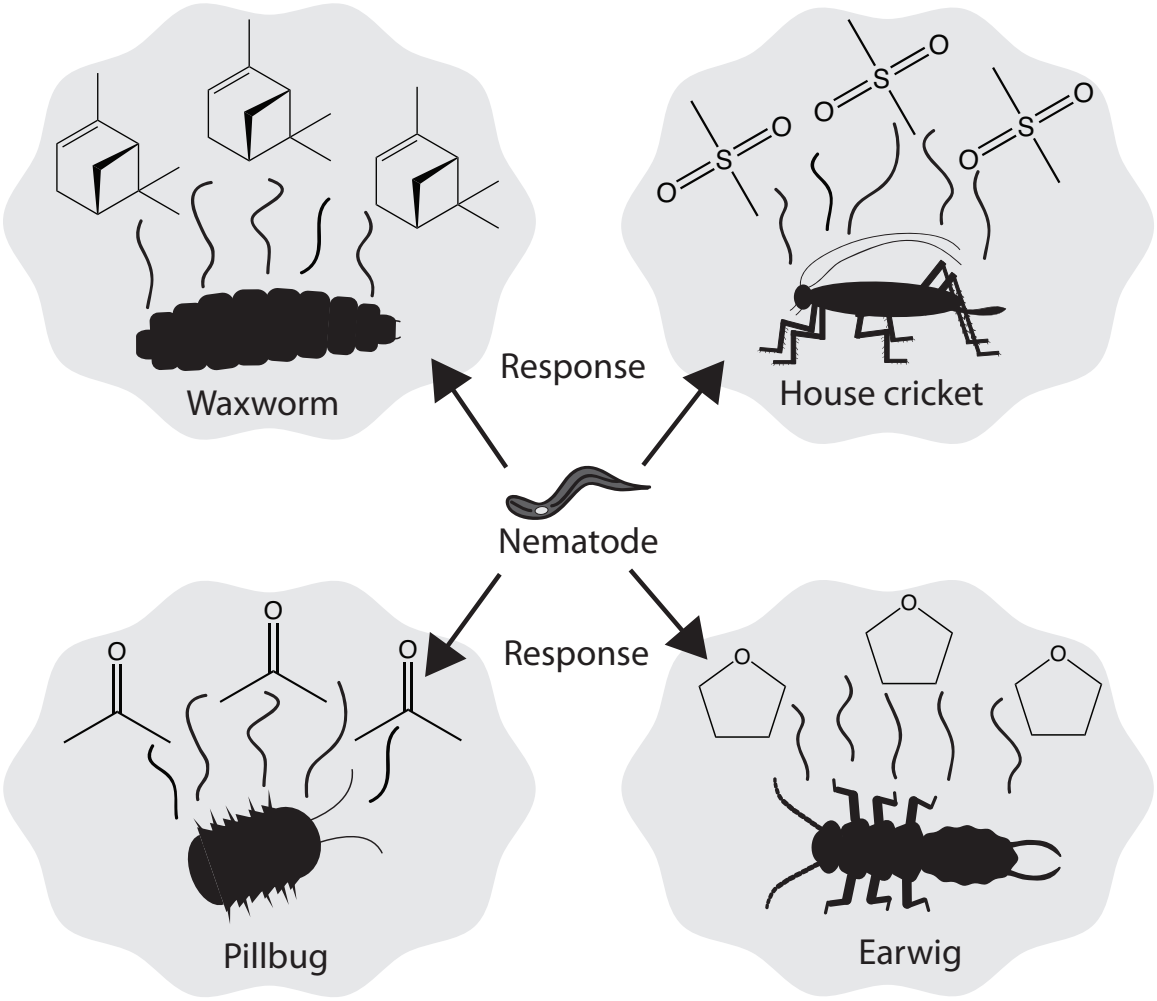

Figure 1: A cartoon depicting nematodes responding to chemical signals released by prey insects. Each prey insect produces and secretes multiple organic compounds that nematodes chemotax towards and use to hunt the insect. Wavy lines indicate production of volatile compounds. Examples of compounds shown are (from top left, clockwise): α-pinene, $C_{10}H_{16}$ (waxworm), dimethylsulfone, $C_2H_6O_2S$ (house crickets), furan, C_4H_8O (earwig), and acetone, C_3H_6O (pillbug). Note that while we only depict one compound for simplicity, insects release many organic compounds.

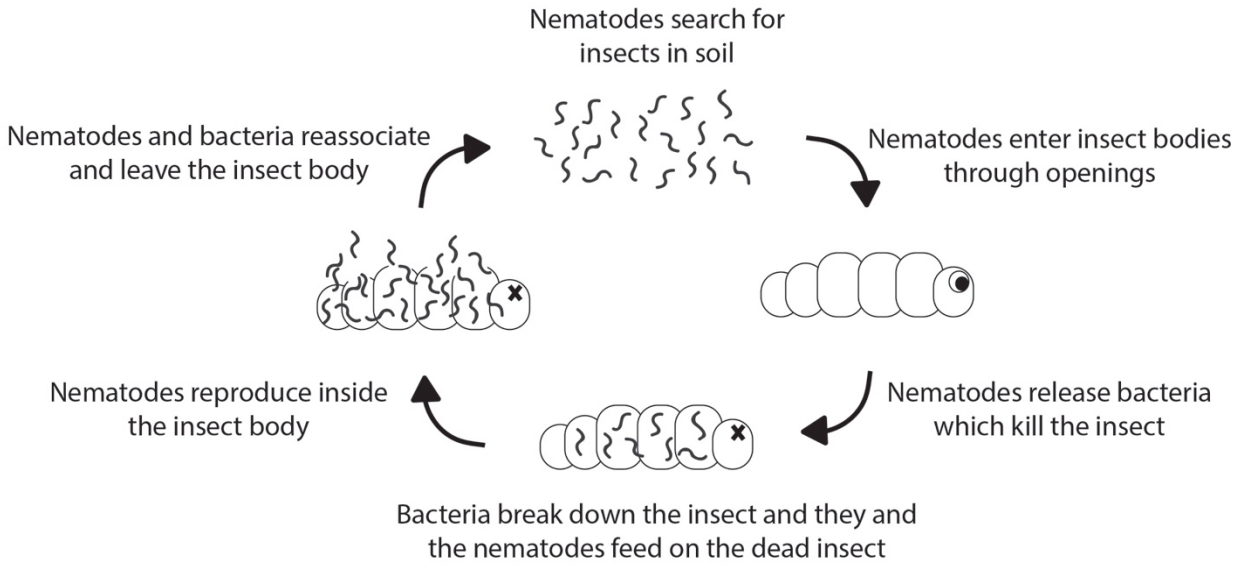

Figure 2: A cartoon depicting the life cycle of entomopathogenic nematodes. Nematodes traverse soil in search of insect prey, infect the insect, and subsequently release their symbiotic bacteria to kill the insect. The nematodes and bacteria feed on the dead insect until the nutrients are depleted, at which point they re-associate and exit the insect cadaver in search of new prey.

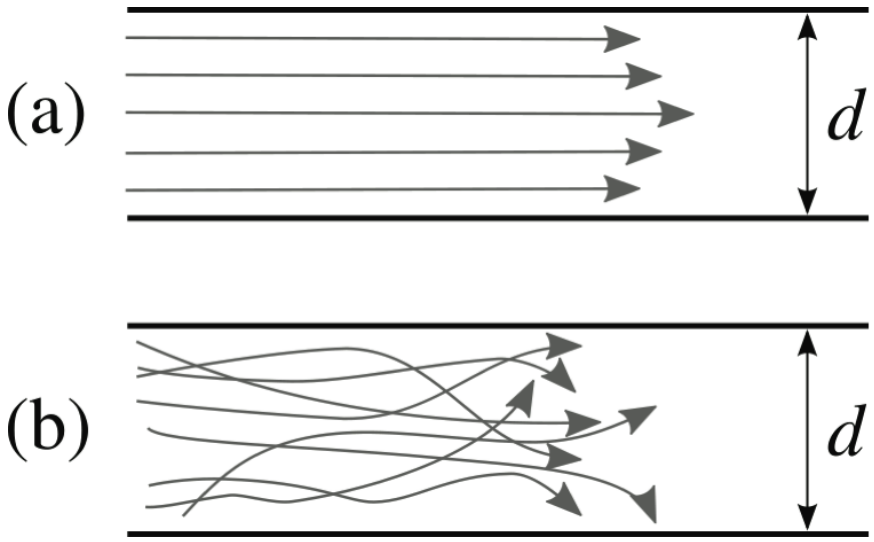

Figure 3: A depiction of laminar flow and turbulent flow. A) Laminar flow causes fluids to move in sheets such that the fluids only mix by diffusion. B) Turbulent flow causes fluids to readily mix and is the state we commonly observe when watching liquids. A convenient way to adjust between laminar and turbulent flow is by adjusting the diameter of a channel, '*d*'.

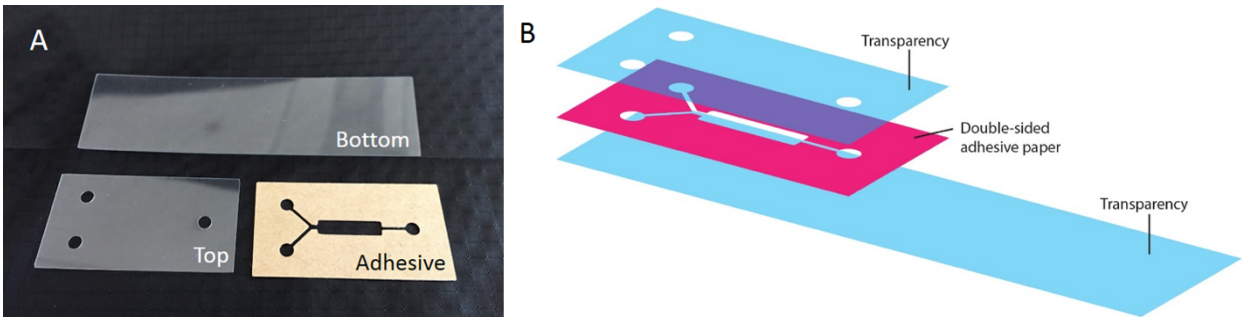

Figure 4: Schematic of a reusable basic microfluidic device. (A) Device components. (B) Device assembly diagram.

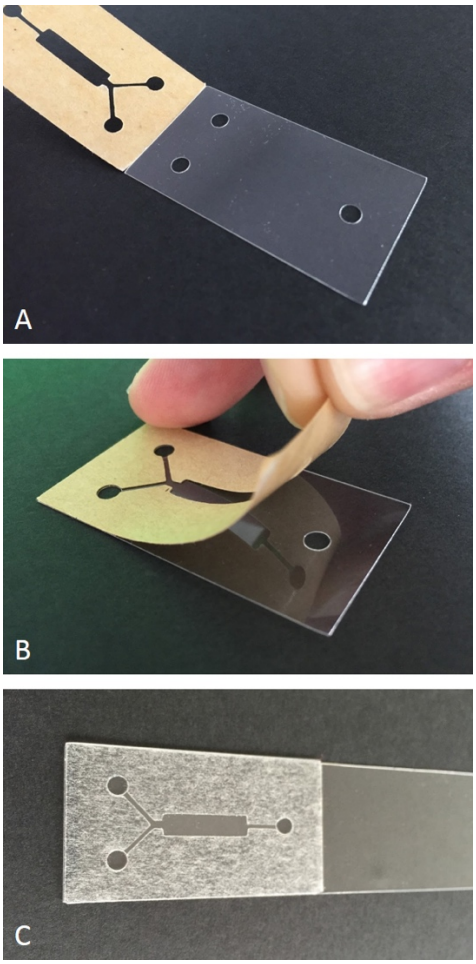

Figure 5: Step-by-step basic microfluidic device assembly. (A) Edges of "Top" and "Adhesive" device pieces lined up. (B) Rolling the adhesive side down onto the top transparency piece. (C) Image of a completed device.

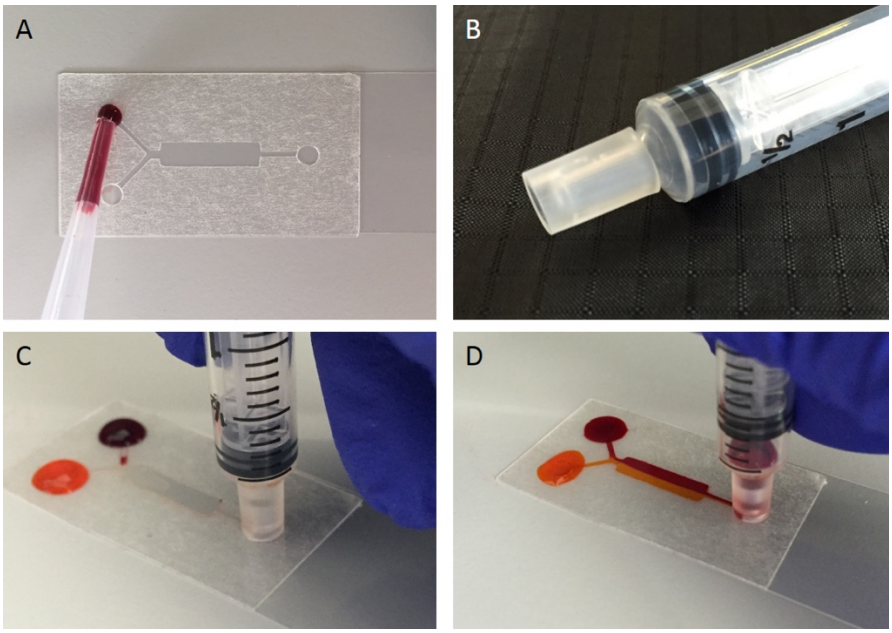

Figure 6: Filling of the basic microfluidic device channels. (A) Inlets are loaded with liquids using a plastic transfer pipet. (B) Tubing is added over a syringe tip to allow easier positioning. (C) The syringe is positioned over the outlet hole to create a seal. (D) Slowly drawing up the syringe plunger pulls liquid from the inlets into the central channel of the microfluidic device. The liquids display laminar flow in a microfluidic device.

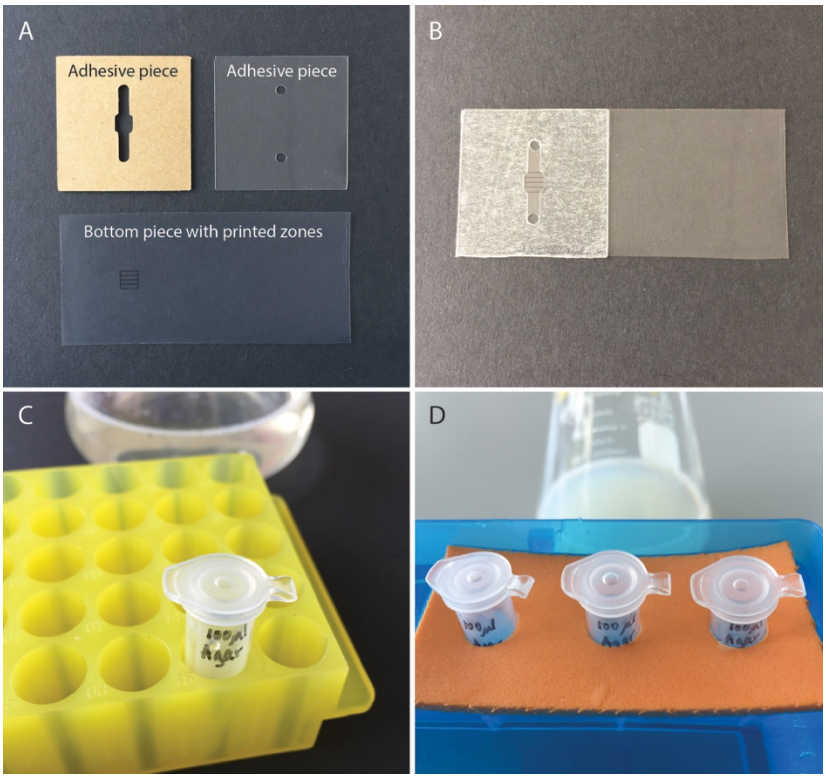

Figure 7: Material Preparations for Electrotaxis Activity: (A) Electrotaxis device pieces. (B) Assembled electrotaxis device. C) Agar solution and aliquot in microcentrifuge tube. (D) Agar solution aliquots in craft foam float in the hot water bath.

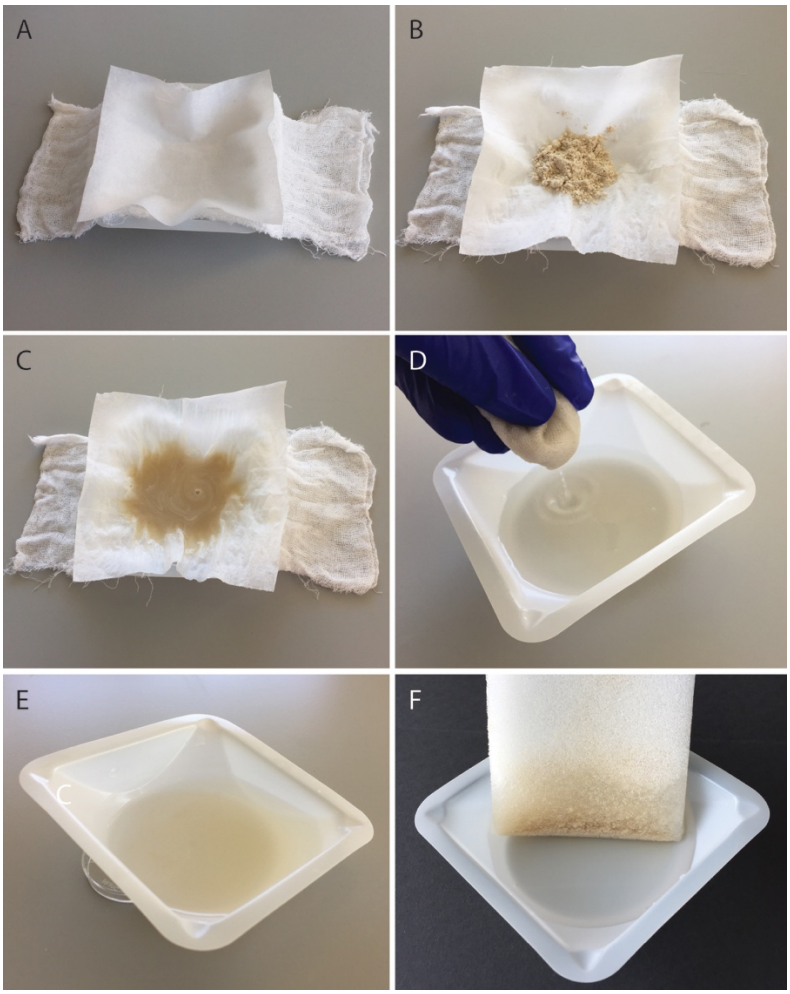

Figure 8: Nematode Extraction: (A) Delicate task wipe on top of cheesecloth in shallow dish. (B) Nematode-containing sand on wipe and cheesecloth in dish. (C) Sand dissolved in water. (D) Squeezing water out of cheesecloth. (E) Tilted dish to collect nematodes. (F) Nematode-containing sponge in shallow dish.

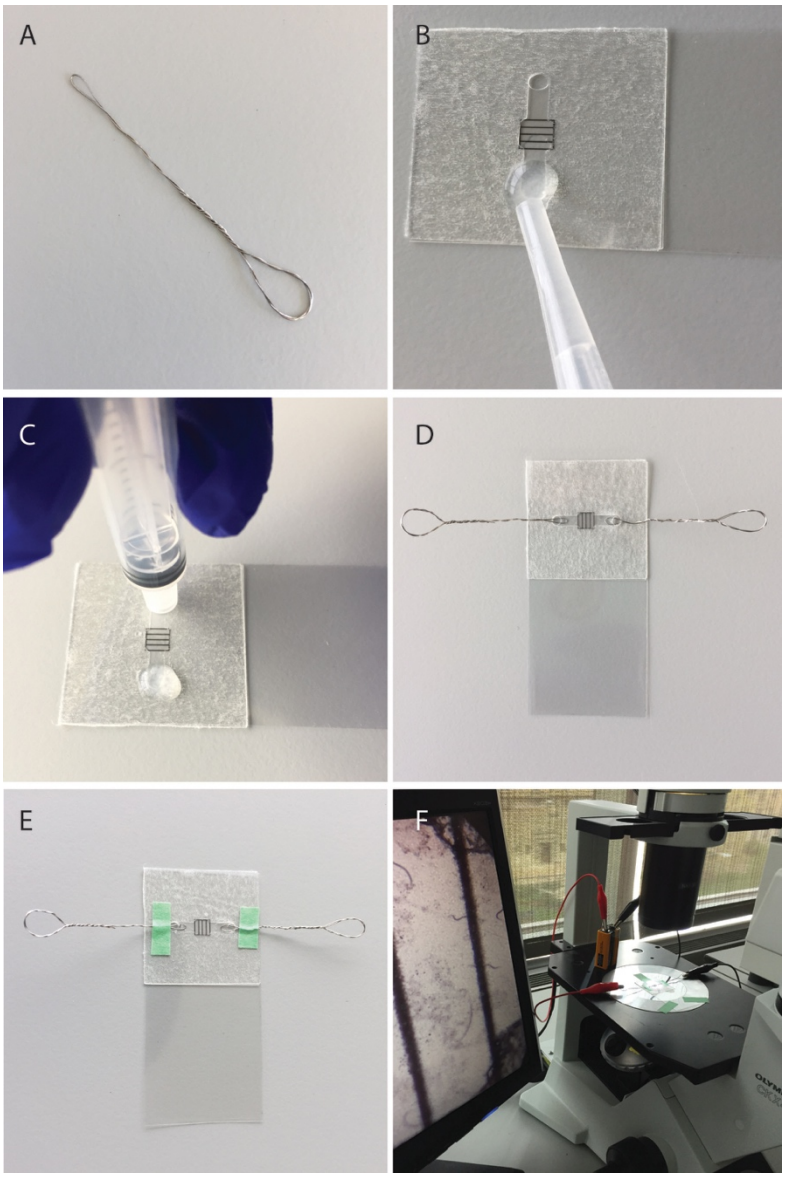

Figure 9: Loading Electrotaxis Device and Inserting Titanium Electrodes: (A) Titanium electrode. (B) Drop of nematode preparation onto device inlet hole. (C) Pulling nematodes into microfluidic device using syringe with tubing on the end. (D) Titanium electrodes inserted into inlet/outlet holes of microfluidic device. (E) Electrodes taped down onto microfluidic device. (F) Loaded microfluidic device taped to microscope

platform with alligator clips attached to a 9V battery. Screen to the left of the microscope shows magnification with 10X objective.

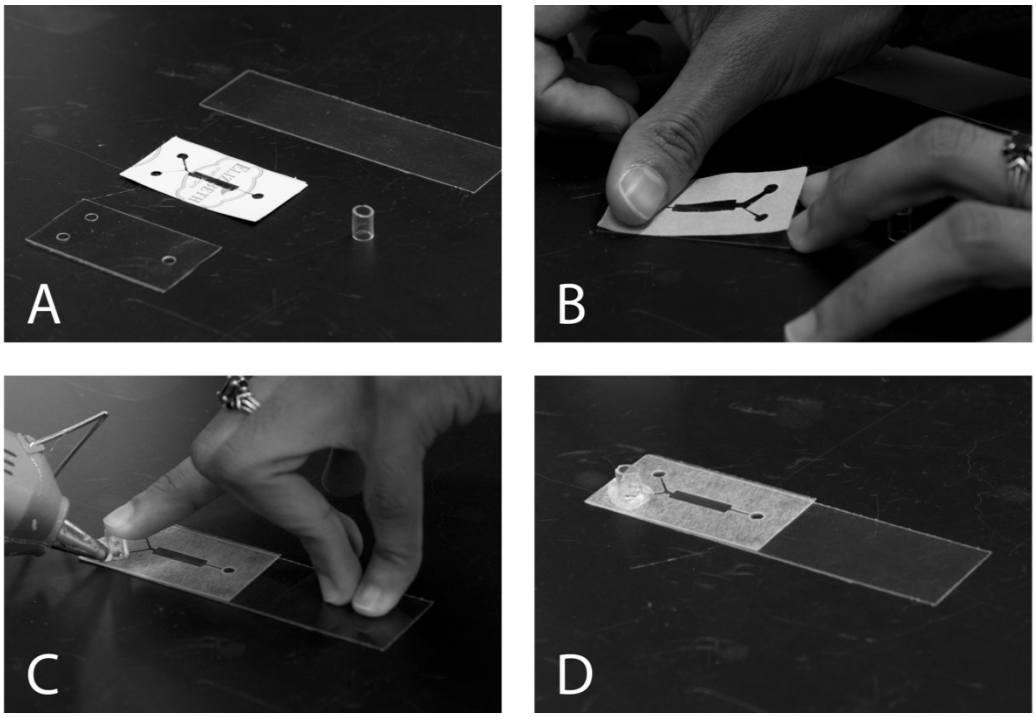

Figure 10. A sequence of photos showing the structure of the microfluidic channels and their assembly. A) The components of a single channel. B) Carefully aligning the adhesive with the smaller piece of transparency. C) After attaching the second transparency, the plastic tubing is hot glued onto only one inlet. D) The finished channel.

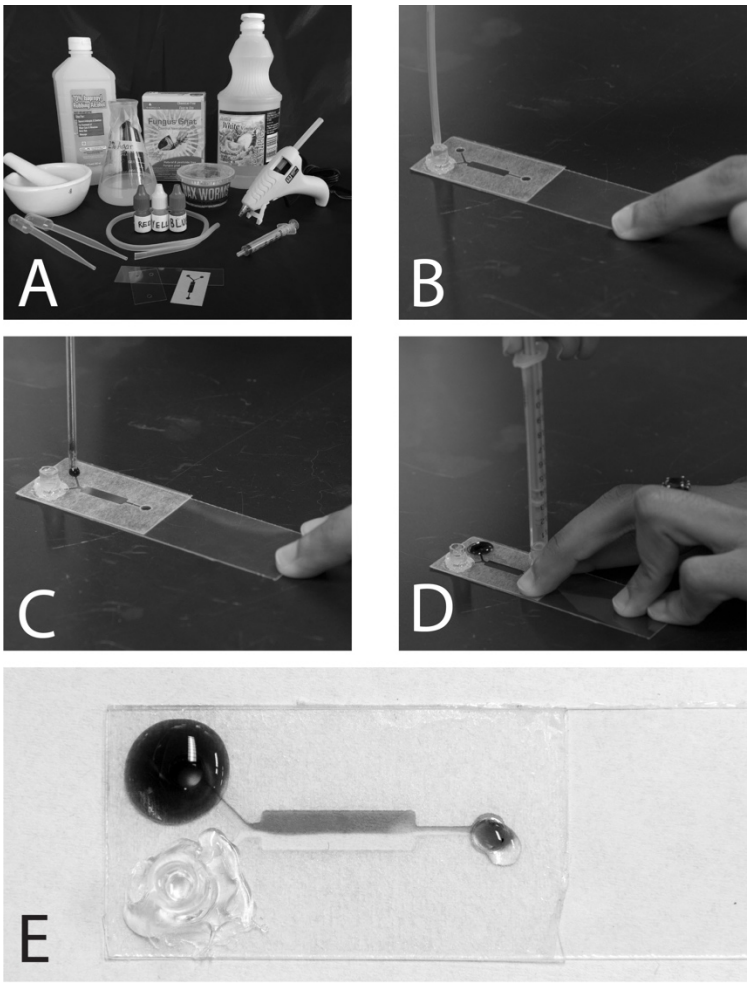

Figure 11: Set of images showing how the experiments are performed. A) An image depicting all of the materials required for this experiment. B) The tubing at one inlet is filled with chemoeffector. C) The agar is loaded into the other inlet. D) The fluids are drawn into the microfluidic channels using a tubing-tipped syringe. E) An image of the laminar flow profile.

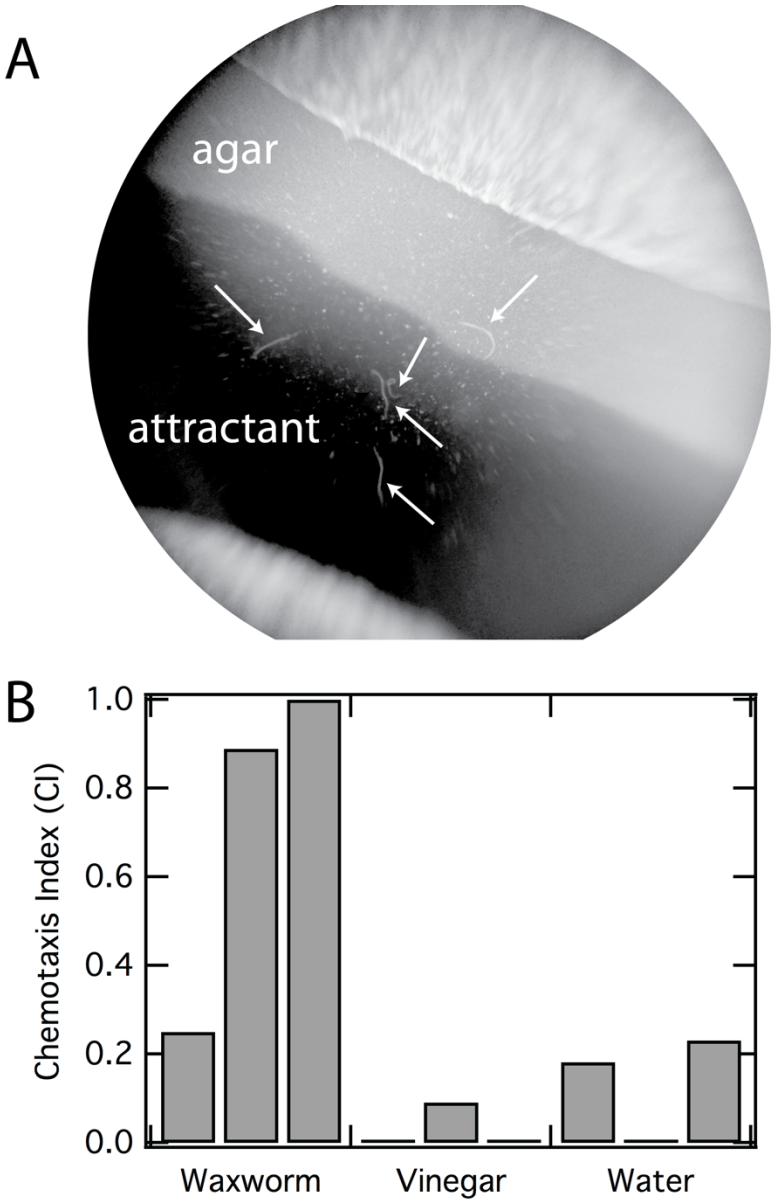

Figure 12: A) An image of 5 nematodes in a channel loaded with attractant (waxworm extract); the image was taken ~5 minutes after loading the chemoattractant using an LG® G3 smartphone and a platform microscope outfitted with the lens from a laser pointer (Tangen 2016). Arrows indicate live nematodes. B) Chemotaxis indices calculated from 3 separate experiments.

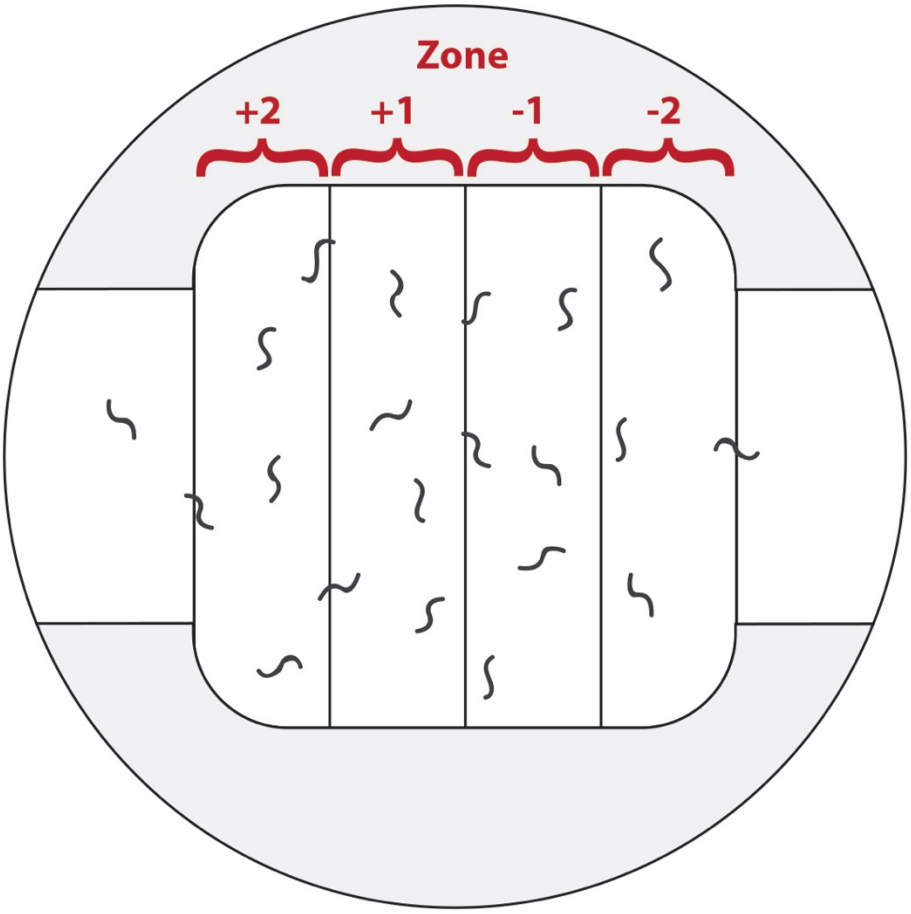

Figure 13: Diagram of nematodes in zones under microscope. Nematodes respond to an applied electric field by moving through different zones of a microfluidic channel.

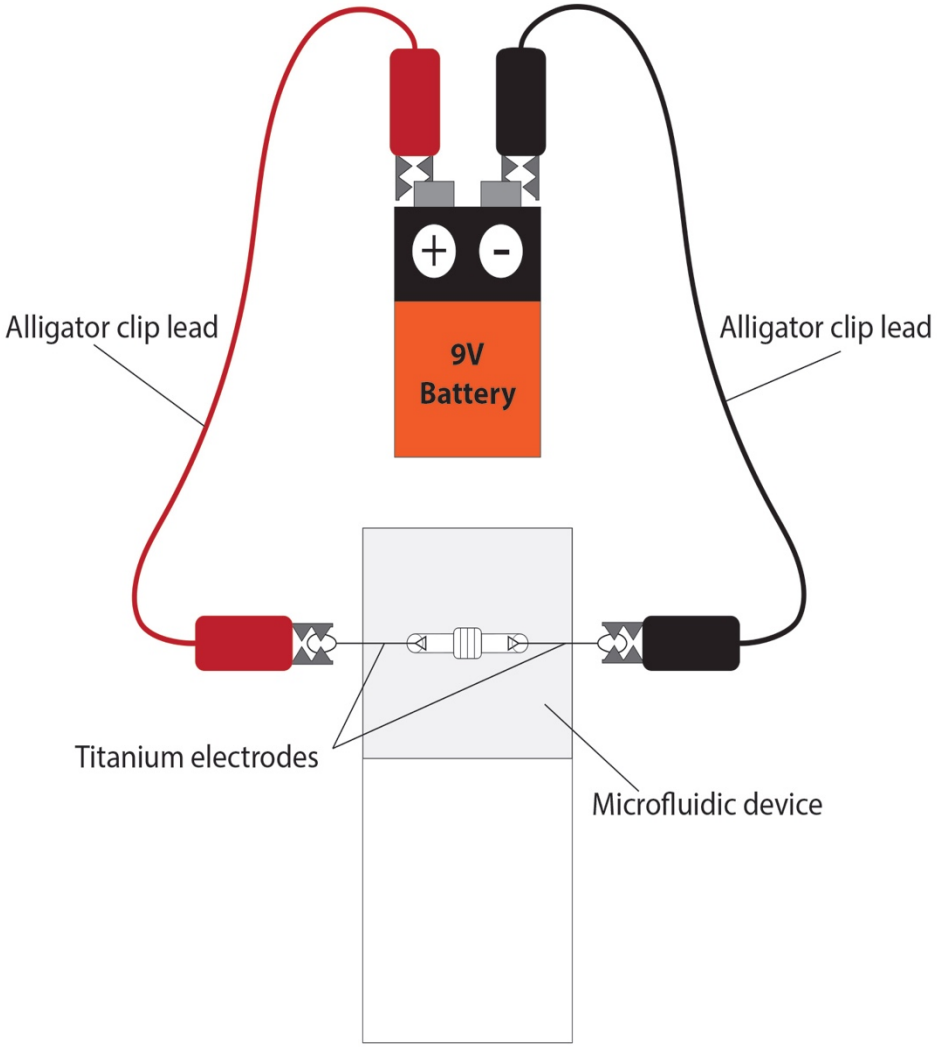

Figure 14: Microfluidic setup for the electrotaxis activity. A 9V battery supplies an electric field across a microfluidic channel.

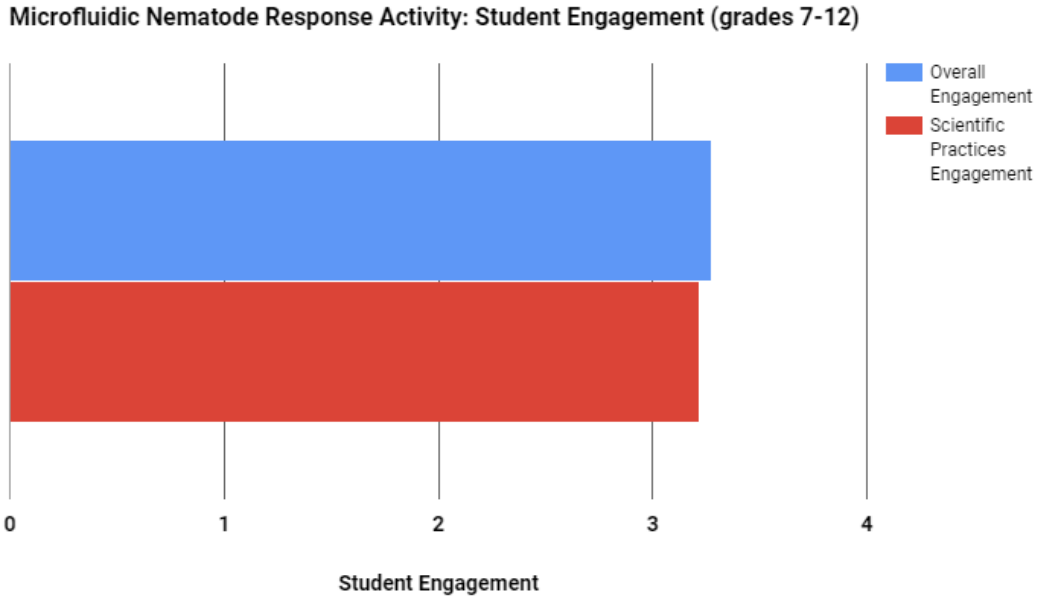

Figure 15: Analysis of student engagement (N=40). An engagement score of 3 or above is a high level of engagement based on the survey.

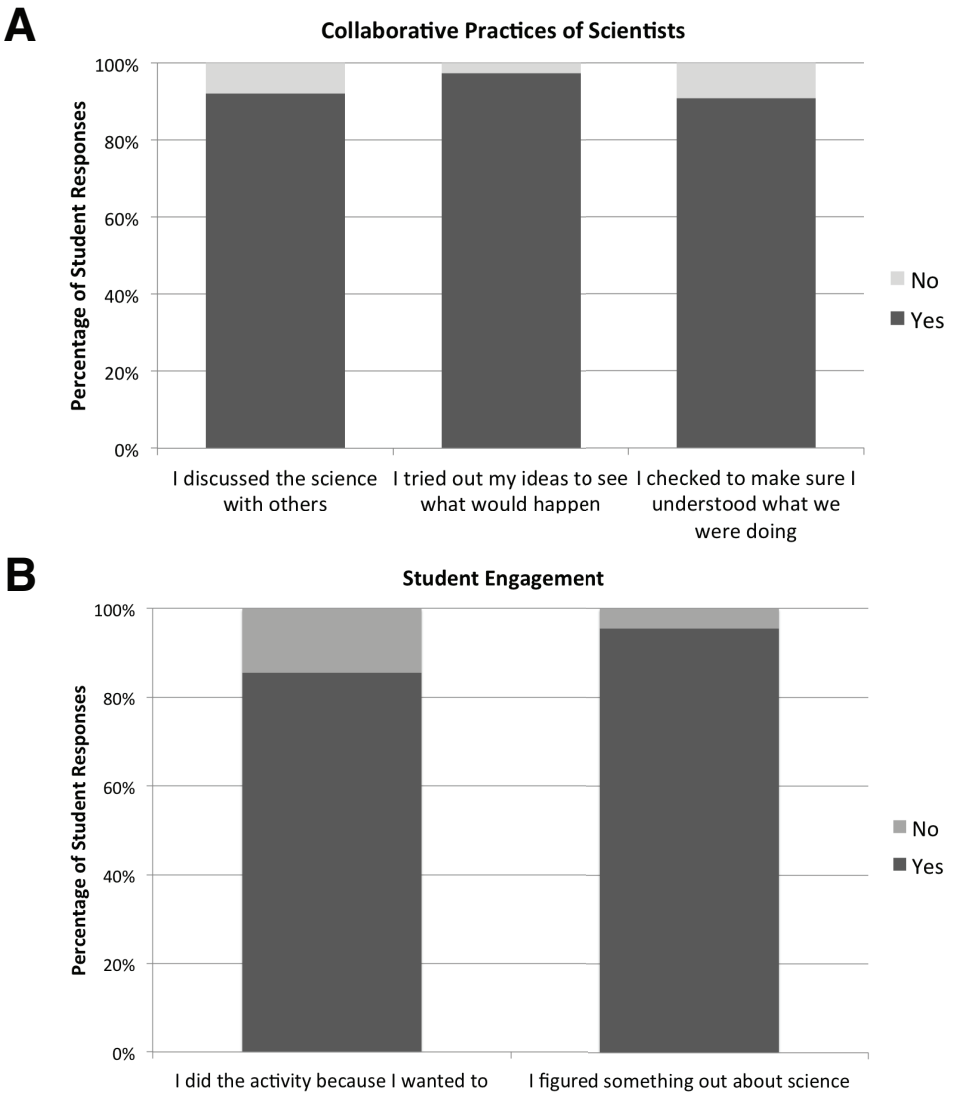

Figure 16: Student responses to survey questions regarding the activity. A) Student responses to questions concerning collaboration and exploration. N = 76. Students reported that they were actively checking their own understanding of the experiment. N = 22.B) Students were actively engaged in the experiment. The majority of students participated in the activity because they wanted to, not because they were instructed to. N = 76. Most of the students felt they learned something about science. N = 22.

Table 1: Nematode chemotaxis results using the microfluidic channels

	Number of nematodes in agar side	**Number of nematodes in chemoeffector side**	**Chemotaxis Index**
Waxworm Extract	3	1	0.25
	1	8	0.89
	0	4	1.00
Vinegar (5% acetic acid)	10	0	0
	10	1	0.09
	7	0	0
Water	9	2	0.18
	6	0	0
	10	3	0.23

REFERENCES

1. Saffo MB. Mutualistic Symbioses. Encyclopedia of Life Sciences, 2014.

2. Fautin DG. The anemonefish symbiosis: what is known and what is not. Symbiosis. 1991;10:23-46.

3. Miller A. Intricate relationship allows the other to flourish: the sea anemone and the clownfish [Available from: http://www.asknature.org/strategy/fb410d8500af30a5daf5b647954b7fa5.

4. Mengesha YA. A study of oxpecker-mammal symbiosis in Ethiopia. East African Agricultural and Forestry Journal. 1978;43:321-7.

5. Chen ZX, Chen SY, Dickson DW. Nematology: Advances and Perspectives: Tsinghua University Press; 2004.

6. Dillman AR, Sternberg PW. Entomopathogenic nematodes. Current biology : CB. 2012;22:R430-1.

7. Ehlers RU. Mass production of entomopathogenic nematodes for plant protection. Applied microbiology and biotechnology. 2001;56:623-33.

8. Hirao A, Ehlers RU. Effect of temperature on the development of Steinernema carpocapsae and Steinernema feltiae (Nematoda: Rhabditida) in liquid culture. Applied microbiology and biotechnology. 2009;84:1061-7.

9. Hui E, Webster JM. Influence of insect larvae and seedling roots on the host-finding ability of Steinernema feltiae (Nematoda: Steinernematidae). Journal of invertebrate pathology. 2000;75:152-62.

10. Hallem EA, Dillman AR, Hong AV, Zhang Y, Yano JM, DeMarco SF, et al. A sensory code for host seeking in parasitic nematodes. Current biology : CB. 2011;21(5):377-83.

11. Shapiro-Ilan DI, Gaugler R. "Nematodes." Biological Control: A Guide to Natural Enemies in North America: Cornell University College of Agricultural and Life Sciences; [Available from: https://biocontrol.entomology.cornell.edu/pathogens/nematodes.php.

12. Lee DL. The Biology of Nematodes: Taylor & Francis; 2002.

13. Lacey LA, Georgis R. Entomopathogenic Nematodes for Control of Insect Pests Above and Below Ground with Comments on Commercial Production. Journal of Nematology. 2012;44:218-25.

14. Kim SK, Flores-Lara Y, Patricia Stock S. Morphology and ultrastructure of the bacterial receptacle in Steinernema nematodes (Nematoda: Steinernematidae). Journal of invertebrate pathology. 2012;110:366-74.

15. Gaugler R. Virulence Mechanisms. Entomopathogenic Nematology: CABI; 2002.

16. San-Miguel A, Lu H. Microfluidics as a tool for C. elegans research. WormBook : the online review of C elegans biology. 2013:1-19.

17. Whitesides GM. The origins and the future of microfluidics. Nature. 2006;442(7101):368-73.

18. Abate AR, Hung T, Sperling RA, Mary P, Rotem A, Agresti JJ, et al. DNA sequence analysis with droplet-based microfluidics. Lab Chip. 2013;13:4864-9.

19. Elvira KS, Casadevall i Solvas X, Wootton RC, deMello AJ. The past, present and potential for microfluidic reactor technology in chemical synthesis. Nature chemistry. 2013;5:905-15.

20. Feng ZV, Edelman KR, Swanson BP. Student-Fabricated Microfluidic Devices as Flow Reactors for Organic and Inorganic Synthesis. Journal of Chemical Education. 2015;92:723-7.

21. Falkovich G. Fluid Mechanics: A Short Course for Physicists: Cambridge University Press; 2011.

22. Xia Y, Whitesides, G.M. Soft Lithography. Angewandte Chemie International Edition. 1998;37:550-75.

23. Stilwell MD, Nepper JF, Clawson ED, Blair V, Tangen T, Weibel DB. Exploring predatory nematode chemotaxis using low-cost and easy-to-use microfluidics. American Biology Teacher. 2017;79.

24. Kruitbos LM, Heritage S, Hapca S, Wilson MJ. The influence of habitat quality on the foraging strategies of the entomopathogenic nematodes Steinernema carpocapsae and Heterorhabditis megidis. Parasitology. 2010;137(2):303-9.

25. Purcell EM. Life at low Reynolds number. American Journal of Physics. 1977;45:9.

26. Park JS, Kim D, Shin JH, Weitz DA. Efficient nematode swimming in a shear thinning colloidal suspension. Soft Matter. 2016;12(6):1892-7.

27. Hida H, Nishiyama H, Sawa S, Higashiyama T, Arata H. Chemotaxis assay of plant-parasitic nematodes on a gel-filled microchannel device. Sensors and Actuators B: Chemical. 2015;221:1483-91.

28. McMullen JG, 2nd, Stock SP. In vivo and in vitro rearing of entomopathogenic nematodes (Steinernematidae and Heterorhabditidae). Journal of visualized experiments : JoVE. 2014(91):52096.

29. Sanders ER. Aseptic laboratory techniques: plating methods. J Vis Exp. 2012(63):e3064.

30. Sicard M, Hinsinger J, Le Brun N, Pages S, Boemare N, Moulia C. Interspecific competition between entomopathogenic nematodes (Steinernema) is modified by their bacterial symbionts (Xenorhabdus). BMC Evol Biol. 2006;6:68.

CHAPTER 6

Conclusions and Future Directions

Bacteria regulate their cell size and shape to help them adapt to their environment (1-3). Small changes in bacterial cell size and shape can have drastic energetic costs on the organism (4). Bacteria respond to changing environmental conditions by changing their cell size and shape to give them a competitive advantage in the new environment (1, 3). For example, *Proteus mirabilis* alters its cell size when it transitions to a state associated with increased virulence (5). Other pathogenic organisms, such as *Candida albicans*, alter their shape and size as part of their virulence mechanisms (6). A better understanding of the genes, proteins, and pathways that dictate cell shape and size may provide us with novel mechanisms of virulence inhibitors. Drugs could be designed to alter or prevent cell shape changes, potentially reducing virulence and bettering patient outcomes.

If different shapes and sizes confer selective advantages to bacteria in different environments, which evidence seems to suggest (1-3), then perhaps we can take advantage of cell shape and size to engineer bacteria for new uses. One could potentially impart a beneficial cell shape and/or size to easily modifiable organisms, like *E. coli* or *C. crescentus*, to help them adapt to toxic environments for bioremediation or material development purposes.

In Chapter 2, we investigated the cell division regulator MipZ in *C. crescentus* (7, 8). We began by following up on preliminary data that suggested the MipZ proteins might be oscillating similar to, but to a lesser extent than, the Min system in *E. coli*. We

performed time-lapse microscopy on cells expressing MipZ-eYFP and performed cross-correlation analyses and fast Fourier transforms of those correlations to determine to what extent the proteins were oscillating. We found that MipZ does not oscillate in the cell, although we did observe protein flux between the two poles. These results are in good agreement with our current understanding of oscillating systems (9-11).

We then attempted to measure the biophysical parameters of the MipZ system in order to recreate the observed, asymmetric, bipolar gradient *in silico*. We used single particle tracking photoactivatable localization microscopy (sptPALM) to track MipZ-Dendra2 molecules in the cell and get estimates for the diffusion coefficients of the different states of the molecule and the rates at which the molecules switch between these states (12, 13). We were mildly successful, showing that MipZ exists in two diffusive states: one slow, DNA-bound state and one fast, freely diffusing state. Using an analytical model of a reaction-diffusion system, we recreated the observed, asymmetric MipZ gradient using biophysical parameters from our experiments and from the literature. The model we developed yielded results similar to those of Shtylla (14).

In an attempt to better understand the nature of the asymmetric MipZ gradient, we performed wide-field epifluorescence microscopy on MipZ-Dendra2, ParB-eGFP, and PopZ-mCherry. We found several novel features of the *C. crescentus* division site location regulation pathway. First, we found that the cell width is non-uniform along

the length of the cell in both wild-type and mutants lacking TipN, which was assumed in the model of Shtylla (14). The change in cell width may not drastically alter her model, but it is worth noting that data from other groups and work presented in this thesis have found the cell width to decrease as the point in the cell is farther from the stalked pole (15). We observed the MipZ gradient to be asymmetric, such that the minimum between the two poles was shifted towards the new pole, as has been reported previously (7, 8, 16). Surprisingly, we found that the distribution of ParB also yielded a gradient with a mid-cell minimum shifted towards the new pole. We also found that the distribution of PopZ was unevenly distributed, such that the minimum was shifted even further towards the new pole than for MipZ or ParB. We quantified the ratio of fluorescence intensity at the stalked pole to the fluorescence intensity at the swarmer pole and found that for MipZ, ParB, and PopZ, the ratio was greater than one. For PopZ, this result was to be expected, as PopZ slowly accumulates at the new pole over the course of the cell cycle (17). Our observation of this ratio is the first such report for either ParB or MipZ.

We performed wide-field epifluorescence microscopy on cells lacking the polar landmark protein TipN as well (18). We found that the cell width followed a similar pattern as for wild-type cells (15). The stalked to swarmer pole fluorescence intensity ratios were all greater than one in these mutants. We observed that the minimums of

the MipZ, ParB, and PopZ gradients were skewed towards the old pole, with the PopZ gradient being shifted further than the MipZ or ParB gradients.

We envision the next steps for understanding the asymmetric MipZ gradient and subsequent asymmetric positioning of the FtsZ-ring in *C. crescentus* to focus on testing the model set forth by Shtylla (14). Shtylla hypothesizes that the asymmetric MipZ gradient arises from competitive interactions between MipZ and ParA for ParB binding sites (14). Studies performed *in vitro* could help provide information on the competitive interactions between MipZ and ParA for ParB. Mutants with inducible ParA expression would enable ParA levels to be gradually increased in the cell. The MipZ gradient and the division ratio for these mutants could be measured, providing more insight into how ParA levels affect the location of cell division. The effect of non-uniform cell width and asymmetric ParB distribution on the model could also be tested, although these effects may be negligible.

The model proposed by Shytlla does not help us understand how the ParB distribution becomes asymmetric (14). Future experiments involving time-lapse microscopy on MipZ, ParB, and PopZ may provide more clues as to how this phenomenon arises. DNA binding by ParB may differ depending on DNA-bound proteins or some post-translational modifications that affect its affinity for the chromosomes.

Bacteria navigate complex environments in search of food and safety. Chemotaxis is a fundamental aspect of this search for survival (19). Other organisms use chemotaxis systems to control genes associated with virulence, expressing those genes when the organism finds itself within the target host (20, 21). Many species of bacteria contain a plethora of chemotaxis receptors, but their specific function is unknown (22, 23). Future studies of bacterial chemotaxis will enable us to understand the greater effect of chemotaxing bacteria on key geochemical processes, such as nitrogen cycling, and may enable us to use novel drugs to prevent certain bacteria from recognizing their target hosts (24, 25). Traditional chemotaxis assays are low throughput and technically challenging, making the assignment of signal to receptor quite difficult (26). Microfluidic chemotaxis devices have the potential to greatly increase the speed and accuracy with which we determine signal-receptor pairs (25).

In Chapter 3, we present a high-throughput microfluidic device that creates multiple, stable chemical gradients that are sustained for hours at a time (23). We use this device to measure the response of *E. coli* to various chemicals and demonstrate that our device measures bacterial chemotaxis as well as, if not better than, traditional capillary assays, while also removing the need for technical finesse and sources of potential error. Using our device, we found that bacteria tune their global chemotaxis strategy depending on their culturing conditions.

We envision this microfluidic device being used for high-throughput screens to determine the function of unknown chemoreceptors in a wide array of organisms. Higher throughput devices, such as the one we present in Chapter 3, will enable faster screens of small molecules, which will be instrumental for determining the function of chemical receptors (25). For instance, *Vibrio fischeri* responds to many different chemicals, but many of its chemical receptors are of unknown function (19). We envision our device having the capability to determine the function of these proteins. The device we present is easy to operate and can easily be adapted for other uses. We think the ease-of-use will make our device accessible to many laboratories and we look forward to the creative uses of the device that other labs generate.

Symbiosis is a fundamental part of every ecological niche (27). Switching between the two extremes of symbiosis, i.e. pathogenesis and mutualism, is observed in bacteria, but the mechanisms these organisms use to do so is unclear (28-30). These switching events typically occur during host transfer, but many of the molecular details are unclear (31-33). Increasing our fundamental understanding of this switch will have applications spanning agriculture, human health, and ecology (34, 35).

In Chapter 4, we present a microfluidic device capable of isolating and maintaining individual, living nematodes for weeks-long experiments. Using the device, we performed epifluorescence microscopy on the symbiotic bacteria within a specialized pocket of the intestine, i.e. the receptacle, over five days. We also

demonstrated the ability of the microfluidic device to enable confocal microscopy of bacteria within living nematodes, and do so over three weeks. We observed bacterial outgrowth within living nematodes initiating from a few founder cells, giving credence to the colonization bottleneck hypothesis that few cells begin the colonization process and grow to fill the receptacle (36). With the aid of the device, we observed dynamic bacterial outgrowth and persistence, indicating that cells within the bacterial population may be growing and dying in alternating periods within the nematode host. The reason for these observed dynamics are still unclear and will require future experimentation with increased spatiotemporal resolution.

Future experiments using this microfluidic device are numerous, but we will list a few here that we think will be of some value. First, investigating the dynamic bacterial outgrowth within the receptacle would help differentiate between a few models of outgrowth. Nematodes cultured on bacterial lawns containing clones expressing different colors of fluorescent proteins would enable real-time visualization of bacterial outgrowth in receptacles, terminating with mono- or bi-clonal populations of bacteria (36, 37).

Second, the global genetic regulator Lrp controls the phenotypic variation of X. nematophila (32). Mutants with a dual color fluorescence reporter would enable detailed insight into how the bacterial population switches between pathogenesis and mutualism. One fluorescence protein within the cell would act as a baseline while the

other would be controlled by an Lrp-dependent gene and serve as a proxy for virulence. Fluorescence could be monitored in individual nematodes during bacterial outgrowth using our microfluidic device. These experiments would provide a unique, real-time view into the mutualistic/pathogenic switch in bacteria-animal symbioses.

Third, introduction of hemolymph into microfluidic devices containing nematodes cultured with these dual color reporter bacteria would enable the observation of global genetic changes of the bacteria in the living host. Experiments of this kind could potentially reveal the bacterial population altering their genetic profile in preparation for the next round of insect killing.

Engaging, hands-on science activities are vital to bringing new people into science, as well as for garnering interest in science among the public (38). These activities can be difficult to develop, especially at a price point that public educators can afford on small budgets (38). Additionally, engaging, quantitative experiments in biology can be challenging to organize in a classroom setting, as many organisms are large and difficult to care for in a school environment (39). Nevertheless, if we hope to build a strong community of scientists and engaged citizens, we must create activities that will educate and engage. Microfluidics can offer precision to enable these types of activities in classrooms (38). Traditional methods of microfluidic device fabrication are prohibitively expensive for classroom use (40).

In Chapter 5, we present engaging, quantitative biology activities using microfluidics. The method of microfluidic device fabrication we employ enables rapid prototyping with inexpensive materials. Our activities enable students to probe the behavior of living nematodes to external chemical and electrical stimuli in a quantitative manner and in a period of time that fits into most classroom periods. We implemented these activities in a local outreach setting and evaluated the activities based on anonymous responses from the student participants.

The activities we present can be expanded to teach other concepts of microbiology, ecology, and fluid dynamics using steps we outline in Chapter 5. For instance, the microfluidic device enables the study of other species of nematodes and their responses to other stimuli. These activities encourage students to think creatively, experiment with new ideas, and hopefully piques their interest to engage with science.

New methodologies, such as single molecule tracking or microfluidics, enable new insights into our world. Endless surprises and wonder pervade all scales of the universe, waiting to be discovered. Novel ways of studying the universe are the keys to unlock the doors of the unknown. I believe new approaches, like those outlined in this dissertation, are vital to exploring and appreciating the beauty all around us.

REFERENCES

1. Young KD. The selective value of bacterial shape. Microbiol Mol Biol Rev. 2006;70(3):660-703.

2. Young KD. Bacterial morphology: why have different shapes? Curr Opin Microbiol. 2007;10(6):596-600.

3. Yang DC, Blair KM, Salama NR. Staying in Shape: the Impact of Cell Shape on Bacterial Survival in Diverse Environments. Microbiol Mol Biol Rev. 2016;80(1):187-203.

4. Mitchell JG. The energetics and scaling of search strategies in bacteria. Am Nat. 2002;160(6):727-40.

5. Schaffer JN, Pearson MM. Proteus mirabilis and Urinary Tract Infections. Microbiol Spectr. 2015;3(5).

6. Hogan DA, Vik A, Kolter R. A Pseudomonas aeruginosa quorum-sensing molecule influences Candida albicans morphology. Mol Microbiol. 2004;54(5):1212-23.

7. Thanbichler M, Shapiro L. MipZ, a spatial regulator coordinating chromosome segregation with cell division in Caulobacter. Cell. 2006;126(1):147-62.

8. Kiekebusch D, Michie KA, Essen LO, Lowe J, Thanbichler M. Localized dimerization and nucleoid binding drive gradient formation by the bacterial cell division inhibitor MipZ. Mol Cell. 2012;46(3):245-59.

9. Loose M, Fischer-Friedrich E, Ries J, Kruse K, Schwille P. Spatial regulators for bacterial cell division self-organize into surface waves in vitro. Science. 2008;320(5877):789-92.

10. Bonny M, Fischer-Friedrich E, Loose M, Schwille P, Kruse K. Membrane binding of MinE allows for a comprehensive description of Min-protein pattern formation. PLoS Comput Biol. 2013;9(12):e1003347.

11. Zieske K, Schwille P. Reconstitution of self-organizing protein gradients as spatial cues in cell-free systems. Elife. 2014;3.

12. Manley S, Gillette JM, Lippincott-Schwartz J. Single-particle tracking photoactivated localization microscopy for mapping single-molecule dynamics. Methods Enzymol. 2010;475:109-20.

13. Flomenbom O, Klafter J, Szabo A. What can one learn from two-state single-molecule trajectories? Biophys J. 2005;88(6):3780-3.

14. Shtylla B. Mathematical modeling of spatiotemporal protein localization patterns in C. crescentus bacteria: A mechanism for asymmetric FtsZ ring positioning. J Theor Biol. 2017;433:8-20.

15. Wright CS, Banerjee S, Iyer-Biswas S, Crosson S, Dinner AR, Scherer NF. Intergenerational continuity of cell shape dynamics in Caulobacter crescentus. Sci Rep. 2015;5:9155.

16. Schofield WB, Lim HC, Jacobs-Wagner C. Cell cycle coordination and regulation of bacterial chromosome segregation dynamics by polarly localized proteins. EMBO J. 2010;29(18):3068-81.

17. Bowman GR, Comolli LR, Zhu J, Eckart M, Koenig M, Downing KH, et al. A polymeric protein anchors the chromosomal origin/ParB complex at a bacterial cell pole. Cell. 2008;134(6):945-55.

18. Lam H, Schofield WB, Jacobs-Wagner C. A landmark protein essential for establishing and perpetuating the polarity of a bacterial cell. Cell. 2006;124(5):1011-23.

19. Wadhams GH, Armitage JP. Making sense of it all: bacterial chemotaxis. Nat Rev Mol Cell Biol. 2004;5(12):1024-37.

20. Aihara E, Closson C, Matthis AL, Schumacher MA, Engevik AC, Zavros Y, et al. Motility and chemotaxis mediate the preferential colonization of gastric injury sites by Helicobacter pylori. PLoS Pathog. 2014;10(7):e1004275.

21. Josenhans C, Suerbaum S. The role of motility as a virulence factor in bacteria. Int J Med Microbiol. 2002;291(8):605-14.

22. Lacal J, Garcia-Fontana C, Munoz-Martinez F, Ramos JL, Krell T. Sensing of environmental signals: classification of chemoreceptors according to the size of their ligand binding regions. Environ Microbiol. 2010;12(11):2873-84.

23. Crooks JA, Stilwell MD, Oliver PM, Zhong Z, Weibel DB. Decoding the Chemical Language of Motile Bacteria by Using High-Throughput Microfluidic Assays. Chembiochem. 2015;16(15):2151-5.

24. Stocker R, Seymour JR. Ecology and physics of bacterial chemotaxis in the ocean. Microbiol Mol Biol Rev. 2012;76(4):792-812.

25. Bi S, Yu D, Si G, Luo C, Li T, Ouyang Q, et al. Discovery of novel chemoeffectors and rational design of Escherichia coli chemoreceptor specificity. Proc Natl Acad Sci U S A. 2013;110(42):16814-9.

26. Adler J. A method for measuring chemotaxis and use of the method to determine optimum conditions for chemotaxis by Escherichia coli. J Gen Microbiol. 1973;74(1):77-91.

27. McFall-Ngai M, Hadfield MG, Bosch TC, Carey HV, Domazet-Loso T, Douglas AE, et al. Animals in a bacterial world, a new imperative for the life sciences. Proc Natl Acad Sci U S A. 2013;110(9):3229-36.

28. Goodrich-Blair H, Clarke DJ. Mutualism and pathogenesis in Xenorhabdus and Photorhabdus: two roads to the same destination. Mol Microbiol. 2007;64(2):260-8.

29. Herbert EE, Goodrich-Blair H. Friend and foe: the two faces of Xenorhabdus nematophila. Nat Rev Microbiol. 2007;5(8):634-46.

30. Newton AC, Fitt BD, Atkins SD, Walters DR, Daniell TJ. Pathogenesis, parasitism and mutualism in the trophic space of microbe-plant interactions. Trends Microbiol. 2010;18(8):365-73.

31. Park Y, Herbert EE, Cowles CE, Cowles KN, Menard ML, Orchard SS, et al. Clonal variation in Xenorhabdus nematophila virulence and suppression of Manduca sexta immunity. Cell Microbiol. 2007;9(3):645-56.

32. Hussa EA, Casanova-Torres AM, Goodrich-Blair H. The Global Transcription Factor Lrp Controls Virulence Modulation in Xenorhabdus nematophila. J Bacteriol. 2015;197(18):3015-25.

33. Cao M, Patel T, Rickman T, Goodrich-Blair H, Hussa EA. High Levels of the Xenorhabdus nematophila Transcription Factor Lrp Promote Mutualism with the Steinernema carpocapsae Nematode Host. Appl Environ Microbiol. 2017;83(12).

34. Beck JJ, Vannette RL. Harnessing Insect-Microbe Chemical Communications To Control Insect Pests of Agricultural Systems. J Agric Food Chem. 2017;65(1):23-8.

35. Chaston J, Goodrich-Blair H. Common trends in mutualism revealed by model associations between invertebrates and bacteria. FEMS Microbiol Rev. 2010;34(1):41-58.

36. Martens EC, Heungens K, Goodrich-Blair H. Early colonization events in the mutualistic association between Steinernema carpocapsae nematodes and Xenorhabdus nematophila bacteria. J Bacteriol. 2003;185(10):3147-54.

37. Chaston JM, Murfin KE, Heath-Heckman EA, Goodrich-Blair H. Previously unrecognized stages of species-specific colonization in the mutualism between Xenorhabdus bacteria and Steinernema nematodes. Cell Microbiol. 2013;15(9):1545-59.

38. Yang CW, Ouellet E, Lagally ET. Using inexpensive Jell-O chips for hands-on microfluidics education. Anal Chem. 2010;82(13):5408-14.

39. Mengesha YA. A Study of Oxpecker-Mammal Symbiosis in Ethiopia. East African Agricultural and Forestry Journal. 1978;43(4):321-6.

40. Xia Y, Whitesides, G.M. Soft Lithography. Angewandte Chemie International Edition. 1998;37:550-75.